Downloaded from orbit.dtu.dk on: May 05, 2023

DTU Library

Phase Transformations in Supermartensitic Stainless Steels

Nießen, Frank

Publication date:
2018

Document Version
Publisher's PDF, also known as Version of record

Link back to DTU Orbit

Citation (APA):
Nießen, F. (2018). *Phase Transformations in Supermartensitic Stainless Steels*. Technical University of Denmark.

General rights
Copyright and moral rights for the publications made accessible in the public portal are retained by the authors and/or other copyright owners and it is a condition of accessing publications that users recognise and abide by the legal requirements associated with these rights.

- Users may download and print one copy of any publication from the public portal for the purpose of private study or research.
- You may not further distribute the material or use it for any profit-making activity or commercial gain
- You may freely distribute the URL identifying the publication in the public portal

If you believe that this document breaches copyright please contact us providing details, and we will remove access to the work immediately and investigate your claim.

Phase Transformations in Supermartensitic Stainless Steels

PhD Thesis

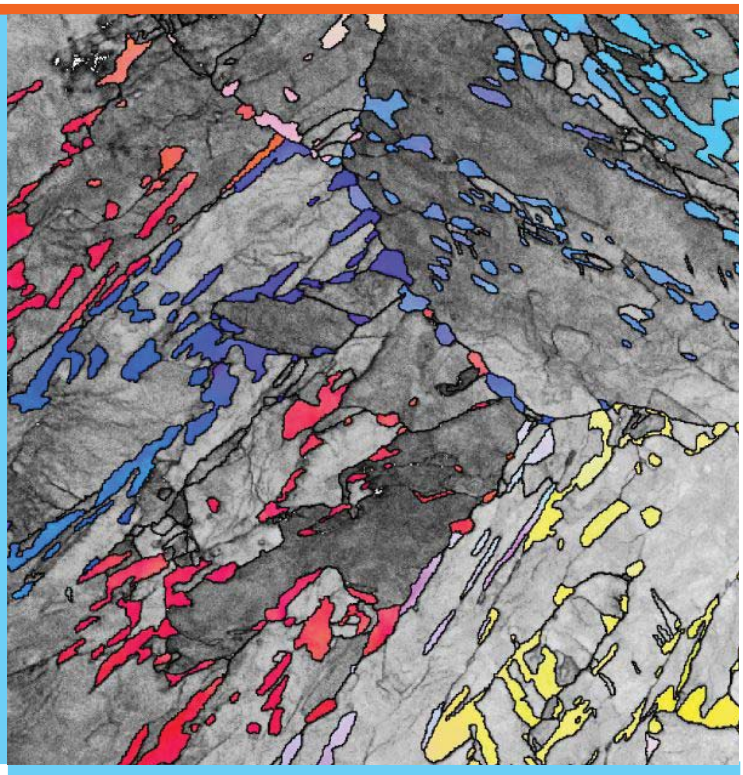

Frank Nießen
April 2018

DTU Mechanical Engineering
Department of Mechanical Engineering

PHASE TRANSFORMATIONS IN SUPERMARTENSITIC STAINLESS STEELS

A THESIS SUBMITTED TO THE TECHNICAL UNIVERSITY OF DENMARK FOR THE DEGREE OF DOCTOR OF PHILOSOPHY IN THE DEPARTMENT OF MECHANICAL ENGINEERING

April 2018

By

Frank Nießen

Technical University of Denmark

Department of Mechanical Engineering

Section of Materials and Surface Engineering

Phase transformations in supermartensitic stainless steels

A doctoral thesis by

Frank Nießen
E-mail: contact@fniessen.com
Technical University of Denmark
Danish Hydrocarbon Research and Technology Centre
Building 425, room 111
DK-2800 Kgs. Lyngby

Principal Supervisor:

Prof. Marcel A.J. Somers
E-Mail: somers@mek.dtu.dk
Technical University of Denmark
Department of Mechanical Engineering
Produktionstorvet
Building 425, room 120
DK-2800 Kgs. Lyngby

Co-Supervisor:

Prof. John Hald
E-Mail: jhald@mek.dtu.dk
Technical University of Denmark
Department of Mechanical Engineering
Produktionstorvet
Building 425, room 121
DK-2800 Kgs. Lyngby

Copyright:	Reproduction of this publication in whole or in part must include the customary bibliographic citation, including author attribution, Phase transformations in supermartensitic stainless steels.
Published by:	Department of Mechanical Engineering, Section of Materials and Surface Engineering, Produktionstorvet, Building 425, DK-2800 Kgs. Lyngby

Preface

This doctoral thesis is submitted in partial fulfilment of the requirements for obtaining the degree of PhD at the Department of Mechanical Engineering at the Technical University of Denmark (DTU). The project was funded by the Danish Hydrocarbon Research and Technology Centre, DTU, and was partially carried out the Danish Hydrocarbon Research and Technology Centre and the Department of Mechanical Engineering, Section of Materials and Surface Engineering, during the period June 1st 2015 to April 30th 2018. The project was supervised by Prof. Marcel A.J. Somers and Prof. John Hald from the Department of Mechanical Engineering, Section of Materials and Surface Engineering, at the Technical University of Denmark (DTU).

Frank Nießen
Kongens Lyngby, Denmark, April 30th, 2018

Declaration

I declare that, if not explicitly stated, none of the presented work in this doctoral thesis has been submitted in support of an application for another degree of this or any other university. I further declare that the presented work is my own work and that I have correctly acknowledged work of others.

Abstract

This doctoral thesis presents research work that elucidates the major phase transformations in supermartensitic stainless steels and their impact on the mechanical properties. Supermartensitic stainless steels are martensitic steels with particularly low C and N content and are based on the Fe-Cr-Ni system. This class of steels is weldable, strong, tough and shows good resistance to wet-corrosion. Thus, it is of special interest for off-shore applications in the oil and gas industry.

Supermartensitic stainless steels solidify as δ-ferrite, transform largely to austenite during cooling above A_3 and transform almost entirely to martensite during cooling to room temperature. In this condition, the material is hard and brittle. The above listed properties are obtained by annealing the material in the inter-critical temperature region (in between A_1 and A_3), by which the material is softened as a result of tempering of martensite and partial reversion of austenite at grain boundaries. Just above A_1 reverted austenite forms enriched in Ni in an attempt to fulfill thermodynamic equilibrium. Partitioning of Ni stabilizes reverted austenite against martensite transformation during cooling to room temperature.

In the present work, the most relevant phase transformations were analyzed and are presented in the order of their occurrence during materials processing. A first study investigated the kinetics of the δ-ferrite-to-austenite transformation during solidification and cooling with the aim of predicting the amount of retained δ-ferrite at room temperature. Another study concerned the in-situ measurement of the evolution of lattice strains and stresses in austenite and martensite during martensite formation. Subsequently, tempering of martensite was studied by analyzing the redistribution of interstitial elements, C and N, relaxation of phase-specific stresses and recovery of the martensite substructure.

The role of Ni-diffusion in austenite reversion from lath martensite was clarified by conducting kinetics analysis of austenitization during isochronal heating. Two distinct stages of transformation were observed experimentally and predicted by kinetics modeling and were found to be governed by redistribution of Ni. Microstructure characterization of inter-critically annealed samples revealed austenite formation as thin films on lath boundaries and other grain boundaries. Analysis of compositional measurements indicated that reverted austenite is mainly stabilized by a redistribution of Ni. The stable fraction of reverted austenite at room-temperature was not noticeably affected by immersion in boiling N_2, but progressively reduced during holding at 194.5 K. Strain-induced martensite formation from reverted austenite during tensile testing of differently annealed conditions was studied in-situ with in-situ synchrotron X-ray diffraction. The experiments yielded data on stress-partitioning, evolution of the substructure, and anisotropy of lattice strains of austenite and martensite, which could be associated to the macroscopic stress.

Finally, the presented research contains a study on the recently developed materials characterization method transmission Kikuchi diffraction in on-axis configuration.

Resumé

Denne afhandling præsenterer forskning, som belyser de væsentligste faseomdannelser i supermartensitisk rustfrit stål og deres betydning for de mekaniske egenskaber. Supermartensitisk rustfrit stål er martensitiske stål med særligt lavt indhold af C og N og de er baseret på Fe-Cr-Ni systemet. Denne klasse af stål har god svejsbarhed, høj styrke og sejhed og udviser god korrosionsbestandighed. Derfor er materialet særligt interessant for olie- og gasindustrien.

Supermartensitisk rustfrit stål størkner som δ-ferrit, som under videre afkøling stort set omdannes til austenit over A_3 temperaturen. Austenitten transformeres næsten fuldstændigt til listemartensit under afkøling til stuetemperatur. I denne tilstand er materialet hårdt og sprødt. De endelige mekaniske egenskaber opnås ved varmbehandling i det inter-kritiske temperatur interval (mellem A_1 og A_3), og det gør materialet blødere, ved anløbning af martensitten og ved dannelse af en begrænset mængde af reverseret austenit på korngrænser. Austenitten dannes lige over A_1 med et forøget indhold af Ni for at opfylde termodynamisk ligevægt. Det forøgede Ni indhold stabiliserer den reverserede austenit mod martensit dannelse ved afkøling til stuetemperatur.

I dette arbejde er de mest relevante faseomdannelser blevet analyseret og de præsenteres i den rækkefølge, som forekommer ved materialets behandlings proces. Først blev kinetikken af δ-ferrit-til-austenit omdannelsen under størkning og afkøling analyseret for at forudsige δ-ferrit indholdet ved stuetemperatur. En anden undersøgelse omhandlede in-situ målinger af tøjnings- og spændings-forløbet i austenit og martensit under martensittransformationen. Derefter blev anløbningen af martensit undersøgt ved at analysere omfordelingen af de interstitielle elementer, C og N, relaksation af fase-specifikke spændinger og ændringer i den martensitiske substruktur.

Betydningen af Ni-diffusion for dannelsen af reverseret austenit ud fra listemartensit blev klarlagt ved at udføre kinetisk analyse af austenitdannelse under kontinuerlig opvarmning. To distinkte transformations trin blev observeret eksperimentelt og forudsagt ved kinetisk modellering. Det blev fundet, at den trinvise omdannelse styres af omfordelingen af Ni. Karakterisering af mikrostrukturen af inter-kritisk varmebehandlede emner viste, at reverseret austenit dannes i form af tynde film på martensitliste grænser og på andre korngrænser. Analyser af lokale kemiske sammensætninger viste, at reverseret austenit hovedsageligt stabiliseres af opkoncentreringen af Ni. Den stabile faseandel af reverseret austenit ved stuetemperatur blev ikke påvirket af nedsænkning i kogende nitrogen, men reduceredes med tid ved en konstant temperatur på 194.5 K. Tøjnings-induceret omdannelse af reverseret austenit til martensit under trækprøvning af forskellige varmebehandlede emner blev målt in-situ med synkrotron røntgendiffraktion. Forsøget frembragte data om fordeling af indre spændinger på austenit og martensit, udvikling af substrukturen og anisotropi af gittertøjninger i austenit og martensit, som kunne henføres til den makroskopiske spænding.

Det præsenterede forskningsarbejde indeholder desuden en undersøgelse af Transmission Kikuchi Diffraction (TKD) i on-axis konfiguration, som er en nyligt udviklet metode til materialekarakterisering.

Acknowledgements

At first I would like to express my sincere gratitude towards my principal supervisor Prof. Marcel A.J. Somers for his knowledgeable guidance, inspiring passion for science and reliable support throughout the project. He encouraged me to follow my own ideas and supported my initiatives, which was a great motivation for me. He gave me the proper attention and supported me with competent guidance, whenever it was required. I could not have asked for a better advisor and mentor.

I am equally grateful for the support I received from my co-supervisor, Prof. John Hald. He was an inspiring source of knowledge and an important point of guidance. I am especially thankful for his early support during the time leading up to this project, in which he was an encouraging key figure that sparked my enthusiasm for metallurgical research.

I would like to thank the Danish Hydrocarbon Research and Technology Centre for the initiation, funding and continued support of this project. I want to in particular express my gratitude for the support from my manager Lars Simonsen and secretary Helle Baumann.

I wish to express my gratitude towards Dr. Hemantha Kumar Yeddu (Newcastle University, England) for being a supportive co-supervisor in the early stage of the project and for the continuing collaboration beyond this stage. I would further like to thank Dr. Matteo Villa, for his enthusiastic and inspiring support of this project, for productive scientific and non-scientific discussions, for his contribution with magnetometry measurements and for great collaborations and late night shifts at the synchrotron beamline.

This project would not have been nearly as successful without the support of numerous external research partners. Prof. Christoph Genzel, Dr. Manuela Klaus and Dr. Daniel Apel (Helmholtz Zentrum Berlin, BESSY II) are gratefully acknowledged for their assistance during synchrotron measurements at the EDDI beamline. Prof. Olaf Kessler, Dr. Michael Reich and Kristin Aurich (University of Rostock, Germany) are acknowledged for their support with dilatometry measurements. Dr. Frédéric Danoix (CNRS, Normandie University, UNIROUEN, France) is acknowledged for supporting this project with atom probe tomography analysis. I would like to thank Dr. Ricardo Lebensohn (Los Alamos National Laboratory, USA) for teaching me about numerical modeling of crystal plasticity and his support with modeling activities. Dr. Alice Bastos da Silva Fanta and Adam Fuller (CEN, DTU) are acknowledged for their support with transmission Kikuchi diffraction and technical support in electron microscopy, respectively. Dr. Rasmus Normann Wilken Eriksen (DTU, MEK) is acknowledged for his support with the digital image correlation technique.

I would further like to thank my colleagues at the Section of Materials and Surface Engineering, not only for their assistance and fruitful discussions, but also for providing a pleasant working environment. I in particular want to thank Dr.-Ing. Karen Pantleon and

Dr.-Ing Wolfgang Pantleon for sharing their knowledge on X-ray diffraction, Dr. Kristian Vinter Dahl for support in thermodynamics modeling, Flemming Bjerg Grumsen for support in advanced materials characterization, Gitte Salomon for administrative support, Steffen Munch for support in the metallographic laboratory and Lars Pedersen for his support in the workshop. I am grateful for having shared office 111 (the best office in building 425) with some fantastic people that made work an enjoyable place. A particular thanks goes to the several teams of synchrotron enthusiasts, with which I had the pleasure to spend days and nights acquiring diffractograms: Dr. Matteo Villa, Dr.-Ing. Karen Pantleon, Dr. Chitta Ranjan Das, Dr. Sunday Chukwudi Okoro, Jacob Obitsø Nielsen, Chloé Devos and Yichen Meng.

Last but not least, a sincere thanks goes to my family for their support since day one and to my partner Jaqueline for her love and support.

List of published articles and conference contributions

Peer-reviewed articles included in this thesis in chronological order:

1. **F. Niessen**, M. Villa, J. Hald, M.A.J. Somers, Kinetics analysis of two-stage austenitization in supermartensitic stainless steel, Mater. Des. 116 (2017) 8–15.
2. **F. Niessen**, N.S. Tiedje, J. Hald, Kinetics modeling of delta-ferrite formation and retainment during casting of supermartensitic stainless steel, Mater. Des. 118 (2017) 138–145.
3. M. Villa, **F. Niessen**, M.A.J. Somers, In situ investigation of the evolution of lattice strain and stresses in austenite and martensite during quenching and tempering of steel, Metall. Mater. Trans. A. 49 (2017) 1–13.
4. **F. Niessen**, A. Burrows, A.B. da S. Fanta, A systematic comparison of on-axis and off-axis transmission Kikuchi diffraction, Ultramicroscopy. 186 (2018) 158–170.
5. **F. Niessen**, Austenite reversion in low-carbon martensitic stainless steels – a CALPHAD-assisted review, Materials Science and Technology. (2018), doi: 10.1080/02670836.2018.1449179

Non peer-reviewed article included in this thesis:

1. **F. Niessen**, F.B. Grumsen, J. Hald, M.A.J. Somers, Formation and stabilization of reversed austenite in supermartensitic stainless steel, in: Proc. 24th IFHTSE Congr., 2017: pp. 138–145.

Conference contributions in chronological order:

1. Oral and poster presentation, THERMEC'2016, Graz, Austria, May 31st and June 1st 2016
2. Oral presentation, 24th IFHTSE congress 2017, Nice, France, June 28th 2017
3. Poster presentation, 7th European atom probe workshop, Gullmarstrand, Sweden, October 3rd 2017
4. Oral presentation, TMS 2018 Annual Meeting, Phoenix, Arizona, USA, March 12th 2018
5. Oral presentation, RMS EBSD Meeting 2018, Plymouth, England, April 10th 2018

Peer-reviewed articles not included in this thesis:

F. Niessen, M. Villa, D. Apel, O. Keßler, M. Reich, J. Hald, M.A.J. Somers, In situ techniques for the investigation of the kinetics of austenitization of supermartensitic stainless steel, Mater. Sci. Forum. 879 (2017) 1381–1386.

S.C. Okoro, **F. Niessen**, M. Villa, D. Apel, M. Montgomery, F.J. Frandsen, K. Pantleon, Complementary methods for characterization of corrosion products on a plant exposed superheater tube, Metallogr. Microstruct. Anal. 6 (2017) 22–35.

Table of contents

List of abbreviations and symbols

This list does not contain chemical element symbols, SI-units, product/company names and metric prefixes. Designations may differ locally in the individual result chapters.

Units

Å	Ångström
at.%	Atomic percent
HV	Vickers hardness
Hz	Hertz
Pa	Pascal
ppm	Parts per million
vol.%	Volume percent
wt.%	Weight percent
y	Interstitial atoms per 100 metal atoms

Physical constants

c	Speed of light in vacuum
e	Elementary charge
h	Planck's constant
R	Universal gas constant

Variable parameters

α_s	Shape factor (XRD)
A_1	Lower equilibrium phase-transition temperature of α-ferrite and austenite
A_3	Upper equilibrium phase-transition temperature of α-ferrite and austenite
A_4	Lower equilibrium phase-transition temperature of austenite and δ-ferrite
A_{EA}	Elastic anisotropy parameter
A_R	Elongation until rupture
A_{c1}	Start temperature of ferrite-to-austenite transformation during heating
A_{c3}	Finish temperature of ferrite-to-austenite transformation during heating
F_0	Structure factor (XRD)
H^2	Fourth order ratio (XRD)
K_V	Charpy-V impact toughness
M_f	Martensite finish temperature
M_s	Martensite start temperature
R_e	Outer dislocation cut-off radius (XRD)
R_m	Ultimate tensile strength
R_p	Proof strength / Yield strength
T_C	Curie Temperature
r_0	Inner dislocation cut-off radius (XRD)
s_1 and s_2	X-ray elastic constants
y_{va}	Fraction of vacant lattice sites (Kinetics modeling)

β_0	Average magnetic moment per atom (Thermodynamics modeling)
3Γ	Orientation parameter (XRD)
D	Coherently diffracting particle size
$FWHM$	Full width at half maximum
h, k, l	Miller indices of cubic crystal planes
n	Natural number
x, y, z	3-dimensional spatial coordinates
ΔK	Broadening of the diffraction vector
A	Area
C	Dislocation contrast factor (XRD)
D	Diffusion coefficient
E	Energy
F	Force
G	Gibb's energy
I	Experimental intensity (XRD)
I	Binary interaction parameter (Thermodynamics modeling)
J	Diffusion flux
K	Length of diffraction vector (XRD)
L	Interaction parameter (Thermodynamics modeling)
M	Dislocation distribution parameter (XRD)
M	Magnetic moment (VSM)
M	Diffusion mobility (Kinetics modeling)
P	Pressure
Q	Activation enthalpy
R	Theoretical intensity (XRD)
T	Temperature
U	Voltage
V	Volume
a	Lattice constant
b	Burgers vector (Crystallography)
c	Crystal elastic constants (XRD)
c	Concentration (Kinetics modeling)
d	Planar spacing (Crystallography)
d	Distance
f	Phase fraction
g	Diffraction vector (XRD)
l	Length
m	Multiplicity of crystal planes (Crystallography)
m	Mass
n	Unit-cell volume (Crystallography)
n	Molar fraction (Thermodynamics modeling)
q	Screw-to-edge dislocation ratio (XRD)

t	Time
v	Velocity
x	Alloying content
β	Line profile breadth (XRD)
δ	Kronecker delta
ε	Strain
η	Rotation angle of the sample around the diffraction vector (XRD)
θ	Diffraction semi-angle
λ	Wavelength (XRD)
λ	Coefficient of thermal expansion (Physics)
λ	Lath width (Microstructure)
μ	Absorption factor (XRD)
μ	Chemical potential (Thermodynamics modeling)
ρ	Dislocation density
σ	Stress
φ	Phase variable
ψ	1st angle, diffraction vector to sample reference system (XRD)
ϕ	2nd angle, diffraction vector to sample reference system (XRD)

Abbreviations

3D	3-dimensional
AA	As-austenitized condition
APT	Atom probe tomography
bcc	Body-centered cubic
bct	Body-centered tetragonal
DC	Direct current
DSC	Differential scanning calorimetry
EBSD	Electron backscatter diffraction
EDS	Energy-dispersive X-ray spectroscopy
EFTEM	Energy-filtered transmission electron microscopy
ESR	Effective spatial resolution
fcc	Face-centered cubic
HAADF	High-angle annular dark field
HAGB	High angle grain boundary
HAZ	Heat-affected zone
HC	Hardened condition
IPF	Inverse pole figure
KS	Kurdjumow-Sachs orientation relationship
L	Liquid phase
LAGB	Low angle grain boundary
PSR	Physical spatial resolution
SAED	Selected area electron diffraction
SEM	Scanning electron microscopy

STEM	Scanning transmission electron microscopy
TEM	Transmission electron microscopy
TKD	Transmission Kikuchi diffraction
TRIP	Transformation-induced plasticity
VSM	Vibrating sample magnetometry
XEC	X-ray elastic constant
XRD	X-ray diffraction
α	Low-temperature ferrite
α'	Martensite
γ	Austenite
δ	High-temperature ferrite

1 Background

1.1 Stainless steel

Stainless steels are ferrous alloys with at least 10.5 wt.% of Cr content. Cr forms a thin Cr-oxide/hydroxide -rich surface layer, which acts as an insulating barrier between the metal and a corrosive environment, giving stainless steels a high corrosion resistance. [1]

1.2 Martensitic steel

Martensitic steels are steels that predominantly consist of the martensite phase, which is conventionally formed by a diffusionless transformation with a body-centred tetragonal crystal structure during rapid cooling from the austenite phase field. Martensite formation is associated with a change in volume and a shear strain and leads to hardening of the steel. The transformation to martensite can only occur when austenite is metastable. [2]

1.3 Supermartensitic stainless steel

Supermartensitic stainless steel is a stainless steel with predominantly martensitic microstructure and extremely low content of the interstitial elements C and N, which restricts tetragonal distortion of the martensite unit cell and leads to a reduction in hardness. In order to obtain a transformable alloy, Ni is used to stabilize austenite. Supermartensitic stainless steels are, based on their property combination of high strength, high impact toughness, useful corrosion resistance and good weldability, popular in off-shore oil and gas applications. In cases where the corrosion resistance of carbon steel is not sufficient and the corrosion resistance of a Duplex stainless steel is overspecified, supermartensitic stainless steels offer an economically attractive alternative. [3]

Annealing of supermartensitic stainless steel in the inter-critical temperature region, i.e. the region in which both austenite and ferrite are thermodynamically stable, leads to formation of finely dispersed austenite. Austenite formation is accompanied by diffusion, which induces partitioning of Ni in martensite and austenite. The increased Ni content in austenite stabilizes austenite against martensite formation during cooling. The annealing treatment thus leads to an attractive dual-phase microstructure of tempered martensite and so called “reverted austenite”. Reverted austenite has significant impact on the mechanical properties: It reduces the ultimate tensile strength, yield strength and hardness, and increases impact toughness and ductility. [3]

1.4 Scope and aim

The aim of the present research project is to elucidate the major phase transformations in supermartensitic stainless steel and closely related alloys. The main focus in this work will be on the martensite-to-austenite transformation, as it has the most significant effect on the alloy properties. This particular phase transformation is affected by preceding phase

transformations, such as retainment of δ-ferrite from solidification and cooling, martensite formation after solution treatment and tempering of martensite when heating towards the inter-critical annealing temperature. As the most important property of reverted austenite is its stability against martensite formation, the austenite-to-martensite transformation is regarded as the second most important phase transformation in this work. The thermal and mechanical stability of reverted austenite against martensite formation is thus investigated as well. Finally, the relation between different microstructures and mechanical properties are established. The success criterion of this doctoral thesis is to obtain a holistic understanding of the processing-microstructure and microstructure-property relations in supermartensitic stainless steels. As this aim requires the employment of a multitude of methods, a secondary aim of this work is the development and qualification of advanced experimental methods.

1.5 Scientific approach

In order to obtain a holistic understanding of phase transformations and related properties in supermartensitic stainless steels, correlation of results from several methods is required. The aim of this work, to obtain a deeper understanding of the governing phase transformations, is primarily approached by conducting advanced in-situ experimental studies, and relating them to results from materials characterization and numerical modeling. In-situ studies allow direct observation of phase transformations as a function of several potential processing parameters, such as time, temperature or load. They are indispensable for obtaining a direct understanding of phase transformations and their kinetics. The applied in-situ methods detect the average response of bulk material to a change in temperature or stress. In order to elucidate the precise mechanism occurring on the micro- and nano-scale, advanced materials characterization was applied. Numerical modeling allowed validation of experimental findings and enables predicting transformations for materials design. It further enables the analysis of experimentally inaccessible mechanisms, isolation or disabling of sub-mechanisms and analysis of mechanisms that are either unfeasible or impossible to proof experimentally. Numerical modeling thus served as a well-suited complementary method to the in-situ experiments.

1.6 Terminology

Since there is no consistent terminology in literature, austenite that forms during inter-critical annealing of lath martensite is interchangeably referred to as “reverted” and “reversed” austenite. In some of the manuscript-based result chapters, soft martensitic stainless steel alloys are referred to as “supermartensitic stainless steel”. The correct assignment of the investigated alloys to these alloy classes is given in chapter 3. As the transformation behavior and the investigated properties of the closely related alloy classes are almost identical, the reported findings are not affected by the use of different designations.

1.7 Outline

Figure 1.1 shows a flowchart of the structure of the present doctoral thesis. This thesis is manuscript-based, meaning that the results of this work are subdivided in individual manuscripts (chapters 6 to 14). These result chapters are presented in the order of the

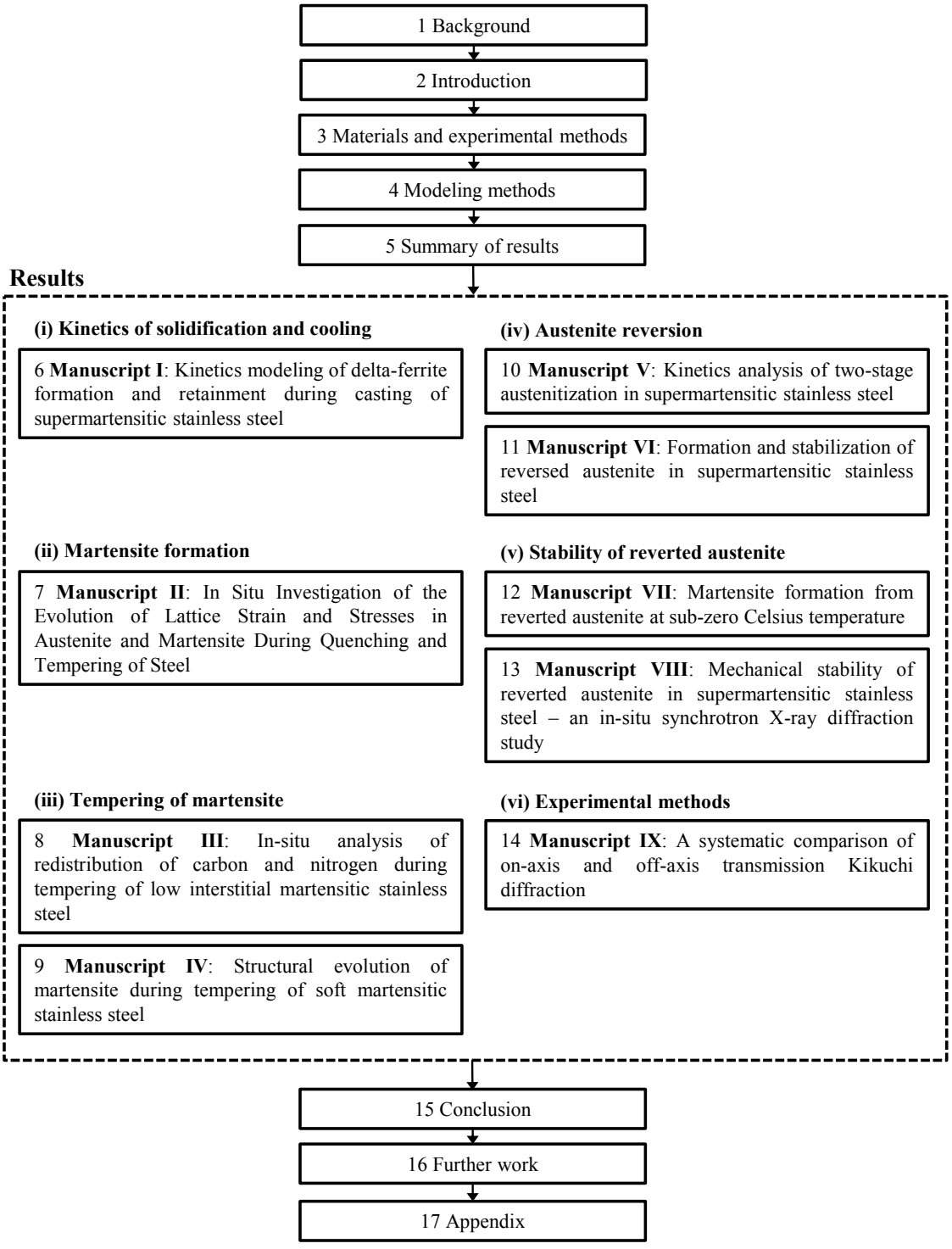

Figure 1.1: Flowchart on the structure of the chapters of the doctoral thesis.

processing steps of supermartensitic stainless steels (i-iv), the material properties (v) and the investigated experimental methods (vi). A summary of the results is given in chapter 5, which is preceeded by an introduction (chapter 2) and the experimental and modeling methods (chapters 3 and 4). The conclusion, remarks on further work and the appendix (chapters 15 to 17) complete the thesis.

References

[1] E. Bardal, Corrosion and Protection, Springer, 2004.

[2] T. Maki, Morphology and substructure of martensite in steels, in: E. Pereloma, D. V. Edmonds (Eds.), Phase Transform. Steels Vol. 2 Diffus. Transform. High Strength Steels, Model. Adv. Anal. Tech., 1st ed., Woodhead Publishing, 2012: pp. 34–58.

[3] F. Niessen, Austenite reversion in low-carbon martensitic stainless steels – a CALPHAD-assisted review, Mater. Sci. Technol. (2018). doi: 10.1080/02670836.2018.1449179

2 Introduction

The introductory chapter covers the historic view on alloy design, the present phases and alloy constituents, the physical metallurgy of austenite reversion and the material properties and application fields of supermartensitic stainless steels. A substantial amount of the introduction is adapted from the manuscript "Austenite reversion in low-carbon martensitic stainless steels – a CALPHAD-assisted review", which is appended (Appendix 1) in order to avoid repetitive content within the thesis.

2.1 Historical view on alloy design and application fields

Supermartensitic stainless steels are built on the Fe-Cr-Ni ternary system with additions of Mn, Mo, Si and particularly low contents of the interstitial elements C and N. In 1960 Irvine et al. [1] comprehensively described aspects of designing transformable 12% Cr steels to obtain a strong and corrosion resistant material. A major challenge consisted of finding alloy compositions that (i) could be solution treated without forming δ-ferrite, (ii) maintained A_1, the α-ferrite to austenite transition temperature, above 700 °C during 5 h isothermal tempering to avoid reaustinitization during tempering, and (iii) kept M_s, the martensite start temperature, above 200 °C to ensure complete transformation to martensite during cooling [1]. An Fe-0.1C-12Cr-2Ni-1.5Mo-0.3V (wt.%) alloy was found most promising with respect to corrosion resistance, strength, ductility and impact toughness (Table 2.1) [1].

The demand of alloys with enhanced corrosion resistance was met by increasing the Cr content, which required further stabilization of austenite in order to maintain a transformable alloy. As further addition of C, one of the most effective austenite stabilizing elements, would lead to precipitation of $M_{23}C_6$ and thus deplete Cr, other substitutional solutes needed to be considered instead [2]. Ni proved to be the most effective element, and substitution of C with Ni further led to useful softening of virgin martensite, which manifests as increased impact toughness [2–4]. Extensive reduction of the C content was difficult before the development of the argon oxygen decarburization (AOD) process in the mid 1950's [5].

Following the paradigm of substituting C with Ni, the Swedish steel manufacturers Bofors and Avesta reduced the C content to 0.06 wt.% to develop cast soft martensitic stainless steels with good corrosion resistance, high strength and high impact in the mid 60's of the last century [6–9] (Table 2.1). These steels contained small amounts of retained austenite and formed reverted austenite upon inter-critical annealing, which increases the ductility and impact toughness remarkably. Soft martensitic stainless steels were developed as weldable substitutes for conventional 13% Cr steels in applications as turbine runners [6]. The high strength, superior impact toughness at low temperature and useful corrosion properties of soft martensitic stainless steels also opened the application field of nuclear pressure vessels, which were continuously growing in size and at the time were

manufactured from carbon-manganese steels, clad-welded with austenitic stainless steel [7–9]. Niederau [10] recommend the application of soft martensitic stainless steel for centrifugal and rotary pumps, compressors, valves and turbines.

Conventional 13% Cr martensitic stainless steels were only weldable under great precaution, making the development of soft martensitic stainless steels a great leap forward [6]. The hardness of the heat affected zone (HAZ) of weld lines was however still too high compared to the annealed bulk material, which made post-weld heat treatment in the majority of cases mandatory. The energy company Statoil became interested in qualifying similar materials for major offshore pipeline projects in the scale of approx. 10,000 tons in 1995, which initiated the development of supermartensitic stainless steels [16]. The aim

Table 2.1: Overview of typical alloy compositions and average mechanical properties of soft martensitic and supermartensitic stainless steels for specified annealing treatments with reference to conventional martensitic stainless steel; R_P: Yield strength, R_m: Ultimate tensile strength, A_R: elongation until rupture, K_V^{RT}: Charpy-V impact toughness at room temperature.

Alloy designation	*Reference*	*Composition* [wt.%]	*Annealing treatment* T[°C] / t[h]	R_P [MPa]	R_m [MPa]	A_R [%]	K_V^{RT} [$\frac{J}{cm^2}$]
Conventional martensitic stainless steel							
generic	Irvine et al., 1960 [1]	Fe-0.1C-12Cr-2Ni-1.5Mo-0.3V	650 / 1	670	860	19	≥ 68
Soft martensitic stainless steels							
Bofors 2RMO	Grounes and Rao, 1969 [7]	Fe-0.06C-13Cr-6Ni-1.5Mo-0.6Mn-0.4Si	590	≥ 620	≥ 830	≥ 15	105
Avesta 248SV	Grounes and Rao, 1969 [7]	Fe-0.035C-16Cr-5Ni-1Mo-0.8Mn-0.5Si	580	≥ 620	≥ 830	≥ 15	132
EN 1.4405 (cast alloy)	Niederau, 1982 [10]	Fe-<0.07C-16Cr-5Ni-1.5Mo-<1Mn-<1Si	580	650	900	≥ 17	105
EN 1.4418	Dawood et al., 2004 [11,12]	Fe-0.05C-15.5Cr-5.6Ni-0.76Mo-0.4Mn-0.4Si	625 / 4	690	880	10	260
Supermartensitic stainless steels							
13CrS (UNS S41525)	Kondo et al., 1999 [2,13]	Fe-0.01C-12Cr-6Ni-2.5Mo-Ti	850 / 0.5 + 630 / 1	≥ 550	≥ 750	/	290
Vítkovice, generic	Tvrdy et al., 2002 [14]	Fe-0.017C-13Cr-6.2Ni-2.4Mo-0.6Mn-0.3Si	600 / 6	540	870	19	185
Industeel, generic	Toussaint and Dufrane, 2002 [15]	Fe-0.008C-11.8Cr-4.8Ni-1.5Mo-1.9Mn-0.2Si-0.5Cu	625	600 - 650	880 - 900	25	195

was to enhance the properties of soft martensitic stainless steels by even further reducing the C content below 0.01 wt.% in order to minimize or fully circumvent post-weld heat treatment and to reduce the risk of corrosion attack due to sensitization. Further, the Mo content was increased to obtain better protection against localized corrosion and sulfide stress cracking [2–4,16–18] (c.f. overview in Table 2.1).

2.2 Phases

The most common phases in the metallurgy of supermartensitic stainless steels are martensite (α'), austenite (γ), δ-ferrite and various carbides and nitrides. The Cr and Ni pseudo-binary phase diagrams in Figure 2.1 show typical temperature ranges of the equilibrium phases ferrite and austenite of an Fe-13Cr-5Ni (wt.%) ternary system, a simplified version of a typical supermartensitic stainless steel. The dashed lines indicate the initial Cr and Ni contents, which are varied on the respective horizontal axes. Martensite is not represented in the phase diagrams as it forms as a metastable phase upon kinetic suppression of the $\gamma \rightarrow \alpha$ phase transformation. In the following the phases are presented in greater detail in the order of their appearance during cooling after solidification.

2.2.1 δ-ferrite

In supermartensitic stainless steels δ-ferrite is the first phase to form from the melt (L) during solidification (Figure 2.1). δ-ferrite has a body-centered cubic (bcc) crystal structure and is crystallographically entirely equivalent to α-ferrite. The distinction of the two forms of ferrite is made based on their thermal history. During cooling, δ-ferrite forms from the melt whereas α-ferrite forms from austenite. The different thermal history goes in hand with different morphologies and phase compositions, which lead to distinct material properties, associated with the individual ferrite types. Most alloys solidify directly to δ-ferrite, while some compositions may be subject to solidification in a peritectic mode involving austenite ($L \rightarrow L + \delta \rightarrow L + \delta + \gamma \rightarrow \delta + \gamma$). The temperature range of the δ-ferrite single phase region in the simplified Fe-13Cr-5Ni (wt.%) alloy (Figure 2.1) is narrower than in industrial alloys, as even small amounts of C and N lead to substantial expansion of the γ-loop. In the case of solidification to δ-ferrite, nucleation of austenite occurs at the interfaces of the collided solidification front and is accompanied by partitioning of Ni and Cr [19]. Partitioning leads to chemical stabilization of δ-ferrite which can be sufficient to retain δ-ferrite during cooling to room temperature (see chapter 6). δ-ferrite that is retained from solidification is associated with an increase in the ductile-brittle transition temperature [20] and is thus considered as a detrimental phase.

2.2.2 Austenite and martensite

During cooling from solidification, austenite, a face centered cubic (fcc) phase, forms either from the melt in a peritectic reaction or, more commonly, from δ-ferrite. In absence of any high-temperature nitrides or carbides, the austenite microstructure is subject to

considerable grain growth at high temperature. In the present alloy grades, alloying with Ni is mainly responsible for a significant expansion of the γ-loop (Figure 2.1b).

The reduction in A_3 and A_1 lead to suppression of the $\gamma \rightarrow \alpha$ transformation. Sufficient undercooling leads to transformation of the metastable austenite to lath martensite. Martensite formation occurs during cooling at a relatively low temperature ($M_s \approx 260 - 130$ °C) and finishes just above [22–27], or in exceptional cases even below [10,28], room temperature. Martensite forms with less than ~ 2 ° deviation [29] from a Kurdjumow-Sachs (KS) orientation relationship with austenite, $(111)_\gamma \parallel (011)_{\alpha'} \wedge [10\bar{1}]_\gamma \parallel [1\bar{1}1]_{\alpha'}$ [30]. Even though the exact nature of the interface associated with the orientation relationship is still subject of current research [31,32], it has to be semi-coherent, consisting of periodic steps with coherent patches [33,34]. Generally the martensite crystal structure is body-centered tetragonal (bct), but the low interstitial content of the present alloys leads to virtually no tetragonality, rendering martensite bcc. The low-carbon martensitic stainless steels have a high hardenability and are insensitive to the applied quenching rate [3,15,35,36]. The martensite start temperature can be predicted by several empirical formulas, of which two formulas, specifically developed for soft-martensitic and supermartensitic stainless steels, are presented in the following. A formula for M_s in soft martensitic stainless steels in welding lines is given by Folkhard [36]:

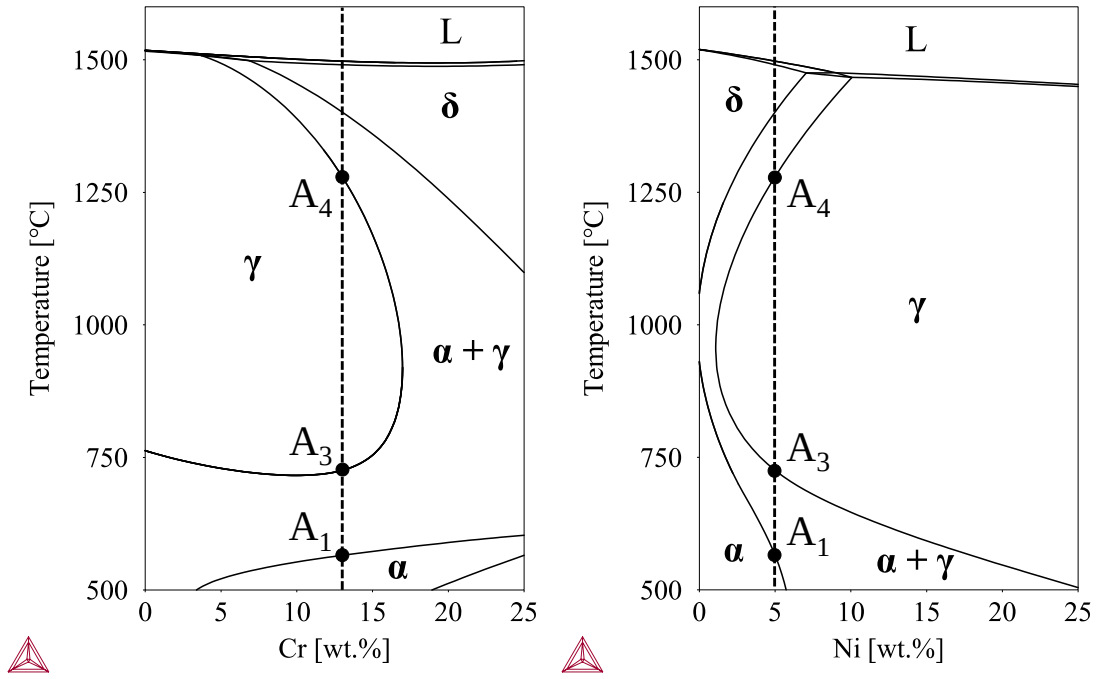

Figure 2.1: Pseudo-binary phase diagrams of Fe-13Cr-5Ni (wt.%) alloy system (a) Fe-Cr phase diagram at 5 wt.% Ni (dashed line in Figure 2.1b). Addition of Cr mainly leads to a reduction of the A_4 and an increase of the A_1, while the A_3 around 13 wt.% Cr is less affected; the lower right phase field indicates the stability of two distinct Fe and Cr bcc sublattices; (b) Fe-Ni phase diagram at 13 wt.% Cr (dashed line in Figure 2.1a). Addition of Ni expands the austenite phase field by substantially lowering A_1 and A_3 while increasing A_4. (Database: TCFE6 [21])

$$M_S^F(°C) = 492 - 125 \times (\text{wt.\% C}) - 65.5 \times (\text{wt.\% Mn}) - 10 \times (\text{wt.\% Cr}) - 29 \times (\text{wt.\% Ni}) \quad (2.1)$$

Gooch developed another formula to predict M_S for the use on supermartensitic stainless steels in welding applications [37]:

$$M_S^G(°C) = 540 - 497 \times (\text{wt.\% C}) - 6.3 \times (\text{wt.\% Mn}) - 36.3 \times (\text{wt.\% Ni}) - 10.8 \times (\text{wt.\% Cr}) - 46.6 \times (\text{wt.\% Mo}) \quad (2.2)$$

After martensite transformation supermartensitic stainless steels consist of lath martensite with typical fractions of retained austenite of approx. up to 5 vol.%. Recent work showed that, as a consequence of the low M_S and interstitial content, no interstitial segregation by auto-tempering or 6 months of room temperature aging was observed [38,39]. In contrast, clustering of carbon at room temperature was reported by Song et al. [40], without specifying the aging time. Martensitic transformation leads to transformation strains, which may be partially accommodated by retained austenite. During the transformation, martensite initially experiences high tensile stress, which then gradually decreases towards the end of the transformation (down to ~40 MPa), while retained austenite experiences significant compressive stress towards the end of the transformation (up to ~ -900 MPa) [38].

Lath martensite shows very high dislocation densities, similar to heavily cold-worked alloys [41]. Quantitative studies on dislocation densities revealed ~4x10^{15} m^{-2} in an Fe-0.03C-15.5Cr-5Ni (wt.%) precipitation hardening steel [42] and ~7x10^{14} m^{-2} in an Fe-0.04C-15.5Cr-5Ni (wt.%) soft martensitic stainless steel [43] in as-quenched conditions. When the dislocation-rich microstructure is reheated to the inter-critical region, C and N partition from solid solution and diffuse to lattice defects in order to minimize local strain fields [39,44]. During further heating, concurrent recovery of the martensite matrix and austenite reversion at grain boundaries commence at approx. 500 to 550 °C [39,43,45], leading to a reduction in dislocation density by approx. an order of magnitude [43].

2.2.3 Carbides and nitrides

Supermartensitic stainless steels may contain micro-alloying elements, such as Ti, Nb or V, to form carbides and nitrides that pin the austenite grain boundaries during solution treatment, limiting grain growth [17,46]. Formation of $M_{23}C_6$ carbides is commonly observed in the temperature range 550 – 900 °C [47]. Those carbides form with a cube-cube orientation relationship with reverted austenite, $\{100\}_\gamma \parallel \{100\}_{M_{23}C_6} \wedge \langle 001\rangle_\gamma \parallel \langle 001\rangle_{M_{23}C_6}$ [28,40,47–50]. Very small Mo_2C carbides at low temperature and M_7C_3 after very long tempering at 570 °C are observed less commonly [47]. Formation of Cr and Mo alloy carbides is generally not desired as it leads to sensitization, i.e. local depletion in Cr and Mo in the diffusion zone around the carbides. Such zones are well known initiation points for pitting corrosion, which likely act as a precursor for intergranular stress corrosion

cracking [51]. Carbide formation involving micro-alloying elements is effective in binding C to avoid the formation of Cr and Mo carbides [27,52].

2.3 Alloy constituents

The main alloy constituents of supermartensitic stainless steels are Cr, Mo, C, N, Ni, Mn and Si. The kind and amount of constituents are optimized to obtain specific alloy properties and microstructure stability.

2.3.1 Chromium

In stainless steels, Cr is essential for obtaining resistance towards galvanic corrosion. In supermartensitic stainless steels, generally 10.5 to 14 wt.% Cr are added [3], where at least 10.5 wt.% are required for the formation of a thin passivating surface layer, which mainly consists of Cr-oxides [53]. The oxide film prohibits anodic dissolution by its good barrier properties and is capable of hosting cathodic reactions at high rates based on its electric conductivity. The latter property makes stainless steels susceptible to pitting and crevice corrosion in regions where the passive layer is interrupted. Homogeneous distribution of Cr is therefore essential to obtain effective passivation. Especially the retainment of Cr-rich δ-ferrite from cooling after solidification and the formation of Cr-carbides may cause local Cr depletion. Material failure by stress corrosion cracking was consistently associated with Cr-depleted zones [51].

Addition of Cr reduces A_4 and increases A_1, while A_3 is less sensitive to the Cr content (Figure 2.1a). Especially the reduction of A_4 and the expansion of the δ-ferrite phase field have considerable impact, as it leads to an increased amount of retained δ-ferrite at room temperature after cooling from solidification or welding [54]. Cr leads to reduction of the M_s by ~10 K per wt.% (see Equ. 2.1 and 2.2).

2.3.2 Molybdenum

Mo is added in order to improve general resistance to galvanic corrosion, but more importantly to obtain increased resistance against pitting corrosion and sulfide stress corrosion cracking [2,55]. Localized corrosion, i.e. pitting corrosion, was identified as a possible precursor to stress corrosion cracking [2].

2.3.3 Carbon and nitrogen

C and N are interstitial alloying elements and are among the most effective elements to stabilize austenite. While austenite stability is required to obtain a transformable material, supermartensitic stainless steels are characteristic for their low or very low interstitial content (ideally $<$ 0.01 wt.% [3,16]) in order to diminish as-quenched hardness and sensitization after welding. The development of soft martensitic stainless steels as a predecessor of supermartensitic stainless steels entailed reduction of C and N to $<$ 0.06 wt.%, respectively [3]. In these materials the impact toughness of weld-lines is not

sufficient without applying a post-weld heat treatment [16], while supermartensitic stainless steels obtain useful, albeit not optimal, toughness also without post-weld heat treatment [18,56].

2.3.4 Nickel

As interstitial elements are not suitable to stabilize austenite in supermartensitic stainless steels, Ni is considered the most effective substitutional element for stabilizing austenite [2]. Ni is balanced with Cr and Mo to obtain a martensitic microstructure and is typically present from 1.5 wt.% in lean supermartensitic stainless steels up to 6.5 wt.% in highly alloyed supermartensitic stainless steels [3]. Nickel tends to increase ductility and toughness and is known for reducing the corrosion rate in the active state [57].

2.3.5 Manganese

Mn is generally added to stainless steels to improve hot ductility [36]. At low temperature Mn is an austenite stabilizer, which can replace Ni in moderate quantities [57]. Addition of Mn enhances the solubility of N [36] and Mn forms sulfides in the presence of S, which are detrimental to the corrosion properties [57,58].

2.3.6 Silicon

Si improves resistance to oxidation at high temperature or strongly oxidizing solutions at low temperature and is a ferrite stabilizing element [57]. Extensive addition of Si promotes the retainment of δ-ferrite, extends the stability range of σ-phase and stabilizes low-melting phases, which may lead to hot-cracking [36]. These detrimental effects limit the use of Si as an alloying element in larger quantities.

2.4 Austenite reversion

Supermartensitic stainless steels obtain a nano-lamellar dual-phase microstructure of reverted austenite and tempered martensite through inter-critical annealing, i.e. annealing in the temperature region in which both ferrite and austenite are thermodynamically stable. The obtained “reverted austenite” is distinguished from “retained austenite”, i.e. austenite that is untransformed during cooling to room temperature [59]. Stabilization of reverted austenite occurs primarily by the partitioning of austenite stabilizing elements during diffusional reversion. The resulting fine-grained dual-phase microstructure lowers the yield strength, ultimate tensile strength and hardness, while ductility and impact toughness are significantly enhanced [7,10,35].

2.4.1 Nucleation and growth close to A_1

A_1, i.e. the ferrite-to-austenite (α-to-γ) phase transition temperature in thermodynamic equilibrium, may conventionally be obtained from thermodynamics modeling. In the present system, the prediction of extensive partitioning of solute in austenite and ferrite at

low temperature leads to a small fraction of stable austenite in thermodynamic equilibrium. In reality, an alloy undergoes martensite formation during cooling, such that austenite forms from an approximately homogeneous distribution of solute during reheating, rendering the prediction of A_1 from thermodynamic equilibrium unfeasible. A_{c1}, the experimentally determined α-to-γ transition temperature during heating, is on the other hand strongly dependent on the heating rate [1,22,60,61] and thus not an explicit quantity. In the present case the phase transition temperatures A_1 and A_3 therefore refer to the phase transition temperatures obtained during very slow heating ($\leq 0.017\ \mathrm{K.s^{-1}}$). Sufficiently fast heating (approx. $> 10\ \mathrm{K.s^{-1}}$ [62,63]) does not allow enough time for long-range diffusion and thus leads to transformation by a displacive mechanism instead.

Close to A_1 (composition dependent at ~500 – 550 °C) allotriomorphic reverted austenite with film morphology forms at lath boundaries [48,49,63–66] with little or no deviation from the Kurdjumow-Sachs orientation relationship [30,67,68]. All reported micrographs of annealed microstructures in the temperature range 500 to 575 °C reveal that austenite grows from the lath boundary into only one of the laths (Figure 2.2a) [48,59,63,69]. Above this temperature, austenite films begin to grow into both laths adjacent to a lath boundary (Figure 2.2b) [48,49,63]. In the case of pre-existing inter-lath retained austenite, immediate growth from retained austenite occurs, as no nucleation is required [66]. For the film morphology, austenite memory, i.e. the tendency of reverted austenite to form in the orientation of the prior austenite grain, is commonly observed [22,66,70]. Further, reverted austenite has been reported to form cooperatively with $M_{23}C_6$ carbides with a cube-cube orientation relationship, $\{100\}_\gamma \parallel \{100\}_{M_{23}C_6}, \langle 001\rangle_\gamma \parallel \langle 001\rangle_{M_{23}C_6}$ [28,40,48–50]. According to thermodynamic equilibrium, growth of austenite requires an inward-flux of Ni and outward-flux of Cr [22] (Figure 2.3), while growth of $M_{23}C_6$ requires the opposite fluxes. Cooperative growth should thus be facilitated by a gradient in chemical potential and a resulting net flux of Ni and Cr across the interface. It was shown experimentally that $M_{23}C_6$ can bind sufficient carbon to leave austenite and martensite virtually carbon free [40,71,72].

Figure 2.3 shows the equilibrium austenite fraction and Cr and Ni concentrations in austenite and ferrite as a function of temperature for a simple Fe-Cr-Ni system with typical Ni and Cr concentrations of a supermartensitic stainless steel. At low temperature, enhanced partitioning of Ni is required to form austenite which, together with slow substitutional diffusion kinetics, significantly limits the kinetics of austenite reversion [22,68,74]. Nevertheless, the kinetics of austenite reversion at low temperature were measured to be significantly faster than predicted by modeling of bulk-diffusion, suggesting that grain boundary diffusion and diffusion along dislocations are important mechanisms that significantly increase the transformation kinetics at these temperatures [22,28,74].

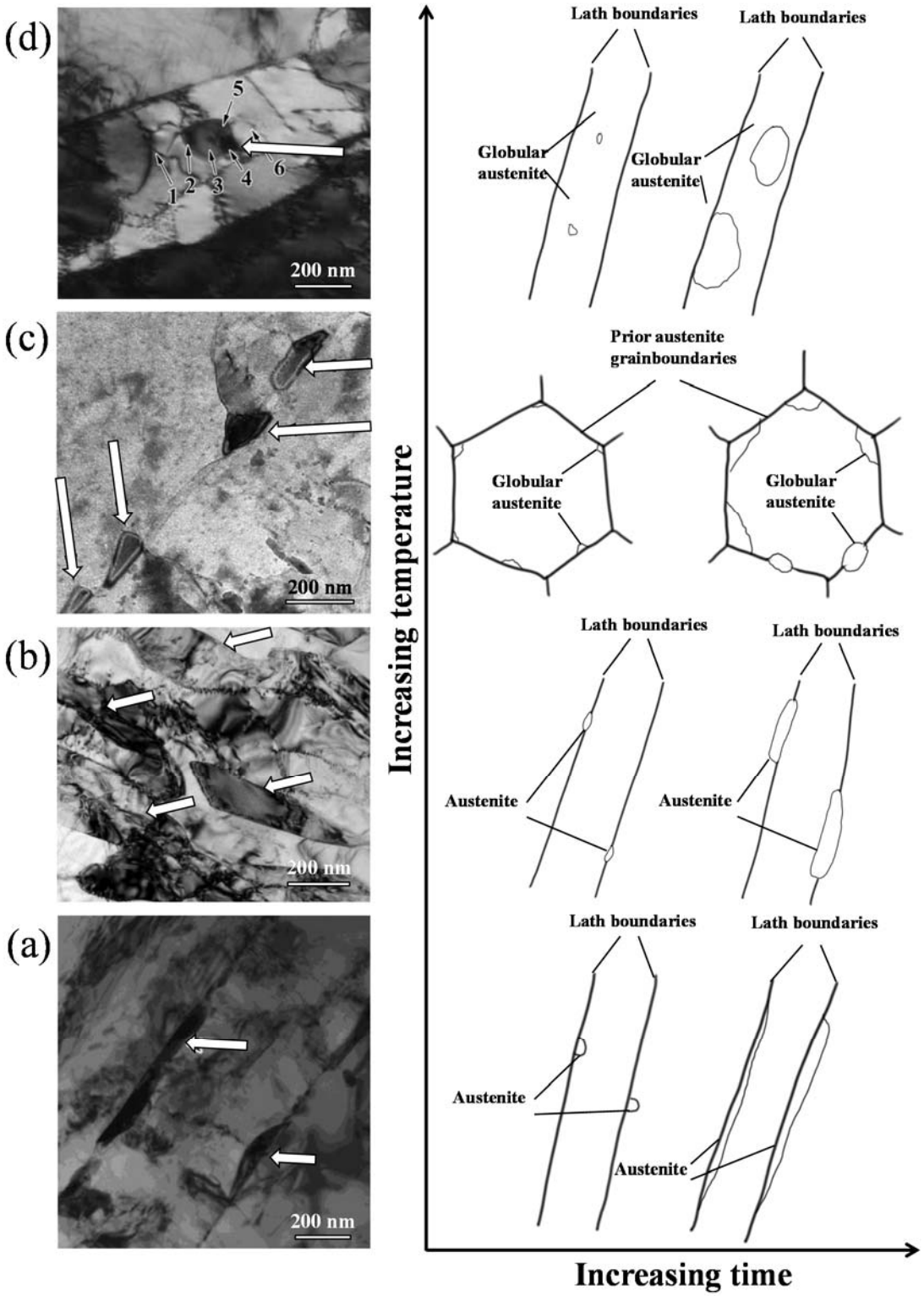

Figure 2.2: Bright-field micrographs and schematics of the evolution of the reverted austenite morphology with temperature and time in LMSSs: (a) low temperature acicular morphology (footage from Ref. [59]); (b) elevated temperature acicular morphology (footage from Ref.[58]) ; (c) globular morphology at prior austenite grain boundaries (footage from Ref. [1]); (d) globular morphology inside martensite laths (numbers are from the original footage from Ref. [54]); reverted austenite is marked with white arrows in the micrographs. [73]

2.4.2 Nucleation and growth towards A_3

At elevated temperature, typically 600 – 700 °C, reverted austenite tends towards a globular morphology, first at prior austenite grain boundaries (Figure 2.2c) [64–66] and at higher temperature within martensite laths (Figure 2.2d) [48,63,75]. The reversion kinetics are significantly faster, mainly because of lower required partitioning of Ni (Figure 2.3), accelerated diffusion kinetics and increased prominence of bulk diffusion. Further, the increased driving force for austenite formation in this temperature range renders also incoherent interfaces [64] or the formation of new interfaces energetically favorable [48,63,75], manifested as more nucleation sites. Song et al. [72] reported that in a Fe-0.05C-12Cr-4Ni-0.5Mo (wt.%) steel austenite reversion occurred without diffusion during isothermal annealing above 680 °C. Upon further heating, grain growth and dissolution of $M_{23}C_6$ carbides continue towards a fully austenitic microstructure, which was reported to recrystallize spontaneously at 900 °C when heating with 0.17 K.s^{-1}, 70 °C above A_{c3} [65].

2.4.3 Stability of reverted austenite against martensite formation

Reverted austenite that is formed close to A_1 is generally more stable against martensite formation upon cooling (or deformation) as compared to reverted austenite formed at higher temperature. There is a consensus that Ni-enrichment in austenite decreases with increasing annealing temperature [22,24,26,40,50,63,66,68,69,71,72,74,76–79], which is in qualitative agreement with the concentrations from thermodynamic equilibrium in Figure 2.3. A detailed comparison of literature data on partitioning in austenite and martensite with predictions from thermodynamics modeling is given in Appendix 1. The Ni concentration determines mainly the stability of reverted austenite against martensite formation, as more Ni reduces M_s (c.f. Equ. 2.1 and 2.2). However, the compositional

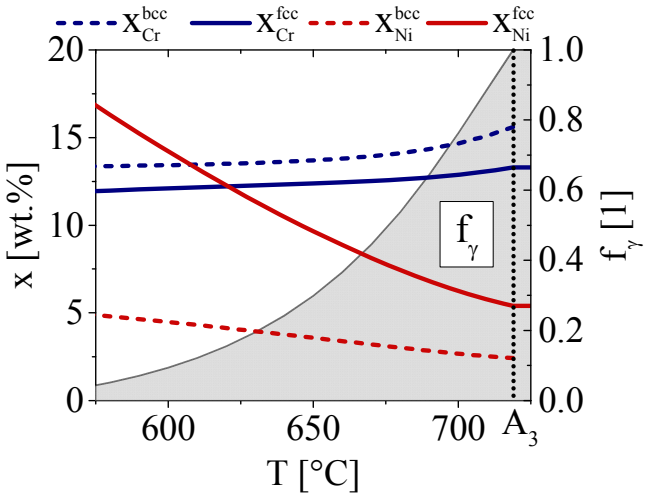

Figure 2.3: Ni and Cr concentration (x) in austenite (fcc) and ferrite (bcc) as well as the molar fraction of austenite (f_γ, grey area) from an equilibrium calculation of a representative Fe-13.3Cr-5.4Ni (wt.%) ternary alloy. Partitioning of Ni increases with lower austenite fraction and temperature. (Allowed phases: liquid, fcc, bcc; software and thermodynamics database: Thermo-Calc 2017a - TCFE6 [21]). [73]

effect is considered insufficient to explain the stability of reverted austenite alone [40,77]. The increase in grain size [50,69,80,81], the transition to a more globular grain morphology [50,69] and softening of the surrounding martensitic matrix [12,50] with increasing annealing temperature are anticipated to reduce the contribution of strain energy to the critical driving force for martensite nucleation [82], i.e. the stability of austenite. Findings by Zhang et al. [50] are particularly supportive of this mechanism, as inter-critical annealing at 620 °C was found to lead to higher fractions of reverted austenite with annealing time up to a maximum value, after which the fraction decreased again on further annealing. Even though the phase fraction of austenite approached equilibrium content, compositional equilibration (partitioning), carbide growth, recovery of martensite and spheroidization of austenite continue [50,71], which may affect the stability of reverted austenite.

Bilmes et al. [77] claimed that also a high dislocation density in reverted austenite could contribute to the stability of reverted austenite. This finding is doubtful, as the high dislocation density was identified by the dark appearance of austenite in a bright-field micrograph, which is generally indicative of an orientation contrast when using an objective aperture rather than the presence of dislocations [83]. Further, reverted austenite developed under continued diffusion is known to have low dislocation density [28,84], as opposed to reverted austenite formed by a displacive mechanism [85].

Reverted austenite either remains stable upon cooling, or transforms partially or completely to martensite [25,43,68]. Reverted austenite was reported to even have remained stable after sub-zero treatment at boiling N_2 [10,77,79] and boiling He temperatures [40]. It is critically remarked that martensite formation in lath martensite, especially at sub-zero Celsius temperatures, is time-dependent, i.e. thermally activated, and kinetically suppressed at very low temperature. Transformation generally occurs in the temperature range -150 °C to room temperature, which means that in the referenced cases [10,40,77,79] martensite formation may be fully suppressed if cooling to, or heating from, boiling N_2 temperature is performed sufficiently fast to suppress the thermally activated phenomena that control the rate of the austenite-to-martensite transformation in steel [86] (c.f. chapter 12). In a single case, it was claimed that the fraction of austenite increases by applying sub-zero treatment [58], which is in obvious conflict with all above referenced observations.

Reverted austenite may also transform to martensite by strain-induced transformation and in this way enhance the plastic regime [43,76,77,87]. This mechanism known as transformation induced plasticity (TRIP), has not been treated in depth in low-carbon martensitic stainless steels, but advanced in-situ experiments and modeling of strain-induced martensite formation have been performed in other variations of steels [88–94]. The present work contains an experimental investigation of the TRIP effect in chapter 13.

2.5 Alloy properties

The following section gives an overview of the mechanical properties, welding properties and corrosion properties.

2.5.1 Mechanical properties

Figure 2.4 shows the mechanical properties of an Fe-16Cr-5Ni-1Mo (wt.%) soft martensitic stainless steel (EN 1.4418) at room temperature after 4 h soaking at various temperatures, adapted from Dawood et al. [11,12]. At first the ultimate tensile strength, the 0.2 % proof strength and the hardness increase by heat-treating up to 475 °C, which is an effect of secondary hardening from precipitation of Mo_2C. Then softening occurs up to 625 °C, mainly due to austenite reversion and recovery of martensite. A new increase in ultimate tensile strength, 0.2 % yield strength and hardness is observed upon heat treatment at 700 °C and above, originating from transformation of reverted austenite to fresh martensite and precipitation of $M_{23}C_6$ carbides. The elongation and impact toughness develop in inverse relation to the ultimate tensile strength, 0.2 % yield strength and hardness with soaking temperature, i.e. are enhanced by reverted austenite formation and recovery of martensite.

In the presence of reverted austenite, soft martensitic and supermartensitic stainless steels show remarkable impact toughness also at sub-zero Celsius temperature (> 100 J at -80 °C [3]).

Solheim et al. [95] showed that reverted austenite increased the solubility of hydrogen in supermartensitic stainless steel samples dramatically, and that the ductility of such samples was greatly reduced, suggesting that reverted austenite plays an important role in hydrogen embrittlement. Carrouge et al. [20] showed that δ-ferrite in the microstructure significantly reduces the toughness, while δ-ferrite in the heat affected zone

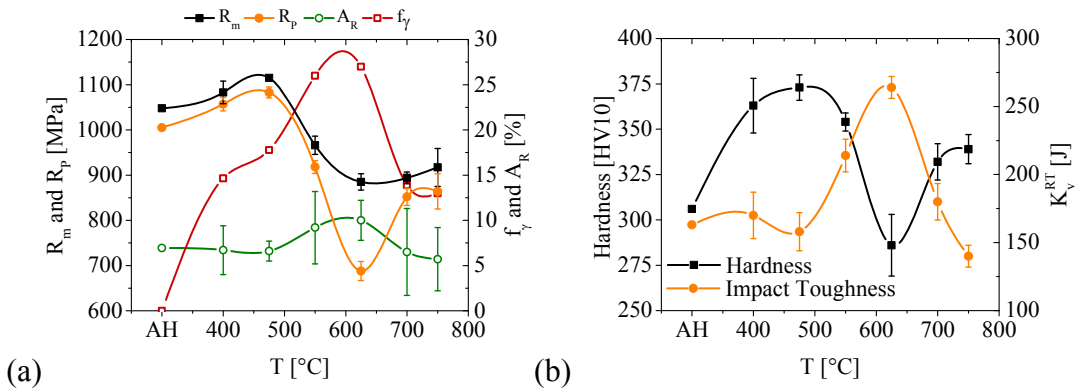

Figure 2.4: Fraction austenite and mechanical properties of a 16Cr-5Ni-1Mo stainless steel at room temperature in the hardened condition (AH) and after 4 h soaking at various temperatures: (a) Ultimate tensile strength (R_m), 0.2% proof strength (R_p), elongation to rupture (A_R) and fraction austenite (f_γ); (b) Hardness and Charpy V impact toughness (K_V^{RT}); The lines are spline functions of measured data (symbols) and do not represent physical values. (adapted from Dawood et al. [11,12])

(HAZ) of a weld line did not noticeably affect impact toughness. A more detailed overview on the mechanical properties of supermartensitic stainless steels and related alloy groups can be obtained from Refs. [3,11,35,96].

2.5.2 Welding properties

Supermartensitic stainless steels have been optimized towards good weldability, which is why they are also referred to as "weldable martensitic stainless steels". Martensitic steels are generally difficult to weld, as high or intermediate interstitial content in conventional martensitic steels leads to high hardness and unsatisfactory impact toughness in the as-welded / HAZ microstructure. Figure 2.5 shows that only below 0.01 wt.% C the as-quenched hardness becomes in-sensitive to the carbon content

Welding may either be carried out with Duplex/Superduplex [16,17,97,98] or matching filler material [4,16,56,77,98–101]. The prior leads to an over-matching of corrosion properties and an under-matching of the yield strength [3,17]. Welding is generally carried out without preheating. Sometimes no post-weld heat treatment is applied, but it has been reported that a short 5 min post-weld heat treatment at 650 °C leads to softening of the HAZ without having a detrimental effect on the superduplex or duplex weld metal microstructure and toughness [3]. The hardness of the HAZ is mainly a function of C content and may be further reduced by adding approx. 0.1 wt.% Ti [2]. In order to avoid hydrogen cracking, the uptake of hydrogen during welding needs to be minimized. It was found that most hydrogen is introduced by the filler material and that some hydrogen can originate from moisture in the shielding gas [102]. A more detailed overview on the welding properties of supermartensitic stainless steels and related alloy groups is given in Refs. [3,36].

2.5.3 Corrosion properties

Compared to conventional 13 Cr steels, further lowering of the C content to mitigate Cr sensitization and increasing the Mo content in supermartensitic stainless steels significantly

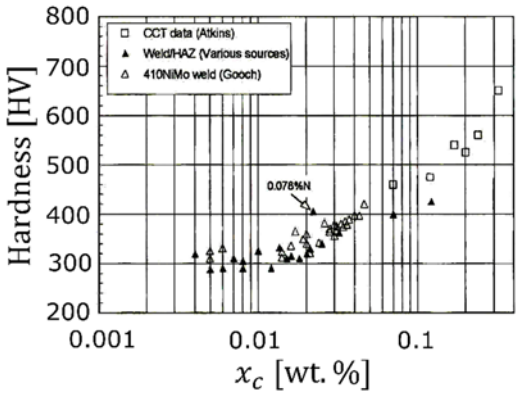

Figure 2.5: Influence of carbon content, x_C, on the as-quenched/HAZ hardness of 12%Cr martensitic steels. (adapted from Ref. [3])

improved corrosion properties in sour environments. Compared to 13 Cr martensitic stainless steels that obtain their hardenability from C rather than Ni (420 type of steels), the general corrosion rates are typically 10 to 20 times lower at pH $\geq$ 3.5, an H_2S partial pressure of $\leq$ 0.1 bar and chloride levels of $\geq 10^5$ ppm [3]. Supermartensitic stainless steels are not immune to sulfide stress cracking. It was found that cracking mostly initiates at Cr-depleted zones and follows prior austenite grain boundaries. Post-weld heat treatment can somewhat increase the resistance to sulfide stress cracking [51]. Further, the higher Mo grades are recommended in S-containing corrosive environments, as Mo impedes local corrosion [17]. A more detailed overview on corrosion properties of supermartensitic stainless steels is given in Refs. [3,51,103].

References

[1] K.J. Irvine, D.J. Crowe, F.B. Pickering, The physical metallurgy of 12 % chromium steels, J. Iron Steel Inst. 193 (1960) 386–406.
[2] K. Kondo, M. Ueda, K. Ogawa, H. Hirata, H. Takabe, Y. Miyazaki, Alloy design of Super 13Cr martensitic stainless steel, in: Supermartensitic Stainl. Steels 1999, 1999: pp. 11–18.
[3] A.W. Marshall, J.C.M. Farrar, Welding of Ferritic and Martensitic 11-14% Cr Steels, Weld. World. 45 (2001) 19–42.
[4] L. Karlsson, S. Rigdal, W. Bruins, M. Goldschmitz, Development of matching composition supermartensitic stainless steel welding consumables, Svetsaren. 54 (1999) 3–7.
[5] W.A. Krivsky, The linde argon-oxygen process for stainless steel; A case study of major innovation in a basic industry, Metall. Trans. 4 (1973) 1439–1447.
[6] G. Baggström, New Steel for Turbine Runners, Water Power. 16 (1964) 516–521.
[7] M. Grounes, S. Rao, New Alloy Steels for Nuclear Reactor Pressure Vessels and Vessel Internals, Trans. ASM. 62 (1969) 902–914.
[8] M. Grounes, Swedish Work on Brittle-Fracture Problems in Nuclear Reactor Pressure Vessels, AB Atomenergi, Sweden. (1966) 1–34.
[9] M. Grounes, P. Lindhagen, Irradiation Effects in Pressure Vessel Materials for Steam-Cooled Fast Reactors, in: Irradiat. Eff. Struct. Alloy. Therm. Fast React. ASTM STP 457, 1969: pp. 156–179.
[10] H.J. Niederau, Eigenschaften und Anwendungsmöglichkeiten der Guss- und Schmiedelegierung (G)X-5 CrNiMo 16 5 (Werkstoff-Nr. 1.4405), Zeitschrift Des Vereins Dtsch. Ingenieure Für Maschinenbau Und Met. Eig. 21 (1982) 801–808.
[11] M. Al Dawood, I.S. El Mahallawi, M.E. Abd El Azim, M.R. El Koussy, Thermal aging of 16Cr – 5Ni – 1Mo stainless steel Part 1 – Microstructural analysis, Mater. Sci. Technol. 20 (2004) 363–369.
[12] M. Al Dawood, I.S. El Mahallawi, M.E. Abd El Azim, M.R. El Koussy, Thermal aging of 16Cr – 5Ni – 1Mo stainless steel Part 2 – Mechanical property characterisation, Mater. Sci. Technol. 20 (2004) 370–374.
[13] M. Sagara, K. Yamada, A. Taniyama, K. Ogawa, D. Motoya, H. Takabe, H. Amaya, M. Ueda, Development for Material and Application Technique of Stainless Steel Line Pipes, Nippon Steel Sumitomo Met. Tech. Rep. (2015) 59–64.
[14] M. Tvrdy, V. Vodarek, G. Roznovska, A. Korcak, J. Seliga, J. Barta, P. Tkacik, Production, development and industrial application of 12Cr-6Ni-2.5Mo steels, in: Supermartensitic Stainl. Steels 2002 Brussels, 2002: pp. 29–33.
[15] P. Toussaint, J.-J. Dufrane, Advances in the making and base material properties of supermartensitic stainless steels (SMSS), in: Supermartensitic Stainl. Steels 2002 Brussels, KCI Publishing, 2002: pp. 23–27.
[16] P.E. Kvaale, O. Stein, Experience with supermartensitic stainless steels in flowline applications, in: Stainl. Steel World 99, 1999: pp. 19–26.
[17] K. Kondo, K. Ogawa, A. Amaya, M. Ueda, H. Ohtani, Development of Weldable Super 13Cr Martensitic Stainless Steel for Flowline, in: Proc. Twelfth Int. Offshore Polar Eng. Conf., 2002: pp. 303–309.
[18] H. Van der Winden, P. Toussaint, L. Coudreuse, Past, present and future of weldable supermartensitic alloys, in: Supermartensitic Stainl. Steels 2002 Brussels, 2002: pp. 9–13.
[19] F. Niessen, N.S. Tiedje, J. Hald, Kinetics modeling of delta-ferrite formation and retainment during casting of supermartensitic stainless steel, Mater. Des. 118 (2017)

138–145.
[20] D. Carrouge, H.K.D.H. Bhadeshia, P. Woollin, Effect of δ -ferrite on impact properties of supermartensitic stainless steel heat affected zones, Sci. Technol. Weld. Join. 9 (2004) 377–389.
[21] Thermo-Calc Software TCFE6 Steels/Fe-alloys database version 6.2, Thermo-Calc Softw. TCFE6 Steels/Fe-Alloys Database Version 6.2 (Accessed Novemb. 2009).
[22] F. Niessen, M. Villa, J. Hald, M.A.J. Somers, Kinetics analysis of two-stage austenitization in supermartensitic stainless steel, Mater. Des. 116 (2017) 8–15.
[23] M. Villa, K. Pantleon, M. Reich, O. Kessler, M.A.J. Somers, Kinetics of anomalous multi-step formation of lath martensite in steel, Acta Mater. 80 (2014) 468–477.
[24] C.N. Hsiao, C.S. Chiou, J.R. Yang, Aging reactions in a 17-4 PH stainless steel, Mater. Chem. Phys. 74 (2002) 134–142.
[25] F. Niessen, M. Villa, D. Apel, O. Keßler, M. Reich, J. Hald, M.A.J. Somers, In situ techniques for the investigation of the kinetics of austenitization of supermartensitic stainless steel, Mater. Sci. Forum. 879 (2017) 1381–1386.
[26] A. Bojack, L. Zhao, P.F. Morris, J. Sietsma, In-situ determination of austenite and martensite formation in 13Cr6Ni2Mo supermartensitic stainless steel, Mater. Charact. 71 (2012) 77–86.
[27] C.A.D. Rodrigues, P.L.D. Lorenzo, A. Sokolowski, C.A. Barbosa, J.M.D.A. Rollo, Titanium and molybdenum content in supermartensitic stainless steel, Mater. Sci. Eng. A. 460–461 (2007) 149–152.
[28] M. De Sanctis, G. Lovicu, R. Valentini, A. Dimatteo, R. Ishak, U. Migliaccio, R. Montanari, E. Pietrangeli, Microstructural Features Affecting Tempering Behavior of 16Cr-5Ni Supermartensitic Steel, Metall. Mater. Trans. A Phys. Metall. Mater. Sci. 46 (2015) 1878–1887.
[29] B.P.J. Sandvik, C.M. Wayman, Characteristics of Lath Martensite: Part I. Crystallographic and Substructural Features, Metall. Trans. A. 14 (1983) 809–822.
[30] G. Kurdjumow, G. Sachs, Über den Mechanismus der Stahlhärtung, Zeitschrift Für Phys. 64 (1930) 325–343.
[31] C. Bos, J. Sietsma, B.J. Thijsse, Molecular dynamics simulation of interface dynamics during the fcc-bcc transformation of a martensitic nature, Phys. Rev. B - Condens. Matter Mater. Phys. 73 (2006) 1–7.
[32] F. Maresca, W.A. Curtin, The austenite/lath martensite interface in steels: Structure, athermal motion, and in-situ transformation strain revealed by simulation and theory, Acta Mater. 134 (2017) 302–323.
[33] H.K.D.H. Bhadeshia, Worked examples in the geometry of crystals, 2nd editio, 2001.
[34] M.G. Hall, H.I. Aaronson, K.R. Kinsma, The structure of nearly coherent fcc: bcc boundaries in a CuCr alloy, Surf. Sci. 31 (1972) 257–274.
[35] P. Brezina, B. Sonderegger, Wärmebehandlung, Gefüge und Eigenschaften des korrosionsträgen martensitaushärtbaren Stahles X 5 CrNiMoCuNb 14 5 (14-5 PU), Härterei-Technische Mitteilungen. 33 (1978) 1–12.
[36] E. Folkhard, Welding metallurgy of stainless steels, in: Weld. Metall. Stainl. Steels, 1988: pp. 98–181.
[37] T.G. Gooch, Welding Martensitic Stainless Steels, Weld. Inst. Researach Bull. (1977) 343–349.
[38] M. Villa, F. Niessen, M.A.J. Somers, In situ investigation of the evolution of lattice strain and stresses in austenite and martensite during quenching and tempering of steel, Metall. Mater. Trans. A. 49 (2017) 1–13.

[39] F. Niessen, M. Villa, F. Danoix, J. Hald, M.A.J. Somers, In-situ analysis of redistribution of carbon and nitrogen during tempering of low interstitial martensitic stainless steel, Submitted (2018).
[40] Y. Song, D.H. Ping, F.X. Yin, X.Y. Li, Y.Y. Li, Microstructural evolution and low temperature impact toughness of a Fe–13%Cr–4%Ni–Mo martensitic stainless steel, Mater. Sci. Eng. A. 527 (2010) 614–618.
[41] T. Maki, Morphology and substructure of martensite in steels, in: E. Pereloma, D. V. Edmonds (Eds.), Phase Transform. Steels Vol. 2 Diffus. Transform. High Strength Steels, Model. Adv. Anal. Tech., 1st ed., Woodhead Publishing, 2012: pp. 34–58.
[42] F. Christien, M.T.F. Telling, K.S. Knight, Neutron diffraction in situ monitoring of the dislocation density during martensitic transformation in a stainless steel, Scr. Mater. 68 (2013) 506–509.
[43] M. Wiessner, E. Gamsjäger, S. van der Zwaag, P. Angerer, Effect of reverted austenite on tensile and impact strength in a martensitic stainless steel−An in-situ X-ray diffraction study, Mater. Sci. Eng. A. 682 (2017) 117–125.
[44] F. Niessen, F. Danoix, J. Hald, M.A.J. Somers, Structural analysis in atom probe tomography - application to tempering of supermartensitic stainless steel, in: 7th Eur. Atom Probe Work. 2017, Gullmarsstrand, Sweden, 2017.
[45] Z.M. Shi, W. Gong, Y. Tomota, S. Harjo, J. Li, B. Chi, J. Pu, Study of tempering behavior of lath martensite using in situ neutron diffraction, Mater. Charact. 107 (2015) 29–32.
[46] X. Ma, L. Wang, S. V. Subramanian, C. Liu, Studies on Nb microalloying of 13Cr super martensitic stainless steel, Metall. Mater. Trans. A Phys. Metall. Mater. Sci. 43 (2012) 4475–4486.
[47] C. Servant, E.H. Gherbi, G. Cizeron, TEM investigation of the tempering behaviour of the maraging PH 17.4 Mo stainless steel, J. Mater. Sci. 22 (1987) 2297–2304.
[48] W.H. Yuan, X.H. Gong, Y.Q. Sun, J.X. Liang, Microstructure Evolution and Precipitation Behavior of 0Cr16Ni5Mo Martensitic Stainless Steel during Tempering Process, J. Iron Steel Res. Int. 23 (2016) 401–408.
[49] Y.Y. Song, X.Y. Li, L.J. Rong, D.H. Ping, F.X. Yin, Y.Y. Li, Formation of the reversed austenite during intercritical tempering in a Fe-13%Cr-4%Ni-Mo martensitic stainless steel, Mater. Lett. 64 (2010) 1411–1414.
[50] S. Zhang, P. Wang, D. Li, Y. Li, Investigation of the evolution of retained austenite in Fe-13%Cr-4%Ni martensitic stainless steel during intercritical tempering, Mater. Des. 84 (2015) 385–394.
[51] P. Woollin, Understanding and Avoiding Intergranular Stress Corrosion Cracking of Welded Supermartensitic Steel, in: NACE Corros. Conf. Expo (Corrosion 2007), 2007: pp. 5379–5394.
[52] E. Ladanova, J.K. Solberg, T. Rogne, Carbide precipitation in HAZ of multipass welds in titanium containing and titanium free supermartensitic stainless steels Part 1 - Proposed precipitation mechanisms, Corros. Eng. Sci. Technol. 41 (2006) 143–151.
[53] E. Bardal, Corrosion and Protection, Springer, 2004.
[54] H.F. Reid, W.T. DeLong, Making sense out of ferrite requirements in welding stainless steels, Met. Prog. (1973) 73–77.
[55] M. Kimura, Y. Miyata, Y. Yamane, T. Toyooka, Y. Nakano, F. Murase, Corrosion resistance of high-strength modified 13% Cr steel, Corrosion. 55 (1999) 756–761.
[56] R. Aune, H. Fostervoll, O.M. Akselsen, High heat input welding of 12Cr-6Ni-2.5Mo

supermartensitic stainless steel, in: 22nd Int. Conf. Offshore Mech. Arct. Eng., 2003: pp. 1–6.
[57] Outokumpu, Handbook of Stainless Steel, (2013) 1–89.
[58] S.D. Washko, G. Aggen, Wrought Stainless Steels, in: C. Allen, B. Boardman (Eds.), ASM Handbook, Vol. 1, Prop. Sel. Irons, Steels, High Perform. Alloy. Sect. Spec. Steels Heat-Resistant Alloy., 2005: pp. 1303–1408.
[59] R. Schnitzer, R. Radis, M. Nöhrer, M. Schober, R. Hochfellner, S. Zinner, E. Povoden-Karadeniz, E. Kozeschnik, H. Leitner, Reverted austenite in PH 13-8 Mo maraging steels, Mater. Chem. Phys. 122 (2010) 138–145.
[60] A. Bojack, L. Zhao, P.F. Morris, J. Sietsma, Austenite Formation from Martensite in a 13Cr6Ni2Mo Supermartensitic Stainless Steel, Metall. Mater. Trans. A. 47 (2016) 1996–2009.
[61] X.P. Ma, L.J. Wang, B. Qin, C.M. Liu, S.V. Subramanian, Effect of N on microstructure and mechanical properties of 16Cr5Ni1Mo martensitic stainless steel, Mater. Des. 34 (2012) 74–81.
[62] D.-S. Leem, Y.-D. Lee, J.-H. Jun, C.-S. Choi, Amount of retained austenite at room temperature after reverse transformation of martensite to austenite in an Fe–13%Cr–7%Ni–3%Si martensitic stainless steel, Scr. Mater. 45 (2001) 767–772.
[63] Y.-K. Lee, H.-C. Shin, D.-S. Leem, J.-Y. Choi, W. Jin, C.-S. Choi, Reverse transformation mechanism of martensite to austenite and amount of retained austenite after reverse transformation in Fe-3Si-13Cr-7Ni (wt-%) martensitic stainless steel, Mater. Sci. Technol. 19 (2003) 393–398.
[64] N. Nakada, T. Tsuchiyama, S. Takaki, N. Miyano, Temperature Dependence of Austenite Nucleation Behavior from Lath Martensite, ISIJ Int. 51 (2011) 299–304.
[65] L. Liu, Z.G. Yang, C. Zhang, W.B. Liu, An in situ study on austenite memory and austenitic spontaneous recrystallization of a martensitic steel, Mater. Sci. Eng. A. 527 (2010) 7204–7209.
[66] L. Liu, Z.-G. Yang, C. Zhang, Effect of retained austenite on austenite memory of a 13% Cr–5% Ni martensitic steel, J. Alloys Compd. 577 (2013) 654–660.
[67] S. Morito, H. Tanaka, R. Konishi, T. Furuhara, T. Maki, The morphology and crystallography of lath martensite in Fe-C alloys, Acta Mater. 51 (2003) 1789–1799.
[68] F. Niessen, F.B. Grumsen, J. Hald, M.A.J. Somers, Formation and stabilization of reversed austenite in supermartensitic stainless steel, in: Proc. 24th IFHTSE Congr., 2017: pp. 138–145.
[69] Y.Y. Song, X.Y. Li, L.J. Rong, Y.Y. Li, T. Nagai, Reversed austenite in 0Cr13Ni4Mo martensitic stainless steels, Mater. Chem. Phys. 143 (2014) 728–734.
[70] N. Nakada, T. Tsuchiyama, S. Takaki, S. Hashizume, Variant Selection of Reversed Austenite in Lath Martensite, ISIJ Int. 47 (2007) 1527–1532.
[71] J.D. Escobar, J.D. Poplawsky, G.A. Faria, J. Rodriguez, J.P. Oliveira, C.A.F. Salvador, P.R. Mei, S.S. Babu, A.J. Ramirez, Compositional analysis on the reverted austenite and tempered martensite in a Ti-stabilized supermartensitic stainless steel: Segregation, partitioning and carbide precipitation, Mater. Des. 140 (2018) 95–105.
[72] Y. Song, X. Li, L. Rong, Y. Li, The influence of tempering temperature on the reversed austenite formation and tensile properties in Fe-13%Cr-4%Ni-Mo low carbon martensite stainless steels, Mater. Sci. Eng. A. 528 (2011) 4075–4079.
[73] F. Niessen, Austenite reversion in low-carbon martensitic stainless steels – a CALPHAD-assisted review, Mater. Sci. Technol. (2018). doi: 10.1080/02670836.2018.1449179
[74] J.D. Escobar, G. Faria, L. Wu, J.P. Oliveira, P.R. Mei, A.J. Ramirez, Austenite

reversion kinetics and stability during tempering of a Ti-stabilized supermartensitic stainless steel: correlative in situ synchrotron x-ray diffraction and dilatometry, Acta Mater. 138 (2017) 92–99.
[75] Y. Song, X. Li, L. Rong, Y. Li, Anomalous Phase Transformation from Martensite to Austenite in Fe-13%Cr-4%Ni-Mo Martensitic Stainless Steel, J. Mater. Sci. Technol. 26 (2010) 823–826.
[76] P. Wang, N. Xiao, S. Lu, D. Li, Y. Li, Investigation of the mechanical stability of reversed austenite in 13%Cr-4%Ni martensitic stainless steel during the uniaxial tensile test, Mater. Sci. Eng. A. 586 (2013) 292–300.
[77] P.D. Bilmes, M. Solari, C.L. Llorente, Characteristics and effects of austenite resulting from tempering of 13Cr–NiMo martensitic steel weld metals, Mater. Charact. 46 (2001) 285–296.
[78] W. Jiang, D. Ye, J. Li, J. Su, K. Zhao, Reverse Transformation Mechanism of Martensite to Austenite in 00Cr15Ni7Mo2WCu2 Super Martensitic Stainless Steel, Steel Res. Int. 85 (2014) 1150–1157.
[79] A. Bojack, L. Zhao, P.F. Morris, J. Sietsma, In Situ Thermo-magnetic Investigation of the Austenitic Phase During Tempering of a 13Cr6Ni2Mo Supermartensitic Stainless Steel, Metall. Mater. Trans. A Phys. Metall. Mater. Sci. 45 (2014) 5956–5967.
[80] A. García-Junceda, C. Capdevila, F.G. Caballero, C.G. de Andrés, Dependence of martensite start temperature on fine austenite grain size, Scr. Mater. 58 (2008) 134–137.
[81] H.S. Yang, H.K.D.H. Bhadeshia, Austenite grain size and the martensite-start temperature, Scr. Mater. 60 (2009) 493–495.
[82] G. Ghosh, G.B. Olson, Kinetics of F.C.C. → B.C.C. heterogeneous martensitic nucleation-I. The critical driving force for athermal nucleation, Acta Metall. Mater. 42 (1994) 3361–3370.
[83] D.B. Williams, C.B. Carter, 9.3.B Bright-Field and Dark-Field Imaging, in: Transm. Electron Microsc. Part 1 Basics, Second edi, Springer.
[84] P. Wang, S. Lu, D. Li, X. Kang, Y. Li, Investigation of phase tranformation of low carbon martensitic stainless steel ZG06Cr13Ni4Mo in tempering process with low heating rate, Acta Metall. Sin. 44 (2008) 681–685.
[85] K. Tomimura, S. Takaki, Y. Tokunaga, Reversion Mechanism from Deformation Induced Martensite to Austenite in Metastable Austenitic Stainless Steels., ISIJ Int. 31 (1991) 1431–1437.
[86] M. Villa, M.A.J. Somers, Thermally activated martensite formation in ferrous alloys, Scr. Mater. 142 (2018) 46–49.
[87] T. LeBrun, T. Nakamoto, K. Horikawa, H. Kobayashi, Effect of retained austenite on subsequent thermal processing and resultant mechanical properties of selective laser melted 17-4 PH stainless steel, Mater. Des. 81 (2015) 44–53.
[88] A. Kromm, S. Brauser, T. Kannengiesser, M. Rethmeier, High-energy synchrotron diffraction study of a transformation induced plasticity steel during tensile deformation, J. Strain Anal. Eng. Des. 46 (2011) 581–591.
[89] X.C. Xiong, B. Chen, M.X. Huang, J.F. Wang, L. Wang, The effect of morphology on the stability of retained austenite in a quenched and partitioned steel, Scr. Mater. 68 (2013) 321–324.
[90] S. Brauser, A. Kromm, T. Kannengiesser, M. Rethmeier, In-situ synchrotron diffraction and digital image correlation technique for characterizations of retained austenite stability in low-alloyed transformation induced plasticity steel, Scr. Mater.

63 (2010) 1149–1152.
[91] K. Yan, K.-D. Liss, I.B. Timokhina, E. V. Pereloma, In situ synchrotron X-ray diffraction studies of the effect of microstructure on tensile behavior and retained austenite stability of thermo-mechanically processed transformation induced plasticity steel, Mater. Sci. Eng. A. 662 (2016) 185–197.
[92] E.C. Oliver, M.R. Daymond, P.J. Withers, T. Mori, Stress Induced Martensitic Transformation Studied by Neutron Diffraction, Mater. Sci. Forum. 404–407 (2002) 489–494.
[93] M.I. Latypov, S. Shin, B.C. De Cooman, H. Seop, Micromechanical finite element analysis of strain partitioning in multiphase medium manganese TWIP + TRIP steel, Acta Mater. 108 (2016) 219–228.
[94] H. Liu, L.-X. Du, J. Hu, H.-Y. Wu, X.-H. Gao, R.D.K. Misra, Interplay between reversed austenite and plastic deformation in a directly quenched and intercritically annealed 0.04C-5Mn low-Al steel, J. Alloys Compd. 695 (2016) 2072–2082.
[95] K.G. Solheim, J.K. Solberg, J. Walmsley, F. Rosenqvist, T.H. Bjørnå, The role of retained austenite in hydrogen embrittlement of supermartensitic stainless steel, Eng. Fail. Anal. 34 (2013) 140–149.
[96] H.J. Niederau - Eigenschaften UDd Anwendungsmoglichkeiten der Gun- und Schmiedelegierung (G)X-5 CrNiMo 16 5 (Werkstoff-Nr. 1.4405), Zeitschrift Des Vereins Dtsch. Ingenieure fUr Maschinenbau Und Met. Eig. 21 (1982) 801–808.
[97] J.E. Ramirez, Weldability Evaluation of Supermartensitic Stainless Pipe Steels, Weld. Res. 86 (2007) 125–134.
[98] H. Heuser, C. Jochum, E. Perteneder, J. Tösch, Girth welding of supermartensitic stainless steels with matching filler metals, in: Proc. 3rd Int. Pipeline Technol. Conf., Brugge, Belgium, 2000: pp. 307–317.
[99] L. Karlsson, S. Rigdal, J. Van Den Broek, M. Goldschmitz, R. Pedersen, Welding of supermartensitic stainless steels recent developments and application experience, ESAB Weld. Cut. J. 2 (2002) 14–20.
[100] J. Van Den Broek, M. Goldschmitz, L. Karlsson, S. Rigdal, Efficient welding of supermartensitic pipes with matching metal cored wires, Svetsaren. 56 (2001) 42–46.
[101] P.B. Srinivasan, S.W. Sharkawy, W. Dietzel, Environmental Cracking Behavior of Submerged Arc-Welded Supermartensitic Stainless Steel Weldments, J. Mater. Eng. Perform. 13 (2004) 232–236.
[102] G. Rørvik, P.E. Kvaale, O.M. Akselsen, Sources and levels of hydrogen in TIG welding of 13 % Cr martensitic stainless steels, in: Supermartensitic Stainl. Steels, Brussels, 1999: pp. 196–203.
[103] N. Anselmo, J.E. May, N.A. Mariano, P.A.P. Nascente, S.E. Kuri, Corrosion behavior of supermartensitic stainless steel in aerated and CO2-saturated synthetic seawater, Mater. Sci. Eng. A. 428 (2006) 73–79.

3 Materials and experimental methods

This chapter grants an overview of the employed materials and experimental methods. Sections on the individual experimental methods give a brief introduction to the general method with reference to further reading and therefrom focus on the specific setups used in this project. Specific experimental parameters are given in the individual result chapters.

3.1 Materials and heat-treatments

Three different materials were investigated in this research work, a supermartensitic stainless steel, a soft martensitic stainless steel and a cast soft martensitic stainless steel with the alloy compositions in Table 3.1.

The material Super 13 Cr (UNS S41427) is a wrought super martensitic stainless steel, which was manufactured by *BGH Edelstahl Siegen Gmbh* and supplied by *Sverdrup Steel*. As this material is amongst the most widely applied alloys in the offshore oil and gas sector, it was chosen to conduct studies on the microstructure-property relationship (chapter 13). Thus, the fundamental findings on the microstructure in this work can directly be linked to properties that are of interest when applying the material on an industrial scale. The steel was delivered as a bar with 200 mm in diameter (8”) and supplied in quenched and tempered condition (985 °C / 4 h + 600 °C / 7.5 h). The material for experimental investigation was taken in close proximity to the center of the bar. Extracted samples were homogenized for 60 min at 1050 °C to reverse the given tempering treatment. The individual inter-critical annealing treatments for experimental investigation are given in chapter 13.

The material EN 1.4418 (X4CrNiMo16-5-1) is a wrought soft martensitic stainless steel, which was received as an extruded bar of 10 mm in diameter in non-tempered condition. This material was used to study the fundamental phase transformations, i.e. the kinetics of austenitization (chapter 10), the build-up of stresses during martensite formation (chapter 7), tempering of martensite (chapter 8 and 9) and the formation and stabilization of reverted austenite (chapter 11). The standard austenitization treatment was either at 920 or 950°C for 10 min and the specific inter-critical annealing treatments are given in the respective results chapters.

Table 3.1: Chemical compositions of the analyzed steels in wt.% as determined by optical emission spectroscopy (OES) in balance with Fe.

Alloy	C	N	Cr	Ni	Mn	Mo	Si	Cu	Co	V	Ti
Super13 Cr	0.02	0.05	12.5	5.6	0.46	2.02	0.30	0.11	0.02	0.05	0.02
EN 1.4418	0.03	0.04	15.0	5.8	0.86	1.03	0.39	0.32	0.11	0.05	0.01
EN 1.4405	0.01	0.08	15.3	6.3	0.58	1.22	0.70	0.09	0.04	0.03	0.01

The material EN 1.4405 (GX4CrNiMo16-5-1) is a cast soft martensitic stainless steel which was provided by the *Frese metal and steel foundry A/S* in non-tempered condition. The material was cast in a special heat in keel blocks of 230 x 110 x 60/25 mm with bottom filling to study the kinetics of δ-ferrite formation and retainment during solidification and cooling (chapter 6). The castings were cut horizontally at 40 mm height to disregard the impurity-rich last solidified material. Examination of the material was carried out on a cross-section in the center of the extracted bars. No homogenization treatment was performed as the aim of the study was to analyze the material in the as-cast condition.

The methods for specimen preparation were optimized towards the individual experimental methods and are therefore reported in the following method sections.

3.2 X-ray diffraction

In this section, the general principle of X-ray diffraction is briefly introduced with an extension to energy-dispersive X-ray diffraction, which was exclusively applied in this work. Thereafter the principles in quantitative phase analysis and stress measurement in X-ray diffraction are introduced, covering the specific methods used in this work. Finally the method for diffraction line-profile analysis and the applied experimental setups for in-situ studies are described.

X-ray diffraction is amongst the most popular diffraction methods to measure planar spacings in crystals. Results from X-ray diffraction measurements can be used for qualitative or quantitative phase analysis or detecting changes in chemistry, temperature or stress. X-rays were discovered in 1895 by W. C. Röntgen [1] and the first X-ray diffraction from a crystal was reported in 1912 by W. Friedrich, P. Knipping and M. Laue [2]. Father and son W.H. and W.L. Bragg presented a revolutionary equation, now known as Bragg's equation, in 1913 [3], for which they received the Nobel Prize in 1915:

$$n\lambda = 2d\sin\theta \;\Leftrightarrow\; d = \frac{n\lambda}{2\sin\theta} \tag{3.1}$$

Bragg's equation states that the planar spacing d of a set of coherently diffracting crystal planes is associated with constructive interference of the diffracted beam at the Bragg angle θ, when the wavelength λ is constant. A visual representation of this relation is given in Figure 3.1. In practical diffraction setups, the diffraction angle 2θ is generally reported rather than the Bragg angle θ. The diffraction vector g, also called reciprocal lattice vector, is defined perpendicular to a set of diffracting crystal planes and has the length $K = \frac{1}{d}$.

3.2.1 Energy-dispersive X-ray diffraction

For a variety of mostly economic reasons, most conventional X-ray diffractometers are angular dispersive, i.e. systematically vary the angular position of a monochromatic X-ray source and a scintillation counter with respect to a sample to scan a range of 2θ (c.f. Figure

3.1). Alternatively, the planar spacing from Bragg's equation (Equ. 3.1) can be obtained for an arbitrarily chosen and fixed value for 2θ when instead of a monochromatic X-ray source a white beam with a continuous photon spectrum is used. Such diffraction method is termed energy-dispersive X-ray diffraction, for which insertion of the Planck relation $\lambda = \frac{hc}{E}$ into Bragg's equation (Equ. 3.1) yields an inversely proportional dependence of energy E with the planar spacing of a set of coherently diffracting hkl [4]:

$$n\frac{hc}{E} = 2d\sin\theta \;\Leftrightarrow\; d = \frac{nhc}{E2\sin\theta} = \frac{Constant}{E} \tag{3.2}$$

where h is the Planck constant and c the speed of light in vacuum. As energy-dispersive X-ray diffraction requires a beam of white X-rays, the method is generally confined to modern third-generation synchrotron light sources [5]. A typical diffraction setup for energy-dispersive X-ray diffraction is shown in Figure 3.2. The primary beam is attenuated by an absorber mask and a filter system and reduced to a defined cross-section by a slit system. The equatorial (i.e. vertical) divergence of the diffracted beam is limited to $\Delta 2\theta < 0.01°$ by a double slit system on the secondary beam side to prevent geometrically induced energy broadening of the diffraction lines [5].

Some important characteristics of energy-dispersive X-ray diffraction are [6]:

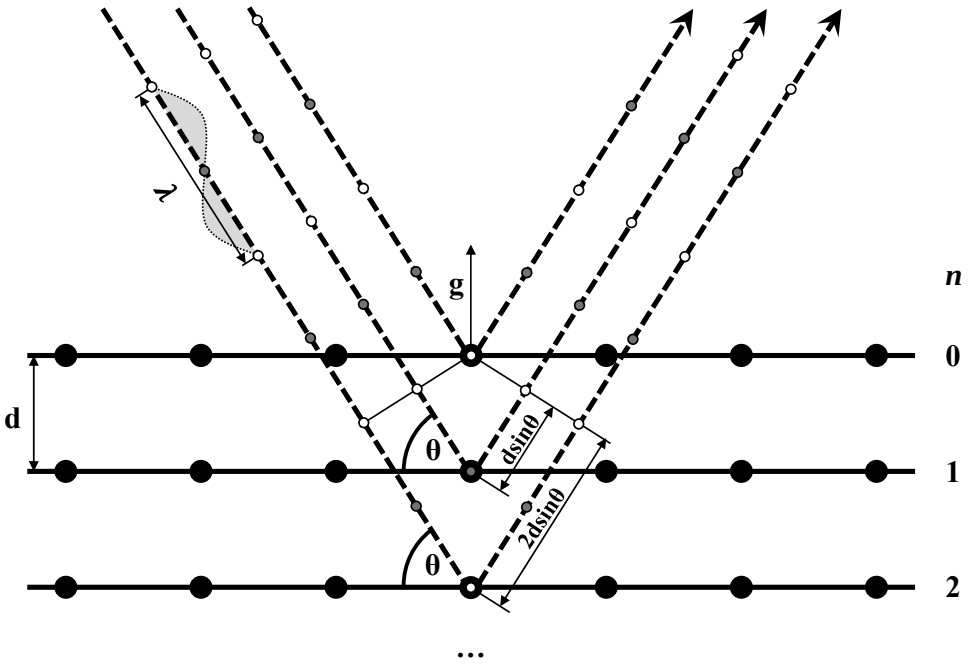

Figure 3.1: Visual representation of Bragg's law (Equ. 3.1). Three X-ray beams with equal phase and wavelength λ are scattered by a set of crystal planes ($n = 0, 1, 2, ...$) with interplanar distance d. Scattering at the Bragg angle θ leads to constructive interference of the diffracted beams, while scattering away from the Bragg angle leads to increasing destructive interference of the diffracted beam with increasing n. The diffraction vector g is perpendicular to a diffracting crystal plane and has the length $K = 1/d$.

- Entire diffraction patterns with multiple diffraction lines are acquired under fixed geometrical conditions, i.e. no scanning is required.
- Because of different photon energies, the information depth varies for diffraction lines at different energies E
- Equ. 3.2 shows that the diffracted spectrum can be "compressed" or "stretched" towards smaller or higher energies by adapting the diffraction angle 2θ. To a certain degree, this enables tuning of the information depth.

All X-ray diffraction studies in this project were conducted at the synchrotron beamline EDDI [6] of the BESSY II synchrotron facility, Helmholtz Zentrum Berlin für Materialien und Energie (HZB).

3.2.2 Quantitative phase analysis

Quantitative phase analysis was carried out by using the direct comparison method, as originally proposed by Arnell [7] in 1968 and applied on the determination of retained austenite in steel according to ASTM standard E975 [8]. The method enables the determination of the austenite and ferrite (martensite) volume fractions, f_γ and f_α, in a steel with near random crystallographic orientation by comparing the theoretic intensities of different hkl and phases ϕ, R_{hkl}^{ϕ}, with the integrated intensities from diffraction measurements, I_{hkl}^{ϕ}. The theoretical intensities are obtained by:

$$R_{hkl}^{\phi} = m_{hkl} \cdot \left|F_{0}{}_{hkl}^{\phi}\right|^2 \cdot e^{(-2M)} \cdot {n^{\phi}}^{-2} \cdot {\mu_E}^{-1} \cdot \left(\frac{hc}{E_{hkl}^{\phi}}\right)^3 \tag{3.3}$$

where m_{hkl} is the hkl-dependent multiplicity factor, $\left|F_{0}{}_{hkl}^{\phi}\right|^2$ is the hkl- and phase-dependent structure factor, $e^{(-2M)}$ is the Debye-Waller factor, n^{ϕ} is the phase-specific unit cell volume and ${\mu_E}^{-1}$ the energy-dependent absorption factor. The Debye-Waller factors were calculated according to Ref. [9] with a constant Debye-Waller parameter.

Comparison of the integrated intensities with the theoretical intensities are averaged for all peaks and lead to the volume fraction of austenite and ferrite (martensite):

$$f_\gamma = 1 - f_{\alpha'} = \left(\frac{1}{q}\sum_{j=1}^{q}\frac{I_{\gamma j}}{R_{\gamma j}}\right) \Big/ \left[\left(\frac{1}{p}\sum_{j=1}^{p}\frac{I_{\alpha' j}}{R_{\alpha' j}}\right) + \left(\frac{1}{q}\sum_{j=1}^{q}\frac{I_{\gamma j}}{R_{\gamma j}}\right)\right] \tag{3.4}$$

where p and q are the number of peaks for martensite and austenite. More available peaks and high integrated intensities increase the accuracy of the method. ASTM norm E975 states a reproducibility within 4% of retained austenite for a 95 % confidence limit from an interlaboratory evaluation [10].

3.2.3 Stress analysis

In stress analysis, all stresses σ, strains ε and crystal elastic constants $-s_1$ and $\frac{1}{2}s_2$ are hkl- and phase-dependent. For the sake of clarity, this dependence is omitted in the following notation.

Stress-strain relation

Bragg's equation opened up the possibilities of non-destructive strain measurement by diffraction methods, which was first reported by M. Joffe and F. Kirpitcheva [11] in 1922. The development of stress analysis as a non-destructive diffraction-based method started in the 30's of last century and continues into the present. A great and comprehensive overview of the important milestones can be found in Ref. [12].

Stress cannot be measured directly by diffraction methods, but only indirectly by the associated lattice strain. Bragg's equation shows that, using either a diffractometer with a fixed wavelength λ and a variable diffraction angle 2θ or vice-versa, the measurement of a planar spacing d enables determination of the corresponding lattice strain:

$$\varepsilon = \frac{d - d_{ref}}{d_{ref}} \tag{3.5}$$

where d_{ref} is a strain free planar spacing. Since only crystal planes with the normal vector parallel to the diffraction vector g contribute to the diffraction pattern, tilting of the sample is required to obtain all 6 independent principal strains of the strain tensor. Translation of the sample coordinate system, x^S, to the laboratory coordinate system, x^L, by means of the diffractometer angles φ and ψ, the laboratory strain $\varepsilon^L_{\varphi,\psi}$ can be represented by the principal strains, ε_{ij}, of the sample coordinate system [13]:

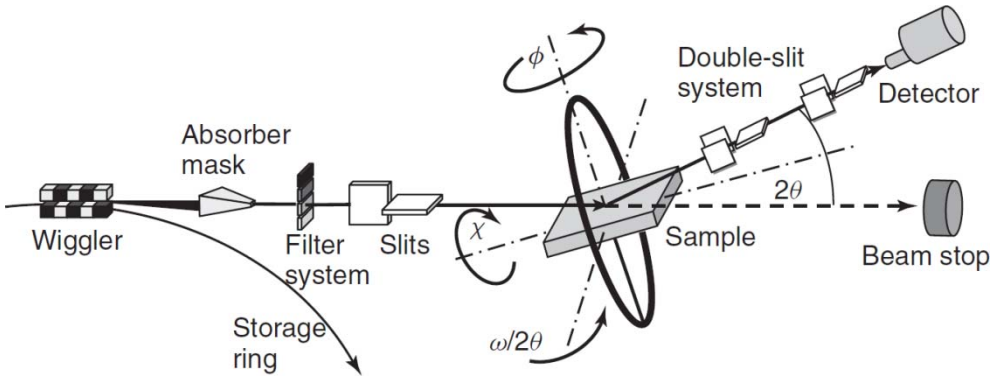

Figure 3.2: Setup of a white beam synchrotron beamline for energy-dispersive diffraction and residual stress analysis. The diffractometer angles φ and χ correspond to the azimuth and inclination angle ϕ and ψ in Figure 3.1b, respectively, which define the orientation of the diffraction vector in the sample system x^S. ω and 2θ are the angles of rotation of the sample and the detector, respectively, around an axis perpendicular to the (vertical) diffraction plane. [5]

$$\varepsilon^L_{\varphi,\psi} = \frac{d_{\varphi,\psi} - d_{ref}}{d_{ref}} = \varepsilon_{11}\cos^2\varphi\sin^2\psi + \varepsilon_{12}\,sin\,2\varphi\sin^2\psi + \varepsilon_{13}\,cos\,\varphi\sin 2\psi + \varepsilon_{22}\,sin^2\varphi\sin^2\psi + \varepsilon_{23}\,sin\,\varphi\sin 2\psi + \varepsilon_{33}\cos^2\psi \quad (3.6)$$

The coordinate systems, the diffraction vector and the angles are shown in Figure 3.3a. The principal strains are translated to principal stresses with help of the hkl-dependent X-ray Elastic Constants (XEC's), s_1 and $\frac{1}{2}s_2$:

$$\varepsilon^L_{\varphi,\psi} = \tfrac{1}{2}s_2(\sigma_{11}\cos^2\varphi\sin^2\psi + \sigma_{22}\,sin^2\varphi\sin^2\psi + \sigma_{33}\cos^2\psi) + \tfrac{1}{2}s_2(\sigma_{12}sin2\varphi\sin^2\psi + \sigma_{13}cos\varphi\,sin\,2\psi + \sigma_{23}\,sin\,\varphi\sin 2\psi) + s_1(\sigma_{11}+\sigma_{22}+\sigma_{33}) \quad (3.7)$$

Types of stress

Stresses can be categorized in three types by the length scale over which they equilibrate: Macro-stresses (type I), σ^I, occur over considerable length in a sample, micro-stresses of type II, σ^{II}, equilibrate at the grain or phase scale, and micro-stresses of type III, σ^{III}, are stresses that occur at a considerably smaller scale than the grain scale [13,14].

Due to the characteristic length scales of the different stress types, type II and type III stresses can only be measured as average values over the probed volume with common diffraction methods ($\overline{\sigma}^{II}$ and $\overline{\sigma}^{III}$ in Figure 3.3b). For dual-phase polycrystalline materials

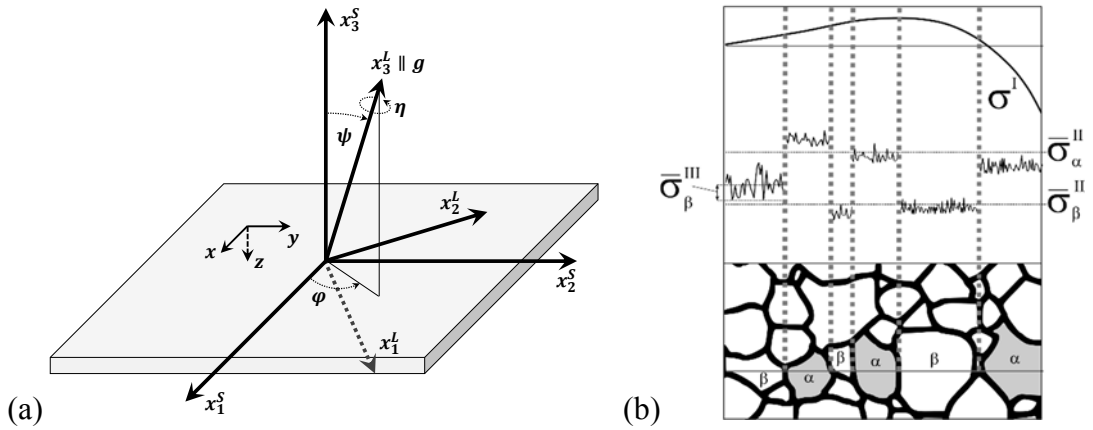

Figure 3.3: (a) Diffraction geometry in X-ray stress analysis. x^S and x^L denote the sample reference and the laboratory system, respectively. Note that the positive z-axis of the sample system is directed towards the interior of the material. The angle set (ϕ, ψ) defines the orientation of the diffraction vector g with respect to x^S, whereas η describes the rotation of the sample around g (adapted from [5]); (b) Distinction of residual stress types I to III by distance of equilibration; Stress of type I, macro-stress, equilibrates over the length of the sample, micro-stress of type II equilibrates over the distance of a grain (the example shows micro-stresses for grains of phases α and β), and micro-stress of type III equilibrates on atomic scale. Measured quantities of type II and III stresses represent an average value of the probed microstructure.

with no preferred grain orientation, as considered in the present work, stresses of type I are partitioned into phase specific stresses of type II, which lead to phase specific line profile shifts, while broadening of the line profiles reflects the variation in phase specific stresses of type II and stresses of type III. Consequently, determination of either type I or type II stresses cannot be conducted alone without adequately addressing the effect of both contributions.

Separation of stresses of type I and type II

Separation of type I and type II stresses is generally required, for example when stresses of type I after constrained cooling of a manufactured part, or stresses of type II as a result of nucleation of a second phase with different density are of interest. In such cases the difference in characteristic length scale of the stress types can be used to separate the individual contributions.

Macherauch and Müller presented in their famous publication on the $\sin^2\psi$ method [15] in 1961, that lattice strains as a results of a rotationally symmetric biaxial state of stress directly correspond to the slope of the relative change in planar spacing as a function of $\sin^2\psi$

$$\varepsilon_{\parallel} = \frac{1}{d_{ref}} \frac{\partial d_{\psi}}{\partial sin^2\psi} \tag{3.8}$$

and that the corresponding biaxial stress is given by multiplying with the XEC $\frac{2}{s_2}$:

$$\sigma_{\parallel} = \frac{2}{s_2 d_{ref}} \frac{\partial d_{\psi}}{\partial sin^2\psi} \tag{3.9}$$

Considering the large characteristic length of stresses of type I in comparison to the penetration depth of conventional laboratory X-rays (few µm for ferrous samples) it can be argued that these stresses are relaxed normal to the surface, i.e. $\sigma_{\perp}^{I} = 0$. Stresses of type II in contrast are not necessarily nill parallel to the surface normal, when considering a polycrystal with relatively small grain size. Type II stresses can then often be considered hydrostatic, as they reflect an average value from several grains. Consequently, the stresses normal to the surface only consist of the average hydrostatic stress of type II: $\sigma_{\perp} = \overline{\sigma}^{II}$. In order to separate the two types of stress, the assumption of a biaxial state of stress in Equ. 3.9 can be extended by assuming an additional hydrostatic stress of type II:

$$\sigma_{\parallel} - \sigma_{\perp} = \left(\sigma^{I} + \overline{\sigma}^{II}\right) - \overline{\sigma}^{II} = \sigma^{I} = \frac{2}{s_2 d_{ref}} \frac{\partial d_{\psi}}{\partial sin^2\psi} \tag{3.10}$$

Reducing the general stress-strain relation in Equ. 3.7 to a triaxial stress state with rotational symmetry of the surface stresses, a simplified version of the stress-strain relation is obtained [13]:

$$\varepsilon_{\psi}^{L} = s_1(2\sigma_{\parallel} + \sigma_{\perp}) + \frac{1}{2}s_2\sigma_{\perp} + \frac{1}{2}s_2(\sigma_{\parallel} - \sigma_{\perp})\sin^2\psi) \tag{3.11}$$

The stress component $\sigma_{\parallel} - \sigma_{\perp} = \sigma^{I}$ corresponds directly to the slope of the $\sin^2\psi$ plot from Equ. 3.10 multiplied with $\frac{1}{2}s_2$, and $s_1(2\sigma_{\parallel} + \sigma_{\perp}) + \frac{1}{2}s_2\sigma_{\perp}$ is given by the y-intercept (c.f. Figure 3.4). Rearrangement of Equ. 3.11 to solve for $\overline{\sigma}^{II}$ yields:

$$\overline{\sigma}^{II} = \sigma_{\perp} = \frac{\varepsilon_{\psi}^{L} - \sigma^{I}(2s_1 + ½s_2 sin^2\psi)}{3s_1 + ½s_2} \tag{3.12}$$

3.2.4 Diffraction line-profile analysis

There are essentially three contributions to the broadening of line-profiles in X-ray diffraction. The first contribution is associated with micro-strains, which originate from stress of type III (c.f. "Types of stress" in section 3.2.3). The second contribution originates from the average size of coherently scattering domains. The third contribution is based on deviations of type II stresses from the average value in different grains. The prior two contributions are generally considered in literature and are referred to as size-broadening and strain broadening, respectively. Since the individual contributions of these effects are associated with different types of line-profiles with different dependence on the diffraction order, the effects can be separated and analyzed to obtain structural information on the polycrystal. In the following, the relations are derived for the less common case of energy-dispersive X-ray diffraction, as applied in this work.

Size broadening

For a given planar distance d and diffraction angle 2θ, constructive interference occurs at the Bragg energy E_0 (c.f. Equ. 3.2). Destructive interference for all energies that deviate from the Bragg energy, $E \neq E_0$, would require an infinite crystallite size with $n \to \infty$ crystal planes. For finite crystals, the diffracted intensity increases in close proximity to the Bragg energy, $E \approx E_0$, meaning that the Bragg condition is relaxed. The relaxation of the Bragg condition becomes more prominent with decreasing crystallite size, i.e. fewer coherently scattering crystal planes n, which leads to broadening of the diffraction line. The distribution of the intensity in the case of size broadening results in a Lorentz profile with line breadth β_L, which is related to the size of coherently diffracting domains, *D*, by the Scherrer equation [16,17]:

$$\beta_L(E) = \frac{\alpha_s hc}{2D\sin(\theta_0)} \tag{3.13}$$

where α_s is the shape factor, or the Scherrer constant, h the Planck constant and c the speed of light. The shape factor is unity for columnar grains of identical length and may be adapted for different grain shapes and cases of anisotropy.

Strain broadening

Micro-strains ε^{III} within crystal planes originate from lattice defects and manifest as local variations in the planar spacing, Δd_{hkl}. It is evident from Bragg's equation (Equ. 3.2) that these variations lead to broadening of the energy spectrum, ΔE. The effect of micro-strain on the energy spectrum is assumed to follow a Gaussian distribution. The Gauss profile with line breadth β_G, is related to the mean square strain, $\langle {\varepsilon^{III}}^2 \rangle$, by [17]:

$$\beta_G(E) = 2E\sqrt{\langle {\varepsilon^{III}}^2 \rangle} \tag{3.14}$$

Besides of contributions by stacking faults and planar defects, the major source of micro-strain is from dislocation strain-fields. Wilkens described the relation of the density and distribution of dislocation with micro-strain as [18]:

$$\langle \epsilon^2_{hkl,r_0} \rangle \approx \frac{\rho C b^2}{4\pi} ln\left(\frac{R_e}{r_0}\right) \tag{3.15}$$

where b is the Burgers vector, ρ the dislocation density, C the contrast factor, R_e the outer cut-off radius and r_0 the inner cut-off radius of the dislocations.

When combining equations Equ. 3.14 and Equ. 3.15, the line-broadening from dislocation strain fields is expressed as:

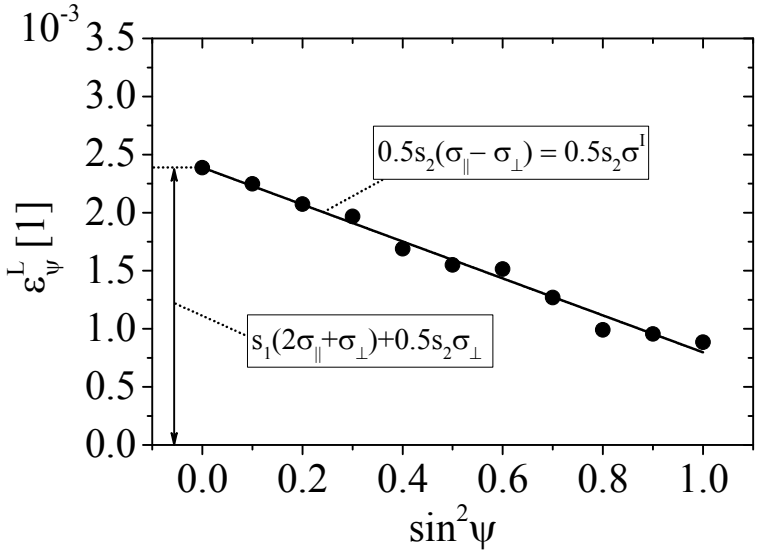

Figure 3.4: Example of $\sin^2\psi$ plot for the separation of biaxial (type I) and hydrostatic (type II) stresses. Biaxial stresses ($\sigma^I = \sigma_\parallel - \sigma_\perp$) are a linear function of $\sin^2\psi$ and are directly obtained by multiplying the linear regression line with ½s_2. The hydrostatic stress ($\overline{\sigma}^{II} = \sigma_\perp$) is obtained from the y-intercept. The example shows compressive stress of type I and an average tensile hydrostatic stress of type II.

$$\beta_G(E) \approx 2E\frac{b}{2\sqrt{\pi}}\sqrt{\rho C}ln(M) \tag{3.16}$$

where M is the dislocation distribution parameter $M = R_e\sqrt{\rho}$.

Determination of integral breadths

The intensity which is acquired in a powder-diffraction measurement is a convolution of several profiles:

$$\beta_{meas} = \beta_{inst} \otimes \beta_{phys} + \beta_{BG} = \beta_{inst} \otimes (\beta_{size} \otimes \beta_{strain}) + \beta_{BG} \tag{3.17}$$

where β_{meas} is the measured profile, β_{inst} the instrumental profile, β_{BG} the background profile and β_{phys} the physical profile, which consists of the size and strain profiles β_{size} and β_{strain}, respectively.

In order to carry out line profile analysis, it is necessary to separate the profiles β_{size} and β_{strain} from the remaining profiles. The background profile can be approximated from the profile far away from constructive interference and subtracted from the measured profile. The instrumental profile, β_{inst}, can be determined by measurement of a reference sample, for which the physical profile is negligible, such that after background subtraction $\beta_{meas}^{ref} = \beta_{inst}^{ref}$. This is generally done by measurement of a standard powder with negligible micro-strain and a sufficiently large crystallite size to minimize the effect of size broadening (an example is shown in Figure 3.5).

Both the measured and the instrumental profile are Voigt profiles, i.e. a convolution of Lorentz and Gauss profiles, and require deconvolution to their individual Gauss and Lorentz profiles to obtain the physical profile. Since the mathematical procedure for the convolution and deconvolution of the Voigt profile is difficult, it is generally approximated by a Pseudo Voigt profile, which is based on a linear combination of the Lorentz and the Voigt profiles [19]. After subtraction of the background profile β_{BG}, the measured Lorentz and Gauss profiles can be corrected for the effect of the instrument to obtain the physical profiles, $\beta_{phys,L}$ and $\beta_{phys,G}$ [20]

$$\beta_{phys,L} = \beta_{meas,L} - \beta_{instr,L} \tag{3.18}$$

and

$$\beta_{phys,G}^2 = \beta_{meas,G}^2 - \beta_{instr,G}^2 \tag{3.19}$$

Convolution of the Gaussian and Lorentzian profiles can be approximated with about 0.02 % inaccuracy with an expression by Olivero et al. [21]:

$$\Delta K = 0.5\left(1.0692\beta_{phys,L} + \sqrt{0.86639\beta_{phys,L}^2 + 4\beta_{phys,G}^2}\right) \quad (3.20)$$

Finally, the physical profile may be used for further analysis.

Williamson-Hall method

In 1953 Williamson and Hall introduced a method for the distinction of size and strain broadening by their dependence on the diffraction order, now known as the Williamson-Hall (WH) method: [22]

$$\Delta K \approx \frac{\alpha_s}{D} + Nb\sqrt{\rho}K \quad (3.21)$$

where $\Delta K = 2\sin(\theta_0)\frac{\beta_{phys}}{hc}$, $K = 2\sin(\theta_0)\frac{E}{hc}$, N is a constant (0.263) and θ_0 the fixed diffraction semi-angle. When plotting ΔK as a function of K, the diffraction order independent particle size D and the diffraction order dependent dislocation density ρ can be directly determined by the y-intercept and the slope of a linear regression line, respectively. An example of a measurement on an SRM660A LaB_6 standard is given in Figure 3.5.

Modified Williamson-Hall method

For most polycrystals ΔK is not a linear function of K. The reason for this is that the contrast of dislocation varies with the relative orientation of the Burgers and line vectors of dislocations, b and l, and the diffraction vector, g. Therefore different *hkl* show a characteristic deviation from linear ΔK- K behavior [23].

In order to compensate for the anisotropic behavior, dislocation contrast factors, *C*, can be calculated [24]. Since the dislocation contrast factors depend on different combinations of b, l, g and the anisotropic constants, a concise representation of the dislocation contrast factors is difficult to obtain. Ungár et al. [25] therefore introduced an adaption of the Williamson-Hall method, termed the modified Williamson-Hall (MWH) method, in which the dependence of the dislocation density on the dislocation contrast in different *hkl* was taken into account by an average dislocation contrast factor, $\overline{C}$:

$$\Delta K \approx \frac{0.9}{D} + bM\sqrt{\frac{\pi}{2}\rho}(K\overline{C}^2) \quad (3.22)$$

An example of a Williamson-Hall plot with anisotropic line broadening and the corresponding modified Williamson-Hall plot after scaling with $\overline{C}$ is given in Figure 3.6. The procedure for the calculation of the average dislocation contrast factor, $\overline{C}$, is described in greater detail in the following subsection. As the MWH method contains two unknowns, M and ρ, the method is by itself semi-quantitative under the assumption of a fixed value

for M. M can either be found in literature or determined from the tails of the line profiles by a Fourier expansion according to the Warren-Averbach method [26].

Determination of the average dislocation contrast factors

The following description of the procedure for determining the average dislocation contrast factors, $\overline{C}$, follows the notations in Refs. [23,27].

In an untextured polycrystal, for which the population of Burgers vectors can be assumed random, the average dislocation contrast factors $\overline{C}_{hkl}$ can readily be determined when the average contrast factor $\overline{C}_{h00}$ of the *{h00}* reflections and the parameter q is known [23]:

$$\overline{C}_{hkl} = \overline{C}_{h00}(1 - qH^2) \tag{3.23}$$

where q is a parameter describing the edge- or screw-character of dislocations and can be determined experimentally (see Equ. 3.25). H^2 is the fourth order ratio and can be calculated from the *hkl*: $H^2 = \frac{h^2l^2+h^2k^2+l^2k^2}{(h^2+k^2+l^2)^2}$. $\overline{C}_{h00}$ is determined by the dislocation contrast factors C_{h00} for pure screw and edge dislocations and the fraction of screw and edge dislocations. C_{h00} depends on the three elastic constants c_{11}, c_{12} and c_{44} of the material:

$$C_{h00,i} = a_i^c \left(1 - \exp\left(-\frac{A_{EA}}{b_i^c}\right)\right) + c_i^c A + d_i^c \tag{3.24}$$

where A is the elastic anisotropy parameter $A_{EA} = \frac{2c_{44}}{c_{11}-c_{12}}$ and the index i indicates screw and edge dislocations. The parameters a_i^c, b_i^c, c_i^c, and d_i^c depend on the ratio c_{12}/c_{44} and are tabulated in Ref. [23]. In order to experimentally determine the parameter q, Equ. 3.23 is inserted into the squared form of Equ. 3.22 to yield the following expression [23]:

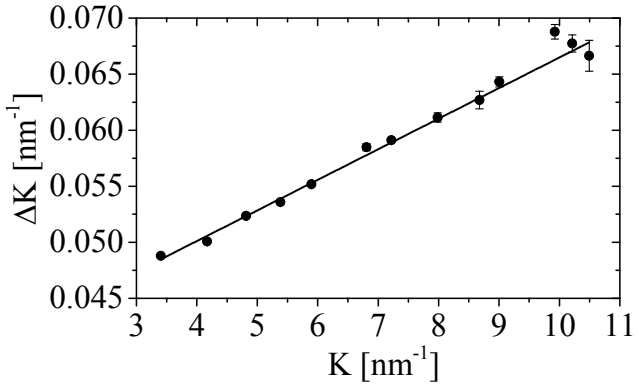

Figure 3.5: Williamson-Hall plot of SRM660A LaB_6 standard showing linear dependence of diffraction order and strain broadening.

$$\frac{\Delta K^2 - \alpha}{K^2} \approx \beta \overline{C}_{h00}(1 - qH^2) \tag{3.25}$$

where $\alpha = \left(\frac{0.9}{D}\right)^2$ and $\beta = \pi M^2 b^2 \rho/2$. Linear regression of the left hand of Equ. 3.25 over H^2 then yields the experimental value for q as the inverse x-intercept. An example of the determination of q is given in Figure 3.7.

Knowing the experimental value of q, the fraction of edge- and screw-dislocations can be determined by:

$$f_{edge} = 1 - f_{screw} = \frac{q_{screw}^{th} - q}{q_{screw}^{th} - q_{edge}^{th}} \tag{3.26}$$

The parameters q_{screw}^{th} and q_{edge}^{th} are the theoretical q values for full screw- and edge-dislocation contribution, respectively. These factors also depend on the ratio c_{12}/c_{44} of the material:

$$q_i^{th} = a_i^q \left(1 - \exp\left(-\frac{A_{EA}}{b_i^q}\right)\right) + c_i^q A + d_i^q \tag{3.27}$$

where i indicates screw and edge dislocations and the parameters a_i^q, b_i^q, c_i^q, and d_i^q can be found in Ref. [23].

3.2.5 Experimental setups for in-situ studies

The majority of X-ray diffraction experiments in this work were in-situ investigations on the structural changes in supermartensitic stainless steel in response to applied temperature or load. In this section the applied experimental setups for in-situ experiments are described.

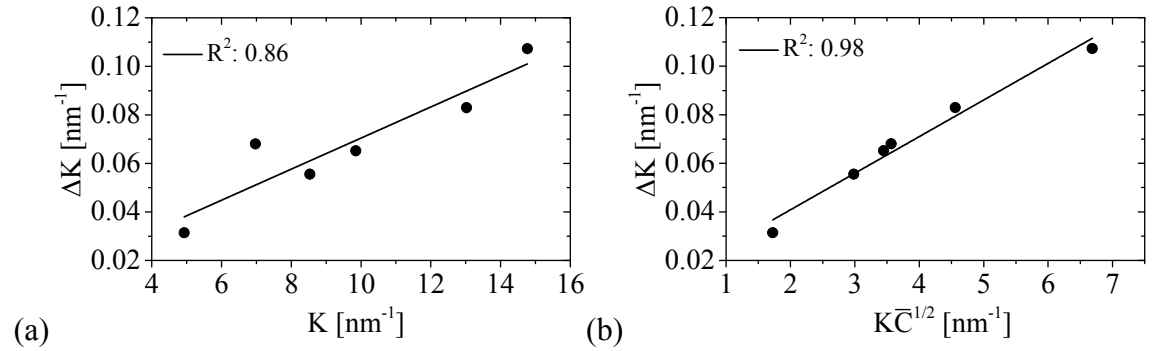

Figure 3.6: (a) Williamson-Hall (WH) plot of a lath martensite sample showing anisotropic line broadening; (b) modified Williamson-Hall (MWH) plot with assumption M=1.4, showing a linear dependence of ΔK vs. $K\overline{C}^{1/2}$.

In-situ high temperature setup

The high-temperature experiments were conducted on an Anton Paar DHS 1100 domed hot stage (Figure 3.8). Disc-shaped samples for high-temperature X-ray measurements in reflection geometry were electro-polished to remove the strain-affected surface layer. The thickness of the samples was 100 – 150 µm, thin enough to enable dynamic homogenization of the temperature field and to minimize the build-up of macro-stresses in the sample, and thick enough to stay above the penetration depth of the primary X-ray beam. Samples were loosely fixed by indirect clamping with thin steel foils, which additionally served as sacrificial material to minimize oxidation of the sample at high temperature (Figure 3.8). While the clamping pressure was held at minimum to avoid warping or build-up of macro-stresses at high-temperature, loose clamping was required to ensure proper contact to the heating stage and to maintain the sample position during tilting of the stage. Before high-temperature measurements, the heating stage was enclosed with a sealed graphite dome. The atmosphere within the domed hot stage was evacuated and purged with Ar three times, after which a low and continuous Ar flow was maintained during the measurements. The temperature was controlled with an Anton Paar TCU 200 temperature control unit. Heating was possible up to approx. 1100 °C, and the maximum heating and cooling rates were generally in the range of 3.5 $K.s^{-1}$, while cooling below 200 °C was only possible at reduced rates.

In-situ tensile testing setup

Standardized samples were exposed to in-situ tensile testing on a Walter+Bai LFV tensile testing machine (Figure 3.9a). The tensile testing machine was capable of operating at a maximum load of 20 kN and a maximum dilatation of 20 mm. The standardized samples were manufactured according to DIN 50125 type E, with thickness a_0 = 2 mm, width b_0 = 6 mm and an original gauge length L_0 = 20 mm (Figure 3.9d). The loading was controlled in a close loop with a constant strain rate of 0.01 $mm.s^{-1}$ and displacement steps of 0.2 and 0.4 mm. In between the loading steps the tensile testing machine was tilted to acquire

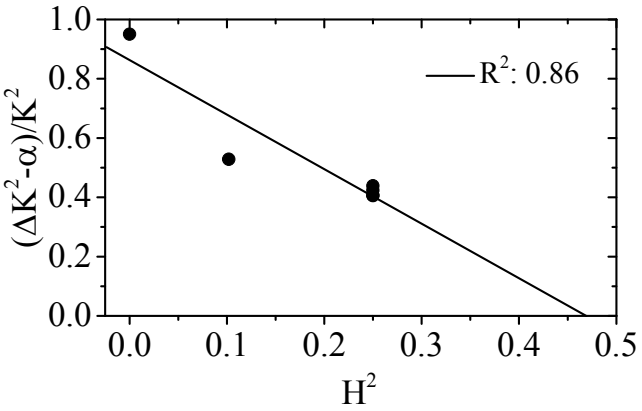

Figure 3.7: Experimental determination of parameter *q* by linear regression analysis of Equ. 3.25 for a measurement on lath martensite, where *q* is obtained from the inverse x-intercept.

diffractograms at different ψ angles (Figure 3.9c).

The macroscopic true strain and stress values were measured with a 3D Digital Image Correlation (DIC) system. For this purpose two cameras with 4096 × 3072 pixels image resolution and 75 mm lenses were installed on the side of the diffracted beam in 245 mm distance to the sample and 12.5 ° horizontal tilt with respect to the direct beam (Figure 3.9b and c). The DIC system continuously acquired images with a frequency of 1 Hz during deformation. A uniform white base coating and a black dispersed coating were applied by spray painting to form a speckle pattern shortly before destructive testing (see Figure 3.9d

Figure 3.8: Heating stage for in-situ high temperature investigation with a loosely fixed, disc-shaped sample. Before measurements, the heating stage was enclosed by a graphite dome, evacuated and purged with Ar, and exposed to a low and continuous Ar flow during acquisition.

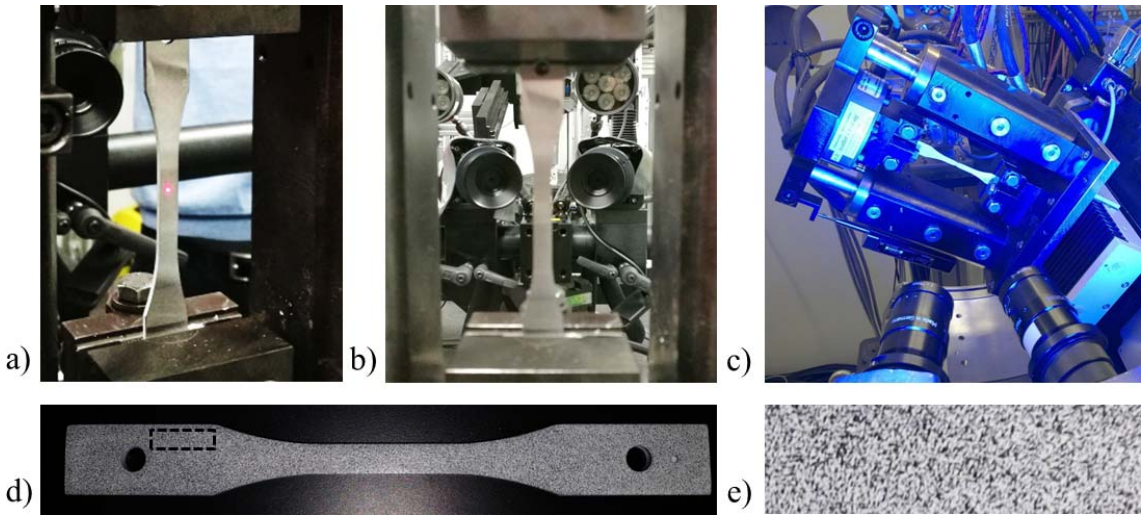

Figure 3.9: (a) Clamped sample in the tensile testing machine from the primary beam side perspective (the center of the XRD gauge volume is marked by a red laser point); (b) Primary beam perspective: After transmission through the sample the diffracted beam passes between the cameras of the DIC system towards the double-slit system (c.f. Figure 3.2); (c) DIC/X-ray detector perspective: The sample is tilted around ψ together with the tensile testing machine (c.f. Figure 3.3a); (d) DIN 50125 type E sample geometry ($a_0 \times b_0 \times L_0 = 2 \times 6 \times 20$ mm^3) with applied stochastic pattern; (e) Magnification of the stochastic pattern in the marked area in Figure 3.9d.

and the magnified image in Figure 3.9e). Tracking of the image enabled the measurement of the displacement fields and computation of strain fields. In contrast to a conventional axial strain gauge extensometer, the technique enables tracking of local changes in displacement and strain in the XRD gauge volume, which is essential during necking. In summary, the in-situ setup enables the measurement of macroscopically applied stress, local stresses and strains in the XRD gauge volume and the partitioning of internal stresses in specific phases and crystal planes.

3.3 Dilatometry

Numerous phase transformations, including the martensite-to-austenite transformation in this work, are associated with a change in specific volume. This property is exploited in dilatometry, in which the length change of a cylindrical sample is measured in response to external stimuli, commonly a change in temperature.

In the present work, dilatometry was applied to analyze the kinetics of the martensite-to-austenite transformation and the formation and stabilization of reverted austenite. For this purpose, Ø10x4 mm cylindrical specimens of EN 1.4418 were machined and solution treated with the default parameters (c.f. section 1.1). The investigations were carried out on a Bähr DIL 805A/D dilatometer at the Faculty of Mechanical Engineering and Marine Technology at the University of Rostock. The temperature of samples was measured with a type-S thermocouple, which was spot-welded to the surface of the samples at half the specimen length before acquisition. The chamber of the instrument was purged with He to minimize oxidation at high temperature.

An example of a dilatation vs. temperature curve is given in Figure 3.10. The volume fractions of austenite and martensite were determined by the lever rule. The quantification method is applied under the assumptions that austenite and martensite are the only phases contributing to the overall change in volume, that the change in volume is proportional to the measured change in length, that potential redistribution of alloying elements has negligible effect on the specific volumes, and that a change in specific volumes only leads to a negligible change in stress state. Considering the stated assumptions the accuracy of the quantification method is estimated to be in the range of ± 3 vol.%. The volume fractions of austenite and martensite, f_γ and $f_{\alpha'}$, are obtained by comparison of the measured dilatation $\Delta l/l_0$ with the thermal expansion of pure austenite and martensite, $(\Delta l/l_0)_{\alpha'}$ and $(\Delta l/l_0)_\gamma$:

$$f_\gamma = 1 - f_{\alpha'} = \frac{\Delta AB}{\Delta AC}\left(1 - f_\gamma'\right) + f_\gamma' = \frac{\left(\frac{\Delta l}{l_0}\right)_{\alpha'} - \frac{\Delta l}{l_0}}{\left(\frac{\Delta l}{l_0}\right)_{\alpha'} - \left(\frac{\Delta l}{l_0}\right)_\gamma}\left(1 - f_\gamma'\right) + f_\gamma' \qquad (3.28)$$

where f_γ' is the initial volume fraction of retained austenite and ΔAB and ΔAC are the designated changes in dilatation in Figure 3.10.

3.4 Vibrating sample magnetometry (VSM)

In VSM a cylindrical sample is exposed to a uniform magnetic field. Vertical vibration of the sample induces a current in a set of pickup coils which is proportional to the magnetic moment of the sample. The modulated and amplified electric signal is, based on different ferromagnetic properties of the phases, translated into phase fractions of austenite and martensite.

Ex-situ measurement of phase fractions after thermal treatment was determined by the ratio of the specific magnetic moment at saturation (at approx. 1 T) from the average of three hysteresis curves. Comparison of the specific magnetic moment at saturation of annealed samples, M^{sat}, with the one of the as-quenched condition, M_{ref}^{sat}, taking into account the initial amount of retained austenite, $f_{\gamma_{ret}}$, were used to determine the fraction of martensite [28]:

$$f'_{\alpha} = \frac{M^{sat}}{M_{ref}^{sat}(1 - f_{\gamma_{ret}})} \tag{3.29}$$

For in-situ measurement of phase fractions during thermal treatment a baseline was obtained by measuring the as-quenched martensite sample as a reference. It was assumed that no martensite formed in the as-quenched sample and that the magnetization of martensite is independent of temperature. The measured change in magnetization was thus regarded as an effect of the instrument, mainly originating from a relative movement of the sample with respect to the pickup coils. The magnetization curves were therefore corrected for the instrumental contribution by introducing a correction factor $K(t) = M_{ref}(290\ K)/M_{ref}(T)$. Consequently the phase fraction of annealed samples as a function of temperature was obtained by:

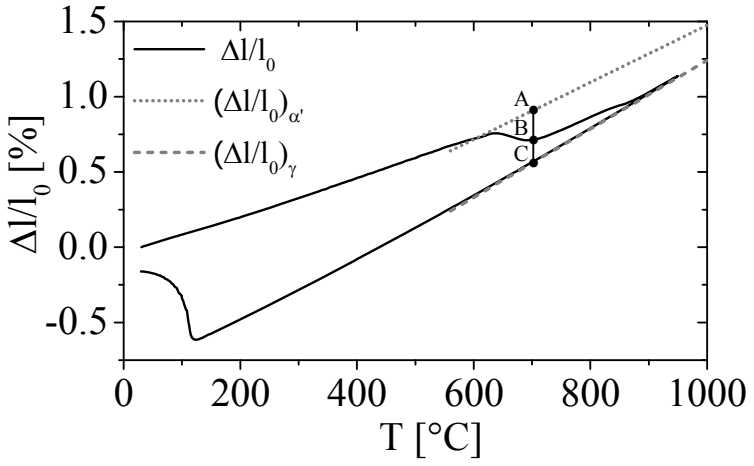

Figure 3.10: Dilatation vs. temperature curve of austenitization and quenching of an EN 1.4418 sample with 0.1 K.s^{-1}, indicating the parameters for the determination of the martensite (α') and austenite (γ) volume fractions by the lever rule according to Equ. 3.28.

$$f'_{\alpha} = \frac{M(T)}{M_{ref}^{sat}(1 - f_{\gamma_{ret}})} K(T) \tag{3.30}$$

The present investigations consisted of subzero Celsius treatments of Ø3mm x 0.75 mm cylindrical samples with a Janis SuperTran-VP continuous flow cryostat and in-situ measurement of the phase fractions with a Lake Shore Cryotronics 7407 vibrating sample magnetometer.

3.5 Electron microscopy

In this work, transmission- and scanning electron microscopy (TEM and SEM) were applied to characterize the microstructure of steels in different annealing conditions. This section will give an overview over the specimen preparation of bulk specimens and electron transparent specimens, the microscopy techniques and the used instruments.

3.5.1 Preparation of bulk specimens

Bulk specimens were used for imaging and orientation mapping with electron backscatter diffraction in the scanning electron microscope. Most samples consisted of metastable reverted austenite and martensite dual-phase microstructures. It was found that abrasive specimen preparation by grinding and polishing in some cases led to strain-induced transformation of reverted austenite to martensite. Consequently, specimens were mechanically ground up to a grit size of 1000 (P-Grade) and then electro-polished for 30 s at 25 V in a Struers LectroPol-5 unit with Struers A2 electrolyte. The last step removed the strain-affected surface layer from mechanical grinding and led to a specimen condition in which metastable austenite at the surface remained untransformed. A comprehensive study on the effect of specimen preparation on the amount of reverted austenite on the sample surface is given in Ref. [29]. The electro-polished condition was crucial for obtaining a representative state of the bulk microstructure for imaging and was a precondition for analysis with electron backscatter diffraction. The method led to electro-chemical pitting reactions around carbides, which, depending on the imaging technique, were visible as holes.

3.5.2 Preparation of electron transparent thin foil specimens

Electron transparent thin foil specimens were prepared by double-jet electro-polishing of mechanically pre-thinned discs. The electro-polishing process was executed on a Struers Tenupol-5 with 10% perchloric acid solved in ethanol at around −10 °C. The applied voltages were determined from voltage scans for all individual materials and tempering conditions.

3.5.3 Transmission electron microscopy (TEM)

An FEI TecnaiT20G^2 TEM with a LaB_6 filament and a JEOL 2000FX TEM with a field emission gun were mainly applied for imaging, selected area diffraction (SAD) and energy dispersive X-ray spectroscopy (EDS). The prior instrument was further operated in scanning mode (STEM), to acquire high-angle annular dark field (HAADF) images, EDS line scans and energy-filtered TEM images to reveal the distribution of Ni. SAD patterns were indexed by using the JEMS software.

3.5.4 Scanning electron microscopy (SEM)

In the present work, SEM was almost exclusively applied in combination with analytical methods for orientation mapping and to a lesser extent used for imaging.

Electron backscatter diffraction (EBSD)

The discovery of XRD in 1912 [2] enabled the measurement of the orientation distribution, or texture, of polycrystals within a probed volume. Discovery of electron diffraction 15 years later [30] paved the way to selected area diffraction in TEM, which today is a well-established method for orientation determination for grains larger than 10 nm with an angular resolution of 0.1 ° [31]. A year later, the first foundation for the development of EBSD was laid by the discovery of Kikuchi patterns by Nishikawa and Kikuchi [32] and the revelation of backscatter Kikuchi patterns by Alam in 1954 [33]. In the 1970s, the first backscatter Kikuchi pattern was obtained in an SEM and its potential for orientation mapping was realized [34]. Implementation of real-time imaging and computer interrogation of these patterns in the 1980s [35] and band detection by the Hough transform [36] were further important milestones towards the EBSD technique that is known today.

Backscatter Kikuchi patterns form, similar to Transmission Kikuchi patterns, in a two-step process in which (i) incoherent scattering of the primary beam in all, but mainly the forward direction, is followed by (ii) elastic scattering, in which Bragg-diffraction leads to characteristic excess and deficient lines within the cone of backscattered intensity, making up the Kikuchi lines. A more detailed treatment of the origin of Backscatter Kikuchi patterns can be found in Refs. [37,38] and a general review on EBSD is given in Ref. [31].

EBSD was applied for mapping of crystal orientations and phases in an intermediate physical spatial resolution (20-50 nm [39]) with respect to XRD and TEM/TKD. EBSD maps show a good level of grain statistics with local phase and orientation discrimination. Data was acquired on a Nova NanoSEM equipped with a Bruker e-FlashHD EBSD system using the Bruker ESPRIT software. The detector was equipped with diodes for forward scatter imaging (see subsection “Imaging”). Post-processing of data was carried out with the texture analysis software MTEX 4.2.1 [40]

Transmission Kikuchi diffraction (TKD)

With the recent advent of nano-science and the development of nano-structured metals a demand for increased spatial resolution for orientation mapping emerged. Attempts to improve the resolution of EBSD by working at very low acceleration voltage were successful, but failed to gain wide popularity, since dedicated specimen preparation and tedious parameter optimization are necessary to achieve satisfactory results [41]. A critical review on TEM-based orientation and phase mapping techniques which were developed to meet this demand can be found in Ref. [42].

In 2011 Keller and Geiss showed that the formation of Kikuchi patterns by transmission through thin specimens in the SEM is an effective way to increase the spatial resolution in orientation mapping [43,44]. The technique was initially termed transmission EBSD (t-EBSD) [43] or transmission electron forward scatter diffraction (t-EFSD) [45,46], but is now generally referred to using the more plausible name Transmission Kikuchi Diffraction (TKD) [47]. TKD can be carried out with standard EBSD-equipment, but requires an electron transparent specimen, that is mounted in a specific specimen-holder. The formation of transmission Kikuchi patterns occurs similar to the formation of backscatter Kikuchi patterns (c.f. section “Electron backscatter diffraction (EBSD)”). A recently published review on TKD can be found in Ref. [39].

TKD was applied for orientation and phase mapping at the nano-scale. In terms of effective spatial resolution, TKD is around a magnitude higher than EBDS (5-10 nm [39]), but below advanced diffraction methods in TEM. Consequently, the grain statistics are lower than for EBSD, i.e. the mapped areas are generally smaller, but are greatly improved with respect to traditional diffraction techniques in TEM such as SAD or micro-beam diffraction. In the present work, TKD was carried out with the same equipment as for EBSD, but with an electron transparent sample in a dedicated sample holder. Further, TKD with a purpose fit detector head was employed, which is positioned at the maximum diffracted intensity below the sample. As Kikuchi patterns are acquired on the axis of the direct beam, the method is termed “on-axis” TKD, in contrast “off-axis” TKD with a conventional EBSD detector. The systematic comparison of on-axis with off-axis TKD was part of the research on method development and resulted in a manuscript, which is referred to for further details on TKD in general and the two different TKD methods (chapter 14).

Imaging

Imaging of dual-phase austenite-martensite microstructures was optimized in an attempt to obtain images that are representable of the bulk-microstructure, low in artefacts and high in contrast. For this purpose, bulk specimens were prepared by electro-polishing according to the method in section 1.4.1, which allowed an optimal representation of the bulk microstructure. Imaging of etched specimens with secondary electron contrast was attempted (see Ref. [48] for details on the reagents and micrographs), but was found to introduce substantial topography by preferential etching of martensite, which seemed to

create a bias towards increased austenite phase fraction. Imaging with a conventional backscatter electron detector did not lead to satisfying contrast of the austenite-martensite microstructure either, as the yield of backscatter electrons is predominantly a function of atomic number and the distribution of alloying elements in the present microstructure was not substantial.

The most contrasting properties of lath martensite with respect to austenite are the micro-strain (dislocation density) and orientation. Originating from the transformation strain during martensite formation, lath martensite is characteristic for its high dislocation density and hierarchical microstructure with distinct grain orientations. In contrast, reverted austenite forms by a diffusion-aided transformation and preferentially inherits the orientation of the prior austenite grains, which are approx. 100 to 200 µm in diameter in the present materials. Austenite grains with almost uniform orientation over large areas and relatively undistorted crystals give rise to a high backscattered electron yield with confined take-off angle. In contrast, the large orientation distribution of lath martensite leads to a wider range of take-off angles. Further, the large distortion of the crystal lattice increases the likelihood of multiple scattering events and absorption of primary electrons.

In order to utilize this orientation contrast, a directional backscattered electron detector at low working distance was used for imaging, which allowed collection of backscattered electrons at high collection angle and separation based on their take-off angle [49]. Optimization of the specimen tilt and angular separation parameters led to a high contrast of austenite with respect to martensite, as shown in Figure 3.11a. This imaging technique was applied on a FEI Helios EBS3 with a field emission gun source. As an alternative, the forward scattered electron detector, which is a common add-on to detectors for EBSD, consists of three diodes which, similar to the directional backscattered electron detector, separate the forward scattered electrons based on their take-off angle to yield a strong orientation contrast (Figure 3.11b). In case of the on-axis detector for TKD, the

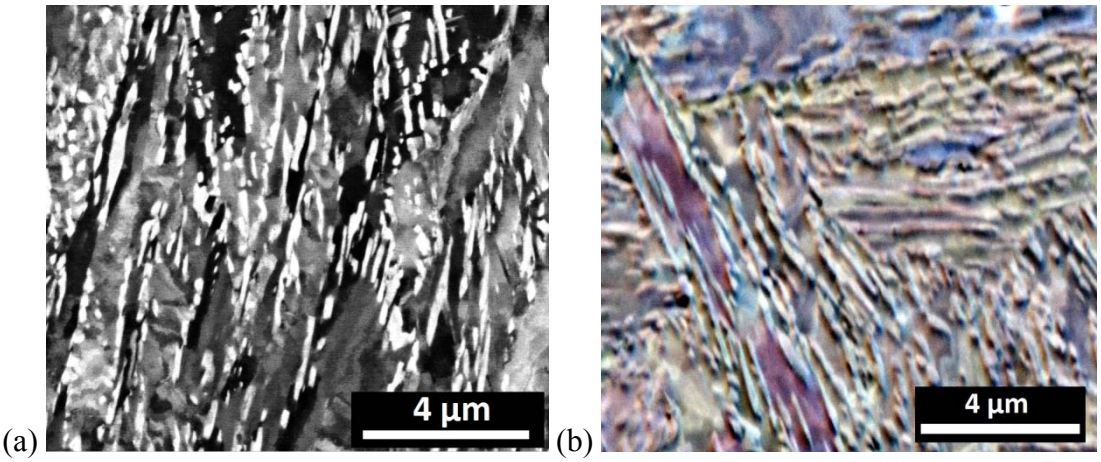

Figure 3.11: Micrographs of austenite (bright films) an martensite (grey/colored background) dual-phase microstructure acquired with (a) a directional backscattered electron detector and (b) a forward scatter detector.

diodes of the forward scatter detector are inserted below the electron-transparent sample and enabled diffraction contrasts in bright- and dark-field mode similar to transmission electron microscopy (Figure 3.12). The forward scatter images were acquired with the FEI NovaSEM, used for EBSD and TKD.

3.6 Atom probe tomography

3.6.1 Fundamentals

In atom probe tomography (APT), field evaporation of atoms is used to build a 3-dimensional (3D) reconstruction of the evaporated volume by analysis of the time of flight and the impact on a 2D detector of the individual ions. Field evaporation is enabled by applying a sufficiently high and directed electric field to a needle shaped sample. In APT, field evaporation is controlled by superimposing the high voltage field with either voltage or temperature pulses by use of a local electrode or a laser, respectively. The nature of individual ions can be determined by converting the time of flight to a mass to charge ratio.

Assuming that an ion is accelerated relatively fast, the velocity of an ion can be assumed constant. The kinetic energy of an ion, E_{kin}, can then be related to the energy of the electric field, E_E, by:

$$E_{kin} = \frac{1}{2}mv^2 = E_E = -neU \tag{3.31}$$

where m is the mass, v the velocity and n the ionization state of an ion. e is the fundamental electric charge and U is the voltage applied to the specimen tip. Equ. 3.31 can be rearranged to solve for the mass to charge ratio:

$$\frac{m}{n} = -\frac{2eU}{v^2} \tag{3.32}$$

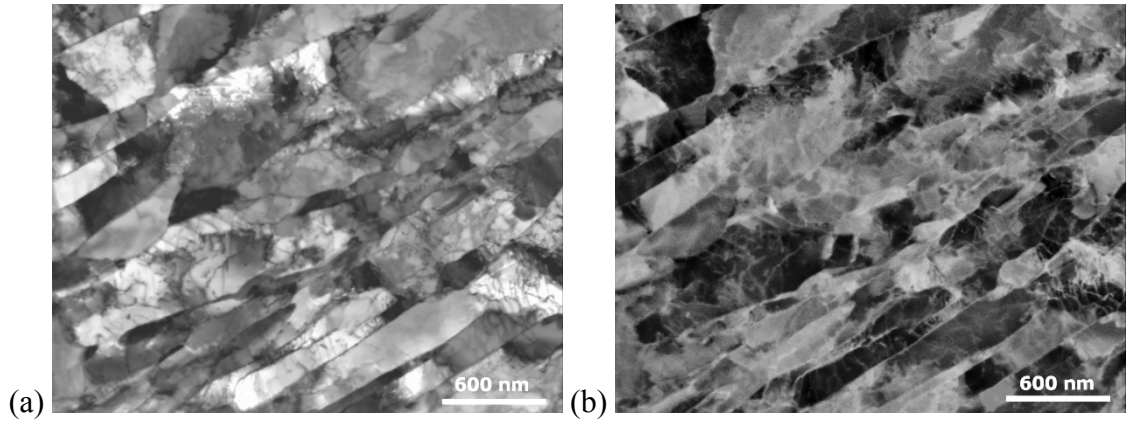

Figure 3.12: Martensitic stainless steel micrographs of the identical site of interest obtained from the forward scatter detector attached to an on-axis TKD-detector head in (a) Bright field mode and (b) dark field mode.

The velocity of an ion, v, is given by the specimen to detector distance, f, and the flight time, t, by $v = \frac{f}{t}$, which can be inserted into Equ. 3.323.32 to yield [50]:

$$\frac{m}{n} = -2eU\left(\frac{t}{f}\right)^2 \tag{3.33}$$

The mass to charge ratio is thus directly deducible from the time of flight and the specimen voltage, and is a direct indicator of the nature of the respective ion.

3.6.2 Specimen preparation

Field evaporation in atom probe tomography requires a needle shaped specimen. The specimen shape is generally obtained by either electrolytic micropolishing or by evaporation with a focused ion beam (FIB).

The prior technique was applied in the present work and requires raw samples of match-shaped geometry of approx. 15 x 0.3 x 0.3 mm^3. Samples are then mounted to a specimen holder, which serves as the anode in a direct current electric circuit. A polishing loop serves as a capillary to hold the electrolyte and is connected to an electric circuit as the cathode. Horizontal penetration of the electrolyte with the sample, while closing and opening of the electric circuit, enables polishing of the specimen to a needle shape [51].

3.6.3 Experimental setup

All investigations were carried out at CNRS, Normandie University, UNIROUEN, France on a CAMECA LEAP 4000 HR atom probe. The instrument controls field evaporation by superimposing a direct current field with a high-voltage pulsed electric field, generated by a local counter electrode in close proximity to the specimen (Figure 3.13). The local electrode is a cone shaped device with an aperture of approx. 40 µm at its tip and receives ions from the specimen during data acquisition. Because of its close proximity to the specimen, only relatively low voltage is required for field evaporation, which enables high

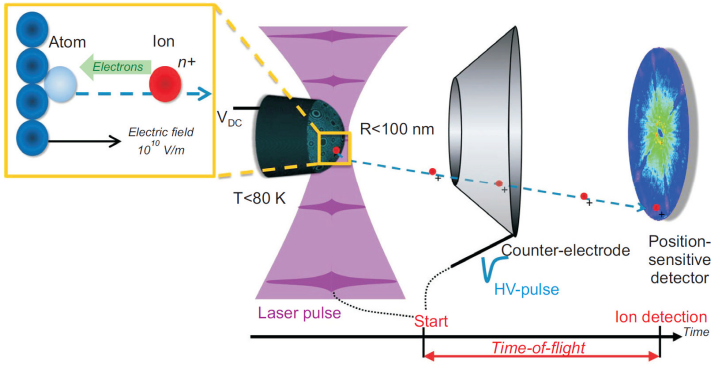

Figure 3.13: Schematic view of an atom probe tomography instrument, with the specimen subjected to a high voltage and illuminated by laser pulses or voltage pulses, triggering the field evaporation of ions that fly through a counter-electrode and are collected by the position-sensitive detector, which also records their time-of-flight allowing for their elemental identification.[2]

pulse frequencies of up to 200 kHz. Generally it is also possible to trigger field evaporation by pulsing a laser instead of voltage.

In the present work, the detection rate, defined as the percentage of pulses that generate at least one ion detection event, was held constant to control field evaporation. After acquisition, the 3D reconstruction was conducted offline by evaluating the time of flight and 2D detector positions of detected ions. Before reconstruction, bowl and voltage corrections were applied, and the mass spectrum was calibrated on a couple of known peaks [52]. Based on the indexed regions the background of the spectrum is estimated and subtracted.

References

[1] W.C. Röntgen, Ueber eine neue Art von Strahlen, Ann. Phys. 300 (1895) 12–17.

[2] W. Friedrich, P. Knipping, M. von Laue, Interferenz-Erscheinungen bei Röntgenstrahlen, Sitzungsberichte Der Math. Cl. Der Königlich-Bayerischen Akad. Der Wissenschaften Zu München. (1912).

[3] W.H. Bragg, W. L. Bragg., The reflection of X-rays by Crystals, Proceedings of the Royal Society (1913) 428–438.

[4] D. Apel, M. Klaus, C. Genzel, D. Balzar, Rietveld refinement of energy-dispersive synchrotron measurements, Zeitschrift Fur Krist. 226 (2011) 934–943.

[5] C. Genzel, I.A. Denks, M. Klaus, Residual Stress Analysis by X-Ray Diffraction Methods, in: E.J. Mittemeijer, U. Welzel (Eds.), Mod. Diffr. Methods, Wiley-VCH, 2013: pp. 127–154.

[6] C. Genzel, I. Denks, M. Klaus, The Materials Science Beamline EDDI for Energy-Dispersive Analysis of Subsurface Residual Stress Gradients, Mater. Sci. Forum. 524–525 (2006) 193–198.

[7] R.D. Arnell, Determination of retained austenite in steel by X-ray diffraction, J. Iron Steel Inst. (1968) 1035–1036.

[8] Standard Practice for X-Ray Determination of Retained Austenite in Steel with Near Random Crystallographic Orientation 1, E975-13, ASTM. (2013).

[9] M. Merisalo, T. Paakkari, Debye-Waller Factor and Debye Temperature for Fe, Mo, Ta, and W, Mater. Res. Bull. 8 (1973) 195–200.

[10] R.W. Hinton, Interlaboratory evaluation of ASTM practice for X-ray determination of retained austenite in steel with near-random crystallographic orientation (E 975), J. Test. Eval. 15 (1987) 95–100.

[11] M.V. Joffe, A.F.Kirpitcheva, Röngtenograms of Strained Crystals, Philos. Mag. J. Sci. 18 (1922) 204–206.

[12] V. Hauk, Highlights in the history of diffraction methods - first notice, entire treatment, in: Struct. Residual Stress Anal. by Nondestruct. Methods, 1997: pp. 17–35.

[13] V. Hauk, Evaluation of Load Stress (LS) and Residual Stress (RS), in: Struct. Residual Stress Anal. by Nondestruct. Methods, Elsevier, 1997: pp. 132–215.

[14] P.J. Withers, H.K.D.H. Bhadeshia, Residual stress part 1 - Measurement techniques, Mater. Sci. Technol. 17 (2001) 355–365.

[15] E. Macherauch, P. Müller, Das sin2psi-Verfahren der röntgenographischen Spannungsmessung, Zeitschrift Für Angew. Phys. 13 (1961) 305–312.

[16] P. Scherrer, Bestimmung der Größe und der inneren Struktur von Kolloidteilchen mittels Röntgenstrahlen, Nachrichten von Der Gesellschaft Der Wissenschaften Zu Göttingen, Math. Klasse. (1918).

[17] L. Gerward, S. Mørup, H. Topsøe, Particle size and strain broadening in energy-dispersive x-ray powder patterns, J. Appl. Phys. 47 (1976) 822–825.

[18] M. Wilkens, The determination of density and distribution of dislocations in deformed single crystals from broadened X-ray diffraction profiles, Phys. Status Solidi. 2 (1970) 359–370.

[19] P. Thompson, D.E. Cox, J.B. Hastings, Rietveld Refinement of Debye-Scherrer Synchrotron X-ray Data from Al2O3, J. Appl. Crystallogr. 20 (1987) 79–83.

[20] T.H. de Keijser, J.I. Langford, E.J. Mittemeijer, A.B.P. Vogels, Use of the Voigt function in a single-line method for the analysis of X-ray diffraction line broadening, J. Appl. Crystallogr. 15 (1982) 308–314.

[21] J.J. Olivero, R.L. Longbothum, Empirical fits to the Voigt line width: A brief review,

J. Quant. Spectrosc. Radiat. Transf. 17 (1977) 233–236.
[22] G.. Williamson, W.. Hall, X-ray Line Broadening from Filed Aluminium and Wolfram, Acta Metall. 1 (1953) 22–31.
[23] T. Ungár, I. Dragomir, Á.;. Révész, A. Borbély, The contrast factors of dislocations in cubic crystals: the dislocation model of strain anisotropy in practice, J. Appl. Crystallogr. 32 (1999) 992–1002.
[24] M. Wilkens, K. Herz, H. Mughrabi, An X-Ray Diffraction Study of Cyclically and of Unidirectionally Deformed Copper Single Crystals, Zeitschrift Für Met. 71 (1980) 376–384.
[25] T. Ungár, A. Borbély, The effect of dislocation contrast on x-ray line broadening: A new approach to line profile analysis, Appl. Phys. Lett. 69 (1996) 3173–3175.
[26] T. Ungár, M. Victoria, P. Marmy, P. Hanák, G. Szenes, New procedure of X-ray line profile analysis applied to study the dislocation structure and subgrain size-distributions in fatigued MANET steel, J. Nucl. Mater. 276 (2000) 278–282.
[27] F. HajyAkbary, J. Sietsma, A.J. Böttger, M.J. Santofimia, An improved X-ray diffraction analysis method to characterize dislocation density in lath martensitic structures, Mater. Sci. Eng. A. 639 (2015) 208–218.
[28] M. Villa, Isothermal Martensite Formation, 2013.
[29] J.R. Tolchard, A. Sømme, J.K. Solberg, K.G. Solheim, On the measurement of austenite in supermartensitic stainless steel by X-ray diffraction, Mater. Charact. 99 (2015) 238–242.
[30] G.P. Thomson, A. Reid, Diffraction of Cathode Rays by Thin Film, Nature. 119 (1927) 890.
[31] D.J. Dingley, V. Randle, Microtexture determination by electron back-scatter diffraction, J. Mater. Sci. 27 (1992) 4545–4566.
[32] S. Nishikawa, S. Kikuchi, Diffraction of Cathode Rays by Mica, Nature. 121 (1928) 1019–1020.
[33] M.N. Alam, M. Blackman, D.W. Pashley, High-angle Kikuchi patterns, Proc. R. Soc. A Math. Phys. Eng. Sci. 221 (1954) 224–242.
[34] J.A. Venables, C.J. Harland, Electron Back-Scattering Patterns - A new crystallographic technique for use in the S.E.M., in: Scanning Electron Microsc. Syst. Appl., Newcastle, 1973: pp. 20–54.
[35] D.J. Dingley, Diffraction from sub-micron areas using electron backscattering in a scanning electron microscope, Scan. Electron Microsc. (1984) 569–575.
[36] N.C. Krieger Lassen, D. Juul Jensen, K. Conradsen, Image processing procedures for analysis of electron back scattering patterns, Scanning Microscoy. 6 (1992) 115–121.
[37] S. Zaefferer, On the formation mechanisms, spatial resolution and intensity of backscatter Kikuchi patterns, Ultramicroscopy. 107 (2007) 254–266.
[38] D.B. Williams, C.B. Carter, Kikuchi Diffraction, in: Transm. Electron Microsc., 2009: pp. 311–322.
[39] G.C. Sneddon, P.W. Trimby, J.M. Cairney, Transmission Kikuchi diffraction in a scanning electron microscope: A review, Mater. Sci. Eng. R Reports. 110 (2016) 1–12.
[40] F. Bachmann, R. Hielscher, H. Schaeben, Texture Analysis with MTEX – Free and Open Source Software Toolbox, Solid State Phenom. 160 (2010) 63–68.
[41] D.R. Steinmetz, S. Zaefferer, Towards ultrahigh resolution EBSD by low accelerating voltage, Mater. Sci. Technol. 26 (2010) 640–645.
[42] S. Zaefferer, A critical review of orientation microscopy in SEM and TEM, Cryst.

Res. Technol. 46 (2011) 607–628.
[43] R.R. Keller, R.H. Geiss, Transmission EBSD from 10 nm domains in a scanning electron microscope, J. Microsc. 245 (2012) 245–251.
[44] R. Geiss, R. Keller, S. Sitzman, P. Rice, New Method of Transmission Electron Diffraction to Characterize Nanomaterials in the SEM, Microsc. Microanal. 17 (2011) 386–387.
[45] N. Brodusch, H. Demers, M. Trudeau, R. Gauvin, Acquisition parameters optimization of a transmission electron forward scatter diffraction system in a cold-field emission scanning electron microscope for nanomaterials characterization, Scanning. 35 (2013) 375–386.
[46] N. Brodusch, H. Demers, R. Gauvin, Nanometres-resolution Kikuchi patterns from materials science specimens with transmission electron forward scatter diffraction in the scanning electron microscope, J. Microsc. 250 (2013) 1–14.
[47] P.W. Trimby, Orientation mapping of nanostructured materials using transmission Kikuchi diffraction in the scanning electron microscope, Ultramicroscopy. 120 (2012) 16–24.
[48] F. Niessen, Heat treatment, microstructure and mechanical properties of a Cast Supermartensitic Stainless Steel, 2014.
[49] FEI, Application Note: Information from Every Angle - Directional BSE Detector for Next-Level Imaging, 2013.
[50] T.T. Tsong, Atom-probe field ion microscope, in: Atom-Probe F. Ion Microsc., 2009: p. 129.
[51] M.K. Miller, G.D.W. Smith, Atom probe microanalysis: principles and applications to materials problems, Materials Research Society, USA, 1989.
[52] J.T. Sebastian, O.C. Hellman, D.N. Seidman, New method for the calibration of three-dimensional atom-probe mass spectra, Rev. Sci. Instrum. 72 (2001) 2984–2988.

4 Modeling methods

This chapter provides an overview of the modeling methods applied in the present work.

4.1 Thermodynamics modeling

Thermodynamics modeling in material science is a powerful tool for the determination of phase equilibria and the calculation of thermochemical quantities. The here described thermodynamics modeling approach follows the CALPHAD (CALculation of PHAse Diagrams) method, in which databases of experimental and theoretical information on phase equilibria and thermochemical properties are collected and assessed to predict phase diagrams of entire alloy systems. The following subsections consist of a brief history of CALPHAD and a description of the fundamentals.

4.1.1 A brief history of CALPHAD

This outline of the history of CALPHAD is mainly based on a comprehensive review by Spencer [1], which is referred to for further reading.

The relation between the thermodynamics functions and the equilibrium phase diagram of a binary phase diagram was first described by Van Laar in 1908 [2]. Due to a lack of quantity and accuracy of experimental thermodynamic data it was first around half a century later by the efforts of Wagner and Meijering, that phase boundaries in alloy systems were evaluated by using thermodynamic data [3,4]. At this time phase diagrams were derived by common tangent constructions of manually calculated Gibbs energy curves.

A major advancement in the field was made by the introduction of the concept of "lattice stability" by Kaufman. The difference in Gibbs energy for a stable and metastable crystallographic form of an element as a function of temperature, the so called lattice stability values, allowed more accurate calculation of equilibrium phase boundaries between different phases of a system [5,6]. In 1968, Hillert outlined the significant advances which could be gained by combining experimental thermodynamics and phase diagram data with the use of computational techniques. The first scientific meetings to include sessions on computer calculations of phase diagrams were held in the early 70's and led to the formation of a working group on CALPHAD. 1977 marked the year of first appearance of the CALPHAD journal. A French funded project (1969 – 1974) aimed at establishing a common database of many participating parties and led to the foundation of the SGTE (Scientific Group Thermodata Europe). The resulting SGTE data now forms an important basis for nearly all CALPHAD systems used worldwide [7]. Recent developments are the extension of thermodynamics databases to low temperatures and database optimization to obtain smoother descriptions over large temperature intervals by including results from first principles calculations [8]. Thermodynamics databases on new

alloy systems are constantly explored and made commercially available [9,10]. While the major development and supply of CALPHAD software is nowadays commercial, some recent advances in developing open-source CALPHAD software deserve attention [11,12].

4.1.2 Principles

In CALPHAD, thermodynamic properties of phases are described with help of an adjustable mathematical model for calculation of the Gibbs energy of phases. By optimizing the adjustable parameters based on experimental or modeling results, Gibbs energy expressions are obtained, which are stored in thermodynamic databases. With help of these expressions, thermodynamic equilibria are computed by minimization of the Gibbs energy, G, of a given system [13]:

$$G = \min\left(\sum_{\varphi=1}^{p} n^{\varphi} G^{\varphi}\right) \tag{4.1}$$

where n^{φ} is the molar fraction and G^{φ} the molar Gibbs energy of phase φ. The molar Gibbs energy of a phase G^{φ} is described by the configurational entropy of an ideal mixture, G^{φ}_{ideal}, and an excess Gibbs energy term, G^{φ}_{E}, to account for interactions between the different atoms. When only binary interactions are considered, the molar Gibbs energy of phase φ is given as:

$$G^{\varphi} = G^{\varphi}_{ideal} + G^{\varphi}_{E} = \sum_{i} x_i^{\varphi} G^{\varphi}_{0,i} + RT \sum_{i} x_i^{\varphi} \ln\left(x_i^{\varphi}\right) + \sum_{i} \sum_{j>i} x_i^{\varphi} x_j^{\varphi} I_{ij}^{\varphi} \tag{4.2}$$

where x_i^{φ} is the composition and $G^{\varphi}_{0,i}$ the molar Gibbs energy of element i in phase φ. The excess molar Gibbs energy term G^{φ}_{E} for interaction of the elements i and j is described by the binary interaction coefficient I^{φ}_{ij} to account for deviation from ideal behavior. Such coefficients are subject to direct study and modeling and are generally described as a power series, known as the Redlich-Kister polynomial [14–16]:

$$I_{ij}^{\varphi} = \sum_{k=0}^{n} L_k \left(x_i^{\varphi} - x_j^{\varphi}\right)^k \tag{4.3}$$

where L_k is the interaction parameter of k^{th} order. In more complex alloy systems also ternary interactions are considered in the excess molar Gibbs energy term, in which case interactions may be represented by more complex formalisms than the Redlich-Kister polynomial [17].

The concentration dependent Gibbs energy $G^{\varphi}_{0,i}$ of element i in phase φ is described as the sum of different Gibbs energy contributions [18]:

$$G_{0,i}^{\varphi} = G_{0,i,T}^{\varphi}(T,x) + G_{0,i,P}^{\varphi}(P,T,x) + G_{0,i,m}^{\varphi}(T_c,\beta_0,T,x) \quad (4.4)$$

where $G_{0,i,T}^{\varphi}$ is the contribution by temperature (T), $G_{0,i,P}^{\varphi}$ by pressure (P), and $G_{0,i,m}^{\varphi}$ by magnetic contribution of the Curie-temperature (T_c) and the average magnetic moment per atom (β_0). Expressions for the contributions of pressure and magnetism can be found in Ref. [7,13,14] and can in many condensed systems be neglected.

Consequently, the temperature expression, $G_{0,i,T}^{\varphi}$, is the most relevant expression and is described by a power series of T:

$$G_{0,i,T}^{\varphi} = a_i^{\varphi} + b_i^{\varphi}T + c_i^{\varphi}T\ln(T) + \sum d_{i,n}^{\varphi}T^n \quad (4.5)$$

where a_i^{φ}, b_i^{φ}, c_i^{φ}, and $d_{i,n}^{\varphi}$ are coefficients and n integers, typically taking values of 2, 3 and -1.[7,13] Parameter values for the most common elements can be found in Ref. [7].

4.1.3 Application of thermodynamics modeling in the present work

In the present work different versions of the commercial thermodynamics modeling software Thermo-Calc [19] in conjunction with the thermodynamic database TCFE6 [20] were applied to compute phase equilibria for the prediction of equilibrium phase fractions and component concentrations. The applied parameters varied with the specific application and are therefore given in the respective result manuscripts.

4.2 Kinetics modeling of diffusion

Kinetics modeling of diffusion in multi-component alloy systems is a powerful method to model the kinetics of diffusion controlled phase transformations in material science. With the rise of computational thermodynamics modeling in the 80's of the last century, the potential for investigation of non-equilibrium processes became apparent and in 1990 the diffusion-controlled transformations (DICTRA) software was introduced, which at present is one of the most widely applied models for multicomponent diffusion [21,22]. The following notation of the fundamental equations follows the description in Ref. [23], which is recommended for further reading.

4.2.1 Principles

The rate of a diffusion-controlled phase transformation can be approximated from the rate of volume diffusion of the individual components and by assumption of local equilibrium at the moving phase interface. Accordingly, when the thermodynamic behavior and the volume diffusivities of a system are known, the migration rate of an interface can be determined without further experimental effort, enabling modeling of the kinetics of diffusion-controlled phase transformations [22].

Fick's first law of diffusion correlates the diffusion flux J_k and the concentration gradient of a diffusing species k in direction z in a single phase alloy at constant temperature and pressure as follows:

$$J_k = -D_k \frac{\partial c_k}{\partial z} \tag{4.6}$$

where D_k is the inter-diffusion coefficient and c_k the concentration of a particular unit volume of the diffusing species k. The diffusion flux J_k in this context is defined in respect to a volume-fixed frame of reference. When combining Fick's first law with the continuity equation,

$$\frac{\partial c_k}{\partial t} = \frac{\partial}{\partial z}(-J_k) \tag{4.7}$$

the fundamental differential equation of diffusion, Fick's second law, is obtained:

$$\frac{\partial c_k}{\partial t} = \frac{\partial}{\partial z}(D_k \frac{\partial c_k}{\partial z}) \tag{4.8}$$

When considering diffusion in multi-component alloys, the diffusivities in Equ. 4.6 do not solely depend on concentration, but also on concentration gradients. In 1931 Onsager postulated that each thermodynamic flux is linearly related to every thermodynamic force, which led to the formulation of a multicomponent extension of Fick's first law [24]:

$$J_k = -\sum_{i=1}^{n} L'_{ki} \frac{\partial \mu_i}{\partial z} \tag{4.9}$$

The μ_i parameter is the chemical potential of species i and L'_{ki} is a proportionality factor which is based on the mobilities of species' k and i.

It is generally more convenient to express the flux as a function of the concentration gradients rather than gradients in chemical potential, which can be achieved by applying the chain rule of derivation on Equ. 4.6:

$$J_k = -\sum_{i=1}^{n} L'_{ki} \sum_{j=1}^{n} \frac{\partial \mu_i}{\partial c_j} \frac{\partial c_j}{\partial z} \tag{4.10}$$

Furthermore, Equ. 4.6 can be expressed by introducing the unreduced diffusivities, D_{kj}:

$$J_k = -\sum_{j=1}^{n} D_{kj} \frac{\partial c_j}{\partial z} \tag{4.11}$$

By substituting J_k in Equ. 4.10 with the expression in Equ. 4.11, a definition of the unreduced diffusivity D_{kj} is obtained:

$$D_{kj} = -\sum_{i=1}^{n} L'_{ki} \frac{\partial \mu_i}{\partial c_j} \tag{4.12}$$

The obtained definition reveals that the diffusivities consist of pure thermodynamic and kinetic contributions, $\partial \mu_i / \partial c_j$ and L'_{ki}, respectively. As the concentration gradients are not independent from each other, generally only $n-1$ concentration gradients are considered in Equ. 4.11 to yield J_k. The reduced diffusivities, i.e. the diffusivities relative to the concentration gradient of species n, under assumption of equal partial molar volume of all substitutional species and no contribution to the volume by interstitial elements, are given as:

$$D^n_{kj} = D_{kj} - D_{kn} \text{ (for a substitutional species } j) \tag{4.13}$$

and

$$D^n_{kj} = D_{kj} \text{ (for an interstitial species } j) \tag{4.14}$$

By reformulating Equ. 4.11, including the reduced diffusivities, the following equation is obtained:

$$J_k = -\sum_{i=1}^{n-1} D^n_{kj} \frac{\partial c_j}{\partial z} \tag{4.15}$$

which in combination with the continuity Equ. 4.7 yields the main equation of kinetics modeling of diffusion:

$$\frac{\partial c_k}{\partial t} = \frac{\partial}{\partial z}\left(\sum_{i=1}^{n-1} D^n_{kj} \frac{\partial c_j}{\partial z}\right) \tag{4.16}$$

The equation represents a system of coupled partial differential equations (PDEs) which can be solved by numerical methods [21].

4.2.2 Kinetics databases

The system of PDEs given by Equ. 4.16 requires both thermodynamics and kinetics data to be solved. The thermodynamics data is generally obtained by CALPHAD methods and the kinetics data is produced and obtained in a similar way as in CALPHAD. The proportionality factor L'_{kj} which is used to describe the diffusivities in Equ. 4.12 is defined as:

$$L'_{kj} = \sum_{i=1}^{n} (\delta_{ik} - c_k V_i) c_i y_{va} M_i \tag{4.17}$$

where δ_{ik} is the Kronecker delta ($\delta_{ik}(j=k)=1; \delta_{ik}(j\neq k)=0$), c_k and c_i are the concentrations of species i and k in the partial volume V_i, y_{va} is the fraction of vacant lattice sites, and the term M_i is the mobility of a substitutional species i divided by y_{va} or the mobility of an interstitial species i.

In the expression for L'_{kj} the main unknown parameter is the mobility M_i. The atomic mobility of individual species in a multicomponent solution phase is therefore modelled by an absolute-reaction rate theory argument, divided into a frequency factor M_k^0 and an activation enthalpy Q_k of a species k:

$$M_k = \frac{M_k^0}{RT}\exp\left(-\frac{Q_k}{RT}\right) \tag{4.18}$$

where R is the gas constant and T the absolute temperature. Similar to the approach in CALPHAD, the composition dependence of both M_k^0 and Q_k are described by a Redlich-Kister polynomial:

$$\Phi_k = \sum_i x_i \Phi_k^i + \sum_i \sum_{j>i} x_i x_j \left(\sum_{r=0}^{m} {}^r\Phi_k^{i,j} \left(x_i - x_j\right)^r \right) \tag{4.19}$$

where Φ_k represents either $\ln(M_k^0)$ or Q_k. Parameter Φ_k^i refers to the value of Φ_k for the pure species i and the parameter ${}^r\Phi_k^{i,j}$ represents the r^{th} order binary interaction parameter of species i and j. The model parameters, Φ_k^i and ${}^r\Phi_k^{i,j}$, are determined by optimization on experimental data and are stored in mobility databases.

4.2.3 Moving boundary model

One of the most applied models, generally within the diffusion kinetics model DICTRA and specifically in the present work, is the moving boundary model [23,25]. The model is used to predict diffusion controlled growth or dissolution of phases within a matrix. In the model two-phase regions are separated by a sharp interface, i.e. the chemical potential gradients are discontinuous while the chemical potentials are equal. The migration of a phase boundary of two phases α and β is determined by the rate of diffusion to and from the interface, which is controlled by a flux balance equation:

$$\frac{v^\alpha}{V_m^\alpha} = \sum_{k=1}^{n-1} \frac{J_k^\alpha - J_k^\beta}{x_k^\alpha - x_k^\beta} \tag{4.20}$$

where v^α is the interface migration rate, V_m^α the molar volume of phase α, x_k^α and x_k^β the concentrations of species k in phases α and β, and J_k^α and J_k^β the corresponding diffusional fluxes.

For a given time step, initially the equilibrium at the interface is computed. When the interfacial reactions are fast compared to the migration rate of the interface, local equilibrium can be assumed and applied as a boundary condition. The diffusion problem can then be solved separately in each region. The migration of the interface is then determined by solving the flux balance equation (Equ. 4.18). All these equations are coupled and are solved iteratively.

The assumption of local equilibrium at the phase interface is equivalent to equal chemical potentials at each side of the sharp interface. This means that movement of the phase interface is solely controlled by the diffusion rates from and to the interface. This boundary condition is an assumption which needs to be checked for validity to apply the model for reasonable predictions of the phase transformation kinetics.

4.2.4 Application of kinetics modeling in the present work

In the present work, the commercial kinetics model DICTRA [23], an extension to the thermodynamics modeling software Thermo-Calc [19], was applied in conjunction with the kinetics database MOB2 [26]. The model was primarily applied to determine the kinetics of solidification and cooling (chapter 6) and the kinetics of austenitization (chapter 10). The specifically applied parameters are given in the respective result manuscripts.

References

[1] P.J. Spencer, A brief history of CALPHAD, Calphad Comput. Coupling Phase Diagrams Thermochem. 32 (2008) 1–8.

[2] J.J. van Laar, Die Schmelz- oder Erstarrungskurven bei binären Systemen, wenn die feste Phase ein Gemisch (amorphe feste Lösung der Mischkristalle) der beiden Komponenten ist, Zeitschrift Für Phys. Chemie. 24 (1908) 20–54.

[3] J.L. Meijering, Paper 5A, Vol 2, in: Phys. Chem. Met. Solut. Intermet. Compd., 1959.

[4] C. Wagner, Thermodynamics of alloys, Addison-Wesley Press, 1952.

[5] L. Kaufman, The lattice stability of the transition metals, in: Phase Stab. Met. Alloy., 1966: pp. 125–148.

[6] L. Kaufman, H. Bernstein, Computer Calculation of Phase Diagrams : With Special Reference to Refractory Metals, 1970.

[7] A.T. Dinsdale, SGTE Data for Pure Elements, Calphad. 15 (1991) 317–425.

[8] S. Bigdeli, H. Mao, M. Selleby, On the third-generation Calphad databases: An updated description of Mn, Phys. Status Solidi Basic Res. 252 (2015) 2199–2208.

[9] Thermo-Calc Software, TCTI1: TCS Ti/TiAl-based Alloys Database, 2017.

[10] Thermo-Calc Software, TCNOBL1 - TCS Noble Metal-based Alloy Database, 2017.

[11] R. Otis, Z.-K. Liu, pycalphad: CALPHAD-based Computational Thermodynamics in Python, J. Open Res. Softw. 5 (2017) 1–11.

[12] B. Sundman, U.R. Kattner, M. Palumbo, S.G. Fries, OpenCalphad - a free thermodynamic software, Integr. Mater. Manuf. Innov. 4 (2015) 1.

[13] H.L. Lukas, S.G. Fries, B. Sundmann, Computational Thermodynamics - The Calphad Method, 1st ed., 2007.

[14] M. Hillert, Phase Equilibria, Phase Diagrams and Phase Transformations - Their Thermodynamic Basics, 2008.

[15] O. Redlich, A.T. Kister, Algebraic Representation of Thermodynamic Properties and the Classification of Solutions, Ind. Eng. Chem. 40 (1948) 345–348.

[16] M. Hillert, Partial Gibbs energies from Redlich-Kister polynomials, Thermochim. Acta. 129 (1988) 71–75.

[17] M. Perrut, Thermodynamic modeling by the calphad method and its applications to innovative materials, AerospaceLab. (2015) 1–11.

[18] U.R. Kattner, The thermodynamic modeling of multicomponent phase equilibria, Jom. 49 (1997) 14–19.

[19] J.O. Andersson, T. Helander, L. Höglund, P. Shi, B. Sundman, Thermo-Calc & DICTRA, computational tools for materials science, Calphad Comput. Coupling Phase Diagrams Thermochem. 26 (2002) 273–312.

[20] Thermo-Calc Software TCFE6 Steels/Fe-alloys database version 6.2, Thermo-Calc Softw. TCFE6 Steels/Fe-Alloys Database Version 6.2 (Accessed Novemb. 2009).

[21] J. Ågren, Diffusion in phases with several components and sublattices, J. Phys. Chem. Solids. 43 (1982) 421–430.

[22] J.O. Andersson, J. Ågren, Models for numerical treatment of multicomponent diffusion in simple phases, J. Appl. Phys. 72 (1992) 1350–1355.

[23] A. Borgenstam, A. Engström, L. Höglund, J. Ågren, DICTRA, a tool for simulation of diffusional transformations in alloys, J. Phase Equilibria. 21 (2000) 269–280.

[24] L. Onsager, Reciprocal relations in irreversible processes. II., Phys. Rev. 38 (1931) 2265–2279.

[25] H. Larsson, A model for 1D multiphase moving phase boundary simulations under local equilibrium conditions, Calphad Comput. Coupling Phase Diagrams

Thermochem. 47 (2014) 1–8.
[26] Thermo-Calc Software TCS Alloys Mobility Database MOB2 (accessed 08 April 1998).

5 Summary of results

This chapter provides a summary of the results in chapters 6 to 14. The statement of quantitative results is kept to a minimum and no references are given. For these, the reader is referred to the respective result chapters.

5.1 Manuscript I

Kinetics modeling of delta-ferrite formation and retainment during casting of supermartensitic stainless steel

This chapter investigates the suitability of different empirical and numerical models to predict the amount and composition of retained δ-ferrite in the microstructure after solidification of a cast soft martensitic stainless steel. The employed models were the Schaeffler-diagram, thermodynamics modeling, the extended Scheil-model and kinetics modeling of diffusion. The investigated material was an EN1.4405 soft-martensitic stainless steel. After solidification the cast material revealed 11 % area fraction of vermicular δ-ferrite, embedded in a lath martensite matrix. δ-ferrite was enriched in Cr and depleted in Ni.

The Schaeffler-diagram gave an acceptable prediction of the amount or retained δ-ferrite, while the austenite stability was significantly overestimated. While thermodynamics modeling was useful for predicting a solidification sequence, it was unsuitable for the prediction of the phase fraction of δ-ferrite at low temperature, as the microstructure was found to strongly deviate from thermodynamic equilibrium with decreasing temperature. The Scheil-model significantly overestimated the amount of segregation during solidification by assuming no back-diffusion of substitutional elements into the melt.

Kinetics modeling of diffusion was found most suitable for predicting the phase fraction and composition of δ-ferrite at room temperature. The domain-size of the kinetics model was determined from half the δ-ferrite spacing and the cooling rate was determined from a solidification simulation. It was found that the material entirely solidified as δ-ferrite and that the transformation of δ-ferrite to austenite was fastest in the two phase region above A_4. Below that temperature the transformation slowed down significantly, mainly originating from impingement of the diffusion field, and virtually halted below 900 °C. The composition profiles across martensite / δ-ferrite phase boundaries were in reasonable agreement with predictions from kinetics modeling. A systematic comparison of the δ-ferrite phase fractions obtained from transformation along different linear cooling rates showed that slower cooling led to less retained δ-ferrite. It was further found that a smaller domain size, i.e. smaller δ-ferrite spacing, had an equivalent effect on the transformation kinetics as decreasing the cooling rate. In order to qualify kinetics modeling

as a tool for quantitative prediction, calibration of the model with respect to cooling rate and domain size should be further improved.

5.2 Manuscript II

In Situ Investigation of the Evolution of Lattice Strain and Stresses in Austenite and Martensite During Quenching and Tempering of Steel

No consistent picture of the evolution of stress in austenite and martensite in steel consists. Thus, high-temperature synchrotron X-ray diffraction was applied to measure the lattice strains and stresses in austenite and martensite during quenching and tempering of an EN1.4418 soft martensitic stainless steel. In one experiment, lattice strains in austenite and martensite were measured perpendicular to the surface and in a second experiment, lattice strains in austenite and martensite were measured with the $\sin^2\psi$ method to distinguish between macro-stresses and phase-specific micro-stresses.

Determination of lattice strains is based on comparing the planar spacing of a particular reflection with a value for a strain-free planar spacing. The strain-free lattice parameter of austenite as a function of temperature was determined by extrapolating a second-order polynomial fitted through the temperature interval 920 – 145 °C during cooling from austenitization before the onset of martensite transformation. As there is no condition in which martensite is the only phase, the stress-free lattice parameter of martensite at room-temperature was determined by considering stress-equilibrium with austenite. The thermal expansion was determined from fitting the lattice parameter of martensite during cooling from tempering to 475 °C.

Stress analysis showed that phase-specific micro-stresses have a significant magnitude for the minority phase, i.e. for martensite in the beginning of the transformation and austenite towards the end of the transformation. These stresses are compressive in the minority phase and are balanced by tensile stress in the majority phase. The strain in austenite was anisotropic. The maximum amount of compression was experienced by the $\{222\}_\gamma$ and $\{220\}_\gamma$ crystal planes, while the $\{200\}_\gamma$ planes experienced a tensile strain. Strain anisotropy in austenite and oscillations of the martensite lattice parameter as a function of $\sin^2\psi$ indicated that both phases are subject to plastic deformation. An in-depth evaluation of the state of stress thus requires further investigation of the effect of plasticity on the determination of stresses in steels. Tempering of martensite led to a large decrease in lattice parameter, which is consistently explained by a rejection of interstitial elements.

5.3 Manuscript III

In-situ analysis of redistribution of carbon and nitrogen during tempering of low interstitial martensitic stainless steel

The redistribution of carbon and nitrogen during tempering of EN1.4418 soft martensitic stainless steel containing 0.032 wt.% C and 0.034 wt.% N was investigated by in-situ synchrotron X-ray diffraction (XRD) and atom probe tomography. In XRD the lattice parameter of martensite was measured during isochronal heating with 0.033 $K.s^{-1}$, starting from the hardened condition. Applying the identical heating cycle a second time after tempering yielded a reference lattice parameter, which was used to determine the relative change in lattice parameter as a result of tempering. The martensite lattice parameter decreased progressively with respect to the reference lattice parameter and increasing tempering temperature.

A relative change in lattice parameter may either be interpreted as a mechanical effect, i.e. a lattice strain, or as a chemical effect. Interpreting the relative change in lattice parameter by a pure effect of change in interstitially dissolved elements, i.e. C and N, the change in lattice parameter corresponded to a progressive rejection of C and N. In order to validate this hypothesis, the distribution of C and N were analyzed with atom probe tomography in the hardened condition, and two tempered conditions. Atom probe tomography revealed a rather homogeneous distribution of C and N in the hardened condition and progressive segregation of C and N to lattice defects, mainly grain boundaries. By excluding segregated features and adjacent depleted zones, bulk regions were defined in analyzed volumes to determine an average C and N content in the bulk of the three conditions.

The C and N content in the bulk from APT agreed excellently with the interpretation of a relative change in lattice parameter as a result of interstitial segregation from XRD. It therefore appears as if the relative change in lattice parameter during tempering of martensite in the present system can only be interpreted in terms of interstitial partitioning. The alternative hypothesis, a purely mechanical effect, would correspond to a build-up of significant compressive stress in martensite during tempering, which exceeds the required stress for relaxation of the tensile residual stress from martensite formation by a factor of 8. Furthermore, relaxation of the tensile state of stress in martensite compared to a compressive state of stress in austenite would induce partitioning of interstitials in the reverse direction, i.e. martensite can release the tensile hydrostatic component of the stress state by absorbing more interstitials, while austenite can release the hydrostatic component of the compressive stress by depletion of interstitials. Atom probe tomography showed that the reverse is happening, implying that a reduction of the strain energy is not the dominant driving force for partitioning of the interstitials.

5.4 Manuscript IV

Structural evolution of martensite during tempering of soft martensitic stainless steel

The structural evolution of lath martensite during tempering in EN1.4418 was studied by line profile analysis of diffractograms from energy-dispersive synchrotron X-ray

diffraction (XRD), atom probe tomography (APT) and site-specific orientation mapping with electron microscopy.

Martensite formation occurred without autotempering and storage of the samples at room temperature for 6 months did not lead to noticeable aging. After martensite formation, the dislocation density was $\sim 1.8 \times 10^{15}\ \mathrm{m}^{-2}$. Tempering with $0.033\ \mathrm{K.s}^{-1}$ to 475 °C led to progressive partitioning of C and N to lattice defects, mainly grain boundaries. Recovery commenced above 550 °C and led to a steady decrease in dislocation density to a seemingly steady value of $\sim 3.5 \times 10^{14}\ \mathrm{m}^{-2}$ at 700 and 750 °C. Further tempering led to a new decrease in dislocation density at room-temperature, which originated from martensite formation from reverted austenite.

The evolution of the coherently diffracting particle size was qualitatively in line with recovery of martensite, in which low-angle grain boundaries are annealed out. Quantitatively, the measured average coherently diffracting domain size was in the order of 50 nm in the hardened condition, which cannot be related to any microstructural features. The effect has been reported in literature and may be attributed to loss of X-ray coherency for low misorientations in plastically deformed metals.

5.5 Manuscript V

Kinetics analysis of two-stage austenitization in supermartensitic stainless steel

The kinetics of austenitization of an EN1.4418 soft martensitic stainless steel was investigated by correlated high-temperature synchrotron X-ray diffraction and kinetics modeling of diffusion. Samples were heated with 2, 6 and 18 $\mathrm{K.min}^{-1}$ to transform from an initially mostly lath martensite microstructure to a fully austenitic microstructure. It was found that the transformation from martensite to austenite occurred in two stages, separated by a temperature region in which the transformation was strongly decelerated.

To obtain insight into the responsible mechanisms for austenitization in two-stages, the transformation was modeled with kinetics modeling of diffusion. Microstructure characterization revealed that austenite reversion initially occurs mostly on lath boundaries. The characteristic diffusion domain was thus identified as the martensite lath, in which nucleation and growth of austenite was allowed from lath boundaries during heating. The modeled transformation kinetics were in good agreement with the measured kinetics. Both a thermal activation of the transformation and the separation in two distinct transformation stages were reproduced.

Investigation of the evolution of concentration profiles with time and temperature revealed that soft-impingement of the diffusion field is responsible for the interruption of the transformation. Just after nucleation, substantial partitioning leads to enrichment of austenite in Ni. With further heating austenite becomes more stable and is able to grow with less enrichment in Ni. Soft-impingement occurs when martensite is depleted in Ni,

and thus cannot supply Ni to the interface any longer. At this stage, the transformation is interrupted and relies on diffusion of Ni from the Ni-rich region in austenite to the interface. The second stage of the transformation occurs at a lower transformation rate than the first stage. This observation is consistent with experimental findings, even though towards the end of the transformation, further nucleation in the center of martensite laths and grain growth in the experimental microstructure affect the validity of the kinetics model, which is based on a simpler geometry.

By analyzing the Ni redistribution at different transformation stages and individually increasing the diffusion mobility of Ni and Cr in ferrite and austenite by an order of magnitude, it was found that the rate of the first stage of austenitization was determined by Ni diffusion in ferrite and the second stage by Ni diffusion in austenite. As the transformation rate just after nucleation is rather slow, consideration of a nucleation barrier for austenite had an insignificant effect on the overall transformation kinetics. Increasing the domain size, i.e. austenite reversion in wider laths, had the same effect on the transformation kinetics as increasing the heating rate.

5.6 Manuscript VI

Formation and stabilization of reversed austenite in supermartensitic stainless steel

Various electron-microscopy techniques, thermodynamics and kinetics modeling, as well as dilatometry were applied to elucidate the mechanisms responsible for formation and stabilization of reverted austenite in an EN.14418 soft martensitic stainless steel. After martensite formation, heat-treating the material for 2 h at different temperatures led to secondary hardening at 475 °C and a minimum hardness at 650 °C. Heating at higher temperature led to a second increase in hardness. Annealing in the inter-critical region in which austenite and ferrite coexist, led to increasing amounts of reverted austenite, with annealing temperature. It was found that at maximum 37 vol.% of austenite could be stabilized at room temperature. Larger amounts of reverted austenite did not remain stable and transformed to new martensite during cooling. The measured softening effect induced by the heat-treatment was therefore mainly caused by formation of reverted austenite, and partially by recovery of martensite. Characterization of inter-critically annealed samples with a large field backscatter electron detector in a scanning electron microscope revealed that austenite mainly formed at grain boundaries, mainly lath boundaries. Electron backscatter diffraction revealed that reverted austenite adapted the orientation of its prior austenite grain, which is known as the austenite memory effect. The martensite orientation of single prior austenite grains showed that the orientation-relationship was close to Kurdjumow-Sachs.

Analysis of electron-transparent samples of the inter-critically annealed condition in the transmission electron microscope with EDS showed that austenite was noticeably enriched in Ni while Cr was homogeneously distributed. Thermodynamics modeling predicted partitioning of both Ni and Cr in austenite and martensite, which could not be

confirmed experimentally. Kinetics modeling of diffusion for isothermal inter-critical annealing revealed that the kinetics of austenite formation are strongly dependent on the annealing temperature. Apart from the effect of slower diffusion at lower temperature, more partitioning is required with lower temperature, which slows down the transformation kinetics. The composition of austenite from thermodynamics modeling at different annealing temperatures was inserted to empirical formulas for M_S. It was found that the stability of reverted austenite mainly originates from a chemical effect, while a further mechanical stabilitzation was anticipated.

5.7 Manuscript VII

Martensite formation from reverted austenite at sub-zero Celsius temperature

Samples of EN1.4418 soft martensitic stainless steel were inter-critically annealed on a heating stage during in-situ energy-dispersive synchrotron XRD. All samples heated to 898 – 973 K contained reverted austenite at room-temperature, which is mainly stabilized by enrichment in Ni. While the austenite fraction increased with annealing temperature, not all austenite formed above 923 K remained stable during cooling to room-temperature.

The thermal stability of reverted austenite at sub-zero Celsius temperature was investigated by measuring the austenite fraction with a vibrating sample magnetometer, equipped with a cryostat. Immersion of the annealed samples in boiling N_2 (77 K) did not lead to a noticeable change in austenite fraction, which is consistent with the current state of literature. Reverted austenite was however partially transformed during isothermal holding at 194.5 K for 15.3 ks. This result can be understood in terms of thermally activated martensite formation. Accordingly, martensite formation is kinetically suppressed at 77 K, while holding too close to room temperature does not yield sufficient driving force. The most effective temperature for isothermal martensite formation in lath martensite is approx. 180 – 210 K.

Based on the present results testing of the stability of reverted austenite is suggested for several days at frozen CO_2 temperature (194.5 K). Further, it is anticipated that impact toughness values at sub-zero temperature may be time dependent, as they scale with the fraction of reverted austenite. Thus, the cooling time of samples should be stated for impact toughness testing at sub-zero Celsius temperature and tests should be carried out for different cryogenic holding times.

5.8 Manuscript VIII

Mechanical stability of reverted austenite in supermartensitic stainless steel – an in-situ synchrotron X-ray diffraction study

The mechanical stability of reverted austenite in a Super 13 Cr supermartensitic stainless steel was investigated by in-situ synchrotron X-ray diffraction during tensile testing.

Differently annealed samples were exposed to stepwise displacement-controlled straining. The macroscopic true strain was determined from 3D direct image correlation (DIC) and the true stresses were determined by dividing the load by the cross-sectional area at each strain point. At each strain increment, diffractograms were acquired at different angles of the diffraction vector with respect to the tensile direction. Diffraction data enabled the determination of the strain-free lattice parameter, X-ray elastic constants (XEC's), lattice strains, lattice stresses, fraction of austenite and micro-strains as a function of externally applied stress.

It was found that reverted austenite can in fact transforms to martensite by a strain-induced mechanism during uniaxial loading. Especially the yield strength and the total extension at maximum stress were sensitive to the annealing treatments, while the ultimate tensile strength was less affected by differences in annealing treatments. Double annealing, i.e. applying a first annealing step at 670 °C before conducting the second annealing step, led to a higher initial fraction of austenite and increased ductility compared to single annealed specimens at the same temperature.

Higher total fractions of transformed reverted austenite correlated with increased ductility. The lattice stress in tempered martensite follows the applied stress, while austenite appears to follow the deformation without accommodating the applied stress. Plastic deformation seems to be partly accomplished by γ-to-α' transformation which enables elongation without dislocation production. Martensite mainly formed with <220> oriented parallel to the tensile axis.

5.9 Manuscript IX

A systematic comparison of on-axis and off-axis transmission Kikuchi diffraction

Transmission Kikuchi diffraction (TKD) is a recently developed diffraction technique for the scanning electron microscope that enables orientation and phase mapping on the nano-scale. Because in TKD, adverse to the well-known electron backscatter diffraction (EBSD), the maximum diffracted intensity is below the electron-transparent sample, an optimized detector for TKD has been developed. The detector is positioned below the sample to capture the maximum intensity on the axis of the direct beam, and is thus termed "on-axis" TKD. TKD with a conventional EBDS detector occurs off the axis of the direct beam and is thus termed "off-axis" TKD.

The appearance of Kikuchi patterns from both techniques were compared when systematically varying individual parameters from a set of reference parameters. Comparison of the reference on- and off-axis Kikuchi patterns showed that the on-axis pattern was disturbed by an overexposed area of the direct beam. The bands in on-axis patterns were thinner and 70 % additional area of the Kikuchi map could be captured. The direct beam, when filtered out of the image, did not appear to disturb the Hough-space for automated band detection. Increasing the beam current led to increasing pattern contrast in

both techniques, while in on-axis TKD also the area of the Kikuchi pattern and the overexposed area became larger. Lowering the beam energy led to blurring and broadening of Kikuchi bands in both techniques, as it is a general scattering effect. In on-axis TKD also the spot-pattern and over-exposed area of the direct beam decreased. Reducing the detector distance in off-axis TKD led to gradual downward-movement of the pattern and a loss in pattern intensity. In on-axis TKD, increasing the detector distance led to a magnification of the pattern without affecting the position or intensity of the pattern.

The physical spatial resolution was compared on grain-boundaries of a 316L austenitic stainless steel thin foil. Applying an image correlation technique, it was found that the physical spatial resolution of on-axis TKD was slightly better than the one of off-axis TKD. This could be an effect of the smaller beam current and probe size or an effect of the different source region of the pattern. The effective spatial resolution was tested on a nano-crystalline Au-sample. Both detectors managed to resolve grains of approx. 10 nm in diameter. Both techniques produced well-resolved orientation maps, while the faster acquisition speed of on-axis TKD enabled the capturing of larger maps because of reduced beam-drift. The performance of automated band detection by the Hough-transform was tested by comparing the amount of indexed bands by automated and manually refined band detection. The Hough-transform worked better on on-axis patterns, for which no significant improvement by manual band detection could be obtained. The off-axis pattern revealed difficulties in detecting gnomonically distorted bands in the lower part of the pattern. Manual refinement led to a noticeable improvement in band detection.

6 Manuscript I

Kinetics modeling of delta-ferrite formation and retainment during casting of supermartensitic stainless steel*

Frank Niessen[a,†], Niels S. Tiedje[b], John Hald[c]

[a] Technical University of Denmark (DTU), Danish Hydrocarbon Research and Technology Centre (DHRTC) , Elektrovej building 375, 2800 Kgs. Lyngby, Denmark

[b] Technical University of Denmark (DTU), Department of Mechanical Engineering, Produktionstorvet building 427, 2800 Kgs. Lyngby, Denmark

[c] Technical University of Denmark (DTU), Department of Mechanical Engineering, Produktionstorvet building 425, 2800 Kgs. Lyngby, Denmark

[†] Corresponding author

Abstract

The kinetics model for multi-component diffusion DICTRA was applied to analyze the formation and retainment of δ-ferrite during solidification and cooling of GX4-CrNiMo-16-5-1 cast supermartensitic stainless steel. The obtained results were compared with results from the Schaeffler diagram, equilibrium calculations and the Scheil model in Thermo-Calc, and validated by using microscopy and Energy Dispersive X-ray Spectroscopy for chemical analysis on a cast ingot. The kinetics model showed that micro-segregation from solidification homogenizes within 2 - 3 s (70 °C) of cooling, and that retained δ-ferrite originates from the incomplete transformation to austenite. The kinetics model predicted the measured amount of δ-ferrite and the partitioning of Cr and Ni reasonably well. Further, it showed that slower cooling for the investigated alloy leads to less retained δ-ferrite, which is in excellent agreement with experimental results.

* Published work: F. Niessen, N.S. Tiedje, J. Hald, Kinetics modeling of delta-ferrite formation and retainment during casting of supermartensitic stainless steel, Mater. Des. 118 (2017) 138–145. The format of the published article was adapted to the format of the doctoral thesis.

6.1 Introduction

Since the 1960s, when supermartensitic stainless steels were developed, this type of alloys has found increasing use in many industries [1,2]. Specifically in the offshore oil and gas industry such alloy grades were introduced in the 1990s [3]. Supermartensitic stainless steels combine high strength, good toughness as well as reasonable weldability, and they achieve good corrosion performance with relatively low alloy content [4,5].

The optimal properties of the material, extensively described in Refs. [2,6,7], are obtained by normalizing, leading to martensite transformation, followed by tempering in the inter-critical temperature region, in which both austenite (γ) and ferrite (α) are thermodynamically stable. The tempering treatment leads to formation of reversed austenite in a finely dispersed lamellar morphology on grain boundaries of lath martensite. This is accompanied by diffusion of austenite stabilizing elements into austenite, which stabilize this phase to room temperature [8–13]. Since the good mechanical properties of the alloy depend on this stabilization of reversed austenite, it is vital to control the compositional homogeneity of the initial martensitic microstructure prior to tempering. This is particularly challenging for the cast grades, in which macro- and micro-segregation and the retainment of δ-ferrite from solidification and cooling can lead to an inhomogeneous initial microstructure [6,14,15].

The presence of the δ-ferrite phase can cause severe reduction of toughness and ductility [16,17]. Further, it can locally interrupt the passivation layer through Cr-depletion in martensite and formation of Cr carbides near δ-ferrite, which leads to degradation of the corrosion resistance [18]. Such inhomogeneity affects the nucleation and growth of reversed austenite during tempering in the inter-critical region [15].

In the present alloy grade, δ-ferrite is the first solidifying phase, which partially or completely transforms to austenite during cooling. When retained, it is only possible to dissolve δ-ferrite by extensive heat treatment, which is uneconomical and can lead to undesired grain growth [19]. Addition of Ni can largely suppress the retainment of δ-ferrite but it is expensive and it potentially shifts the martensite start (M_s) temperature below room temperature. Previous research demonstrated the influence of the chemical composition and cooling-rate on the retainment of δ-ferrite [20–22].

The phase distribution after solidification can be estimated by a variety of available models, such as the lever rule, the Scheil Model [23] and empirical models such as the Schaeffler diagram [21]. These models are easy to apply, but oversimplify the mechanisms during solidification and cooling to different degrees. Less common and more complex models, which can be used for solidification and cooling analysis in casting or welding, are regression analysis and neural networks [24–26]. Both these kinds of models are able to predict residual δ-ferrite contents accurately, but require adaptation for new sets of processing parameters and are not physics based.

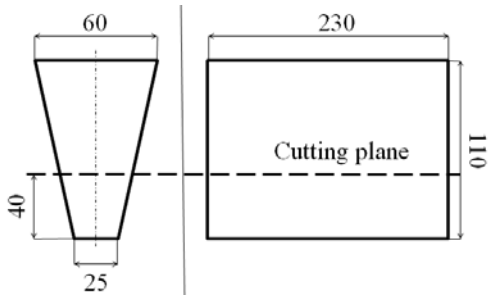

Figure 6.1: Geometry of the ingot marking the area of investigation below the cutting plane. Measures are in mm.

Since formation and retainment of δ-ferrite mainly occur in a temperature region in which phase transformations are primarily controlled by diffusion, it should be possible to predict the formation and retainment of δ-ferrite by kinetics modeling of diffusion. Moving boundary kinetics models, which predict the kinetics of diffusion controlled phase transformations based on constitutive diffusion and flux balance equations, a set of boundary conditions, and thermodynamics and kinetics databases, can be used for this purpose [27]. The aim of the present investigation was therefore to investigate the applicability of the kinetics model DICTRA on predicting the formation and retainment of δ-ferrite during cooling of GX4-CrNiMo-16-5-1 cast supermartensitic stainless steel. The results obtained by simulation with different cooling rates were related to the results of the conventional models and validated on micrographs and chemical analysis of an ingot.

6.2 Material Characterization

6.2.1 Procedures

The examined cast material GX4-CrNiMo-16-5-1 with the composition given in Table 6.1 was cast in a keel block of 230 x 110 x 60/25 mm with bottom filling. The casting was cut horizontally at 40 mm height to exclude the impurity-rich last solidified material (Figure 6.2). A cross-section in the center of the bar was cut out, embedded, ground and polished for microstructure characterization. Specimens prepared for light optical microscopy (LOM) were etched in Vilella's reagent [28].

The light optical microscope was an Olympus GX41 bright field microscope. The image analysis for the determination of the amount of δ-ferrite in the microstructure was carried out using the MATLAB Image Processing Toolbox. The micrograph was filtered with a Gaussian filter, the background was determined and subtracted, brightness and contrast were adjusted, and the micrograph was converted to a binary image. Then all

Table 6.1: Chemical composition of the investigated alloy GX-CrNiMo-16-5-1 balanced with Fe (wt%) from optical emission spectroscopy (OES).

C	N	Cr	Ni	Mo	Mn	Si	P	S
0.011	0.078	15.30	6.30	1.22	0.58	0.70	0.013	0.006

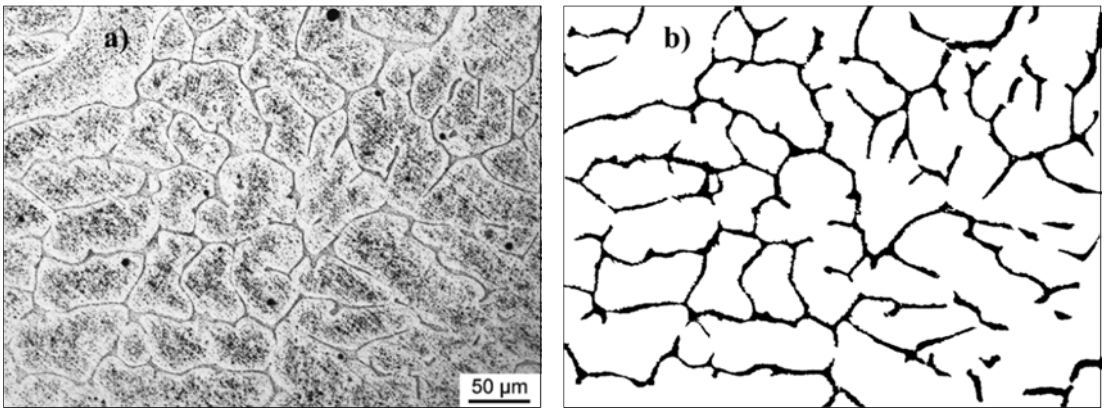

Figure 6.2: LOM (a) Microstructure in as-cast condition showing vermicular δ -ferrite (dark grey) in the martensite matrix (light grey); (b) Image Analysis - Isolated δ -ferrite (black) extracted from the micrograph in Figure 6.2a by Image Analysis, yielding a δ –ferrite area-fraction of 11 %.

connected components in the image were determined and filtered by applying a minimum area criterion. The final step consisted of manual refinement of artefacts and determination of the area-fraction.

A JEOL 5900 scanning electron microscope (SEM) with a tungsten filament was used for imaging and energy dispersive X-ray spectroscopy (EDS). The EDS measurement was carried out on an area map between a set of parallel δ-ferrite stringers with 22 µm distance between their centerlines. The area scans were averaged in parallel orientation to the δ-ferrite stringers to yield a one-dimensional composition profile, as described in Ref. [29]. This averaging procedure allowed direct comparison with the results of the one-dimensional kinetics model. The acceleration voltage was 18 kV and the step size for the measurement was 100 nm. The EDS-system was calibrated on pure Cu as a reference just before acquisition. Under consideration of the spatial resolution limit given by the interaction volume of EDS analysis, the acquired data points were averaged to steps of 500 nm.

6.2.2 Results

Light optical microscopy

After austenitization the steel consisted of lath martensite and vermicular δ-ferrite [30,31] (Figure 6.2a). The δ-ferrite was distributed uniformly over the entire microstructure with varying spacing of approx. 15 to 50 µm and changed to a lace-like morphology near the surface of the casting. The area fraction of δ-ferrite was determined as 11 % by using image analysis (Figure 6.2b). The statistical error of this analysis is estimated to be ± 2 %.

Energy dispersive X-ray spectroscopy

The EDS measurement across the phase interfaces of two parallel δ-ferrite stringers and martensite (Figure 6.3a) showed that partitioning between the adjacent phases was most

evident for Cr and Ni (Figure 6.3b). The average concentration of Cr and Ni within δ-ferrite were 21 and 2.5 wt.%, respectively. The composition of martensite was close to the average alloy composition and approached the composition of δ-ferrite in a smooth transition across the interface.

6.3 Modeling

Modeling was applied to study the phase transformations, which led to the characterized microstructure in Figure 6.2 and Figure 6.3. The main focus was on the prediction of the solidification reaction and the kinetics analysis of the subsequent solid state phase transformations during cooling. Various models for the prediction of solidification microstructures and phase equilibria are available and the most common ones were evaluated for this purpose.

6.3.1 Conventional models

The Schaeffler-diagram is an empiric model that was established for the prediction of weld-microstructures in 1947 [32]. It predicts phase fractions after solidification and cooling based on the input of Cr- and Ni-equivalents. The alloy investigated here had Cr- and Ni-equivalents of 17.6 and 6.9 wt.%, respectively. Due to an appreciable amount of N in the alloy the modification by DeLong and Reid was evaluated too [33]. It attributes N the same influence on austenite stability as C, which led to a Ni-equivalent of 9.3 wt.%. The equation of Schaeffler resulted in prediction of martensite with approx. 18 % of retained δ-ferrite and a small fraction of retained austenite. The formulation by DeLong and Reid led to approx. 6 % of retained δ-ferrite and more than 50 % of retained austenite next to martensite (Figure 6.4).

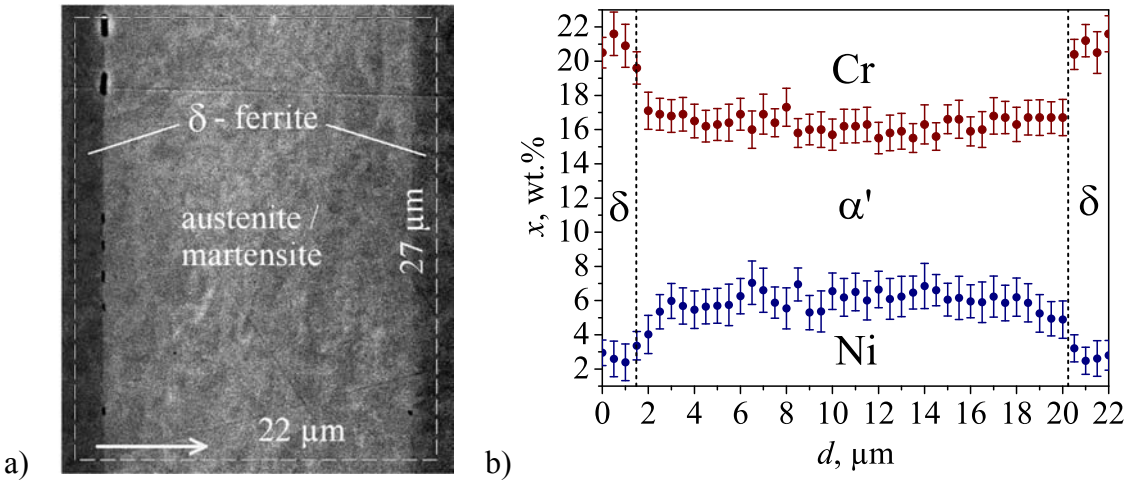

Figure 6.3: EDS-Measurements on δ/γ-interfaces (a) SEM backscatter micrograph of area scan; (b) Cr- and Ni- concentration, x, integrated and averaged parallel to the δ -ferrite orientation to a 1-dimensional line profile over distance d. The error bars indicate the statistical error of the quantification method.

The models, which are presented in the following, are run in Thermo-Calc/DICTRA. All simulations are run with the alloy composition in Table 6.1, with exclusion of S, P and N. This was done because the trace elements S and P are not implemented in the used databases. In the kinetics model including N led to numerical instability.

Global equilibrium phase fractions as function of temperature (lever rule) during solidification and cooling were modeled by equilibrium calculations in Thermo-Calc (database TCFE6 [34]; phases: face centered cubic (*fcc*), body centered cubic (*bcc*) and liquid). The model predicted solidification to δ-ferrite with a subsequent two phase region of austenite and δ-ferrite, which extended over a span of approx. 250 °C. The liquidus temperature, T_{liq}, and the solidus temperature, T_{sol}, were predicted as 1480 and 1457 °C, respectively (Figure 6.5a). The model gives general predictions on solidification and cooling under thermodynamic equilibrium, but is not able to take the kinetics of the governing phase transformations into account.

The Scheil module in Thermo-Calc assesses solidification by a modified version of the Scheil model, that allows rapid diffusion of C in the liquid and solid (*fcc* and *bcc*). The model predicted that δ-ferrite was the first phase to form during solidification. δ-ferrite had increased Cr- and decreased Ni-content relative to the average alloy composition, leading to Ni-enrichment and Cr-depletion in the melt (Figure 6.5b). Austenite was predicted to nucleate in a peritectic reaction at a fraction solid of 92 %, which led to severe partitioning of Ni and Cr towards the end of solidification. With this model T_{liq} and T_{sol} were predicted as 1481 and 1397 °C, respectively. It is generally known that the Scheil model overestimates segregation towards the end of solidification and is not designed to predict subsequent solid-state phase transformations during cooling [25].

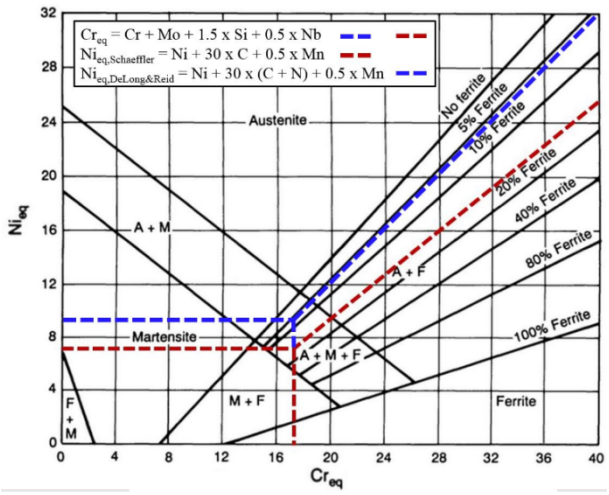

Figure 6.4: Schaeffler constitution diagram of 1949 for stainless steel weld metal [36]. The red dashed lines indicate the equivalent compositions and ferrite prediction according to Schaeffler, the blue dashed lines include the effect of N on the Ni_{eq} and the ferrite prediction according to DeLong and Reid [34].

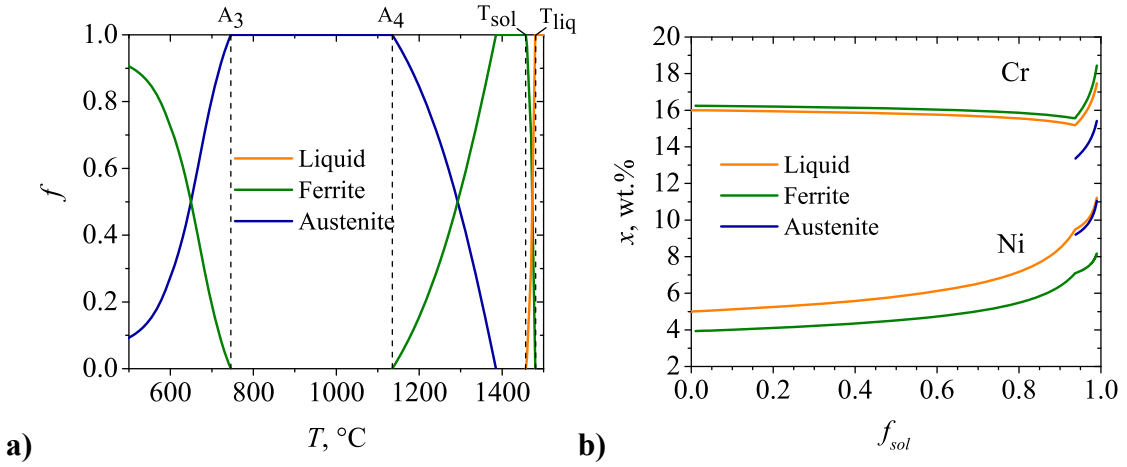

Figure 6.5: (a) Equilibrium calculation: Phase-fraction, f, vs. temperature, T, determined by carrying out a step-equilibrium calculation in Thermo-Calc; (b) Scheil model: Cr- and Ni-content x, vs. the total solid fraction, f_{sol}, for the phases liquid, ferrite (bcc) and austenite (fcc).

6.3.2 Kinetics modeling

The moving boundary model in the kinetics model DICTRA gives predictions on the kinetics of phase transformations during solidification and cooling [27]. The model is able to overcome most limitations of the previously introduced conventional models by describing movement of the phase boundary, based on the rate of diffusion to and from the interface. Diffusion is modelled by multi-component diffusion equations and assuming local equilibrium at the phase interface. As the model is designed for diffusion controlled transformations only it is not suitable for handling displacive transformations as e.g. martensite formation. [36].

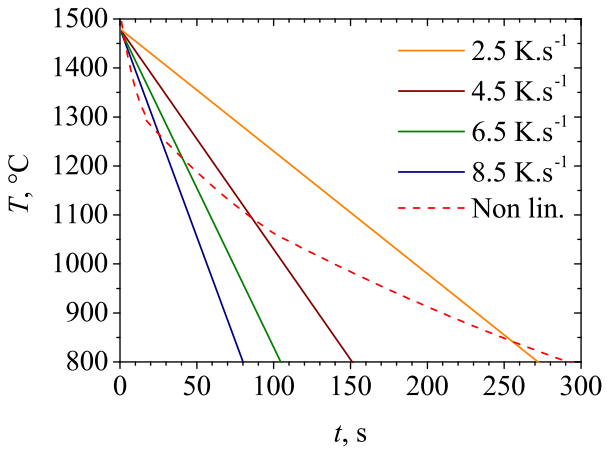

Figure 6.6: Non-linear cooling curve modeled with MAGMA5 (red dashed line) and four linear cooling curves (solid lines).

Table 6.2: Comparison of characteristic temperatures, phase fractions and solute contents obtained from the modeled and experimental results; the solute contents represent the average within the respective phases.

	T_{liq} [°C]	T_{sol} [°C]	f_δ [v.%]	$x_{\delta,Cr}$ [wt.%]	$x_{\delta,Ni}$ [wt.%]	$x_{\gamma,Cr}$ [wt.%]	$x_{\gamma,Ni}$ [wt.%]
Schaeffler:	-	-	18[a]	-	-	-	-
DeLong, Reid:	-	-	6[a]	-	-	-	-
Equilibrium Model:	1480	1457	-	20.1[b]	2.9[b]	15.3[b]	6.3[b]
Scheil Model:	1481	1397	-	16.4[c]	6.2[c]	14.4[c]	10.1[c]
Kinetics Model:	1480	1449	17[b]	20.1[b]	3.2[b]	14.7[b]	6.5[b]
Experimental:	-	-	11[a]	21.0[a]	2.7[a]	16.4[a]	5.9[a]

T_{liq}: Liquidus temperature; T_{sol}: Solidus temperature; f_δ: Fraction of δ-ferrite; $x_{phase,component}$: Solute content of component in phase; [a]: At room temperature; [b]: at 800 °C; [c]: at T_{sol} of Scheil Model

Model initialization

The model was initialized with the purpose of predicting the experimentally determined phase distribution and concentration profiles in Figure 6.3. The solidification front was defined as a one-dimensional planar geometry. The simulation commenced in a liquid domain. The domain size was defined as half the length of the typical δ-ferrite spacing, which in this case was 11µm, c.f. Figure 6.3a. Ferrite was set to nucleate in one end the domain (to the left in Figure 6.7a). Austenite was set to nucleate on the ferrite-liquid interface, in order to allow a potential peritectic solidification reaction to take place. However, the model did not predict a peritectic reaction, therefore austenite nucleated in the final ferrite (to the right in Figure 6.7a). All phases were required to overcome a critical driving force for precipitation, $-dG_m/(RT)$ of 10^{-5} , where G_m is the molar Gibbs energy, R is the universal gas constant and T the temperature in K. This value is a default value in

DICTRA and follows the Thermo-Calc/DICTRA convention of defining all driving forces dimensionless [37]. The thermodynamics database TCFE6 [34] and the mobility database MOB2 [38] were used. The choice of spatial and temporal discretization was determined by evaluating the trade-off between spent computational time and reasonable physical representation of the phase transformations. The calculations were thus carried out with a linear spatial resolution of 80 cells, i.e. a discretization of 137.5 nm, and a maximum time step of 0.1 s. For lower temporal and spatial resolutions numeric instabilities occurred. The stability of the numeric simulation was enhanced by using a fully implicit scheme and by variation of the chemical activities instead of chemical potentials.

The kinetics model DICTRA requires the input of cooling rates to simulate the time and temperature dependent phase transformation kinetics. In order to obtain a cooling rate, which resembled the actual cooling rate during casting, a simulation of solidification and cooling of the actual casting geometry was carried out in a casting process modeling software (MAGMA5) using the keel block geometry and with material properties calculated in JMatPro. The procedure for this and application examples are described in Ref. [39–41]. The resulting cooling curve was separated into three parts, each fitted by a 2nd order polynomial fit, which together resulted in the non-linear cooling curve in Figure 6.6. To analyse the effect of cooling rate on the phase distribution an additional set of four constant cooling rates were selected for input to DICTRA. These four linear cooling curves were chosen so that they matched the varying cooling conditions in the casting process modeling software (see Figure 6.6).

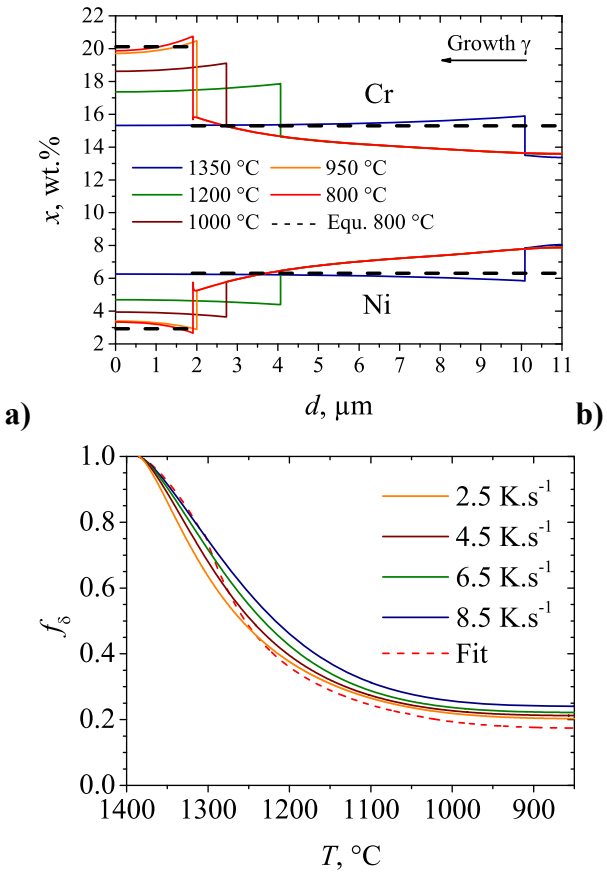

Figure 6.7: Kinetics model (a) Isothermal Cr- and Ni-content, *x*, vs. distance, *d*, determined by using kinetics modeling for the non-linear cooling curve in Figure 6. The phase-interface is at the discontinuity of the concentration profiles. The dashed lines show the global equilibrium contents of metastable ferrite and austenite at 800 °C; (b) Volume-fraction of δ-ferrite, f_δ, vs. temperature, *T*, for the cooling curves in Figure 6 (solid lines).

Solidification and cooling prediction

According to the kinetics model, the melt solidified as δ-ferrite in the solidification interval T_{liq} to T_{sol} of 1480 °C to 1449 °C. Solidification to δ-ferrite led to micro-segregation, but this was homogenized within 2 to 3 s (corresponding to a temperature change of approx. 70 °C) before austenite nucleated. Austenite then formed from δ-ferrite at 1389 °C. Because of the immediate homogenization of δ-ferrite after solidification, the choice of nucleation site, either at the left domain boundary, the right domain boundary, or the right boundary of ferrite, did not affect the nucleation and growth of austenite. Growth of austenite led to significant partitioning of the major alloying elements Cr and Ni (Figure 6.7a), which increased with further cooling. It is noted that the minor alloying elements were also subject to partitioning. The maximum transformation rate was reached at 1275 °C. Upon further cooling the transformation slowed down and 17 vol.% of δ-ferrite was retained after cooling to 800 °C (Figure 6.7b). At lower temperatures numerical instabilities were experienced.

Variation of the cooling rate

Solidification and cooling with four linear cooling rates ranging from 2.5 to 8.5 $K.s^{-1}$ were simulated to investigate the effect of the cooling rate on the ferrite to austenite transformation (Figure 6.6).

The analysis revealed that slower cooling led to lower fractions of retained δ-ferrite (Figure 6.7b). Comparison of the linear cooling curves with the modeled non-linear cooling curve showed that the maximum transformation rate of ferrite to austenite occurred between 1300 and 1200 °C.

In order to illustrate the kinetics of the described phase transformations and to demonstrate the effect of cooling-rate, the course of the transformations vs. temperature, as shown in Figure 6.7a for the non-linear cooling curve, is available for the fastest cooling rate, 8.5 $K.s^{-1}$, and the slowest cooling rate, 2.5 $K.s^{-1}$ as online material.

6.4 Discussion

The discussion focuses on the predictions of solidification and cooling obtained from the kinetics model based on the characterized microstructure in Figure 6.3a and the results from the other evaluated models. An overview of the measured and predicted solidification temperatures and solute partitioning is given in Table 6.2.

6.4.1 Microstructure evolution during solidification

The kinetics model using the non-linear cooling rate predicted, that the melt solidified entirely as δ-ferrite and the resulting micro-segregation from solidification was homogenized completely within 2 to 3 s of cooling, corresponding to approx. 70 °C, i.e. before the nucleation of austenite. Since the kinetics model simulates the diffusion in the liquid and solid, based on thermodynamic and kinetic quantities the prediction of rapid

homogenization is considered to be reliable. The Scheil model, which does not account for back-diffusion of substitutional elements into the solid, predicted severe micro-segregation, especially at the end of solidification. In the case of the present experimental casting, the Scheil model did therefore not give reasonable predictions. The keel block used here is a standard geometry used for validating mechanical properties of medium size stainless steel castings in the industry. It thus represents typical conditions for this class of commercial castings. Commercial castings vary in size and cooling conditions. In large castings diffusion distances can be much larger so that back-diffusion does not occur to any significant degree. Smaller castings will experience higher cooling rates and have a finer microstructure. The kinetics model is applicable for all casting geometries, since it in contrast to the Scheil model, simulates solidification under direct assessment of diffusion distances and cooling rates and thus takes geometrical conditions into account.

Both the kinetics model and the lever rule predicted complete solidification to δ-ferrite and subsequent nucleation of austenite, whereas the Scheil model predicted peritectic solidification, in which austenite nucleates at the interface of δ-ferrite and the melt (Figure 6.5). The deviating prediction of the Scheil model is based on the above mentioned overestimation of micro-segregation. It is apparent from Figure 6.8 that the different solidification reactions have an influence on the predicted solidus temperatures. The nucleation of austenite in peritectic solidification has a retarding effect on solidification, which is evident from the kink in the Scheil solidification curve at 92 % of solidification (Figure 6.8).

6.4.2 Microstructure evolution during cooling

Transformation kinetics and mechanisms

After solidification to δ-ferrite with almost immediate homogenization of the segregated microstructure, nucleation and growth of austenite at the last solidified material led to severe partitioning during cooling (Figure 6.7a). The maximum growth rate of austenite

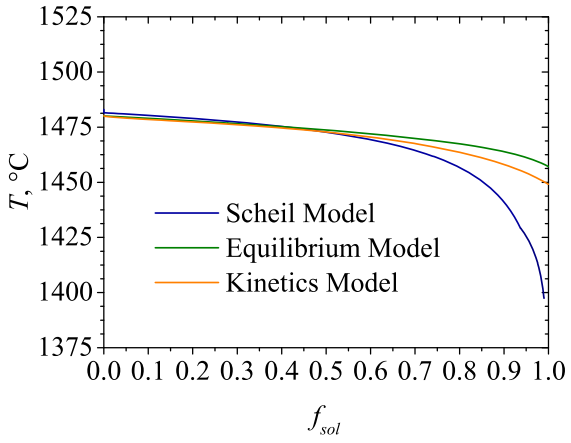

Figure 6.8: Comparison of the solidification curves, predicted by using the equilibrium model, the Scheil model and the kinetics model.

was at 1275 °C. Upon further cooling, the growth rate decreased and δ-ferrite was retained (Figure 6.7b).

The model showed, that the nucleation and growth kinetics of austenite are independent of the defined nucleation site, because of complete compositional homogenization in δ-ferrite before nucleation of austenite. Assuming that this prediction is valid, austenite is still expected to nucleate at the last solidified melt, as the interfaces of solidified δ-ferrite grains facilitate potent heterogeneous nucleation sites. Such nucleation sites would then imply that retained δ-ferrite in the microstructure in Figure 6.2a to some degree corresponds to the first solidified material. The δ-ferrite pattern could indeed correspond to the cores of partially transformed δ-ferrite dendrites, as observed for a similar microstructure in Ref. [42]. Alternatively it could resemble a cellular solidification structure, or even a microstructure that is not directly related to the solidification microstructure, but influenced by the temperature gradient during the ferrite to austenite transformation. Further research is required to accurately relate the as-cast microstructure to the solidification microstructure at high temperature.

The initial partitioning after the nucleation of austenite (*fcc)* led to enrichment of Cr and depletion of Ni in ferrite (*bcc)*. In order to achieve full transformation of δ-ferrite to austenite at lower temperature, the concentration profile is required to flatten. This requires diffusion of Cr from ferrite into austenite and diffusion of Ni from austenite into ferrite. It is well known that diffusion of Ni and Cr occurs slower in *fcc* than in *bcc* [9,43–46]. The decrease of the diffusion rate during cooling thus kinetically freezes the transformation, so that δ-ferrite is retained.

The equilibrium calculations revealed a temperature interval of approx. 400 °C for the austenite single phase region over the cooling sequence (Figure 6.5a). The strong divergence from the prediction of the equilibrium model and the characterized microstructure emphasizes, that kinetics play a vital role in the ferrite to austenite transformation during cooling, and that the equilibrium based models are thus no appropriate method to predict the as-cast microstructure.

Fraction of retained δ-ferrite and partitioning

The predicted amount of 17 vol.% retained δ-ferrite at 800 °C from the kinetics model is in reasonable agreement with the measured 11 vol.% (Figure 6.2) and the predicted concentration profile by applying the kinetics model was in excellent agreement with the measured concentration profile in the as-cast microstructure (Figure 6.9). Since the concentration gradient in austenite during cooling cannot be fully homogenized, it is retained when the transformation comes to a halt. This gradient, even though less prominent, could be measured with EDS analysis in martensite (Figure 6.9). The δ/γ-interface almost completely halted at 800 °C, which implies that no significant change in phase fraction and elemental concentration is to be expected below this temperature (Figure 6.7b).

Discrepancies between the results of the model and the measurements could be caused by the limitation of the model to a single spatial dimension, whereas heat flow, diffusion, and consequently grain growth in fact occur in three dimensions. Furthermore the δ-ferrite area fraction determined by image analysis (Figure 6.2b) was estimated to comprise a statistical error of ± 2%. The amount of predicted retained δ-ferrite by using the kinetics model would certainly have been further reduced, if N was included in the composition for the kinetics model. As previously stated, this was not possible due to numeric instability. Ma et al. in fact showed in an extensive experimental study that addition of N is an effective way of reducing the δ-ferrite content in lath martensite, which however promotes formation of Cr_2N precipitates during tempering [47]. Also the Schaeffler diagram predicted 18 % δ-ferrite without considering the addition of N, and 6 % δ-ferrite by including the effect of N, according to DeLong and Reid [33]. The latter prediction however also led to an extensive overestimation of the stable fraction of austenite.

Another simple method of predicting the composition of δ-ferrite in the as-cast microstructure for the present alloy, was by determining the Cr and Ni concentration of metastable ferrite by equilibrium calculations at 800 °C, approx. 50 °C above A_3 (Figure 6.5a). The prediction was fairly accurate, because the local equilibrium at the interface approximately followed the global equilibrium (Figure 6.7a). Further investigations are necessary to investigate, whether this method is generally applicable to other alloy systems.

6.4.3 Systematic variation of cooling rate

Slower cooling led to the prediction of less retained δ-ferrite. The transformation curves in Figure 6.7b show, that the temperature interval of 1300 to 1200 °C is of particular importance for reducing the amount of retained δ-ferrite. This becomes apparent when analyzing the transformation kinetics of the non-linear cooling rate (Figure 6.6), which

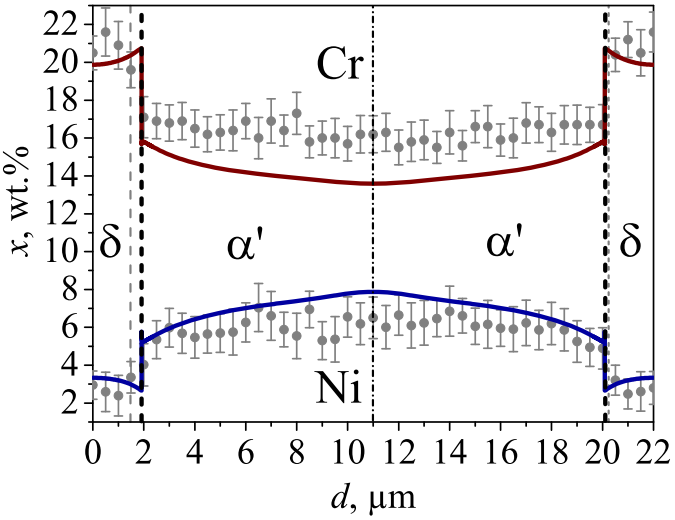

Figure 6.9: Comparison of the Cr and Ni concentration profiles predicted by kinetics modeling at 800 °C (red and blue line, respectively) and the compositional analysis of two δ-ferrite stringers and martensite by EDS analysis in Figure 6.3 (grey points).

initially is the fastest cooling rate and consequently yields the slowest transformation rate. By a decrease in cooling rate in the interval 1290 to 1200 °C rapid transformation of ferrite to austenite occurs, which results in the highest transformed fraction at the end of the simulation (Figure 6.7b). This temperature interval is approx. 100 K above the A_4 temperature, which is the temperature at which δ-ferrite becomes present as a second phase next to austenite in global equilibrium (Figure 6.5a). The fast transformation in this temperature interval is caused by the concurrent presence of a high driving force for austenite formation and sufficiently high diffusion coefficients to drive the transformation.

The influence of varying cooling rates in the range of 1 to 45 $K.s^{-1}$ on the amount of retained δ-ferrite for austenitic stainless steels of various Cr- and Ni-equivalents was investigated experimentally in Ref. [20]. It was concluded that the composition had the strongest influence on the amount of δ-ferrite. Furthermore slower cooling, when fully solidifying as δ-ferrite or in a peritectic reaction, led to smaller fractions of retained δ-ferrite. The authors concluded that the time spent in the γ+δ two phase region was responsible for this effect. This temperature region is in excellent agreement with the identified temperature interval of 1300 to 1200 °C by using kinetics modeling.

This observation has important implications for practical possibilities of homogenizing a casting, after δ-ferrite has been retained during cooling. Since the temperature region of fastest δ-ferrite to austenite transformation rate is not within the austenite single phase region and practically difficult to achieve in industrial heat-treatments, it is not possible to fully transform δ-ferrite within this region. Consequently the temperature range below A_4 has to be applied, which facilitates rather slow transformation kinetics. Thus it is of great importance to avoid the retainment of δ-ferrite from solidification and initial cooling, and kinetics modeling can be used as a tool to achieve this. Research on the application of kinetics modeling to predict the kinetics of homogenization of δ-ferrite after solidification is ongoing.

Close to 800 °C A_3 of 746 °C is approached, which corresponds to a steady increase of the driving force for ferrite formation. This may have contributed to the instability of the simulations, which were run below 800 °C.

6.4.4 Relation between domain size and cooling rate

The kinetics model predictions for a certain cooling rate were found to depend strongly on the chosen domain size. At too large domain sizes relative to the cooling rate the transformation halts before soft impingement takes place at the δ-ferrite centerline, which leads to too high predictions of the δ-ferrite phase fraction and strong concentration profiles inside the δ-ferrite.

In reality, the domain size is coupled to the cooling rate. Solidification theory states that the secondary dendrite arm spacing, which is anticipated to be directly or indirectly related to the δ-ferrite spacing, and thus half the simulation domain, is inversely

proportional to the square root of the liquid/solid interface velocity, which is determined by the cooling rate [48].

In the present analysis the measured δ-ferrite spacing of 22 μm was adequate in relation to the modelled cooling rates. Experiments to calibrate the relation between cooling rate and δ-ferrite spacing, as well as the relation of the δ-ferrite to the solidification microstructure at high temperature, are planned for future research.

6.5 Conclusion

Solidification and cooling of GX-CrNiMo-16-5-1 cast supermartensitic stainless steel were analyzed by applying the kinetics model DICTRA. The results were compared to results of empirical and thermodynamic models and validated on micrographs and EDS analysis of the as-cast microstructure of an ingot.

The main conclusions are:

(1) The kinetics model could predict the kinetics of phase transformations during solidification and cooling. It illuminated the mechanism of δ-ferrite retainment comprehensively and predicted the locally measured amount and composition of δ-ferrite and austenite after solidification and cooling reasonably well.

(2) The kinetics model predicted that micro-segregation originating from solidification is homogenized within 2 - 3 s of cooling (70 °C) after solidification, and that the impinged diffusion field of the δ-ferrite to austenite solid state transformation causes the compositional inhomogeneity in the cast microstructure.

(3) The kinetics model showed that slower cooling leads to less retained δ-ferrite. The amount of time spent between 1300 and 1200 °C was found to be most effective for transformation of δ-ferrite to austenite, which is in excellent agreement with experimental data.

(4) Calculation of the global equilibrium composition of metastable δ-ferrite at 800 °C, approx. 50 °C below A_3, was found as a simple method to predict the phase composition at room temperature for the present alloy.

(5) Soft impingement at the δ-ferrite centerline was found to be necessary for accurate predictions of the kinetics model. Therefore the model domain size needs to be calibrated in dependence of the cooling rate. This dependence might be equivalent to the relationship between the secondary dendrite arm spacing and the solidification rate in casting.

Acknowledgements

The authors would like to thank Frese Metal- & Stålstøberi A/S for providing the examined cast material. The Danish Underground Consortium is gratefully acknowledged for financial support to the Danish Hydrocarbon Research Center (DHRTC).

References

[1] G. Baggström, New Steel for Turbine Runners, Water Power. 16 (1964) 516–521.
[2] M. Grounes, S. Rao, New Alloy Steels for Nuclear Reactor Pressure Vessels and Vessel Internals, Trans. ASM. 62 (1969) 902–914.
[3] P.E. Kvaale, O. Stein, Experience with supermartensitic stainless steels in flowline applications, in: Stainl. Steel World 99, 1999: pp. 19–26.
[4] A.W. Marshall, J.C.M. Farrar, Welding of Ferritic and Martensitic 11-14% Cr Steels, Weld. World. 45 (2001) 19–42.
[5] L.M. Smith, M. Celant, Martensitic stainless steel flowlines - Do they pay?, in: Supermartensitic Stainl. Steels 1999, 1999: pp. 66–73.
[6] H.J. Niederau, A New Low-Carbon 16Cr-5Ni Stainless Martensitic Cast Steel, in: G. Behal, A.S. Melilli (Eds.), Stainl. Steel Cast., ASTM, Bal Harbour, Florida, 1982: pp. 382–393.
[7] P. Brezina, B. Sonderegger, Wärmebehandlung, Gefüge und Eigenschaften des korrosionsträgen martensitaushärtbaren Stahles X 5 CrNiMoCuNb 14 5 (14-5 PU), Härterei-Technische Mitteilungen. 33 (1978) 1–12.
[8] F. Niessen, M. Villa, D. Apel, O. Keßler, M. Reich, J. Hald, M.A.J. Somers, In situ techniques for the investigation of the kinetics of austenitization of supermartensitic stainless steel, Mater. Sci. Forum. 879 (2017) 1381–1386.
[9] F. Niessen, M. Villa, J. Hald, M.A.J. Somers, Kinetics analysis of two-stage austenitization in supermartensitic stainless steel, Mater. Des. 116 (2017) 8–15.
[10] P.D. Bilmes, M. Solari, C.L. Llorente, Characteristics and effects of austenite resulting from tempering of 13Cr–NiMo martensitic steel weld metals, Mater. Charact. 46 (2001) 285–296.
[11] Y.-K. Lee, H.-C. Shin, D.-S. Leem, J.-Y. Choi, W. Jin, C.-S. Choi, Reverse transformation mechanism of martensite to austenite and amount of retained austenite after reverse transformation in Fe-3Si-13Cr-7Ni (wt-%) martensitic stainless steel, Mater. Sci. Technol. 19 (2003) 393–398.
[12] W. Jiang, D. Ye, J. Li, J. Su, K. Zhao, Reverse Transformation Mechanism of Martensite to Austenite in 00Cr15Ni7Mo2WCu2 Super Martensitic Stainless Steel, Steel Res. Int. 85 (2014) 1150–1157.
[13] W. Jiang, K. Zhao, D. Ye, J. Li, Z. Li, J. Su, Effect of Heat Treatment on Reversed Austenite in Cr15 Super Martensitic Stainless Steel, J. Iron Steel Res. Int. 20 (2013) 61–65.
[14] A. Bojack, L. Zhao, J. Sietsma, Thermodynamic Analysis of the Effect of Compositional Inhomogeneity on Phase Transformations in a 13Cr6Ni2Mo Supermartensitic Stainless Steel, Solid State Phenom. 172–174 (2011) 899–904.
[15] G. Blanc, R. Tricot, Solidification, ségrégation et homogénéisation des aciers inoxydables austénitiques contenant de la ferrite delta, Mém. Et. Sci. Rev. Métall. 68 (1971) 735–753.
[16] P. Wang, S.P. Lu, N.M. Xiao, D.Z. Li, Y.Y. Li, Effect of delta ferrite on impact properties of low carbon 13Cr-4Ni martensitic stainless steel, Mater. Sci. Eng. A. 527 (2010) 3210–3216.
[17] S.K. Bhambri, Intergranular fracture in 13 wt% chromium martensitic stainless steel, J. Mater. Sci. 21 (1986) 1741–1746.
[18] T. Hara, H. Asahi, Effect of d-Ferrite on Sulfide Stress Cracking in a Low Carbon 13 mass% Chromium Steel., ISIJ Int. 40 (2000) 1134–1141.
[19] S.H. Kim, H.K. Moon, T. Kang, C.S. Lee, Dissolution kinetics of delta ferrite in AISI 304 stainless steel produced by strip casting process, Mater. Sci. Eng. A. 356

(2003) 390–398.
[20] O.J. Pereira, J. Beech, The effect of cooling rate and heat treatment on the d-ferrite content of cast austenitic stainless steels, Br. Founrdryman. 73 (1980) 324–329.
[21] M.A. Martorano, C.F. Tavares, A.F. Padilha, Predicting Delta Ferrite Content in Stainless Steel Castings, ISIJ Int. 52 (2012) 1054–1065.
[22] S.K.. Kim, Y.K.. Shin, N.J. Kim, Distribution of d-ferrite content in continuously cast type 304 stainless steel slabs, Ironmak. Steelmak. 22 (1995) 316–325.
[23] Q. Chen, B. Sundman, Computation of Partial Equilibrium Solidification with Complete Interstitial and Negligible Substitutional Solute Back Diffusion., Mater. Trans. 43 (2002) 551–559.
[24] P.K. Palani, N. Murugan, Comparison of regression and artificial neural network models for prediction of delta ferrite content in stainless steel claddings, Int. J. Knowledge-Based Intell. Eng. Syst. 10 (2006) 433–443.
[25] M. Vasudevan, A.K. Bhaduri, B. Raj, K. Prasad Rao, Delta ferrite prediction in stainless steel welds using neural network analysis and comparison with other prediction methods, J. Mater. Process. Technol. 142 (2003) 20–28.
[26] M.A.V. Bermejo, Predictive and Measurement Methods for Delta Ferrite Determination, Weld. J. 91 (2012) 113–121.
[27] H. Larsson, A model for 1D multiphase moving phase boundary simulations under local equilibrium conditions, Calphad Comput. Coupling Phase Diagrams Thermochem. 47 (2014) 1–8.
[28] J.R. Vilella, Delving into metal structures, Iron Age. 117 (1926) 761–763.
[29] K.V. Dahl, J. Hald, A. Horsewell, Grey-scale conversion X-ray mapping by EDS of multielement and multiphase layered microstructures., J. Microsc. 225 (2007) 31–40.
[30] A.Y. Jang, D.J. Lee, S.H. Lee, J.H. Shim, S.W. Kang, H.W. Lee, Effect of Cr/Ni equivalent ratio on ductility-dip cracking in AISI 316L weld metals, Mater. Des. 32 (2011) 371–376.
[31] H. Kokawa, T. Kuwana, A. Yamamoto, Crystallographic Characteristics of Delta-Ferrite Transformations in a 304L Weld Metal at Elevated Temperatures, Weld. J. 68 (1989) 92–101.
[32] A.L. Schaeffler, Selection of Austenitic Electrodes for Welding Dissimilar Metals, Weld. J. 26 (1947) 601–621.
[33] D.L. Olson, Prediction of Austenitic Weld Metal Microstructure and Properties, Weld. J. 64 (1985) 281–295.
[34] Thermo-Calc Software TCFE6 Steels/Fe-alloys database version 6.2, Thermo-Calc Softw. TCFE6 Steels/Fe-Alloys Database Version 6.2 (Accessed Novemb. 2009).
[35] K. Chandrasekaran, N.S. Tiedje, J. Hald, Solidification paths in modified Inconel 625 weld overlay material, Int. J. Cast Met. Res. 22 (2009) 306–310.
[36] A. Borgenstam, A. Engström, L. Höglund, J. Ågren, DICTRA, a tool for simulation of diffusional transformations in alloys, J. Phase Equilibria. 21 (2000) 269–280.
[37] M. Selleby, M. Hillert, Additional problems to the book Phase Equilibria, Phase Diagrams and Phase Transformations, Problem 3.7. Evaluation of the driving force, (2007).
[38] Thermo-Calc Software TCS Alloys Mobility Database MOB2 (accessed 08 April 1998).
[39] MAGMA5, Version 5.3 User Handbook, (2015).
[40] N.K. Vedel-Smith, J. Rasmussen, N.S. Tiedje, Thermal distortion of disc-shaped ductile iron castings in vertically parted moulds, J. Mater. Process. Technol. 217

(2015) 262–271.
[41] P. Kotas, C.C. Tutum, J. Thorborg, J.H. Hattel, Elimination of hot tears in steel castings by means of solidification pattern optimization, Metall. Mater. Trans. B Process Metall. Mater. Process. Sci. 43 (2012) 609–626.
[42] C.C. Hsieh, X. Guo, C.M. Chang, W. Wu, Dendrite evolution of delta (d) ferrite and precipitation behavior of sigma (s) phase during multipass dissimilar stainless steels welding, Met. Mater. Int. 16 (2010) 349–356.
[43] F.S. Buffington, K. Hirano, M. Cohen, Self diffusion in iron, Acta Metall. 9 (1961) 434–439.
[44] K. Hirano, M. Cohen, B.L. Averbach, Diffusion of Nickel into Iron, Acta Metall. 9 (1961) 440–445.
[45] B. Jönsson, Assessment of the Mobilities of Cr, Fe and Ni in fcc Cr-Fe-Ni Alloys, Zeitschrift Für Met. 86 (1995) 686–692.
[46] B. Jönsson, Assessment of the Mobilities of Cr, Fe and Ni in bcc Cr-Fe-Ni Alloys, ISIJ Int. 35 (1995) 1415–1421.
[47] X.P. Ma, L.J. Wang, B. Qin, C.M. Liu, S.V. Subramanian, Effect of N on microstructure and mechanical properties of 16Cr5Ni1Mo martensitic stainless steel, Mater. Des. 34 (2012) 74–81.
[48] H. Frederiksson, U. Ålkerlind, Materials Processing during Casting, Wiley, 2006.

7 Manuscript II

In situ investigation of the evolution of lattice strain and stresses in austenite and martensite during quenching and tempering of steel*

Matteo Villa[a, †], Frank Niessen[b], Marcel A.J. Somers[a]

[a] Technical University of Denmark (DTU), Department of Mechanical Engineering, Produktionstorvert building 425, 2800 Kgs. Lyngby, Denmark

[b] Technical University of Denmark (DTU), Danish Hydrocarbon Research and Technology Centre (DHRTC) , Elektrovej building 375, 2800 Kgs. Lyngby, Denmark

[†] Corresponding author

Abstract

Energy dispersive synchrotron X-ray diffraction was applied to investigate in situ the evolution of lattice strains and stresses in austenite and martensite during quenching and tempering of a soft martensitic stainless steel. In one experiment, lattice strains in austenite and martensite were measured *in situ* in the direction perpendicular to the sample surface during an austenitization, quenching and tempering cycle. In a second experiment, the $sin^2\psi$ method was applied in situ during the austenite-to-martensite transformation to distinguish between macro- and phase specific micro-stresses and to follow the evolution of these stresses during transformation. Martensite formation evokes compressive stress in austenite that is balanced by tensile stress in martensite. Tempering to 748 K (475 °C) leads to partial relaxation of these stresses. Additionally, data reveals that (elastic) lattice strain in austenite is not hydrostatic but *hkl* dependent, which is ascribed to plastic deformation of this phase during martensite formation and is considered responsible for anomalous behavior of the 200_γ reflection.

* Published work: M. Villa, F. Niessen, M.A.J. Somers, *In Situ* Investigation of the Evolution of Lattice Strain and Stresses in Austenite and Martensite During Quenching and Tempering of Steel, Metall. Mater. Trans. A 49 (2017) 1–13. The format of the published article was adapted to the format of the doctoral thesis.

7.1 Introduction

Modern steels are multi-phase materials. The response of a multi-phase material to an applied load is a function of the volume fraction, distribution, orientation and shape of the phases present [1,2], as well as of the presence and magnitude of internal stresses, which remain after processing [3]. On loading, the applied external forces are superimposed on the internal stresses [1,2].

Internal stresses can be classified by the length scale over which they equilibrate [1,4,5]. Macro-stresses (type I) act over large distances and are an average over all phases and grains present; micro-stresses vary from grain to grain and from phase to phase (type II) or within a single grain/phase (type III). Internal stress can arise as a consequence of inhomogeneous elastic and thermal properties [2,3], inhomogeneous plastic strain [2], or a phase transition occurring in association with a shape change [5].

The austenite (γ)-to-martensite (α´) transformation in steel is associated with a shape change, the so called transformation strain, which consists of a volume expansion of approx. 3% and a shear [6-9]. Additionally, austenite and martensite have different thermal and elastic properties. Thus, martensite formation is associated with the development of residual stress in the material, with contributions from the transformation itself as well as thermal mismatch [3,9].

The development of macro-stresses during quenching of steel parts is a well described subject [3-5,9,10]. Similarly, the generation of lattice defects (micro-stresses of type III) in austenite during martensite formation has been investigated in details [6-8]. On the other hand, the evolution of micro-stresses of type II is controversial: martensite formation has been reported to invoke compressive stress [11-22], tensile stress [22,23], or no stress [24-27] in austenite, while information about the stress state in the developing martensite is incomplete. The evolution of micro-stresses of type II during martensite formation is of fundamental interest because these stresses affect the transformation kinetics [28].

In the absence of macro-stresses (type I), the grain- or phase-specific micro-stresses (type II) can be evaluated from the lattice strain as experimentally determined by X-ray diffraction (XRD) [1,4] by measuring in the direction i the lattice spacing, $d_i^{hkl_\varphi}$, for a given family of lattice planes, $\{hkl\}$, in the crystalline phase φ. Comparison of the measured lattice spacing with a reference lattice spacing, $d_{ref}^{hkl_\varphi}$, provides the lattice strain, $\varepsilon_i^{hkl_\varphi}$:

$$\varepsilon_i^{hkl_\varphi} = \frac{d_i^{hkl_\varphi} - d_{ref}^{hkl_\varphi}}{d_{ref}^{hkl_\varphi}} \tag{7.1}$$

The hkl-specific strain $\varepsilon_i^{hkl_\varphi}$ represents the average lattice strain, $\langle \varepsilon^{hkl_\varphi} \rangle$, for a given family of lattice planes $\{hkl\}$ in the probed volume and can be converted into an average (hydrostatic) stress, $\langle \sigma^{\varphi} \rangle$, applying the appropriate X-ray elastic constants, XECs [4]:

$$\langle \varepsilon^{hkl_\varphi} \rangle = \left(3 \cdot S_1^{hkl_\varphi} + \tfrac{1}{2} S_2^{hkl_\varphi} \right) \cdot \langle \sigma^{\varphi} \rangle \qquad (7.2)$$

where $S_1^{hkl_\varphi}$ and $\frac{1}{2}S_2^{hkl_\varphi}$ are the XECs of phase φ for probing the family of lattice planes $\{hkl\}$.

Experimental XRD work on the evolution of lattice strain and phase-specific stresses in steel during martensite formation was firstly reported in 1957 [11]. It was suggested that a low content of retained austenite is in a state of compressive stress. In the same year, comparison of the lattice parameter of Fe-30%Ni austenite in as-received condition and after approx. 80 % transformation by sub-zero Celsius treatment did not show a significant change [24]. Therefore, it was concluded that martensite formation did not evoke micro-stresses of type II in austenite.

More than 10 years later [12], Ridley et al. reproduced the results in Ref. [11] and suggested that data could be interpreted in terms of a state of compression in austenite caused by martensite formation. Alternatively, data could indicate depletion of austenite in C during quenching and room temperature storage of the material. Nevertheless, in a study published 1 year earlier, Yeshov and Oslon followed a^{γ} during quenching of several steel samples by probing $\{200\}_\gamma$ lattice planes and showed the build-up of a tensile state of stress in austenite at the beginning of the transformation, followed by relaxation of these stresses at a later stage [23]. Remarkably, later work by the same authors [22] showed that martensite formation evokes a state of tensile lattice strain in austenite for probing $\{200\}_\gamma$, while probing $\{111\}_\gamma$ showed compression. These results seem irreconcilable. However, it should be realized that for f.c.c. metals lattice strains depend non-linearly on the applied load if strained into the plastic region [29-32]. This non-linear behavior is hkl dependent and yields anisotropic strains that are retained upon unloading. The $[200]_\gamma$ direction is elastically the most compliant and plastically the softest and therefore has the most pronounced non-linear behavior. Consequently, the 200_γ reflection is inappropriate for the evaluation of the average state of residual stress in f.c.c. metals subjected to plastic deformation. According to Refs. [29-31], probing 311_γ, or averaging lattice strains over several reflections, is most appropriate. Later, reconsidering the results in Ref. [30], it was suggested that 111_γ or 422_γ are the most appropriate reflections [32]. Evidently, an incorrect choice of the reflections probed for the evaluation of the state of stress in austenite may have played a role in the discrepancy between data.

The first serious attempt to solve the controversy appeared in 1974, when Golovchiner determined *in situ* the evolution of lattice strain in austenite versus the fraction transformed in a large number of ferrous alloys [13]. These alloys were fully austenitic at

room temperature and largely transformed to martensite during cooling to 93 K (-180 °C). Determination of a^{γ} was performed based on the 311_{γ} reflection. In all investigated samples, compression was observed in austenite after martensite formation for transformed fractions beyond 10-60 %, depending on the chemical composition of the alloy.

In 1980, the focus firstly included the state of stress in martensite [14]. It was claimed that martensite formation evoked compressive stresses in both austenite and martensite. Nevertheless, this claim violates the condition that, in absence of external forces, balancing of forces should be obtained for a finite matrix [3-5]:

$$\sum_{\varphi} f^{\varphi} \cdot \langle \sigma^{\varphi} \rangle = 0 \tag{7.3}$$

with f^{φ} volume fraction of phase φ. Hence:

$$f^{\alpha'} \cdot \langle \sigma^{\alpha'} \rangle = -f^{\gamma} \cdot \langle \sigma^{\gamma} \rangle \tag{7.4}$$

with $f^{\alpha'}$ and f^{γ} the volume fraction of martensite and austenite, respectively. Thus, compression in austenite should be balanced by tension in martensite. It is important to realize that the lattice strains determined in Ref. [14], departed from the assumption that stresses were null at the beginning of the transformation. This is unlikely for the minority phase, martensite (cf. Equ. 7.4), suggesting that the analysis may have been faulty. Additionally, data may have been affected by the presence of macro-stresses, implying that Equ. 7.2 could not be used. Unfortunately, similar arguments apply for all references cited above.

The need for more thorough stress analysis was firstly recognized in 1990 [15]. XRD was applied at room temperature to determine a_{γ} (based on 220_{γ}) in Fe-C and Fe-N thin foils. Data indicated that retained austenite experienced compressive strain in the direction perpendicular to the sample surface. To convert strain into stress, measurements were performed in various directions. Because of the shallow penetration depth of laboratory X-rays, all components of stress in martensite in the direction perpendicular to the sample surface, $\sigma_{\perp}^{\alpha'}$, were assumed equal to zero. The principal stress component parallel to the sample surface, $\sigma_{\parallel}^{\alpha'}$ was evaluated applying the $sin^2\psi$ method (cf. Ref. [4]). Data revealed that stresses in martensite were negligible within the probed volume. Since a negligible state of stress in the majority phase (i.e. martensite) does not imply that the balancing stress in the minority phase (i.e. austenite) is negligible, (cf. Equ. 7.4) compressive strain in austenite was interpreted in terms of a state of compressive stress in this phase.

The limitations associated with the shallow penetration/information depth of laboratory X-rays could be overcome by applying Neutron diffraction [25,26] or synchrotron XRD [16-20,27].

In Refs. [25,26], a^{γ} was measured in homogeneous Fe-Ni-C austenite as well as after partial transformation of the austenite into martensite. Data indicated that martensite formation did not affect a^{γ}. Similarly, San. Martin et al. followed the formation of martensite in Fe-Cr-Ni-Mo maraging steel up to 40 % fraction transformed and showed that the averaged value of a^{γ} does not change with $f^{\alpha'}$ [27]. Conversely, Villa et al. showed that martensite formation during sub-zero Celsius treatment of steel induces compressive lattice strain in austenite [16-18]. The application of the $sin^2\psi$ method ex situ indicated that lattice strain was caused by compressive stress in austenite, which was hydrostatic within the probed volume. Similarly, Epp showed that compressive hydrostatic stress build up in austenite during quenching of high C steel [19,20]. Evidently, diffraction experiments at large scale facilities did not provide a unanimous answer.

A last attempt to clarify the picture was presented in Ref. [21]. Laboratory XRD was applied to measure a^{γ} before and after martensite formation in a Fe-Ni alloy and data was complemented with measurement of a^{γ} after tempering to 523 K (250°C). Tempering is expected, at least partially, to lead to relaxation of internal stresses. Data showed that compressive lattice strain develops in austenite during martensite formation for $f^{\alpha'}$>75 %, and that this strain is largely annihilated during tempering. No strain was observed in martensite. Compressive strain in austenite was interpreted in terms of hydrostatic compressive stress in this phase.

Summarizing, no consistent picture exists of the evolution of stress in austenite and martensite during martensite formation in steel. Careful evaluation of the discussed literature reveals that during martensite formation a state of compressive stress builds-up in austenite. The compression is observed by XRD only after a threshold fraction of austenite has transformed to martensite and appears hydrostatic when averaged over the probed volume. The internal stress in austenite is interpreted as micro-stress of type II, but this hypothesis has never been verified with the simultaneous observation of balancing tensile micro-stress of type II in martensite. Tempering may promote relaxation of stresses and give indication on their actual presence. In the present work, experiments were designed to investigate the evolution of phase specific stresses in both austenite and martensite during quenching and tempering of steel.

7.2 Material and methods

The material selected for investigation was commercial EN 1.4418 steel (Table 6.1), which is a soft martensitic stainless steel grade, with a low fraction of interstitials. Martensite in this alloy is body centered cubic b.c.c. and has lath morphology [33,34]. The martensite start temperature, M_s, equals 408 K (135 °C) [34] and the Curie temperature, T_C, of martensite equals 898 K (625 °C) [34].

Two Ø10 mm x 0.15 mm disks, labelled sample 1 and sample 2, respectively, were prepared for synchrotron XRD investigation. Preparation comprised austenitization at 1223 K (950 °C) for 10 min in a continuous flow of Ar gas, followed by cooling to room

temperature at an average rate of approx. 1 K s^{-1}. Thereafter, samples were ground and electro-polished for 5 s at 40 V in Struers A-2 electrolyte. The condition of the material after preparation is labelled "as normalized".

Energy-dispersive XRD investigation was performed in situ at the EDDI beamline of the BESSY II synchrotron facility [35]. In Energy dispersive XRD, the investigation is carried out using a beam of white X-rays at a fixed diffraction angle, 2θ, and diffraction for crystallographic planes, $\{hkl\}$, will occur at a photon energy, E^{hkl}. The energy position, E^{hkl}, of the diffraction lines in the energy spectrum is inversely proportional to the interplanar spacing, d^{hkl} [36]:

$$E^{hkl} = \frac{hc}{2\sin\theta}.\frac{1}{d^{hkl}} \tag{7.5}$$

with h Planck's constant and c the speed of light. The average information depth for each diffraction line is a function of its energy, and of the diffraction geometry applied [37].

In the present investigation, the acquisition time was set to 60 s per spectrogram (i.e. diffractogram) and the experiments were conducted with a 0.5 x 0.5 mm^2 slit configuration on the primary side applying the diffraction geometry $\theta - 2\theta = 7° - 14°$. The equatorial slit aperture was set to 0.03 mm. Two configurations were applied: in the first, the scattering vector was kept perpendicular to the sample surface; in the second, the angle between the scattering vector and the surface normal, ψ, was varied by tilting the sample around an axis parallel to the plane through incident and diffracted beam ($sin^2\psi$ method). The experimental setup is presented in Figure 7.1.

Diffraction lines were fitted with pseudo-Voigt profile functions. Each reflection was analyzed independently to account for anisotropic lattice strain. A gold reference standard was used for calibration of the absolute value of the lattice parameter. The quantification of f^{γ} and $f^{\alpha'}$ was based on a direct comparison of the integrated intensity of the diffraction peaks of austenite and martensite [38]. Additional details were given in Ref. [33]. The analysis included the 200_{γ}, 220_{γ}, 311_{γ} and 222_{γ} reflections of austenite and the $200_{\alpha'}$, $211_{\alpha'}$, $220_{\alpha'}$ and $321_{\alpha'}$ reflections of martensite. The $111_{\gamma}/110_{\alpha'}$ couple was excluded because these reflections largely overlap and because these line profiles correspond to the lowest information depth among all reflections and, thus, are most sensitive for surface effects.

Table 7.1: Chemical Composition of the Steel (in Wt Pct) as determined by Optical Emission Spectroscopy.

Fe	C	N	Cr	Ni	Mn	Mo	Si	Cu	Co	P	S
Bal.	0.03	0.04	15.0	5.8	0.86	1.03	0.39	0.32	0.11	0.025	0.008

Investigation was performed in an Anton Paar DHS 1100 Domed Hot Stage under continuous flow of protective Ar gas at a constant pressure of 1.4 bar. The samples were placed on the heating element (alumina plate) onto which they were secured by mild clamping. The temperature was measured with a Pt-Pt10Rh thermocouple fixed to the stage.

The thermal cycle consisted of a quenching step, immediately followed by a tempering step and it is illustrated in Figure 7.2. During the quenching step, samples were heated to 1193 K (920 °C) at a rate of 0.25 K s^{-1}, austenitized for 180 s, and cooled to 448 K (175 °C) at the same rate. Cooling from 448 K (175 °C) to room temperature was performed at an average rate of 0.017 K s^{-1}. The tempering step consisted of heating the samples to 748 K (475 °C) at a rate of 0.25 K s^{-1} followed by continuous cooling under the

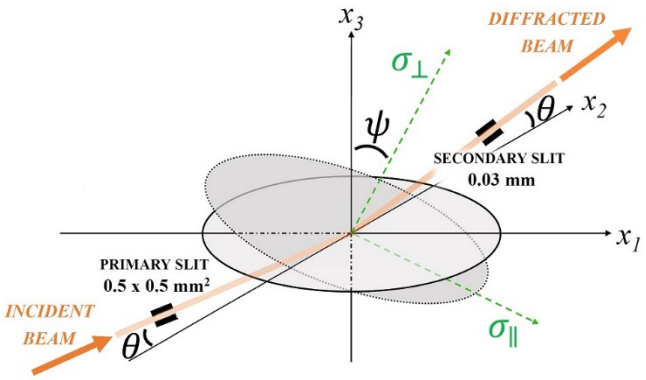

Figure 7.1: Illustration of the applied experimental setup. The scattering vector is parallel to x_3. The tilting axis is x_2. ψ is the angle between the surface normal and the scattering vector.

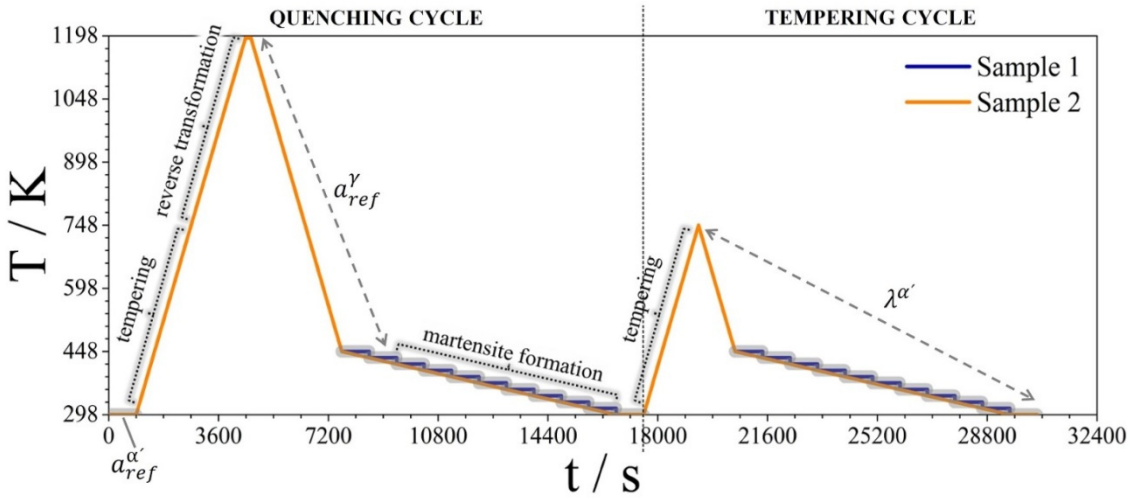

Figure 7.2: Schematic representation of the thermal cycle applied during the XRD investigation and of the various transformations occurring in the material. The graph also indicates the data which were used to estimate the reference values of the lattice parameters of austenite and martensite (see section 7.3.1).

same experimental conditions applied during quenching. The cooling steps from 448 K (175 °C) to room temperature were carried out as follows: sample 1 was cooled in steps of 15 K maintaining an overall average cooling rate of 0.017 K s^{-1} and ψ, was varied from 0° to 72° in steps of 8° at each investigation temperature (in situ $sin^2\psi$ method); sample 2 was continuously cooled at a rate of 0.017 K s^{-1} and ψ was maintained equal to 0°. Additionally, the $sin^2\psi$ method was applied ex situ at the beginning of the thermal cycle and at the end of the investigation.

7.3 Results and interpretation

7.3.1 Evaluation of lattice strains and stress analysis

The calculation of lattice strains in austenite, $\varepsilon_{\psi}^{hkl_{\gamma}}$, and martensite, $\varepsilon_{\psi}^{hkl_{\alpha'}}$, from Equ. 7.1 requires that the strain-free lattice parameter of austenite, a_{ref}^{γ}, and of martensite, $a_{ref}^{\alpha'}$, are known as a function of temperature.

The value of a_{ref}^{γ} was obtained by extrapolating a second order polynomial fitted through $a_{\perp}^{\gamma}$ (averaged over all *hkl*) as measured during cooling in the temperature interval 418-1193 K (145-920 °C), where austenite is the only phase present because T > M_s. In particular, $\lambda^{\gamma} = 1.285 \cdot 10^{-5} + 1.052 \cdot 10^{-8}\, T - 4.677 \cdot 10^{-12}\, T^2$, with T temperature expressed in K, which is consistent with literature data for austenitic stainless steels in the same temperature interval [45].

A similar experimental condition for $a_{ref}^{\alpha'}$, where martensite is the only phase present in the sample, is not available. Therefore, the value of $a_{ref}^{\alpha'}$ at 298 K (25 °C) was calculated under the condition of balancing micro-stresses of type II (cf. Equ. 7.4) at the beginning of investigation. The value of $a_{ref}^{\alpha'}$ for the temperature interval 298-898 K (25-625 °C) was calculated from $a_{ref}^{\alpha'}$ at 298 K (25 °C) and the coefficient of thermal expansion of strain-free martensite, $\lambda^{\alpha'} = 1.266 \cdot 10^{-5}\, K^{-1}$, as evaluated by fitting $a_{\perp}^{\alpha'}$ as measured during cooling tempered martensite from 748 K (475 °C) to room temperature. This is consistent with literature data for martensitic stainless steel in the same temperature interval [45]. For T>898 K (625 °C), martensite is paramagnetic and $\lambda^{\alpha'}$ evaluated for ferromagnetic martensite does no longer apply [45]. This is beyond the scope of the present work.

Lattice strains were converted into stresses. During all thermal steps where $\psi = 0$, the average stresses in the phases, $\langle \sigma^{\varphi} \rangle$, could be determined only under the assumption that the samples are free from macro-stresses (cf. Equ.7.2). Unfortunately, this assumption does not apply in the present case, as will be shown in section 7.3.3.

Table 7.2: XEC for Austenite γ and Martensite α' as Calculated Based on Refs. [40,41,44,45].

φ	γ				α'			
hkl	200	220	311	222	200	211	220	321
$-{s_1}^{hkl_\varphi}$ (10^{-6} MPa^{-1})	2.35	1.42	1.77	1.11	1.9	1.28	1.28	1.28
$\frac{1}{2}{s_2}^{hkl_\varphi}$ (10^{-6} MPa^{-1})	8.86	6.07	7.11	5.14	7.7	5.8	5.8	5.8

In a thin sample, macro-stresses can be considered relaxed, and thus equal to zero, in the direction normal to the sample surface, ⊥. In the direction parallel to the sample surface, ∥, macro-stresses balance over the sample cross section, but are not necessarily balanced within the volume of material probed by XRD, and can thus deviate from zero.

To account for the possible presence of macro-stresses, lattice strains were measured in sample 1 at several ψ angles at fixed temperature. This procedure was applied only to the part of the thermal cycle of most interest for the current investigation. Stresses were determined under the assumption of rotational symmetry within the plane of the sample and the stress components $\sigma_\parallel^\varphi - \sigma_\perp^\varphi$ and $\sigma_\perp^\varphi$ were calculated applying the $sin^2\psi$ method. Assuming that the stress is rotationally symmetric, the lattice strain is given by [4]:

$$\varepsilon_\psi^{hkl_\varphi} = S_1^{hkl_\varphi}\left[2\cdot\sigma_\parallel^\varphi + \sigma_\perp^\varphi\right] + \tfrac{1}{2}S_2^{hkl_\varphi}\cdot\sigma_\perp^\varphi + \tfrac{1}{2}S_2^{hkl_\varphi}\left[\sigma_\parallel^\varphi - \sigma_\perp^\varphi\right]\cdot sin^2\psi \qquad (7.6)$$

The XEC $S_1^{hkl_\varphi}$ and $\frac{1}{2}S_2^{hkl_\varphi}$ (Table 7.2) were calculated from the single crystal elastic constants for ferrite [39] and austenite [40]‡ applying the Eshelby/Kröner model for elastic grain interaction [41,42]§ and the material is assumed free of texture.

For Energy Dispersive XRD, and under the assumption that macro-stresses in the ⊥ direction are null, the slope of the dependence of lattice strain, $\varepsilon_\psi^{hkl_\varphi}$, on $sin^2\psi$ provides $\sigma_\parallel^\varphi - \sigma_\perp^\varphi$ while the intercept equals $S_1^{hkl_\varphi}\left[2\cdot\sigma_\parallel^\varphi + \sigma_\perp^\varphi\right] + \frac{1}{2}S_2^{hkl_\varphi}\cdot\sigma_\perp^\varphi$. The equations for slope and intercept provide the set of equations to assess the individual values of $\sigma_\parallel^\varphi$ and $\sigma_\perp^\varphi$, provided that the XECs are known. The macro-stress $\sigma_\parallel^\varphi - \sigma_\perp^\varphi$ (of type I) in phase φ

‡ The bulk elastic modulus of austenite, B^γ, and of martensite, B^α calculated from Refs. [51,52] are 184 GPa and 167 GPa, respectively. From Ref. [56], for Fe-15%Cr-5%Ni B^γ =164 GPa and is not significantly affected by the presence of interstitials.[57] This indicates that Ref. [52] most likely overestimated the stiffness of austenite. No accurate information is available to evaluate the value of B^α from Ref. [51].

§ It should be noted that the Eshelby/Kröner model for the present case is an approximation, as it assumes elastic interaction of crystals with identical elastic constants, while the present material is two phase with different elastic constants for the two phases.

corresponds to an *hkl*-dependent depth, ζ^{hkl}, and $\sigma_{\perp}^{\varphi}$ represents the average micro-stresses of type II in φ. From Equ. 7.3 it is obtained:

$$\sum_{\phi} \mathrm{f}^{\varphi} \cdot \langle \sigma_{\perp}^{\varphi} \rangle = 0 \tag{7.7}$$

where $\langle \sigma_{\perp}^{\varphi} \rangle$ represents the stress averaged over all investigated hkl for phase φ.[**]

In the present case, ζ^{hkl}can be estimated using the absorption coefficient of Fe for the appropriate energy and equals to approx. 4 µm, 5 µm, 14 µm, 22 µm and 25 µm for the 111_{γ}, 200_{γ}, 220_{γ}, 311_{γ} and 222_{γ} reflections of austenite, respectively, and approx. 4 µm, 10 µm, 18 µm, 27 µm and 55 µm for the $110_{\alpha'}$ $200_{\alpha'}$, $211_{\alpha'}$, $220_{\alpha'}$ and $321_{\alpha'}$ reflections of martensite, respectively.

7.3.2 Evolution of phase fraction and lattice strain during thermal cycling

Phase fraction

The evolution of the fraction of martensite as measured for diffraction vector perpendicular to the surface, $f_{\perp}^{\alpha'}$, is shown in Figure 7.3a versus temperature, T. Data plotted in Figure 7.3a represents the average value over the two investigated samples and is only representative of the fraction of martensite in the material, $f^{\alpha'}$, for the (unlikely) assumption of random grain orientation [46].

At the beginning of the investigation $f_{\perp}^{\alpha'}$ is 0.93 (Figure 7.3a). During heating, reverse austenite formation starts at about 823-848 K (550-575 °C). Austenitization proceeds in two steps and is completed just below 1193 K (920 °C). Two-step kinetics of reverse austenite formation in soft martensitic stainless steel is discussed in detail elsewhere [33,34,47]

On cooling from the austenitization temperature, martensite is firstly observed at 703 K (330 °C), approx. 200 K above M_S, by appearance of the $110_{\alpha'}$ line profile, which is probed at the lowest average information depth of all hkls. On continued cooling, the intensity of $110_{\alpha'}$ increases and is accompanied by $200_{\alpha'}$, $211_{\alpha'}$, $220_{\alpha'}$ and $321_{\alpha'}$ in the order of mentioning, consistent with a gradual increase of the information depth ζ^{hkl}. Evidently, martensite formation starts at 703 K (330 °C) in the near surface region and progresses in the depth direction on continued cooling. It has repeatedly been reported that the formation of lath martensite starts at the free surface at a temperature significantly higher than M_S [47-52]. The present results are fully consistent with these observations.

[**] The multiplicity of the various hkl was not taken into account, implying that all reflections was equally weighted.

The martensite content $f_{\perp}^{\alpha'}$ exceeded 0.03 at about 403 K (130 °C), which is below M_s. Thereafter, on continued cooling, a large fraction of martensite formed within the temperature range 383-353 K (115-85 °C) followed by martensite formation at a progressively reduced rate. At 298 K (25 °C), about 93 % of the austenite had transformed into martensite, consistent with the starting condition.

Upon quenching, the material was tempered to 748 K (475 °C) without affecting the fraction of martensite in the sample.

Lattice strains

The lattice parameters calculated from the lattice spacing for {hkl} are given for austenite in Figure 7.3b and for martensite in Figure 7.3c. The evolutions of lattice strains in these phases are described separately below.

Austenite: At the beginning of the quenching cycle, a^{γ} was significantly smaller than a_{ref}^{γ} (given by the drawn blue line) and varies with the hkl probed, which indicates that austenite experiences anisotropic compressive lattice strain in the direction $\perp$.

On heating, a^{γ} expands at a (hkl-dependent) rate which deviates from the value expected from the thermal expansion coefficient λ_{γ}, indicating changes in lattice strain, $\varepsilon_{\perp}^{hkl_{\gamma}}$. Compressive lattice strains $\varepsilon_{\perp}^{hkl_{\gamma}}$ increase up to 523 K (250 °C), decrease in the temperature range 523-748 K (250-475 °C), where after they increase again up to 798 K (525 °C), and eventually are annihilated at about 848 K (575 °C), when the reverse austenite formation commences.

On cooling, $a^{\gamma} = a_{ref}^{\gamma}$ for $T \geq 418\,K$ (145 °C) (by definition), implying that $\varepsilon_{\perp}^{hkl_{\gamma}} = 0$. Thereafter, for temperatures below M_s, $a^{\gamma} < a_{ref}^{\gamma}$, which indicates that martensite formation is accompanied by compressive lattice strain in austenite in the direction perpendicular to the surface. The observed lattice strain is largest at 298 K (25 °C) and depends on hkl: the largest $\varepsilon_{\perp}^{hkl_{\gamma}}$ is observed for 220_{γ} and 222_{γ}, while $\varepsilon_{\perp}^{hkl_{\gamma}}$ is negligible for 200_{γ} and for 311_{γ} it shows a value close to the average over hkl. This behaviour for the various hkl is analogous to the dependence on hkl for the starting condition.

On tempering, the evolution of $\varepsilon_{\perp}^{hkl_{\gamma}}$ during heating to 748 K (475 °C) reflects the same trends as on heating the "as normalized" condition. On reaching 748 K (475 °C), about half the compressive lattice strain evoked in austenite during quenching has relaxed, assuming that no change in composition occurred. On cooling to 298 K (25 °C), no additional changes of $\varepsilon_{\perp}^{hkl_{\gamma}}$ are observed. Data is largely consistent with recent work in the literature [53], and indicates that residual stresses in austenite are partially relaxed during tempering of martensitic stainless steel to 748 K (475 °C).

Martensite: At the beginning of the investigation, $a^{\alpha'} \approx a_{ref}^{\alpha'}$, which implies that $\varepsilon_{\perp}^{\alpha'} \approx 0$.

On heating, the measurement of $a^{\alpha'}$ shows four distinct regimes:

- for T<423 K (150 °C), the rate of expansion of the unit cell of martensite is consistent with $\lambda_{\alpha'}$;
- for the temperature range 423-748 K (150-475 °C), $a^{\alpha'}$ expands at a rate that varies with hkl and in general is smaller than $\lambda_{\alpha'}$;
- for temperatures in the range 748-898 K (475-625 °C) a significant difference between $a^{\alpha'}$ and $a_{ref}^{\alpha'}$ yields a large deviation between the observed and predicted lattice parameter at 898 K (625 °C);
- at 898 K (625 °C), martensite becomes paramagnetic and $\lambda_{\alpha'}$ increases significantly.

On cooling, martensite reflections have sufficient intensity for a temperature of 403 K (130 °C), when approx. 5 % of the austenite has transformed. For fractions up to $f_{\perp}^{\alpha} \approx 0.2$, data scatters significantly. For martensite fractions beyond 0.2, the lattice strain in martensite varies significantly depending on the probed hkl. On average, $a_{\perp}^{hkl_{\alpha'}} < a_{ref}^{\alpha'}$ and about constant over the whole transformation process.

During tempering, the evolution of $a_{\perp}^{\alpha'}$ on heating to 748 K (475 °C) is consistent with the data obtained on heating the sample "as normalized" and the lattice of martensite expands less than predicted based on $\lambda_{\alpha'}$ in the temperature interval 448-748 K (175-475 °C). This deviation is retained on subsequent cooling to 298 K (25 °C).

Data acquired during the two heating steps indicates that tempering of martensite proceeds in two stages in this alloy: the first stage extends from 423 K (150 °C) to 623 K (350 °C); the second stage from 748 K (475 °C) to 898 K (625 °C). Data is consistent with previous work in the literature [53] and could either be interpreted in terms of the introduction of compressive lattice strains, $\varepsilon_{\perp}^{hkl_{\alpha'}}$, in martensite or as the rejection of C and N from solid solution. Applying the unit cell volumes for Fe-C and Fe-N martensite from Ref. [15],[††] and assuming that $\varepsilon_{\perp}^{hkl_{\alpha'}}$ is not affected by tempering, the observed differences between the variation of $a_{\perp}^{\alpha'}$ with temperature and $\lambda_{\alpha'}$ would correspond to the rejection of approx. 0.03 wt% C+N during the first stage of tempering and 0.04 wt% C+N during the second stage. These values are considered realistic taking into account the alloy composition (cf. Table 7.1), and imply that the effect of tempering on $a_{\perp}^{\alpha'}$ can mainly have its origin in a change of the content of interstitials in solid solution in martensite.

[††] Note that the relative difference between the effects of C and N (in wt%) on the unit cell volume of martensite is <3 %, and can be neglected within the experimental accuracy indicated in Ref. [15].

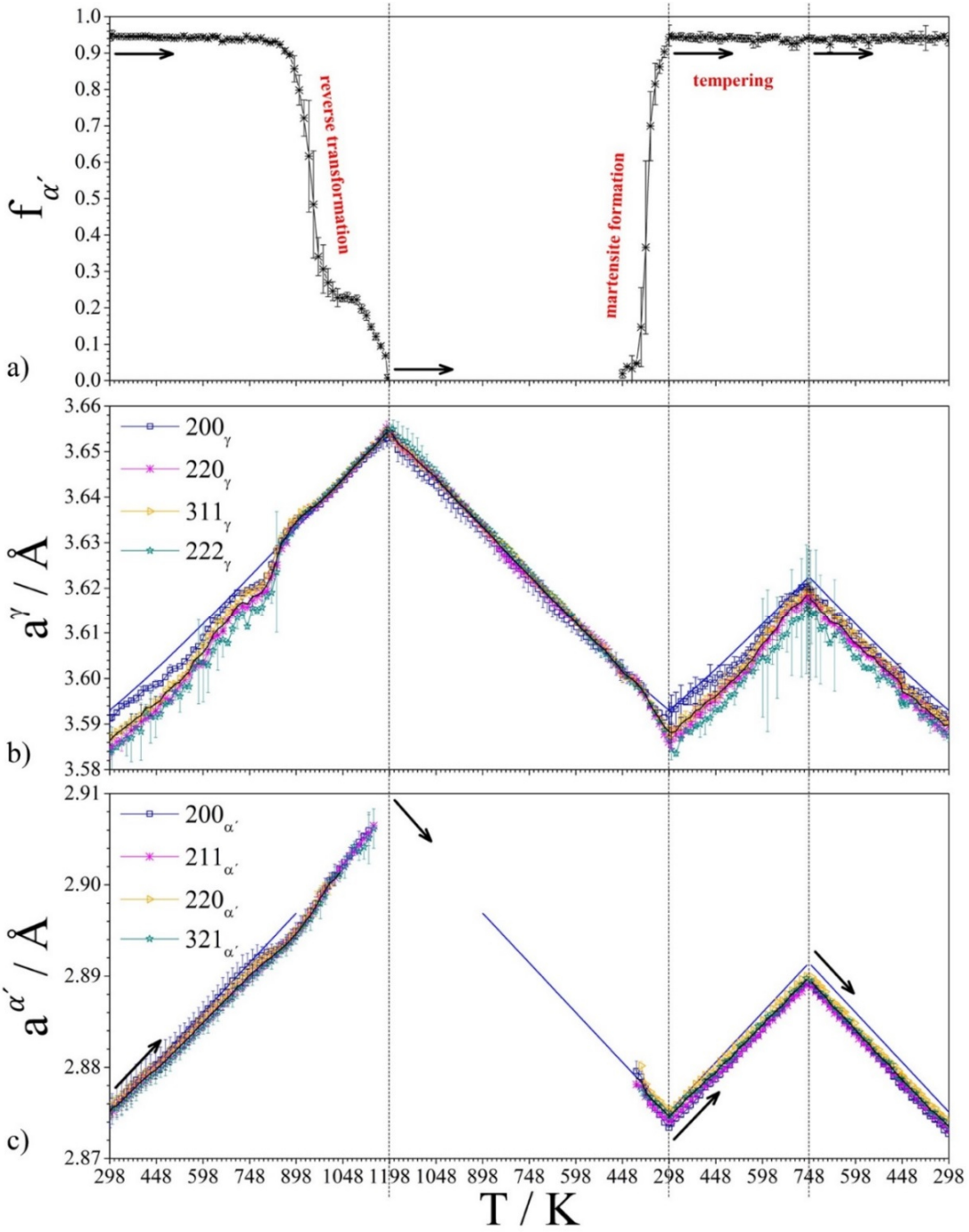

Figure 7.3: (a) Fraction of martensite evaluated in the direction normal to the sample surface $f_{\perp}^{\alpha'}$ plotted versus temperature T (values represent average values for sample 1 and sample 2; the error bars are the standard deviation); b) lattice parameter of austenite measured in the direction normal to the sample surface $a_{\perp}^{\gamma}$ plotted versus temperature T; c) lattice parameter of martensite measured in the direction normal to the sample surface $a_{\perp}^{\alpha'}$ plotted versus temperature T. The blue continuous lines in b) and c) represent the strain free lattice parameter of the phases a_{ref}^{φ}. The black continuous lines in b) and c) show the value of the lattice parameter of the phases a_{ref}^{φ} averaged over the probed reflections, not including $200_{\alpha'}$. In order to compare between the two data sets, 1 data point every 15 K is considered for sample 2 when cooled within the temperature range 298 K<T<448 K (25 °C<T<175 °C).

7.3.3 State of stress – sample 1

"As normalized" condition

In the normalized condition the steel contains a martensite fraction $f^{\alpha'} = 0.95$; the rest is retained austenite. Representative values of a^{γ} and $a^{\alpha'}$, determined from various hkl are presented as a function of ψ in Figure 7.4a and Figure 7.5a, respectively. Some data points at high ψ angles were excluded because the diffracted intensity was insufficient for accurate peak fitting.

Figure 7.4a shows that, within experimental accuracy, a^{γ} is independent of ψ, indicating that the state of stress is effectively hydrostatic (or, trivially, nil), but depends on hkl. Comparing a^{γ} with a^{γ}_{ref} (the latter as represented by the solid blue line in Figure 7.4a) reveals that austenite experiences a hkl dependent compressive lattice strain. Compressive strain is largest for 220_{γ} and 222_{γ}, very small for 200_{γ}, while compression for 311_{γ} is close to the value obtained from averaging over all measured hkl. Stress analysis yields $\sigma^{\gamma}_{\parallel} - \sigma^{\gamma}_{\perp} \approx 0$ and $\sigma^{\gamma}_{\perp}$ equal to -0.21 GPa, -1.22 GPa, -0.85 GPa and -1.29 GPa for probing 200_{γ}, 220_{γ}, 311_{γ} and 222_{γ}, respectively, giving an average stress value $\langle\sigma^{\gamma}\rangle = -0.89$ GPa. It is noted that the order of increasing lattice strain (and associated elastic residual stress), coincides with an increase of the orientation parameter $3\Gamma = 3 \cdot \frac{h^2k^2+k^2l^2+l^2h^2}{(h^2+k^2+l^2)^2}$, which varies from 0 for 200_{γ} to 1 for 222_{γ} and for $311_{\gamma}$is about half-way the range ($3\Gamma = 0.47$) , consistent with 311_{γ} representing the average over all *hkl*. This would suggest that the observed differences for the probed hkls are a consequence of elastic anisotropy in austenite. This contrasts with the zero slope in Figure 7.4a., because for a hydrostatic state of stress no dependence of (elastic) lattice strain over hkl would be expected. In fact, $\left[3 \cdot s_1^{hkl_{\varphi}} + \frac{1}{2}s_2^{hkl_{\varphi}}\right]$, cf. Equ. 7.1, is independent of hkl, as can be verified for the data in Table 7.2. Evidently, the state of stress in austenite is hydrostatic within the probed volume, but not necessarily hydrostatic over the length scale of a single austenite grain (cf. Refs. [19,20]).

Figure 7.5a shows that $a^{\alpha'}$ evaluated from $211_{\alpha'}$, $220_{\alpha'}$ and $321_{\alpha'}$ neither varies with ψ nor with hkl within experimental accuracy. In contrast, the $sin^2\psi$ dependence of $a^{\alpha'}$ derived from $200_{\alpha'}$ is characterized by oscillations (cf. Ref. [4]) and therefore excluded from the analysis. Stress analysis based on $211_{\alpha'}$, $220_{\alpha'}$ and $321_{\alpha'}$ showed that $\sigma^{\alpha'}_{\parallel} - \sigma^{\alpha'}_{\perp} \approx 0$. The average phase specific (hydrostatic) stress in martensite calculated with Equ. 7.4 is $\langle\sigma^{\alpha'}\rangle = 0.04$ GPa.

Stress developing on martensite formation

Representative examples of lattice parameter a^{φ}_{ψ} versus $sin^2\psi$ data, as obtained with in situ application of the $sin^2\psi$ method, are reported in Figure 7.4b-e and Figure 7.5b-e.

Stress values were derived from such a_{ψ}^{φ} versus $sin^2\psi$ relations, applying the XECs from Table 7.2. The stress values obtained are given in Figure 7.6 and Figure 7.7 as a function

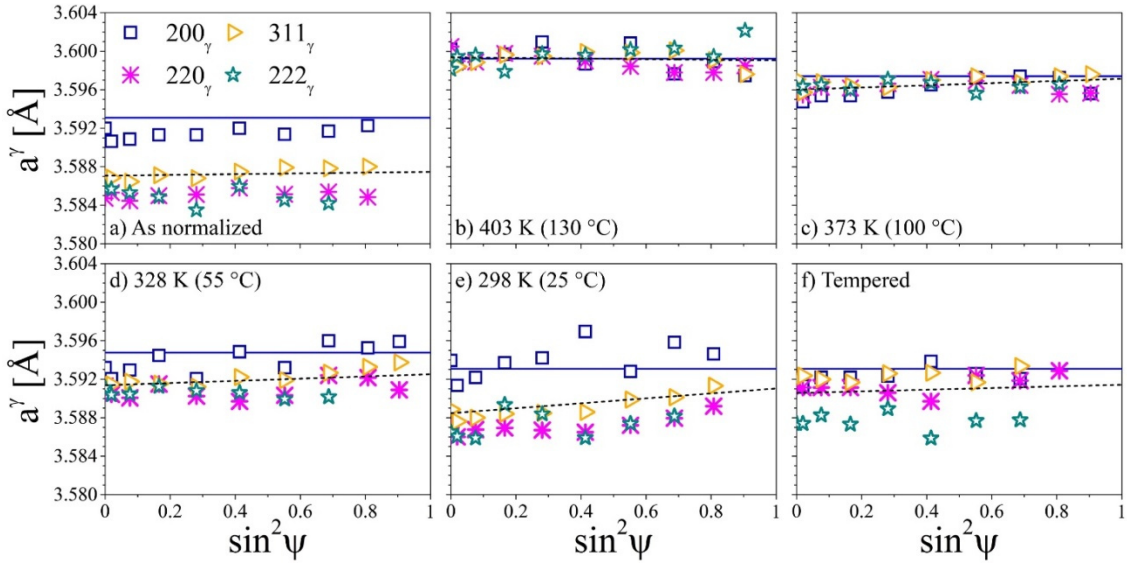

Figure 7.4: Lattice parameter of austenite a^{γ} evaluated from 200_{γ}, 311_{γ}, 220_{γ} and 222_{γ} and plotted versus $sin^2\psi$. Data acquired: (a) at the beginning of the investigation; (b) at 403 K (130 °C) during quenching; (c) at 373 K (100 °C) during quenching; (d) at 328 K (55 °C) during quenching; (e) at the end of the quenching cycle; (f) at room temperature after tempering to 748 K (475 °C). The blue continuous lines represent the strain-free lattice parameter of austenite a_{ref}^{γ}. The black dashed lines were obtained by linear regression among a^{γ} values averaged over the probed hkl.

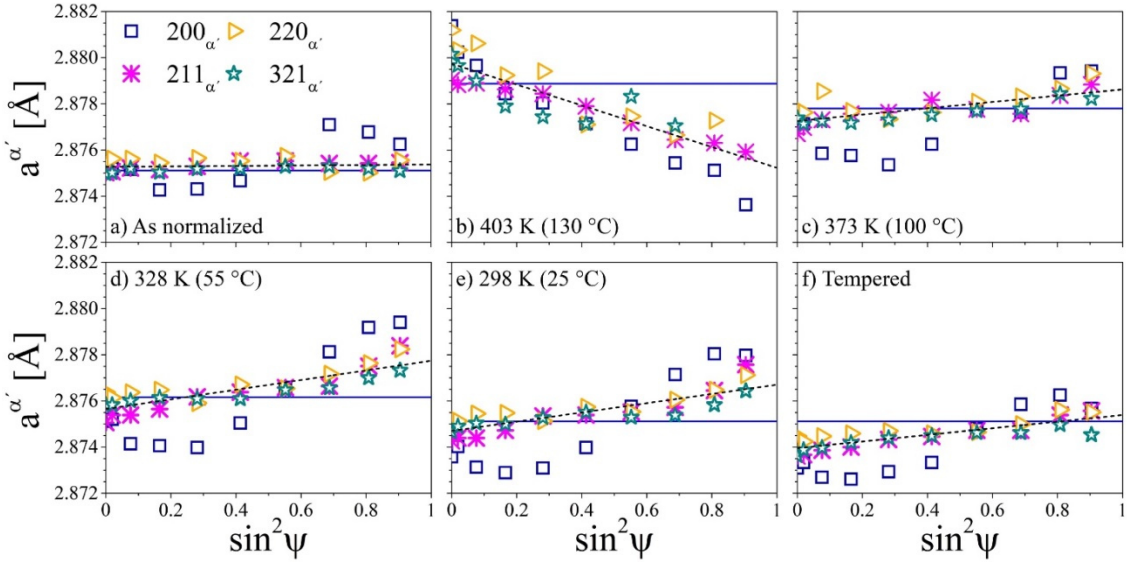

Figure 7.5: Lattice parameter of martensite $a^{\alpha'}$ evaluated from $200_{\alpha'}$, $211_{\alpha'}$, $220_{\alpha'}$ and $321_{\alpha'}$ and plotted versus $sin^2\psi$. Data acquired: (a) at the beginning of the investigation; (b) at 403 K (130 °C) during quenching; (c) at 373 K (100 °C) during quenching; (d) at 328 K (55 °C) during quenching; (e) at the end of the quenching cycle; (f) after tempering to 748 K (475 °C). The blue continuous lines represent the strain free lattice parameter of martensite $a_{ref}^{\alpha'}$. The black dashed lines were obtained by linear regression among $a^{\alpha'}$ values averaged over the probed hkl, excluding $200_{\alpha'}$.

of $f^{\alpha'}$. The fraction of transformed austenite was determined by averaging the values of $f_{\psi}^{\alpha'}$ measured at all the applied tilting angles, ψ. This procedure reduces significantly the uncertainty caused by crystallographic texture [46]. Figure 7.6a and Figure 7.7a show the stresses in austenite and martensite as determined in the ⊥ direction. These stresses are interpreted as phase specific micro-stresses of type II. Figure 7.6b and Figure 7.7b illustrate the difference between the stress components in the ∥ and ⊥ directions versus $f^{\alpha'}$. These stresses are interpreted as macro-stresses of type I, for austenite (Figure 7.6a) and martensite (Figure 7.7a), respectively.

From Figure 7.4, it follows that as long as martensite is the minority phase in the sample, i.e. for $T \geq 388\,K$ (115 °C), the lattice parameter for austenite is about the reference value, $a_{\psi}^{\gamma} \approx a_{ref}^{\gamma}$, implying that $\varepsilon_{\psi}^{hkl_{\gamma}} \approx 0$ (Figure 7.4b). At 373 K (100 °C), a small compressive lattice strain develops in austenite (Figure 7.4c). This lattice strain increases on further cooling (Figure 7.4c-e) and is most pronounced at 298 K (25 °C) (Figure 7.4e). The lattice strain does not depend significantly on ψ, but it does vary with hkl. The variation among the various $\varepsilon_{\psi}^{hkl_{\gamma}}$ increases during continuous cooling and, analogously, is most pronounced at 298 K (25 °C) (Figure 7.4e). Stress analysis reveals that compressive stress of type II builds up in austenite for $f^{\alpha'} > 0.2$ (Figure 7.6a). Compressive stress increases steadily with a reduction of the austenite fraction and depends on the $\varepsilon_{\psi}^{hkl_{\gamma}}$ from which it is evaluated.

After quenching, $\sigma_{\perp}^{\gamma}$ equals $+0.23$ GPa, -0.86 GPa, -0.54 GPa and -0.86 GPa when evaluated from 200_{γ}, 220_{γ}, 311_{γ} and 222_{γ}, respectively, and $\langle\sigma_{\perp}^{\gamma}\rangle = -0.51$ GPa.

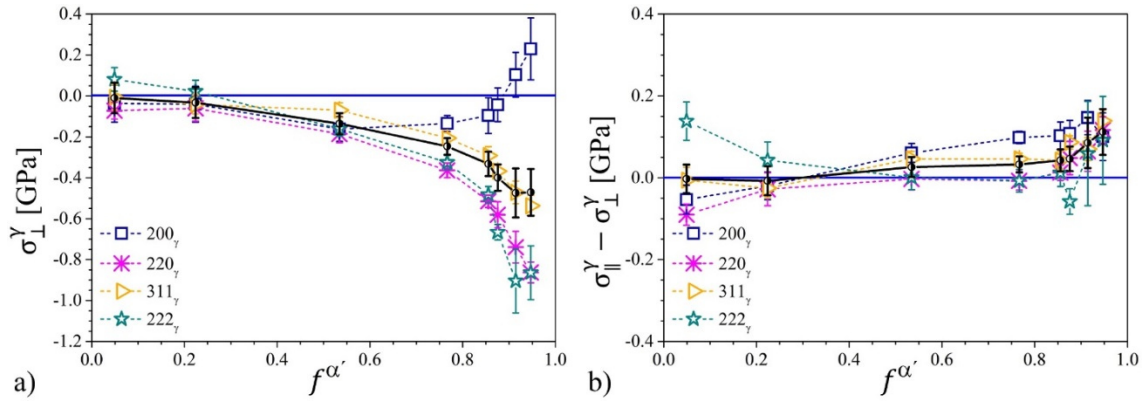

Figure 7.6: State of stress in austenite evaluated from lattice strains obtained for 200_{γ}, 220_{γ}, 311_{γ} and 222_{γ} and plotted versus the fraction of martensite formed $f^{\alpha'}$: a) stress component in the direction perpendicular to the sample surface $\sigma_{\perp}^{\gamma}$; b) difference between the stress components parallel and perpendicular to the sample surface $\sigma_{\parallel}^{\gamma} - \sigma_{\perp}^{\gamma}$. The black lines and symbols represent the state of stress averaged over all probed reflections. Error bars indicate the standard error of the estimate for linear regression of data in Figure 7.2. An additional experimental error related to the alignment of the diffractometer is estimated in the order of ± 30 MPa.

The atypical behaviour of 200_γ cannot be explained solely in terms of elastic anisotropy in austenite (see previous paragraph). This behavior is consistent with observations in the literature on the influence of plastic accommodation of the volume changes on the suitability of *hkl* for the determination of residual stresses in f.c.c. metals [29-32] and strongly suggests that plastic deformation has occurred in austenite during martensite formation.

During the transformation, the state of stress in (untransformed) austenite is close to hydrostatic within the probed volume (i.e. $\sigma_\parallel^\gamma - \sigma_\perp^\gamma \ll \sigma_\perp^\gamma$) . However, measurable macro-stress is present, as reflected by $\sigma_\parallel^\gamma \neq \sigma_\perp^\gamma$ (Figure 7.6b). At the beginning of the transformation, $\sigma_\parallel^\gamma > \sigma_\perp^\gamma$ as evaluated from $\varepsilon_\psi^{222_\gamma}$, which, among the probed γ reflections, offers the largest information depth. Probing the other hkl at shallower information depths it is found that $\sigma_\parallel^\gamma \leq \sigma_\perp^\gamma$. Along with an increase of the fraction of martensite, a small tensile macro-stresses, i.e. $\left(\sigma_\parallel^\gamma > \sigma_\perp^\gamma\right)$, builds up for $f^{\alpha'} > 0.2$.

Figure 7.5 shows that $a_\psi^{\alpha'}$ was linearly dependent on $sin^2\psi$ at $T = 403\ K$ (130 °C), i.e. just below M_s (Figure 7.5b). The slope of $a_\psi^{\alpha'}$ versus $sin^2\psi$ is negative. Upon cooling to T=373 K (100 °C), the slope of $a_\psi^{\alpha'}$ versus $sin^2\psi$ reverts to positive (Figure 7.5c) and a non-linear dependence of $a_\psi^{\alpha'}$ on $sin^2\psi$ is observed for $200_{\alpha'}$, reflecting the oscillations in the $a_\psi^{\alpha'}$ vs. $sin^2\psi$ distribution in the "as normalized" condition (Figure 7.5a). On continuous cooling to 298 K (25 °C), $a_\psi^{\alpha'}$ shrinks at a rate commensurate with the thermal expansion coefficient $\lambda_{\alpha'}$ and $\varepsilon_\psi^{hkl_{\alpha'}}$ does not vary significantly with hkl (Figure 7.5c-e).

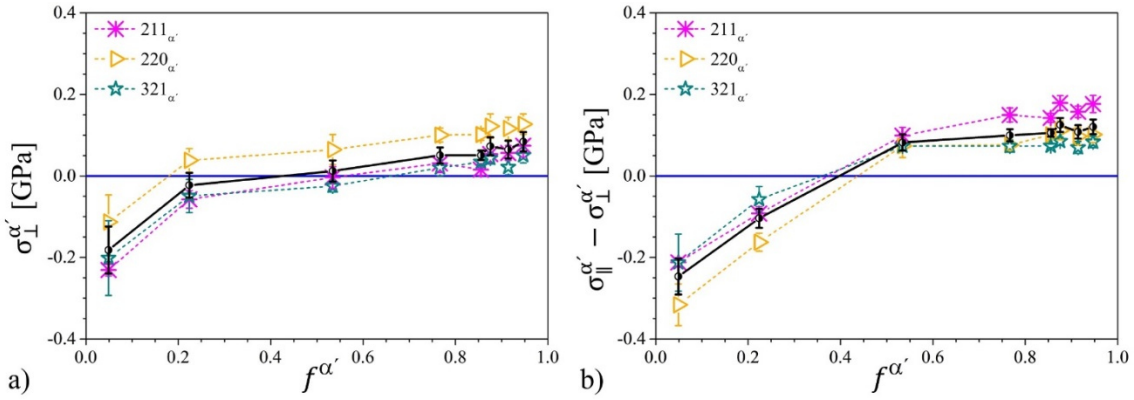

Figure 7.7: State of stress in martensite evaluated from lattice strains obtained for $200_{\alpha'}$, $211_{\alpha'}$, $220_{\alpha'}$ and $321_{\alpha'}$ and plotted versus the fraction transformed $f^{\alpha'}$: a) stress component in the direction perpendicular to the sample surface $\sigma_\perp^{\alpha}$. b) difference between the stress components parallel and perpendicular to the sample surface $\sigma_\parallel^{\alpha'} - \sigma_\perp^{\alpha'}$. The black lines and symbols represent the state of stress averaged over all probed reflections apart from 200_α. Error bars indicates the standard error of the estimate for linear regression of data in Figure 7.2. An additional experimental error related to the alignment of the diffractometer is estimated in the order of ± 30 MPa.

Stress evaluation reveals that martensite experiences an average compressive stress at the beginning of the transformation, which reverts into an average tensile stress for $f^{\alpha'} > 0.5$ (Figure 7.7a). The state of stress is not particularly sensitive to the hkl used for probing the lattice strain. Finally, after quenching, $\langle \sigma_{\perp}^{\alpha'} \rangle = +0.08\ GPa$.

Figure 7.7b also indicates the presence of macro-stresses. At the beginning of the process, macro-stresses are compressive and significant, approx. $-0.25\ GPa$. With increasing martensite content, compression decreases and is reversed into tensile macro-stress for $f^{\alpha'} > 0.2$.

The tempered condition

The values of $a_{\psi}^{hkl_{\gamma}}$ and $a_{\psi}^{hkl_{\alpha'}}$ are shown as a function of $sin^2\psi$ in Figure 7.4f and Figure 7.5f, respectively. The fraction of martensite in the sample is $f^{\alpha'} = 0.95$, consistent with the "as normalized" and "as quenched" conditions. The result in Figure 7.4f shows that $a_{\psi}^{hkl_{\gamma}}$ varies with hkl, but not with ψ. Comparison of a^{γ} with a_{ref}^{γ} reveals that lattice strain evaluated from 200_{γ} and 311_{γ} is negligibly small, whereas $\varepsilon^{222_{\gamma}} \ll 0$. Stress analysis shows that $\sigma_{\perp}^{\gamma}$ is -0.07GPa, -0.23 GPa, -0.08 GPa and -0.86 GPa when evaluated based on 200_{γ}, 220_{γ}, 311_{γ} and 222_{γ}, respectively. The stress is approximately hydrostatic within the probed volume, with $\langle \sigma_{\perp}^{\gamma} \rangle = -0.31$ GPa and $\sigma_{\parallel}^{\gamma} - \sigma_{\perp}^{\gamma} = +0.04$ GPa. The hkl-dependent lattice strain suggests that a hydrostatic state of stress does not apply at the length scale of a single austenite grain.

Figure 7.5f shows that $a_{\psi}^{hkl_{\alpha'}}$ evaluated from $211_{\alpha'}$, $220_{\alpha'}$ and $321_{\alpha'}$ is a linear function of $sin^2\psi$ but does not vary with hkl; $a_{\psi}^{200_{\alpha'}}$, instead, shows a $sin^2\psi$ dependence characterized by oscillations as earlier reported for the material in "as normalized" and "as quenched" conditions. Stress analysis was based on $211_{\alpha'}$, $220_{\alpha'}$ and $321_{\alpha'}$.Under the assumption that the chemical composition of the martensite has not changed during tempering it is obtained $\langle \sigma_{\perp}^{\alpha'} \rangle = -0.09$ GPa and $\sigma_{\parallel}^{\alpha'} - \sigma_{\perp}^{\alpha'} = +0.08$ GPa.

Nevertheless, the material is almost fully martensitic during tempering. A significant variation of $\langle \sigma_{\perp}^{\alpha'} \rangle$ from $\langle \sigma_{\perp}^{\alpha'} \rangle = 0.08$ GPa before to tempering to $\langle \sigma_{\perp}^{\alpha'} \rangle = -0.09$ GPa after tempering would imply an enormous (about 3 GPa) balancing variation in $\langle \sigma_{\perp}^{\gamma} \rangle$, (cf. Equ. 7.7), which is not confirmed by the experimental data. Evidently, the shrinkage of the martensite lattice from the "as quenched" to the "tempered" condition is not due to a change of $\langle \sigma_{\perp}^{\alpha'} \rangle$, but has its origin in a change in chemical composition. The measured change in the lattice parameter corresponds to expelling approx. 0.03 wt% C+N from solid solution in martensite during tempering to 748 K (475 °C).

7.4 Discussion

7.4.1 Partitioning of stresses in austenite and martensite during martensite formation

Historically, the evolution of the phase specific stresses, $\langle\sigma^{\varphi}\rangle$, in austenite and martensite during the austenite-to-martensite transformation has been investigated by measuring the evolution of the phase specific strain, ε^{φ}, as a function of the corresponding phase fraction, f^{φ}, either in a single direction [14,16-18,22,23], or in a set of directions (approx.) normal to the incident beam [19,20,27]. These investigations departed from the hypothesis that macro-stresses are negligible within the volume probed by XRD.

In the present work, the evolution of stress in the material during martensite formation including the separation of macro- and micro-stresses was investigated in situ for the first time (sample 1). To verify whether the measured lattice strains in austenite can be ascribed to (micro-)stresses of type II, a balancing of average stress values in the phases in the sample (cf. Equ. 7.7) with $f^{\alpha'}$ was considered. The results of this verification for the stress values presented in Figure 7.6a and Figure 7.7a are shown in Figure 7.8a.

Figure 7.8a shows that, within experimental accuracy, internal balance of average stresses is satisfied from the onset of the transformation to its completion. At the beginning of the transformation martensite is the minority phase and experiences significant phase specific compressive (micro-)stress of type II, which is balanced by very small tensile (micro-)stress of type II in the dominating austenite. During martensite formation, the state of stress in the phases reverses. For $f^{\alpha} > 0.2$, tension builds up in martensite and compression develops in austenite. At the end of the transformation, significant compressive (micro-)stress of type II in austenite is balanced by small tensile (micro-)stress

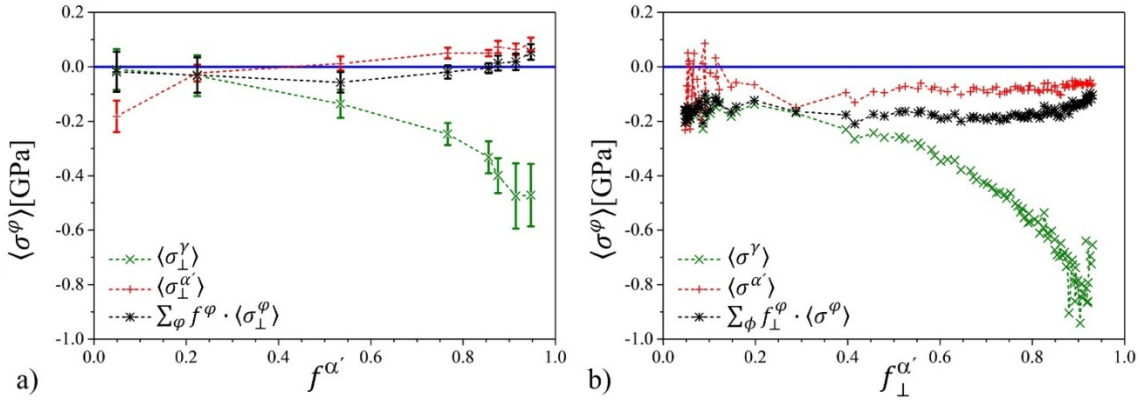

Figure 7.8: Calculated phase-specific stresses $\langle\sigma^{\varphi}\rangle$ for a) sample 1 and b) sample 2. Data re plotted versus fraction transformed $f^{\alpha'}$ (averaged over all ψ) and fraction transformed evaluated in the direction normal to the sample surface $f_{\perp}^{\alpha'}$, for sample 1 and sample 2, respectively. Error bars indicates minimum and maximum values based on data in Figure 7.6a and Figure 7.7a. An additional experimental error related to the alignment of the diffractometer is estimated in the order of ± 30 MPa. Error analysis do not consider uncertainty in the determination of $f^{\alpha'}$ and $f_{\perp}^{\alpha'}$.

of type II in martensite. Data does not provide a reason for the observed reversion of the state of stress in the phases during transformation.

The importance of performing in situ stress analysis to evaluate the state of stress in the phases is clarified from comparing Figure 7.8a and Figure 7.8b. The stress values presented in Figure 7.8b (sample 2) were obtained applying Equ. 7.2, under the assumption that the state of stress in both phases is hydrostatic. Figure 7.8b indicates that martensite formation leads to compressive stresses in both martensite and austenite, in agreement with a previous claim in Ref. [14]. The in situ stress analysis as determined for sample 1 demonstrates that this conclusion is incorrect. Evidently, Equ. 7.2 can be applied only if the assumption that macro-stresses are negligible is validated.

Macro-stresses can be introduced as a consequence of a variation in the degree of transformation over the sample thickness. It is well accepted that martensite formation starts at the surface and is associated with a volume expansion. This expansion is partially relaxed in the ⊥ direction and partially accommodated within the sample. Martensite, which is concentrated at the sample surface, experiences compressive macro-stresses (Figure 7.7b, left), which are balanced by tensile macro-stresses in the bulk austenite, as reflected in Figure 7.6b (left) by probing the 222_γ reflection. Thereafter, continuous cooling promotes continuation of the transformation (from left to right in Figure 7.6 and Figure 7.7), including transformation of the bulk. Transformation of the bulk, is similarly associated with a volume expansion. However, the expansion of the bulk is fully counteracted by the martensitic case, which surrounds it. As a result, macro-stress in the near surface region changes from compressive to tensile during continued transformation, as evidenced in Figure 7.6 and Figure 7.7 at $f^{\alpha'} > 0.2$.

Additionally, hkl dependent lattice strain in austenite should be addressed. Historically, the lattice strain in austenite, ε^γ, developing during martensite formation was obtained from either a^γ evaluated from the position of a single reflection [11-15,23,24], or from an average a^γ value obtained from the simultaneous evaluation of the position of all probed reflections [19,20,27]. In a few studies [16,17,22], hkl-specific ε^{hkl_γ} relying on an independent evaluation of corresponding a^{hkl_γ} were presented. These latter studies revealed that the lattice strain is compressive ($\varepsilon^{hkl_\gamma} < 0$) and largest for $111_\gamma/222_\gamma$ [16,17,22], moderately negative and close to the average value for 311_γ [16,17] and negligible [16,17] or positive, for 200_γ [22]. These observations are confirmed by the results obtained in the present investigation. The hkl-dependence of lattice strain in austenite can partly be explained from the anisotropic elastic properties of austenite (see section 7.3.3). However, lattice strains of opposite sign for different *hkl*, as observed for the material as quenched and as tempered, cannot be reconciled with elastic anisotropy only. Plastic accommodation of the transformation strain is considered responsible for this behavior. When a unit of martensite forms, the transformation evokes tension in the surrounding austenite, which yields heterogeneously. Crystal plasticity in f.c.c. crystals yields *hkl* dependent non-linear stress-strain behaviour in addition to elastic anisotropy and

consequently, a change of the apparent elastic constants. As a result, anisotropic residual stress remains after unloading. Unloading of the state of tension in austenite takes place during continued martensite formation, as revealed by the development of an average compressive state of stress in this phase.

Unfortunately, controversy exists as to which hkls should be chosen to prevent these anisotropy effects (cf. Ref. [29-31] vs. Ref. [32]). If only elastic anisotropy is responsible for *hkl* dependence, averaging is effectively obtained by choosing the 311_γ reflection, as the corresponding orientation parameter 3Γ for this reflection is close to 0.5, i.e. half way the range from 0 to 1. In the present work, $\langle\sigma^\gamma\rangle$ was taken as the average value for stress obtained from lattice strain over ε^{200_γ}, ε^{220_γ}, ε^{311_γ} and ε^{222_γ}. This procedure yielded the conclusion that Equ. 7.3 was satisfied throughout the whole transformation process. It is explicitly mentioned that choosing the 311_γ reflection would have given a comparable result.

Further insight in the elasto-plastic interaction between the phases during transformation is provided by data collected for the ψ-dependent lattice parameter $a_\psi^{200_{\alpha'}}$. A rigorous treatment to interpret a d vs. $sin^2\psi$ distribution characterized by oscillations is missing [4]. However, in a cubic phase, oscillations in the d-vs. $sin^2\psi$ distribution can be caused by texture and/or plastic strain. In textured elastically strained cubic materials, no oscillation of $a_\psi^{\alpha'}$ versus $sin^2\psi$ is expected for the $h00_{\alpha'}$ reflections [4,54]. On the other hand, oscillations will arise in plastically strained crystals, and will be most significant for $200_{\alpha'}$ [4,55]. Hence, the present data indicates that both austenite and martensite are plastically strained during the transformation.

Finally, we suggest that a consistent description of the evolution of strain and phase-specific stresses in the material during the austenite-to-martensite transformation requires that the elasto-plastic interaction of the two phases and the elasto-plastic anisotropy of the two crystal lattices is taken into account. Developing such description is beyond the scope of the present work.

7.5 Conclusion

- Stress analysis was applied to investigate in situ stresses of type II evoked by the austenite-to-martensite transformation in steel. The analysis shows indeed that such stresses do build up.
- Stresses of type II have a significant magnitude for the minority phases, *i.e.* for martensite at the beginning of the transformation and for austenite at the end.
- Stresses of type II in the minority phase are compressive and are balanced by small tensile stresses of type II in the majority phase.
- Strain in austenite is anisotropic: maximum compression is observed for spacings of the $(222)_\gamma$ and $(220)_\gamma$ planes, while tension was revealed in the $[200]_\gamma$

direction. Anisotropic strain in austenite is particularly significant in the latest stage of the transformation.

- Strain anisotropy in austenite and a d-vs. $sin^2\psi$ distribution characterized by oscillations in martensite indicate that both phases are subjected to plastic deformation during quenching.
- An in-depth evaluation of the state of stress in the phases requires further investigation in the effect of plasticity on the determination of stresses in iron-based alloys.
- Tempering of soft martensitic stainless steel to 748 K (475 °C) yields partial relaxation of stresses.

Acknowledgements

M. Klaus, D. Apel and Ch. Genzel from Helmholtz Zentrum für Materialien und Energie (HZME) are acknowledged for their enthusiastic support during the activity at the HZB-BESSY II synchrotron facility and during subsequent data analysis. The activity was supported by the European Commission under the 7th Framework Program through the 'Research Infrastructure' action of the 'Capacities' Programme, CALIPSO (Grant n: 312284) and by the Danish Natural Science Research Council via Danscatt. The Danish Council for Independent Research (G.R. grant: DFF-4005-00223) and the Danish Underground Consortium are gratefully acknowledged for financial support.

References

[1] P. J. Withers, W.M. Stobbs, O.B. Pedersen: Acta metal., 1989, vol. 37, pp. 3061-3084
[2] O.B. Pedersen: Acta Metall., 1983, vol. 31, pp. 1795-1808
[3] P.J. Withers and H.K.D.H. Bhadeshia: Mater. Sci. Tech., 2001, vol. 17, pp. 366-375
[4] V. Hauk: Structural and Residual Stress Analysis by Non-Destructive Methods: Evaluation – Application – Assessment, Elsevier Science, 1997
[5] P.J. Withers and H.K.D.H. Bhadeshia: Mater. Sci. Tech., 2001, vol. 17, pp. 355-365
[6] G.B. Olson and W.S. Owen: Martensite, ASM International, (OH) USA, 1992
[7] Z. Nishiyama, Martensitic Transformation, Academic Press, New York, USA, 1978
[8] J.W. Christian: Proc. Int. Conf. on martensitic Transformation, 1979, pp. 220-233
[9] H.K.D.H. Bhadeshia: Mater. Sci. Eng. A, 2004, vol. 378, pp. 34-39
[10] G.E. Totten, M. Howes, T. Inoue: Handbook of Residual Stress and Deformation of Steel, ASM International, (OH) USA, 2002
[11] V.I. Gridnev, V.I. Trefilov: Dokl. Akad. Nauk SSSR, 1957, vol. 116, pp. 60-62
[12] N. Ridley, H. Stuart, L. Zwell: Trans. AIME, 1969, vol. 245, pp. 1834-1836
[13] K. Ya Golovchiner: Fiz. Metal. Metalloved., 1974, vol. 37, pp. 363-368
[14] Y. Tanaka and K. Shimizu: Trans. JIM, 1980, vol. 21, pp. 42-50
[15] L. Cheng, A. Bottger, T.H. de Keijser, E.J. Mittemeijer: Scripta Mater., 1990, vol. 24, pp. 509-514
[16] M. Villa, F.B. Grumsen, K. Pantleon, M.A.J. Somers: Scripta Mater., 2012, vol. 67, pp. 621-624
[17] M. Villa, K. Pantleon, M.A.J. Somers: J. Alloys Compd., 2013, vol. 577, pp. S543-S548
[18] M. Villa, K. Pantleon, M.A.J. Somers: Acta mater., 2014, vol. 65, pp. 383-392
[19] J. Epp.: Advanced Mater. Res., 2014, vol. 996, pp. 525-531
[20] J. Epp.: Proc. IFHTSE 2016, 2016, pp. 440-447
[21] N. Nakada, Y. Ishibashi, T. Tsuchiyama, S. Takaki: Acta Mater., 2016, vol. 110, pp. 95-112
[22] V.M. Yeshov, M.L. Oslon: Fiz. Metal. Metalloved., 1968, vol. 25, pp. 874-881
[23] V.M. Yeshov, M.L. Oslon: Fiz. Metal. Metalloved., 1972, vol. 33, pp. 215-217
[24] E. Scheil, E. Saftig. Arch. Eisenhuttenw. 1957, vol. 28, pp. 49-51
[25] K. Ullakko and V.G. Gavriljuk: Acta Metall. Mater., 1992, vol. 40, pp. 2471-2482
[26] K. Ullakko: Aging of iron-based martensites at low-temperatures, PhD thesis, Helsinki, 1992
[27] D. San Martin, E. Jimenez-Melero, J.A. Duffy, V. Honkimaki, S. van der Zwaag, N.H. van Dijk: J. Appl. Crystallogr., 2012, vol.45, pp. 748-757
[28] T. Kakeshita, T. Saburi, K. Kind, S. Endo: Phase Transitions, 1999, vol. 70, pp. 65-113.
[29] A.N. Ezeilo, G.A. Webster, P.J. Webster, X. Wang: Physica B, 1992, vol. 180-181, pp. 1044-1046
[30] B. Clausen, T. Lorentzen, T. Leffers: Acta. Mater., 1998, vol. 46, pp. 3087-3098
[31] E.C. Oliver: The generation of internal stresses in single and two phase materials, PhD Thesis, Manchester, 2002
[32] B. Clausen, T. Leffers, T. Lorentzen: Acta. Mater.,, 2003, vol. 51, pp. 6181-6188
[33] F. Niessen, M. Villa, D. Apel, O. Keßler, M. Reich, J. Hald, M.A.J. Somers: Mater. Sci. Forum, 2016, vol. 879, pp. 1381–1386
[34] F. Niessen, M. Villa, J. Hald, M. AJ Somers: Mater. and Design, 2017, vol. 116, pp. 8–15.
[35] Ch. Genzel, I. A. Denks, M. Klaus, Mater. Sci. Forum, 2006, vol. 524-525, pp. 193-

198
[36] B.C. Giessen, G.E. Gordon: Science, 1968, vol. 159, pp. 973–975
[37] Ch. Genzel, I.A. Denks, M. Klaus: Residual Stress Analysis by X-Ray Diffraction Methods, in Modern Diffraction Methods, Wiley-VCH, 2013, pp. 127–154
[38] E.S.U. Laine: J. Phys. F Met. Phys., 1978, vol. 8, pp. 1343-1348
[39] Landoldt-Börnstein, New Series, Group III Vol. 11, Springer, Berlin 1979
[40] H. Behnken: Berechnung und Ermittlung der röntgenographischen Elastizitätskonstanten sowie der Mikro- und Makro-Spannungen heterogener und texturierter Werkstoffe, PhD thesis, RWTH Aachen, 1992
[41] E. Kröner: Z. Physik, 1958, vol. 151, pp. 504-518
[42] J.D. Eshelby: Proc. Roy. Soc. London A, 1957, vol. 241, pp. 376-396
[43] A. Teklu, H. Ledbetter, S. Kim, L.A. Boatner, M. McGuire, V. Keppens: Metall. Mater. Trans. A, 2004, vol. 35, pp. 3149-3154
[44] H.M. Ledbetter and M.W. Austin: Mater Sci Eng, 1985, vol. 70, pp. 143-149
[45] Y.S. Touloukian, Thermophysical Properties of Matter. The TPRC Data Series 12: Thermal Expansion Metallic Elements and alloys, IFI/Plenum, 1975
[46] T. Gnaupel-Herold, A. Creuziger: Mater. Sci. Eng. A, 2011, vol. 528, pp. 3594-3600
[47] A. Bojack, L. Zhao, P.F. Morris, J. Sietsma: Mater. Charact, 2012, vol. 7, pp. 77-86
[48] C.M. Wayman: Iron and Steel Inst. - Special Report, 1965, pp. 153-163
[49] J. Pak, D.W. Suh, H.K.D.H. Bhadeshia: Metall. Mater. Trans. A, 2012, vol. 43, pp. 4520-4524
[50] J.A. Klostermann and W.G. Burgers: Acta Metall., 1964, vol. 12, pp. 355-360
[51] J.A. Klostermann: J. Less-Common Metals, 1972, vol. 28, pp. 75-94
[52] G. Faria, J. Escobar, A.J. Ramirez: Proc. Int. Conf. on Solid-solid Phase Transf. in Inorganic Mater. 2015, 2015, pp. 637-638
[53] A. Beneteau, E. Aeby-Gautier, G. Geandier, P. Weisbecker, A. Redjaimia, B. Appolaire: Acta Mater., 2014, vol. 81, pp. 30-40
[54] A.J.C. Wilson: Acta Cryst., 1952, vol. 5, pp. 318-322
[55] J.W.L. Pang, T.M. Holden, T.E. Mason: J. Strain Analysis Eng. Design, 1998, vol. 33, pp. 373-383

8 Manuscript III

In-situ analysis of redistribution of carbon and nitrogen during tempering of low interstitial martensitic stainless steel

Frank Niessen[a,†], Matteo Villa[b], Frédéric Danoix[c], John Hald[b], Marcel A.J. Somers[b]

[a] Technical University of Denmark (DTU), Danish Hydrocarbon Research and Technology Centre (DHRTC) , Elektrovej building 375, 2800 Kgs. Lyngby, Denmark

[b] Technical University of Denmark (DTU), Department of Mechanical Engineering, Produktionstorvet building 427, 2800 Kgs. Lyngby, Denmark

[c] Normandie Univ, UNIROUEN, INSA Rouen, CNRS, Groupe de Physique des Materiaux, F-76000 Rouen, France

[†] Corresponding author

Abstract

The redistribution of C and N during tempering of X4CrNiMo16-5-1 martensitic stainless steel containing 0.034 wt.% C and 0.032 wt.% N was studied using *in-situ* synchrotron X-ray diffraction (XRD) and atom probe tomography (APT). The unit cell volume of martensite decreased continuously during tempering. APT showed that this volume decrease is accounted entirely for by segregation of the interstitial atoms, implying that in low interstitial martensitic stainless steel stress relaxation only contributes negligibly to changes in the martensite unit cell volume.

Martensitic steels with lath microstructure stand out by an exceptional combination of high strength, good ductility and low cost for numerous structural applications. These properties are conventionally obtained through a hardening and tempering heat treatment cycle. Hardening consists of high temperature austenitization followed by martensite formation during fast cooling to room temperature. With a dislocation density comparable to that of heavily cold rolled ferrite, martensite is brittle and thus unsuitable for practical use [1]. Tempering of the hardened material below A_{c1} promotes optimization of the mechanical properties through redistribution of the interstitial atoms and relaxation of internal stresses [2]. In martensitic stainless steels, annealing in the inter-critical region between A_1 and A_3 leads to formation and stabilization of reversed austenite at lath boundaries [3–5]. Such dual phase microstructure significantly enhances toughness and ductility, and reduces yield strength, hardness and ultimate tensile strength [6–8].

A few *in-situ* studies focused on tempering of martensitic stainless steels with more than 0.6 wt.% interstitial content below A_{c1} [9,10], or on inter-critical annealing of martensitic stainless steels with less than 0.08 wt.% interstitial content [4,11–13]. These in-situ studies were based on measurement of the planar spacings of the present phases as a function of temperature with synchrotron X-ray diffraction (XRD). Tempering below A_{c1} in low interstitial martensitic stainless steels appears still uninvestigated. Generally, it is not possible to distinguish unequivocally between the contributions of changes in interstitial content in solid solution and changes in internal stresses on the evolution of the austenite and martensite unit cell volumes. In martensite, the change in tetragonality of the unit cell with C and N content [14] is a widely applied relation to determine the interstitial content [9,15,16]. In the present system, the martensite unit cell must be regarded as cubic, because of the low total interstitial (C + N) content [14]. Hence, the unit cell volume is represented by a single lattice parameter. For cubic martensite, as well as for austenite, XRD studies which involve both changes in chemistry and stresses are either limited to semi-quantitative conclusions based on assumptions [10,15,17–20], or rely on additional results from numerical modeling [9,21,22]. The present study aims to elucidate the interpretation of changes in the unit cell volume of martensite during tempering by correlating in-situ energy-dispersive synchrotron X-Ray diffraction (XRD) with atom probe tomography (APT) results.

The steel investigated has the metallic composition Fe-15wt.%Cr-5.8wt.%Ni-1.0wt.%Mo-0.86wt.%Mn-0.4wt.%Si (EN 1.4418) measured by optical emission spectroscopy as well as 0.034 ± 0.0048 wt.% C and 0.032 ± 0.0006 N wt.% as interstitials, measured by LECO CS230 and LECO TC500 instruments, respectively. Samples from an extruded rod of Ø10 mm were austenitized at 1223 K for 6 ks in an Ar flow, where the average heating and cooling rate were 0.75 and 1.15 $K.s^{-1}$, respectively. The martensite start temperature (M_s) of the material is 408 K, and the amount of retained austenite at room temperature is 3.5 ± 0.5 vol.% [23]. Microstructure characterization revealed that retained austenite is present as bulky retained austenite, mostly in the corners of martensite packets.

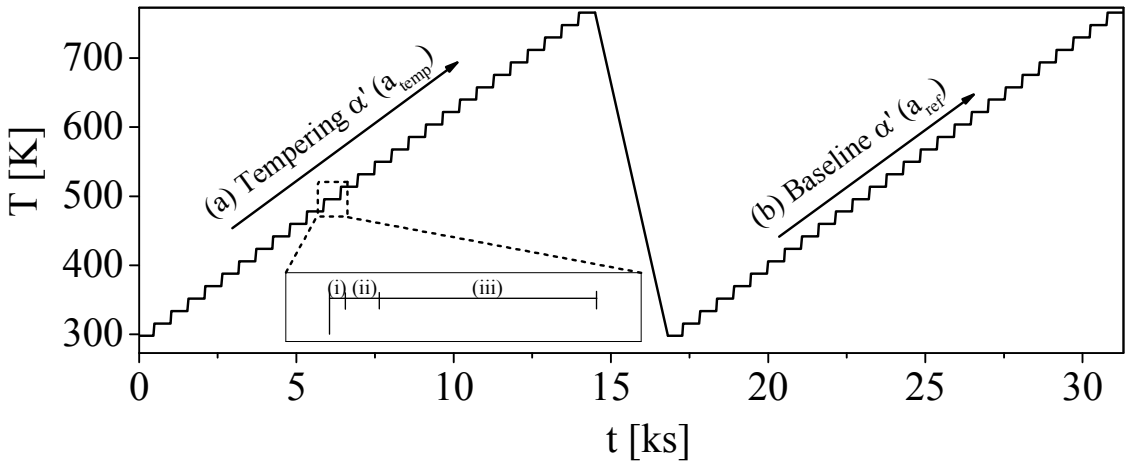

Figure 8.1: Thermal cycles applied for measurement of the lattice parameter during (a) tempering of virgin martensite (a_{temp}) and (b) reheating of tempered martensite (a_{ref}). The average heating and cooling with 0.033 K.s^{-1} was discretized into isothermal plateaus of 540 s consisting of (i) rapid heating (0.6 K.s^{-1}), (ii) 80 s equilibration and (iii) 430 s of sin$^2\psi$-analysis at stationary thermal conditions (see inset).

In-situ XRD was carried out on the EDDI-beamline of the synchrotron facility HZB-BESSY II [24] and consisted of high temperature measurement of the evolution of the unit cell volumes of the phases. Sample preparation, experimental setup and measuring conditions are described in Ref. [23].

Residual stresses can be categorized according to the length scale over which they equilibrate. Macro-stresses (type I) occur over large distances within a sample, micro-stresses of type II equilibrate at the grain or phase scale, and micro-stresses of type III are stresses which occur at a level considerably smaller than the grain size [25,26]. Stresses are manifested as lattice strains and, for polycrystalline mono-phase materials with random grain orientation, lead to line profile shifts (type I) or line profile broadening (type II and III) in XRD. For dual-phase polycrystalline materials, as under consideration in the present work, stresses of type I are partitioned into phase specific stresses of type II, which lead to phase specific line profile shifts, while broadening of the line profiles reflects the variation in phase specific stresses of type II and stresses of type III.

The austenite-to-martensite transformation in steel is associated with a shape change, a so-called transformation strain, which, in average, invokes a state of phase-specific hydrostatic residual stress of type II in the material with contributions from the transformation itself and thermal mismatch [23]. In a thin sample, as under consideration in the present study, macro-stresses (type I) are considered biaxial, i.e. relaxed in the direction normal to the sample surface, and can be separated from hydrostatic type II stresses by measuring over several ψ angles [26,27]. Stresses were determined from the arithmetic average of the lattice parameters from the $211_{\alpha'}$, $220_{\alpha'}$ and $321_{\alpha'}$ reflections, weighted by their multiplicity. Further details on the applied methodology and the X-ray elastic constants are given in Ref. [23].

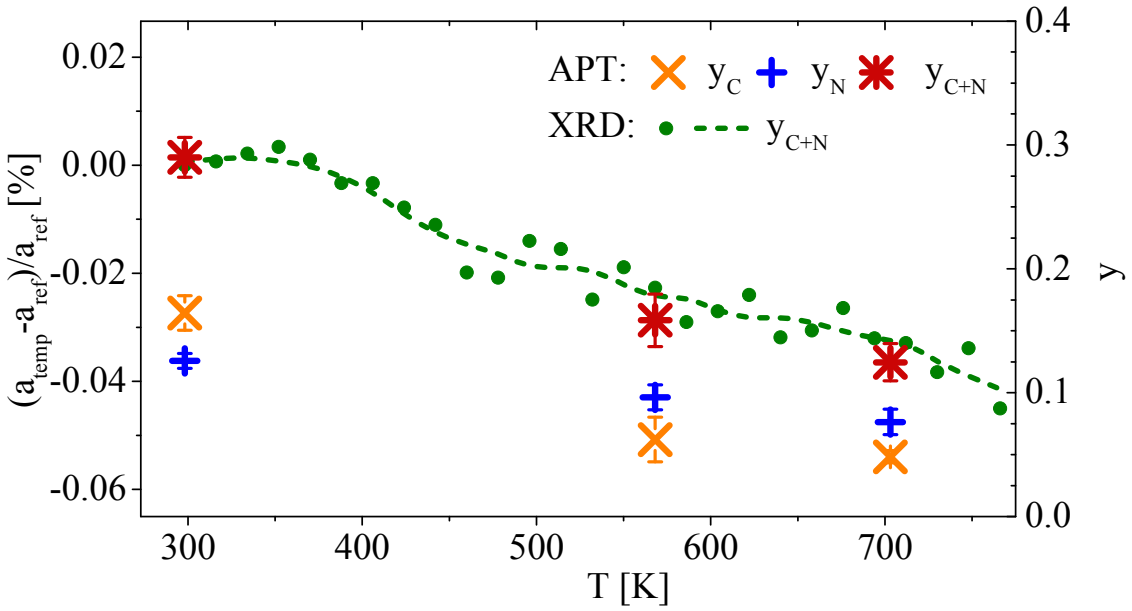

Figure 8.2: The green data points and dashed curve show the relative change in the martensite lattice parameter as determined by XRD during tempering (left y-axis). The conversion of lattice expansion to the change in total interstitial content (Equ. 8.1) starting from the average C and N alloy content is given on the right y-axis. Data points show C and N concentrations from chemical analysis of the bulk by APT, excluding segregated areas at lattice defects. The error bars represent the standard deviation from measurements of different samples of the same tempering condition, weighted by their number of ions. Data originates from $> 5 \times 10^6$ ions per sample and in total $> 50 \times 10^6$ ions per tempering condition.

The lattice parameter of martensite was acquired during the thermal cycles depicted in Figure 8.1. Virgin martensite was heated at 0.033 K.s^{-1} and heating was interrupted at 766 K to prevent nucleation of austenite (Figure 8.1*(a)*). A second heating cycle was applied to obtain the reference lattice parameter of tempered martensite (Figure 8.1*(b)*). For the accurate determination of lattice strains with the sin$^2\psi$ method stationary conditions are required. For this reason, the average heating rate of 0.033 K.s^{-1} was realized by rapid heating by 18 K at 0.6 K.s^{-1}, 80 s of temperature equilibration and 430 s measurement for a range of ψ angles (see inset in Figure 8.1, intervals *(i)*, *(ii)* and *(iii)*, respectively). It was found for martensite that phase specific macro stresses, i.e. biaxial stresses determined by the sin$^2\psi$ method, were in the range of -30 to 30 MPa for the entire thermal cycle and thus can be neglected.

The change in the lattice parameter of martensite during tempering of virgin martensite (a_{temp}, cycle *(a)* in Figure 8.2) relative to the lattice parameter of tempered martensite (a_{ref}, cycle *(b)* in Figure 8.2) is represented by the green dots and the dashed line in Figure 8.2. Since no biaxial stresses are present, this relative change in lattice parameter can be conceived as the average value of the phase specific hydrostatic lattice strains of type II [26]. Evidently, on tempering the volume of the martensite unit cell is reduced relative to the reference condition. The volume fraction of retained austenite was too small to allow accurate lattice strain determination

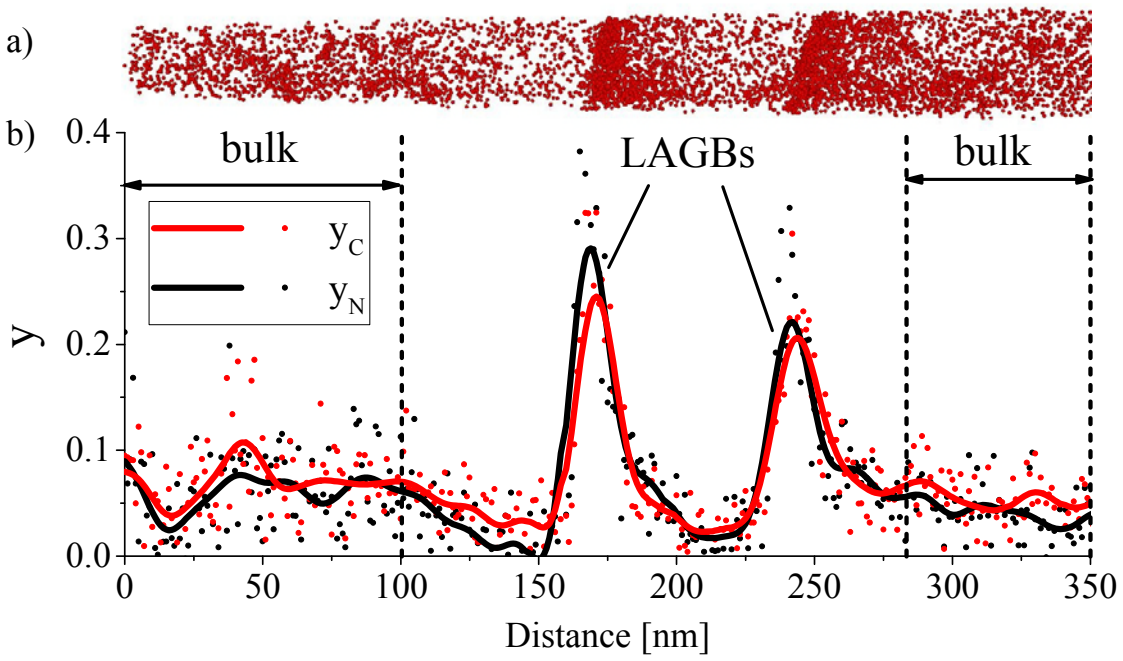

Figure 8.3: Carbon and nitrogen content profiles along the longitudinal axis of an APT analysis of the 703 K tempered condition (b) and reconstruction of the C-atom distribution (a). The bulk contents in Figure 8.2 were determined within the areas indicated "bulk", with distance from segregation features and corresponding depleted zones.

The change in lattice parameter of martensite may be an effect of partitioning of mechanical stress, but may also be the result of a redistribution of interstitials. Interpreting the contraction in terms of a change in total interstitial content, the well-established relationships for Fe-C and Fe-N martensite from Ref. [14] could be applied. Recognizing that both N and C are present, the arithmetic average of the dependence of unit cell volume on interstitial (N or C) content can be used to estimate the change in total interstitial content[‡‡]:

$$V_{Me} = 1.1776\ 10^{-2} + 8.2\ 10^{-5} y_{N+C}\ [\mathrm{nm}^3] \qquad (8.1)$$

where V_{Me} is the volume per metal atom and y_{N+C} is the total number of interstitials per 100 metal atoms. This conversion of relative contraction of the unit cell volume into the change of total interstitial content from the initially average alloy interstitial content is given on the right-hand vertical axis in Figure 8.2.

Assuming a pure effect of rejection of C and N on the relative change in the martensite lattice parameter, the measured change in lattice parameter corresponds to a progressive rejection of C and N from solid solution in martensite (green dashed line in Figure 8.2). Altogether $y_{c+N} = 0.18$ is rejected, while $y_{c+N} = 0.10$ remains in solid solution.

[‡‡] Adopting the average of the lattice expansions caused by C and N an error of maximally 1% is introduced, which is within experimental accuracy.

In order to verify the validity of the hypothesis of a mere rejection of interstitials, local composition measurements with atom probe tomography (APT) were conducted for specimens in the hardened condition and specimens tempered by heating to 568 K and 703 K at the same heating rate as in the XRD investigations. Needle-shaped specimens for APT were prepared by electrolytic polishing [28] and subsequently field-evaporated in a CAMECA LEAP 4000 HR® in voltage mode. The analysis was conducted at 50 K, 20 % pulse fraction, 200 kHz pulse rate and 0.3% detection rate in legacy mode. In mass spectra, carbon was detected as C^{+}, C^{2+}, $(^{2}C)^{2+}$, $(^{3}C)^{2+}$ and C^{3+} ions and compositions were determined following the peak assignment proposed by Sha et al. [29]. Singly charged nitrogen overlaps with doubly charged Si, but as no characteristic shoulder for the Si^{2+} was observed, and nitrogen has a strong tendency to form molecular ions with Mo [30], virtually all N was detected as $(MoN)^{2+}$. Grain boundaries were identified by qualitative structural analysis of the desorption pattern [31]. The standard deviation of interstitial content y in terms of counting statistics [32] of individual measurements was $< 2.5 \times 10^{-3}$ for both C and N.

A representative example of an APT analysis is given in Figure 8.3 for the sample heated to 703 K. Two low-angle grain boundaries (LAGBs), i.e. lath boundaries, are identified by a local increase in the C and N contents. The average bulk contents were determined in the marked region, where the C and N contents are approximately constant and unaffected by segregation at the LAGBs and/or depletion in the adjacent region.

APT revealed that the interstitial and substitutional alloying elements in the hardened condition were approx. homogeneously distributed within the laths and that no segregation occurred at lath boundaries. The uniform distribution of interstitials within each specimen and the low differences between specimens of the same condition (see error bars in Figure 8.2) suggest that martensite formation from 408 K and below occurs without auto-tempering, and that no noticeable aging occurred during storage of the sample at room temperature over 6 months. Clustering of C was observed in the 703 K condition, but no transition- or alloy-carbides were found, which is in agreement with investigations on a maraging stainless steel with 0.05 wt.% C [33].

The average bulk contents of N and C determined by APT for the three conditions are included in Figure 8.2. The determined C and N contents of 0.036± 0.0030 wt.% and 0.032± 0.0015 wt.% in the hardened condition are in excellent agreement with the bulk contents of 0.034± 0.0048 wt.% and 0.032± 0.0006 wt.%, respectively. Comparison of the evolution of the total interstitial content determined by APT with the change in lattice parameter (Figure 8.2) shows excellent agreement. As a consequence, it can be concluded that the evolution of the martensite lattice parameter can be explained solely by a change in total interstitial content in solid solution.

Previously it was found for the same alloy that martensite experiences an average 40 MPa hydrostatic tensile stress and that the minority phase austenite experiences an average of 890 MPa hydrostatic compressive stress in the hardened condition [23], while

the total macro stress is close to nil. It could therefore be argued, that the change in martensite lattice parameter during tempering is an effect of relaxation of the hydrostatic component of the stress state rather than a change of the interstitial content in martensite. Interpretation of the change in martensite lattice parameter before and after tempering in terms of average hydrostatic stress corresponds to -320 MPa, which is too large to account for stress relaxation of 40 MPa. Furthermore, relaxation of the tensile state of stress in martensite compared to a compressive state of stress in austenite would induce partitioning of interstitials in the reverse direction, i.e. martensite can release the tensile hydrostatic component of the stress state by absorbing more interstitials, while austenite can release the hydrostatic component of the compressive stress by depletion of interstitials. APT shows that the reverse is happening, implying that a reduction of the strain energy is not the dominant driving force for partitioning of the interstitials.

Summarizing, the present work shows that C and N are initially homogeneously distributed in the hardened condition in low interstitial martensitic stainless steel and that tempering leads to progressive rejection of C and N from solid solution and segregation to mainly grain boundaries. Interpretation of the change in unit cell volume of martensite during tempering as a change in interstitial content in martensite shows excellent agreement with a change of the bulk interstitial content as determined by APT. Thus, for the present system, the change in unit cell volume of martensite during tempering can be directly interpreted as a change in total interstitial atom content in the martensitic matrix.

M. Klaus, D. Apel and Ch. Genzel from Helmholtz Zentrum für Materialien und Energie (HZME) are acknowledged for their support during the activity at the HZB-BESSY II synchrotron facility. The activity was supported by the European Commission under the 7th Framework Program through the 'Research Infrastructure' action of the 'Capacities' Programme, CALIPSO (Grant n: 312284). The Danish Underground Consortium is gratefully acknowledged for financial support to the Danish Hydrocarbon Research Center (DHRTC).

References

[1] M. Natori, Y. Futamura, T. Tsuchiyama, S. Takaki, Difference in recrystallization behavior between lath martensite and deformed ferrite in ultralow carbon steel, Scr. Mater. 53 (2005) 603–608.

[2] G.R. Speich, Tempering of Low-Carbon Martensite, Trans. Metall. Soc. AIME. 245 (1969) 2553–2564.

[3] F. Niessen, F.B. Grumsen, J. Hald, M.A.J. Somers, Formation and stabilization of reversed austenite in supermartensitic stainless steel, in: Proc. 24th IFHTSE Congr., 2017: pp. 138–145.

[4] F. Niessen, M. Villa, D. Apel, O. Keßler, M. Reich, J. Hald, M.A.J. Somers, In situ techniques for the investigation of the kinetics of austenitization of supermartensitic stainless steel, Mater. Sci. Forum. 879 (2017) 1381–1386.

[5] F. Niessen, Austenite reversion in low-carbon martensitic stainless steels – a CALPHAD-assisted review, Mater. Sci. Technol. (2018). doi: 10.1080/02670836.2018.1449179

[6] P. Brezina, B. Sonderegger, Wärmebehandlung, Gefüge und Eigenschaften des korrosionsträgen martensitaushärtbaren Stahles X 5 CrNiMoCuNb 14 5 (14-5 PU), Härterei-Technische Mitteilungen. 33 (1978) 1–12.

[7] M. Al Dawood, I.S. El Mahallawi, M.E. Abd El Azim, M.R. El Koussy, Thermal aging of 16Cr – 5Ni – 1Mo stainless steel Part 2 – Mechanical property characterisation, Mater. Sci. Technol. 20 (2004) 370–374.

[8] M. Grounes, S. Rao, New Alloy Steels for Nuclear Reactor Pressure Vessels and Vessel Internals, Trans. ASM. 62 (1969) 902–914.

[9] A. Bénéteau, E. Aeby-Gautier, G. Geandier, P. Weisbecker, A. Redjaimia, B. Appolaire, Tempering of a martensitic stainless steel: Investigation by in situ synchrotron X-ray diffraction, Acta Mater. 81 (2014) 30–40.

[10] G. Geandier, E. Aeby-Gautier, A. Settefrati, M. Dehmas, B. Appolaire, Study of diffusive transformations by high energy X-ray diffraction, Comptes Rendus Phys. 13 (2012) 257–267.

[11] J.D. Escobar, G. Faria, L. Wu, J.P. Oliveira, P.R. Mei, A.J. Ramirez, Austenite reversion kinetics and stability during tempering of a Ti-stabilized supermartensitic stainless steel: correlative in situ synchrotron x-ray diffraction and dilatometry, Acta Mater. 138 (2017) 92–99.

[12] M. Wiessner, E. Gamsjäger, S. van der Zwaag, P. Angerer, Effect of reverted austenite on tensile and impact strength in a martensitic stainless steel−An in-situ X-ray diffraction study, Mater. Sci. Eng. A. 682 (2017) 117–125.

[13] F. Niessen, M. Villa, J. Hald, M.A.J. Somers, Kinetics analysis of two-stage austenitization in supermartensitic stainless steel, Mater. Des. 116 (2017) 8–15.

[14] L. Cheng, A. Böttger, T.H. de Keijser, E.J. Mittemeijer, Lattice parameters of iron-carbon and iron-nitrogen martensites and austenites, Scr. Metall. Mater. 24 (1990) 509–514.

[15] J. Epp, T. Hirsch, C. Curfs, In situ X-Ray Diffraction Analysis of Carbon Partitioning During Quenching of Low Carbon Steel, Metall. Mater. Trans. A. 43 (2012) 2210–2217.

[16] B. Kim, J. Sietsma, M.J. Santofimia, Thermodynamic aspects of carbon redistribution during ageing and tempering of Fe–Ni–C alloys, Philos. Mag. 96 (2016) 2632–2648.

[17] B. Kim, J. Sietsma, M.J. Santofimia, The role of silicon in carbon partitioning processes in martensite/austenite microstructures, Mater. Des. 127 (2017) 336–345.

[18] J. Epp, Investigation of Triaxial Stress State in Retained Austenite during Quenching of a Low Alloy Steel by In Situ X-Ray Diffraction, Adv. Mater. Res. 996 (2014) 525–531.
[19] S. Allain, G. Geandier, J.-C. Hell, M. Soler, F. Danoix, M. Gouné, Effects of Q&P Processing Conditions on Austenite Carbon Enrichment Studied by In Situ High-Energy X-ray Diffraction Experiments, Metals (Basel). 7 (2017) 232.
[20] T.D. Bigg, D. V. Edmonds, E.S. Eardley, Real-time structural analysis of quenching and partitioning (Q&P) in an experimental martensitic steel, J. Alloys Compd. 577 (2013) S695–S698.
[21] S.Y.P. Allain, G. Geandier, J.C. Hell, M. Soler, F. Danoix, M. Gouné, In-situ investigation of quenching and partitioning by High Energy X-Ray Diffraction experiments, Scr. Mater. 131 (2017) 15–18.
[22] S.Y.P. Allain, S. Gaudez, G. Geandier, J.-C. Hell, M. Gouné, F. Danoix, M. Soler, S. Aoued, A. Poulon-Quintin, Internal stresses and carbon enrichment in austenite of Quenching & Partitioning steels from High Energy X-Ray diffraction experiments, Mater. Sci. Eng. A. 710 (2017) 245–250.
[23] M. Villa, F. Niessen, M.A.J. Somers, In situ investigation of the evolution of lattice strain and stresses in austenite and martensite during quenching and tempering of steel, Metall. Mater. Trans. A. 49 (2017) 1–13.
[24] C. Genzel, I. Denks, M. Klaus, The Materials Science Beamline EDDI for Energy-Dispersive Analysis of Subsurface Residual Stress Gradients, Mater. Sci. Forum. 524–525 (2006) 193–198.
[25] P.J. Withers, H.K.D.H. Bhadeshia, Residual stress part 1 - Measurement techniques, Mater. Sci. Technol. 17 (2001) 355–365.
[26] V. Hauk, Evaluation of Load Stress (LS) and Residual Stress (RS), in: Struct. Residual Stress Anal. by Nondestruct. Methods, Elsevier, 1997: pp. 192–295.
[27] E. Macherauch, P. Müller, Das sin2psi-Verfahren der röntgenographischen Spannungsmessung, Zeitschrift Für Angew. Phys. 13 (1961) 305–312.
[28] M.K. Miller, G.D.W. Smith, Atom probe microanalysis: principles and applications to materials problems, Materials Research Society, USA, 1989.
[29] W. Sha, L. Chang, G.D.W. Smith, L. Cheng, E.J. Mittemeijer, Some aspects of atom-probe analysis of Fe-C and Fe-N systems, Surf. Sci. 266 (1992) 416–423.
[30] M.K. Miller, R. Forbes, Atom Probe Tomography: The Local Electrode Atom Probe, Springer US, 2014.
[31] B. Gault, M.P. Moody, J.M. Cairney, S.P. Ringer, Atom probe crystallography, Mater. Today. 15 (2012) 378–386.
[32] F. Danoix, G. Grancher, A. Bostel, D. Blavette, Standard deviations of composition measurements in atom probe analyses-Part II: 3D atom probe, Ultramicroscopy. 107 (2007) 739–743.
[33] C. Servant, E.H. Gherbi, G. Cizeron, TEM investigation of the tempering behaviour of the maraging PH 17.4 Mo stainless steel, J. Mater. Sci. 22 (1987) 2297–2304.

9 Manuscript IV

Structural evolution of martensite during tempering of soft martensitic stainless steel

Frank Niessen[a,†], Daniel Apel[b], Frédéric Danoix[c], John Hald[d], Marcel A.J. Somers[d]

[a] Technical University of Denmark (DTU), Danish Hydrocarbon Research and Technology Centre (DHRTC) , Elektrovej building 375, 2800 Kgs. Lyngby, Denmark

[b] Helmholtz-Zentrum für Materialien und Energie, Alberst-Einstein-Straße 15, 12489 Berlin, Germany

[c] Normandie Univ, UNIROUEN, INSA Rouen, CNRS, Groupe de Physique des Materiaux, F-76000 Rouen, France

[d] Technical University of Denmark (DTU), Department of Mechanical Engineering, Produktionstorvet building 427, 2800 Kgs. Lyngby, Denmark

[†] Corresponding author

Abstract

The structural evolution of lath martensite during tempering in X4CrNiMo16-5-1 was studied by line profile analysis of diffractograms from energy dispersive synchrotron X-ray diffraction (XRD), atom probe tomography (APT) and site-specific orientation mapping with electron microscopy. Martensite formation occurred below 135 °C without autotempering and led to a dislocation density in martensite of $\sim 1.8 \times 10^{15}\ \mathrm{m}^{-2}$. Tempering led to progressive segregation of C and N to lattice defects, mainly grain boundaries. Recovery commenced above 550 °C and led to a progressive decrease in dislocation density to a steady value of $\sim 3.5 \times 10^{14}\ \mathrm{m}^{-2}$ at 700 and 750 °C. Further tempering led to a second increase in dislocation density at room temperature, owing to martensite formation from reverted austenite. The evolution of the coherently diffracting domain size with tempering temperatures was qualitatively in line with recovery of martensite.

9.1 Introduction

Soft martensitic stainless steels are essentially Fe-Cr-Ni alloys with particularly low C and N content. The steel grade is known for attractive properties such as good corrosion resistance, good ductility at high strength, superior impact toughness and particular resistance to wet abrasion and cavitation [1–3]. These qualify the material for use in heavy section water turbine components, pump and valve bodies for the power generation and petrochemical industries, and wellhead equipment for the offshore oil and gas industries [4,5].

The material properties are obtained by solution treating the material in the austenite region, martensite formation during cooling, and subsequent formation and stabilization of reverted austenite by annealing in the intercritical region ($A_1 < T < A_3$). Reverted austenite forms mainly by a diffusional mechanism during slow heating or isothermal annealing [6] and chemical analyses have shown that growth of austenite is accompanied by partitioning of austenite stabilizing elements [6–9]. Such partitioning contributes to the stabilization of reverted austenite to room temperature [10]. Reverted austenite leads to softening and significant improvement in impact toughness [3,4].

While the growth stages of reverted austenite at different temperature are well covered in literature [9,11], nucleation close to A_1 seems rather uninvestigated. Before inter-critical annealing, soft martensitic stainless steels are generally austenitized and quenched to form martensite. The transformation to martensite is associated with transformation strains [12] and the generation of a high density of dislocations ($\sim 1 \times 10^{15}$ m^{-2}) [13–15]. On heating the material to a temperature above A_1 to form reverted austenite, the martensite microstructure is tempered [16]. Since the morphology, strain energy and chemical composition of tempered martensite all have an influence on the nucleation of austenite, it is crucial to characterize these microstructure aspects of tempered martensite.

The present work elucidates the changes in micro-strain, morphology and chemical composition which occur during tempering of soft martensitic stainless steel by applying line profile analysis to diffractograms from energy-dispersive synchrotron X-ray diffraction, mapping the local chemical composition with atom probe tomography, and characterizing the martensite morphology with orientation mapping in the scanning electron microscope.

9.2 Experimental procedures

9.2.1 Materials and heat treatments

The analyzed alloy is a X4CrNiMo16-5-1 (EN 1.4418) soft martensitic stainless steel with the composition in Table 9.1. The material was received as a Ø10 mm rod of in as-extruded

Table 9.1: Chemical composition of X4CrNiMo16-5-1 (EN 1.4418) soft martensitic stainless steel in wt.% and at.% from optical emission spectroscopy (OES) and C and N chemical analysis.

	Fe	C	N	Cr	Ni	Mo	Mn	Si
wt.%	bal.	0.034	0.032	15.0	5.8	1.0	0.86	0.39
at.%	bal.	0.157	0.126	15.9	5.5	0.59	0.87	0.77

condition and was normalized at 950 °C for 600 s in an Ar flow prior to investigation. The average heating and cooling rate were 0.75 and 1.16 K.s^{-1}, respectively.

Samples for electron backscatter diffraction were ground and electro-polished for 30 s at 25 V with Struers A2 electrolyte to remove the strain-affected layer in the surface. Electron transparent samples for transmission Kikuchi diffraction were prepared by electrolytic twin-jet polishing in 10 % perchloric acid dissolved in ethanol at -20 °C.

Samples for atom probe tomography analysis were prepared by electrolytic polishing to obtain needle-shaped samples for field-evaporation [17]. The investigated conditions were virgin martensite specimens, and specimens tempered by isochronal heating with 0.033 K.s^{-1} to 295 and 435 °C. The cooling rate exceeded 0.7 K.s^{-1} at temperatures higher than A_{c1} and was 0.25 K.s^{-1} on average.

Samples for line profile analysis in X-ray diffraction were cut to Ø10 x 0.3 mm^2 discs and exposed to isothermal holding for 60 s at 50 °C intervals from 100 - 800 °C in a chamber furnace, followed by quenching in water. A study on the evolution of the dislocation density in lath martensite as a function of holding time at 400 °C revealed no significant change in dislocation density when holding longer than 5 s [18].

9.2.2 Energy-dispersive synchrotron X-ray diffraction

Energy-dispersive synchrotron X-ray diffraction (XRD) was carried on the EDDI-beamline of the synchrotron facility HZB-BESSY II [19] and comprised measurement of the evolution of the diffraction line profiles of annealed samples. In energy-dispersive XRD, the investigation is carried out using a beam of white X-rays at a fixed scattering angle, $2\theta_0$ = 14 °, and reflection geometry. Diffraction for crystallographic planes, $\{hkl\}$, occurs at a photon energy, E_{hkl}, which is inversely proportional to the inter-planar spacing, d_{hkl}, i.e. proportional to the magnitude of the diffraction vector, K_{hkl}:

$$K_{hkl} = \frac{1}{d_{hkl}} = \frac{2E_{hkl}\sin(\theta_0)}{hc} \tag{9.1}$$

A detailed description of the setup of the EDDI-beamline is given in Ref. [23].

Line profile analysis

So far, only little work has been done to apply the well-established methods of line profile analysis to data from energy-dispersive XRD. This is mainly owed to the rather poor

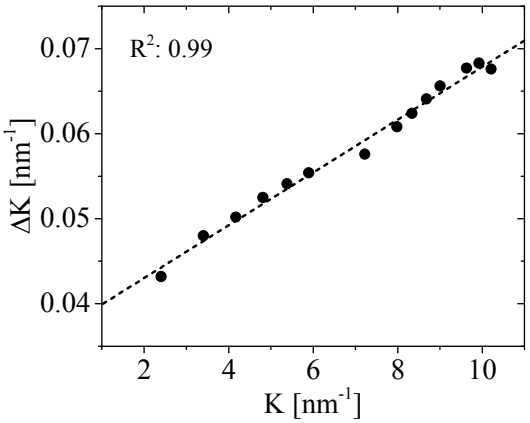

Figure 9.1: Determination of instrumental profile by the Williamson-Hall method on a LaB_6 SRM660a NIST standard.

instrumental resolution [20–22]. While the detector resolution has not improved significantly compared to early studies, the use of state-of-the-art synchrotron radiation and advances in instrumentation enables significantly better geometrical resolution, resulting in narrower instrumental line profiles [20]. In the present study the instrumental resolution was minimized by reducing the cross-section of the primary beam with a 0.5 x 0.5 mm^2 primary slit configuration and limiting the divergence of the diffracted beam by an equatorial slit aperture of 30 µm. The suitability of this specific experimental setup for line profile analysis was demonstrated by analysis of powder samples in Ref. [20]. The instrumental resolution was determined by measuring the line profile of a LaB_6 SRM660b (NIST) standard powder (see Figure 9.1). The profile was dominated by the solid state germanium detector and thus essentially pure Gaussian, as typical for energy-dispersive XRD [20,21].

Diffraction patterns for line profile analysis were acquired for 600 s. An example of the diffraction profile of the hardened condition is given in Figure 9.2. The $110_{\alpha'}$, $200_{\alpha'}$, $211_{\alpha'}$, $220_{\alpha'}$, $321_{\alpha'}$ and $411_{\alpha'}$ reflections of martensite were considered for line profile analysis. The $310_{\alpha'}$ and the $222_{\alpha'}$ reflections overlapped with the 400_{γ} and 331_{γ} reflections, respectively, and were thus excluded from the analysis. Further, the austenite reflections and the $400_{\alpha'}$ reflection of martensite provided insufficient diffracted intensity for accurate peak fitting and were thus also excluded from the analysis.

The diffraction data was fitted with Rietveld refinement with the model described in Ref. [20]. In Rietveld refinement the weighted sum of squared residuals of the measured and calculated intensities of the whole diffraction pattern is minimized by using a couple of refinable parameters. Line profiles were fitted with the generalized Thompson, Cox & Hastings [24] pseudo-Voigt model, which yields a close approximation of the deconvolution of the Gaussian and Lorentzian line profiles [20]. The physical Gaussian line profile, β_G, was obtained by correction of the fitted Gaussian line profile, $\beta_{meas,G}$, with the, in the present case, entirely Gaussian instrumental line profile, β_{instr} [25]:

$$\beta_G = \sqrt{\beta^2_{meas,G} - \beta^2_{instr}} \tag{9.2}$$

The convolution of the physical Gaussian and Lorentzian line profiles is approximated with ≅ 0.02 % inaccuracy by [26]:

$$\beta = 0.5346\beta_L + \sqrt{0.2166\beta_L^2 + \beta_G^2} \tag{9.3}$$

The corrected line profiles were analyzed with the modified Williamson-Hall (MWH) method to determine the dislocation density and particle size. The varying contrast of dislocations in different hkl causes nonlinear behavior of the magnitude of the diffraction vector, K, and the broadening of the line profiles, ΔK [22,27]. The contrast of dislocations depends on the relative orientation of the Burgers and line vectors of dislocations and the diffraction vector. In the MWH method average dislocation contrast factors, $\overline{C}$, are calculated and applied to account for the non-linear behavior [28,29]. The modified Williamson Hall method is given as [29]:

$$\Delta K \cong \frac{0.9}{D} + bM\sqrt{\frac{\pi}{2}\rho}(K\overline{C}^2) \tag{9.4}$$

where M is the dislocation distribution parameter, a dimensionless constant, b = 0.2 nm the magnitude of the Burgers vector, D the size of coherently diffracting domains, and ρ the dislocation density. The detailed procedure for the calculation of the average dislocation contrast factor, $\overline{C}$, is given in Appendix 1. As the MWH method contains two unknowns, M and ρ, the method is by itself semi-quantitative with an assumption for M. HajyAkbary

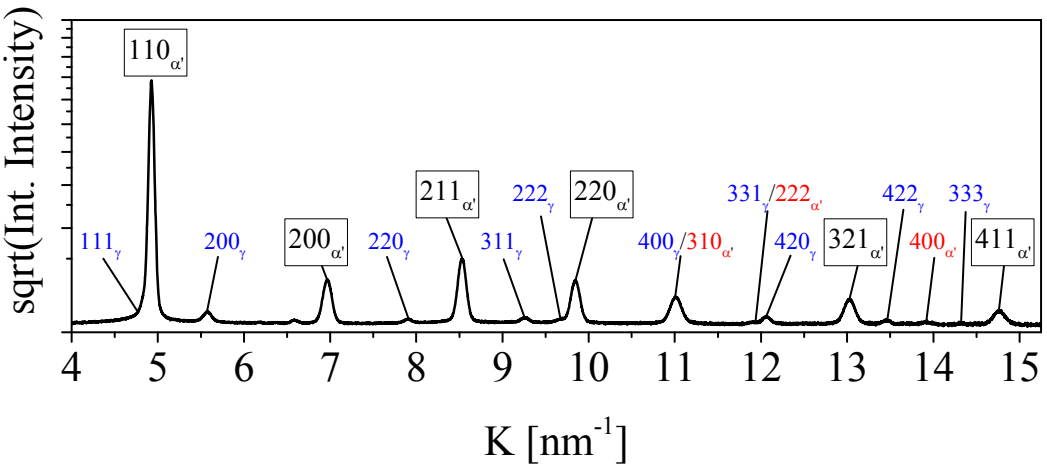

Figure 9.2: Diffractogram of the hardened condition with an overall integrated intensity of >10^9 counts. The vertical axis shows the square-root of integrated intensity to reveal reflections of minor intensity. Reflections of austenite are indicated by the blue labels and reflections of martensite that were excluded from line profile analysis are indicated by red labels. Martensite peaks considered for line profile analysis are indicated by the black, framed labels; The peak at K = 6.6 nm^{-1} is an escape peak of the Ge detector originating from the $211_{\alpha'}$ reflection.

et al. [18] determined 1.4 as a suitable value for M for the modified Williamson Hall method in lath martensite; this value is therefore applied in the present work.

9.2.3 Orientation mapping

Orientation mapping was carried out in an FEI Nova NanoLab 600 scanning electron microscope by applying electron backscatter diffraction (EBSD) on bulk samples and on-axis transmission Kikuchi diffraction (TKD) on electro-polished thin foils. The detector was a Bruker e-Flash EBSD detector. EBSD was carried out with 20 keV beam energy, 4.3 nA beam current, a step-size between Kikuchi patterns of 60 nm and 8.5 mm working distance. In on-axis TKD the untilted sample was positioned above an OPTIMUS™ TKD on-axis detector [30,31]. The beam energy was 30 keV, the beam current 1.7 nA, the step-size between Kikuchi patterns 12 nm and the working distance 3 mm.

9.2.4 Atom probe tomography

The instrument was a CAMECA LEAP 4000 HR®. Field evaporation was enabled by applying a high-voltage pulsed electric field (HV-pulse), generated by a local counter electrode in close proximity to the specimen. The analysis was conducted at 50 K, 20 % pulse fraction and 200 kHz pulse rate. The detection rate was 0.3 % in legacy mode. Most of the substitutional elements were observed as doubly charged ions and are thus detected with a mass over charge ratio half of their atomic mass. Only Mo also showed triply charged ions, in the region 31-33 Da, whereas Cu was the only element to show singly charged ions, at 63 and 65 Da. Regarding interstitial elements, C was detected as C^{+}, C^{2+}, C^{3+}, $(^{2}C)^{2+}$ and $(^{3}C)^{2+}$. Identification of N was more complicated, as this element, single charged, overlaps with the mass-to-charge ratio of doubly charged Si. In steels containing Mo, N has a very strong tendency to form molecular ions, MoN, that are detected as $(MoN)^{2+}$. In the current material virtually all N is detected as $(MoN)^{2+}$, as no characteristic shoulder is observed for the Si^{2+} peak at 14 Da. Average bulk compositions were determined from all data sets with more than 5 million ions. The standard deviation of interstitial content in terms of counting statistics [32] of individual measurements was $< 2.5 \times 10^{-3}$ at.% for both C and N.

9.3 Experimental results

9.3.1 Orientation mapping

Orientation mapping was applied to reveal the microstructure of lath martensite in the hardened condition. The orientation relationship of the present steel was identified as Kurdjumow-Sachs (K-S) in a previous investigation [33]. Figure 9.3a is an inverse pole-figure map from EBSD of a bulk specimen of martensite in the hardened condition. The coloration of the map represents the crystal orientation with reference to the extrusion direction of the material according to the colored triangle in Figure 9.3c. As typical for lath martensite, the microstructure is strictly hierarchical, which is a result of the minimization

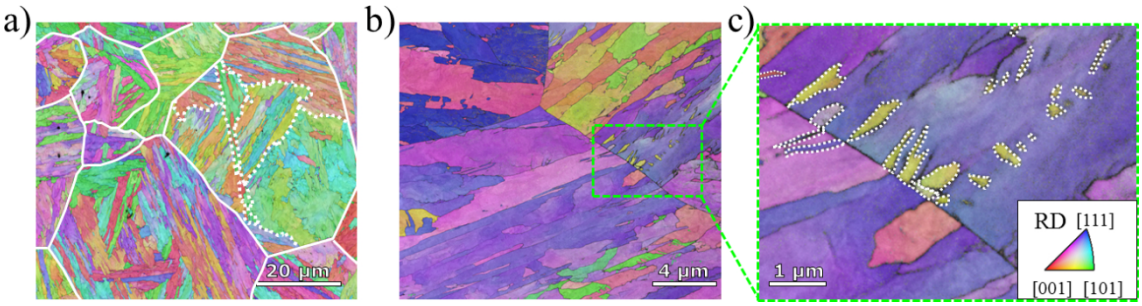

Figure 9.3: Inverse pole-figure maps of the hardened condition (a) Low-resolution map from EBSD showing the hierarchical subdivision of prior austenite grains (solid lines) to packets (examples given by broken lines) and blocks (parallel units within packets); (b) High-resolution map from TKD showing the division of blocks into laths; (c) Magnified section from TKD-map in Figure 9.3b showing individual laths (marked by dashed lines) that were approx. intersected perpendicular to their longitudinal direction. The average lath width, 133 ± 63 nm, was determined along the thinnest direction of the marked laths.

of the total shape strain [34]. Prior austenite grains (solid lines) are subdivided into packets (examples given by broken lines) and blocks (parallel units within packets). Orientation mapping with TKD on an electron-transparent sample at higher spatial resolution (Figure 9.3b) reveals that blocks are further subdivided into sub-blocks and laths. Sub- blocks are made up of laths of two K–S variants that are misoriented by 10.5°. The present intersection of the packet by the sample surface complicates the distinction in terms of blocks and sub-blocks. Figure 9.3c shows a magnified area from the map in Figure 9.3b. Here laths that are intersected approx. perpendicular by the sample surface are marked with dashed lines. Measurement along their thinnest direction yields an average lath width of 133 ± 63 nm. Wider laths in Figure 9.3b may not be intersected perpendicular to their thinnest dimension and would thus give a false estimate of the lath width.

9.3.1 Energy dispersive synchrotron X-ray diffraction

The diffraction pattern of the hardened condition in Figure 9.2 reveals the characteristic peaks for martensite and austenite. No asymmetry or splitting of the $200_{\alpha'}$ reflection is

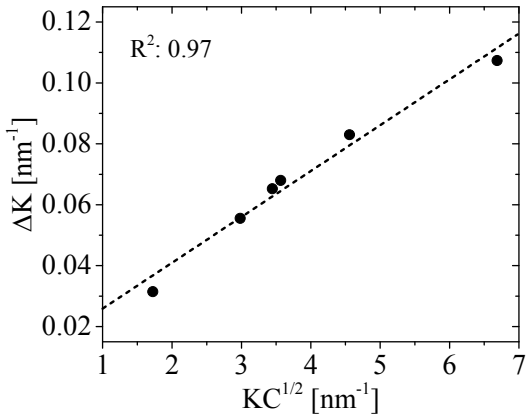

Figure 9.4: Linear ΔK vs. $KC^{1/2}$ plot of the modified Williamson-Hall method for martensite in the hardened condition.

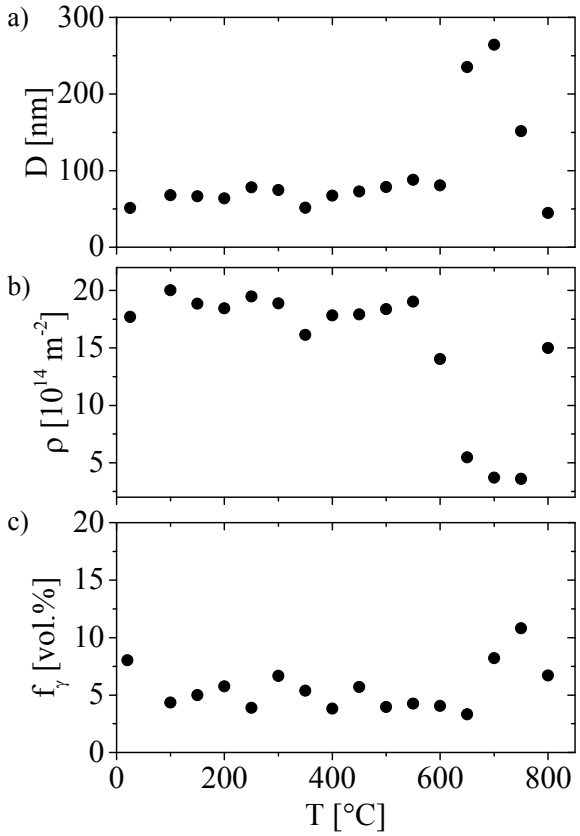

Figure 9.5: (a) Coherently diffracting particle size, d, (b) dislocation density, ρ, and (c) fraction of austenite, f_γ, at room-temperature as a function of tempering temperature.

observed, which confirms the absence of tetragonality for martensite with particularly low interstitial content [16,35]. The fraction of retained austenite was determined as 8 ± 0.5 vol.% by quantitative phase analysis.

Line profile analysis

The modified Williamson Hall analysis was applied to determine the dislocation density and coherently diffracting particle size for different tempering conditions. An example of a modified Williamson Hall plot is given in Figure 9.4. The relationship of ΔK vs. $K\overline{C}^{1/2}$ evidently follows a linear behavior. Evaluation of the y-intercept and slope in Equ. 9.4 yields the coherently scattering domain size, D, and dislocation density, ρ, respectively.

The evolution of dislocation density and coherently diffracting domain size of the hardened condition and tempered samples in the interval 100 to 800 °C is shown in Figure 9.5a and Figure 9.5b. The dislocation density of virgin martensite is $\sim 1.8 \times 10^{15}$ m^{-2} and remains approximately constant for tempering up to 550 °C. Tempering up 700 and 750 °C reduces the dislocation density to a seemingly steady value of 4×10^{14} m^{-2}. Tempering at 800 °C leads to a new increase in dislocation density to 1.5×10^{15} m^{-2}.

The coherently diffraction domain size in the as-hardened condition is initially 50 nm, evolves gradually to ~80 nm during tempering up to 600 °C and then significantly increases to 240 and 260 nm for tempering at 650 and 700 °C. Further tempering to 800 °C leads to a progressive decrease to the initial value of 50 nm.

Figure 9.5c show the fraction of austenite at room temperature as a function of tempering temperature. The fraction of austenite is initially 8 vol.% and gradually decreases to 3 vol.% by tempering to 650 °C. Tempering at 700 and 750 °C leads to a gradual increase in austenite fraction to 11 vol.%, while further tempering to 800 °C leads to a second reduction of the austenite fraction.

9.3.2 Atom Probe Tomography

For all analyzed samples, evaluation of the desorption pattern for multiple hits revealed the presence of a low-index crystallographic pole, at which the evaporation rate was greatly enhanced (see example in Figure 9.6). Analysis of the distribution of alloying elements revealed that Cr was systematically enriched along these poles. The Cr-enrichment is only apparent and originates from loss of Fe ions upon multiple hits. This effect is known as the pile-up effect [36–38]. The artefact was utilized by highlighting crystallographic poles with Cr iso-concentration surfaces of x_{Cr} > 23 at.% (Figure 9.7). The interruption and relative shift of these poles are an indication of the misorientation of adjacent grains and allow discrimination of lath boundaries, which are low angle grain boundaries (LAGBs) and packet, block or prior austenite boundaries, which are high angle grain boundaries (HAGBs).

All elements were approx. homogeneously distributed within laths and at lath boundaries in the virgin martensite condition. Figure 9.7a reveals an essentially homogeneous distribution of C across two martensite laths, indicated by the interrupted

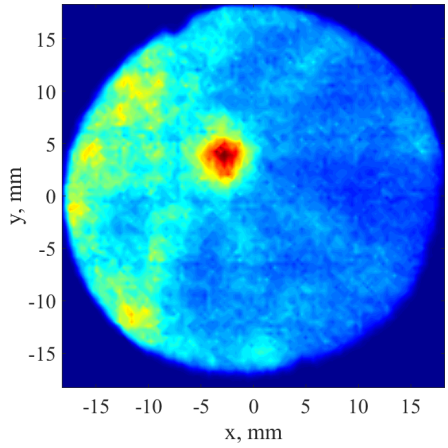

Figure 9.6: Desorption pattern of multiple hits showing the presence of a bcc low-order crystal pole. The high field-evaporation rate led to an artificial enrichment of Cr around the crystal pole (red area) and was used to identify grain boundaries and distinguish LAGBs (lath boundaries) from HAGBs.

Table 9.2: Average C and N concentrations of the hardened and tempered conditions in at.% in the bulk and peak concentrations at LAGBs and HAGBs. The bulk concentrations are average values containing the standard deviation of several measured samples. Peak concentrations at grain boundaries are based on few observations and thus indicative values.

	x_C^{bulk}	x_N^{bulk}	x_C^{LAGB}	x_N^{LAGB}	x_C^{HAGB}	x_N^{HAGB}
Hardened condition	0.164 ± 0.014	0.126 ± 0.006	/	/	/	/
295 °C / 0.033 K.s^{-1}	0.062 ± 0.018	0.096 ± 0.010	0.73	0.28	3.68	0.395
435 °C / 0.033 K.s^{-1}	0.048 ± 0.005	0.076 ± 0.010	0.10	0.09	/	/

crystallographic pole. The pole of the right grain is bent upwards close to the lath boundary, while the pole of the left grain remains straight. The average bulk concentration of C and N in the virgin martensite condition was 0.164 ± 0.014 and 0.126 ± 0.006 at.%,, respectively.

Figure 9.7b shows a sample which was tempered up to 295 °C. Extensive C enrichment and a large shift of the crystallographic pole indicate a HAGB, while the other segregated features are LAGB's, i.e. lath boundaries. The C concentration fluctuated slightly within the laths, which may indicate clustering of C. Segregation of C and N led to reduction of the bulk C and N concentrations to 0.062 ± 0.018 and 0.096 ± 0.010 at.%, respectively (Table 9.2). The C concentration at the HAGB increased by a factor 60 from 0.062 to 3.68 at.%, while the N concentration only increased by a factor of 4 from 0.096 to 0.395 at.%. The HAGB was further enriched in P by a factor 20, in Cr by 2.6 at.%, in Mo by 2.3 at.%, and by minor amounts of Nb and V in balance with Fe.

Samples that were tempered up to 435 °C revealed, similar to samples tempered up to 295 °C, segregation of C and N to lath boundaries, albeit to a lesser degree (Table 9.2).

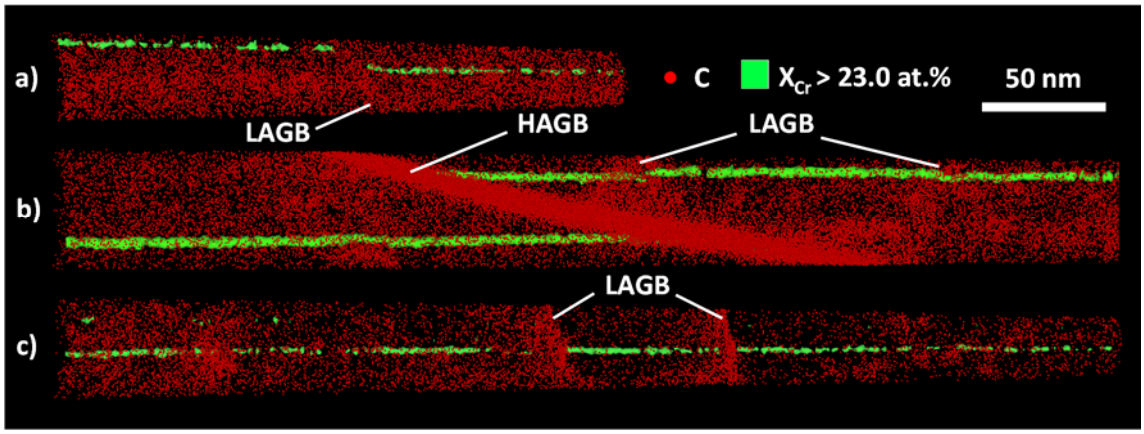

Figure 9.7: Atom probe reconstruction of a) virgin martensite, b) martensite after tempering to 295 °C and c) martensite after tempering to 435 °C. The red dots represent C atoms; the green surfaces are Cr iso-concentration surfaces for x_{Cr} > 23 at.% (artefact from pile-up effect), indicating crystallographic poles that reveal the presence and approx. misorientation of grain boundaries.

No indications of transition carbides were found, while more clustering of C was encountered compared to samples that were tempered up to 295 °C. Progressive segregation of C and N to lattice defects led to a further reduction of the bulk C and N concentration to 0.048 ± 0.005 and 0.076 ± 0.010 at.%. An overview of the bulk concentrations and approximate peak concentrations at grain boundaries of interstitially dissolved C and N is given in Table 9.2.

9.4 Discussion

9.4.1 Redistribution of alloying elements

The redistribution of alloying elements was measured by APT after tempering up to 295 and 435 °C and was compared to the distribution in the hardened condition. No noticeable segregation of interstitial elements was found in the hardened condition. This suggests that martensite formation below 135 °C occurred without autotempering and that no noticeable aging occurred during storage of the sample at room temperature over 6 months. Bending of the pole on the right side of the lath boundary in Figure 9.7a may indicate plastic accommodation of large shape strains during martensite formation. Sandvik and Wayman [39] studied Fe-20Ni-5Mn (wt.%) lath martensite by diffraction analysis in transmission electron microscopy and suggested that a thickening lath may accommodate the shape strain plastically when approaching the adjacent lath.

Heating to 295 °C evidently led to segregation of C and N to LAGBs and HAGBs. The enrichment in ferrite stabilizing elements at the HAGB in Figure 9.7b indicates a prior austenite grain boundary. Significant grain boundary segregation is only feasible at high temperature where austenite is the only matrix phase and the observed segregation profile is typical for grain boundaries in austenitic stainless steels [40,41]. The hardened condition should consequently reveal similar segregation of substitutional elements at prior austenite grain boundaries, while segregation of C and N may differ.

The interstitially dissolved elements, C and N, progressively segregated to crystal defects with increasing tempering temperature. This finding was supported by in-situ synchrotron XRD measurements in previous work [16]. The progressive decrease in C and N bulk content was accompanied by a decrease in segregated C and N content at lath boundaries (Table 9.2). This appears to be an effect of the balance of driving force and thermal activation energy. At low temperature the driving force from micro-strains and supersaturation of the bcc crystal with C and N should be highest, so that little provided thermal activation will induce segregation to microstructural features with particularly high driving force. At higher temperature more thermal activation is provided, leading to segregation at more microstructural features with lower driving force.

9.4.2 Recovery

Martensite formation is associated with a change in shape, which is accommodated by the surrounding retained austenite. The accommodation strain is partitioned between martensite and retained austenite, and amounts to 40 and -890 MPa, respectively, after completion of martensite formation at room temperature (c.f. previous work on the present material [12]). The reduction of this strain energy is not the dominant driving force for partitioning of the interstitials during tempering to 475 °C with a heating rate of 0.033 K s^{-1} (c.f. previous work on the present material [16]).

Speich [42] reported that, for low-carbon Fe-C martensite, dislocations between the lath boundaries recover at 500 – 600 °C, leading to an acicular ferrite grain structure. The recovery process removes LAGBs, while HAGBs are contained. Norström [43] and Grange et al. [44] both reported an effect of alloying additions on recovery. Addition of Mo [43,44] and addition of P, Ni, Si, Cr and V [44] were found to retard recovery by a solid-solution effect relative to Fe-C martensite. The decrease of dislocation density above 550 °C and the increase in particle size above 600 °C in the present investigation are thus consistent with recovery of martensite, i.e. annihilation of dislocations leading to removal of lath boundaries. Krauss [45] reported that the kinetics of recovery accelerate significantly with increasing temperature, which suggests that the present tempering time of 60 s led to noticeable annihilation of dislocations at 600 °C, but was insufficient for annihilation of lath boundaries, which commenced at 650 °C.

In Fe-C martensite, acicular ferrite grains may recrystallize above 600 °C [42,45]. In the present alloy, retarded recovery and low A_1, caused by the high Ni content, lead to austenite formation at lath boundaries instead [9]. Initially, tempering leads to a gradual reduction of the austenite content down to 3 vol.% at 650 °C compared to 8 vol.% in the hardened condition, which is consistent with decomposition of retained austenite reported in Refs. [46,47]. Further heating leads to a second increase in austenite content up to 11 vol.% at 750 °C. This so called reverted austenite is known to obtain its stability mainly from partitioning of Ni [9,33,48]. Further increase of the austenite fraction with annealing temperature leads to dilution of Ni and a consequent reduction in stability of austenite. Thus, new martensite forms upon quenching which manifests as an increase in dislocation density at 800 °C. The reason for the observed decrease in domain size at already 750 °C is not entirely clear. Possibly, the formation of reverted austenite as a second phase leads to reduction of individual coherently diffracting martensite domains.

9.4.3 Dislocation density

Only few quantitative studies on the dislocation density have been reported in literature. In the present study, the dislocation density of the hardened condition was $\sim 1.8 \times 10^{15}$ m^{-2} and decreased by tempering above 550 °C to a steady minimum value of $\sim 3.5 \times 10^{14}$ m^{-2} at 700 and 750 °C.

Measurement of the evolution of the dislocation density during martensite formation in a commercial 17–4PH steel with neutron diffraction by Christien et al. [15] is in good agreement with the present results. In their study, the dislocation density was reported as $\sim 4 \times 10^{15}$ m^{-2} after martensite formation and was reduced to a steady level of $\sim 3 \times 10^{14}$ m^{-2} by annealing at 600 °C for 600 s.

Results from Wiessner et al. [14] obtained with laboratory XRD on a soft martensitic stainless steel with similar composition to the here investigated alloy is in reasonable agreement. The dislocation density in the hardened condition was $\sim 7 \times 10^{14}$ m^{-2} and decreased down to $\sim 1 \times 10^{14}$ m^{-2} after isochronal heating to 600 °C with 0.82 K.s^{-1}. The dislocation density was virtually unaffected by tempering up to 550 °C, which is in line with the present findings.

9.4.4 Coherently diffracting particle size

The studies on the evolution of the dislocation density in low-carbon martensitic stainless steels by Christien et al. [15] and Wiessner et al. [14] both attribute a low effect to the coherently diffracting particle size on the broadening of line profiles. While Christien et al. neglect the effect of particle size completely [15], it is considered in the analysis of Wiessner et al., but found negligible compared to strain-broadening [14].

In the present case, a significant Lorentzian, i.e. particle size related, broadening was measured. The linear combination factor of the Pseudo-Voigt function, which takes the value 0 for pure Gaussian and 1 for pure Lorentzian, ranged from 0.25 to 0.42 for different heat-treatment conditions as an average of all reflections. While the evolution of the particle size with tempering temperature can be qualitatively interpreted in terms of recovery of martensite, the absolute values, ranging from 50 to 280 nm, are too small to be directly associated with either the lath size of 133 ± 63 nm or the block size of several μm (c.f. Figure 9.3b).

Ungár et al. [49] reported that the measured particle size in hierarchically, heavily deformed metallic materials, is commonly found smaller when measured with XRD line profile analysis as compared to measurements from micrographs. While low misorientation in the range of 1 – 2 ° within grains does not invoke a large contrast difference in electron microscopy, scattered X-rays from such regions are not coherent and thus lead to measurement of the sub-grain size rather than the grain size [49]. Sandvik and Wayman [39] showed that in an Fe-20Ni-5Mn (wt.%) lath martensite, apart from small variations in orientation of adjacent laths by < 2°, the orientation also varied along a single lath by < 1°. Consequently the measurement of a coherently diffracting particle size that is lower than the lath width could be a cause of slightly misoriented regions smaller than the lath size.

9.4.5 Austenite nucleation

During tempering, C and N gradually partitioned to lattice defects, mainly grain boundaries. Grain boundaries are known to act as preferred nucleation sites for reverted austenite [9,50–53] close to A_1 and the locally increased interstitial content should support austenite nucleation.

Recovery of martensite commenced above 550 °C, which is close to A_{c1} during heating with $0.033\ \mathrm{K.s^{-1}}$ [54]. Both recovery and nucleation of austenite require sufficient diffusional mobility of substitutional elements. In Fe-C lath martensite, recovery starts by annealing out low-angle grain boundaries, before recrystallization from acicular ferrite grains commences [42,45]. Apparently, the dominating driving force for recovery is a reduction of strain energy and grain boundary area. In the present system, solid solution strengthened martensite leads to delayed recovery with respect to Fe-C martensite [43,44] while nucleation of reverted austenite at lath boundaries leads to a softening of the material [3,55]. Thus, in the present system, recovery of martensite as a dominating process during tempering seems to be superseded by the nucleation and growth of reverted austenite.

9.5 Conclusion

The structural evolution of a X4CrNiMo16-5-1 soft martensitic stainless steel during tempering was investigated by analyzing synchrotron XRD line profiles, studying interstitial segregation with atom probe tomography and characterizing the morphology of martensite with site specific orientation mapping. The main conclusions are:

- Martensite formation below 135 °C occurred without autotempering and leads to a dislocation density in martensite of $\sim 1.8 \times 10^{15}\ \mathrm{m^{-2}}$.
- Tempering of martensite with $0.033\ \mathrm{K.s^{-1}}$ up to 475 °C leads to progressive rejection of C and N from solid solution to lattice defects, mainly grain boundaries.
- Isothermal tempering for 60 s does not affect the dislocation density below 550 °C.
- The dislocation density at room temperature decreases to a steady level of $\sim 3.5 \times 10^{14}\ \mathrm{m^{-2}}$ after tempering at 700 and 750 °C
- Austenite formation at 800 °C leads to formation of new martensite during cooling, leading to a new increase of the dislocation density
- The evolution of the coherently diffracting particle size from line profile analysis with tempering temperature is qualitatively consistent with recovery of martensite. Quantitatively, the obtained values are far smaller than the average lath width of 133 ± 63 nm, which is a known effect attributed to loss of X-ray coherency for low misorientations in plastically deformed metals.

Acknowledgements

M. Klaus and Ch. Genzel from Helmholtz Zentrum für Materialien und Energie (HZME) are acknowledged for their support during the activity at the HZB-BESSY II synchrotron facility. The activity was supported by the European Commission under the 7th Framework

Program through the 'Research Infrastructure' action of the 'Capacities' Programme, CALIPSO (Grant n: 312284). The Danish Underground Consortium is gratefully acknowledged for financial support to the Danish Hydrocarbon Research Center (DHRTC).

Appendix – Determination of average dislocation contrast factors

In an untextured polycrystal, for which the population of Burgers vectors can be assumed random, the average dislocation contrast factors $\overline{C}_{hkl}$ can readily be determined when the average contrast factor $\overline{C}_{h00}$ of the *{h00}* reflections and the parameter q is known: [27]

$$\overline{C}_{hkl} = \overline{C}_{h00}(1 - qH^2) \tag{9.5}$$

where q is a parameter describing the edge- or screw-character of dislocations and can be determined experimentally. H^2 is the fourth order ratio and can be calculated from the *hkl*: $H^2 = \frac{h^2l^2+h^2k^2+l^2k^2}{(h^2+k^2+l^2)^2}$. $\overline{C}_{h00}$ is determined by the dislocation contrast factors C_{h00} of pure screw and edge dislocation and the fraction of screw and edge dislocations. C_{h00} depends on the three elastic constants $c_{11} = 230$ GPa, $c_{12} = 135$ GPa and $c_{44} = 117$ GPa [56] of the material:

$$C_{h00,i} = a_i^c \left(1 - \exp\left(-\frac{A}{b_i^c}\right)\right) + c_i^c A + d_i^c \tag{9.6}$$

where A is the elastic anisotropy parameter $A = \frac{2c_{44}}{c_{11}-c_{12}}$ [57] and the index *i* indicates screw and edge dislocations. The parameters a_i^c, b_i^c, c_i^c, and d_i^c depend on the ratio c_{12}/c_{44} and can be found in Ref. [27]. In order to experimentally determine the parameter q Equ. 9.5 is inserted into the squared form of Equ. 9.4 to yield the following expression:[27]

$$\frac{\Delta K^2 - \alpha}{K^2} \approx \beta \overline{C}_{h00}(1 - qH^2) \tag{9.7}$$

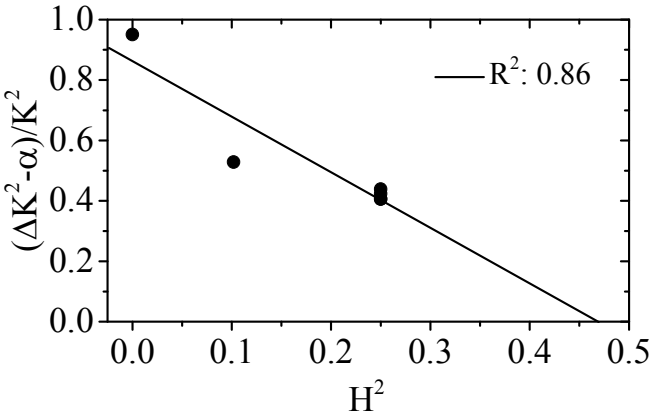

Figure 9.8: Experimental determination of parameter *q* by linear regression analysis of Equ. 9.7 for a measurement of the as austenitized condition.

where $\alpha = \left(\frac{0.9}{D}\right)^2$ and $\beta = \pi M^2 b^2 \rho/2$. Linear regression of the left hand of Equ. 9.7 over H^2 then yields the experimental value for q as the inverse x-intercept. An example of the determination of q is given in Figure 9.8.

Knowing the experimental value of q the fraction of edge- and screw-dislocations can be determined by:

$$f_{edge} = 1 - f_{screw} = \frac{q_{screw}^{th} - q}{q_{screw}^{th} - q_{edge}^{th}} \tag{9.8}$$

The parameters q_{screw}^{th} and q_{edge}^{th} are the theoretical q values for full screw- and edge dislocation contribution, respectively. These factor also depend on the ratio c_{12}/c_{44} of the material:

$$q_i^{th} = a_i^q \left(1 - \exp\left(-\frac{A}{b_i^q}\right)\right) + c_i^q A + d_i^q \tag{9.9}$$

where *i* indicates screw and edge dislocations and the parameters a_i^q, b_i^q, c_i^q, and d_i^q can be found in Ref. [27].

A more comprehensive description of the procedure for the determination of the average dislocation contrast factors, $\overline{C}$, can be found in Refs. [18,27].

References

[1] M. Grounes, S. Rao, New Alloy Steels for Nuclear Reactor Pressure Vessels and Vessel Internals, Trans. ASM. 62 (1969) 902–914.

[2] H.J. Niederau, A New Low-Carbon 16Cr-5Ni Stainless Martensitic Cast Steel, in: G. Behal, A.S. Melilli (Eds.), Stainl. Steel Cast., ASTM, Bal Harbour, Florida, 1982: pp. 382–393.

[3] M. Al Dawood, I.S. El Mahallawi, M.E. Abd El Azim, M.R. El Koussy, Thermal aging of 16Cr – 5Ni – 1Mo stainless steel Part 2 – Mechanical property characterisation, Mater. Sci. Technol. 20 (2004) 370–374.

[4] H.J. Niederau, Eigenschaften und Anwendungsmöglichkeiten der Guss- und Schmiedelegierung (G)X-5 CrNiMo 16 5 (Werkstoff-Nr. 1.4405), Zeitschrift Des Vereins Dtsch. Ingenieure Für Maschinenbau Und Met. Eig. 21 (1982) 801–808.

[5] A.W. Marshall, J.C.M. Farrar, Welding of Ferritic and Martensitic 11-14% Cr Steels, Weld. World. 45 (2001) 19–42.

[6] D.-S. Leem, Y.-D. Lee, J.-H. Jun, C.-S. Choi, Amount of retained austenite at room temperature after reverse transformation of martensite to austenite in an Fe–13%Cr–7%Ni–3%Si martensitic stainless steel, Scr. Mater. 45 (2001) 767–772.

[7] M. Kuzmina, D. Ponge, D. Raabe, Grain boundary segregation engineering and austenite reversion turn embrittlement into toughness: Example of a 9 wt.% medium Mn steel, Acta Mater. 86 (2015) 182–192.

[8] Y. Song, D.H. Ping, F.X. Yin, X.Y. Li, Y.Y. Li, Microstructural evolution and low temperature impact toughness of a Fe–13%Cr–4%Ni–Mo martensitic stainless steel, Mater. Sci. Eng. A. 527 (2010) 614–618.

[9] F. Niessen, Austenite reversion in low-carbon martensitic stainless steels – a CALPHAD-assisted review, Mater. Sci. Technol. (2018). doi:10.1080/02670836.2018.1449179.

[10] W. Jiang, K. Zhao, D. Ye, J. Li, Z. Li, J. Su, Effect of Heat Treatment on Reversed Austenite in Cr15 Super Martensitic Stainless Steel, J. Iron Steel Res. Int. 20 (2013) 61–65.

[11] S. Zhang, P. Wang, D. Li, Y. Li, Investigation of the evolution of retained austenite in Fe-13%Cr-4%Ni martensitic stainless steel during intercritical tempering, Mater. Des. 84 (2015) 385–394.

[12] M. Villa, F. Niessen, M.A.J. Somers, In situ investigation of the evolution of lattice strain and stresses in austenite and martensite during quenching and tempering of steel, Metall. Mater. Trans. A. 49 (2017) 1–13.

[13] T. Maki, Morphology and substructure of martensite in steels, in: E. Pereloma, D. V. Edmonds (Eds.), Phase Transform. Steels Vol. 2 Diffus. Transform. High Strength Steels, Model. Adv. Anal. Tech., 1st ed., Woodhead Publishing, 2012: pp. 34–58.

[14] M. Wiessner, E. Gamsjäger, S. van der Zwaag, P. Angerer, Effect of reverted austenite on tensile and impact strength in a martensitic stainless steel−An in-situ X-ray diffraction study, Mater. Sci. Eng. A. 682 (2017) 117–125.

[15] F. Christien, M.T.F. Telling, K.S. Knight, Neutron diffraction in situ monitoring of the dislocation density during martensitic transformation in a stainless steel, Scr. Mater. 68 (2013) 506–509.

[16] F. Niessen, M. Villa, F. Danoix, J. Hald, M.A.J. Somers, In-situ analysis of redistribution of carbon and nitrogen during tempering of low interstitial martensitic stainless steel, Submitted. (2018).

[17] M.K. Miller, G.D.W. Smith, Atom probe microanalysis: principles and applications to materials problems, Materials Research Society, USA, 1989.
[18] F. HajyAkbary, J. Sietsma, A.J. Böttger, M.J. Santofimia, An improved X-ray diffraction analysis method to characterize dislocation density in lath martensitic structures, Mater. Sci. Eng. A. 639 (2015) 208–218.
[19] C. Genzel, I. a. Denks, M. Klaus, The Materials Science Beamline EDDI for Energy-Dispersive Analysis of Subsurface Residual Stress Gradients, Mater. Sci. Forum. 524–525 (2006) 193–198.
[20] D. Apel, M. Klaus, C. Genzel, D. Balzar, Rietveld refinement of energy-dispersive synchrotron measurements, Zeitschrift Fur Krist. 226 (2011) 934–943.
[21] J.W. Otto, On the peak profiles in energy dispersive powder X-ray diffraction with synchrotron radiation, J. Appl. Crystallogr. 30 (1997) 1008–1015.
[22] L. Gerward, S. Mørup, H. Topsøe, F. Gerward, L. Mørup, H. Topsøe, Particle size and strain broadening in energy-dispersive x-ray powder patterns, J. Appl. Phys. 47 (1976) 822–825.
[23] H.-Z.B. für M. und Energie, The 7T-MPW-EDDI beamline at BESSY II, J. Large-Scale Res. Facil. 2 (2016) 1–6.
[24] P. Thompson, D.E. Cox, J.B. Hastings, Rietveld Refinement of Debye-Scherrer Synchrotron X-ray Data from Al2O3, J. Appl. Crystallogr. 20 (1987) 79–83.
[25] T.H. de Keijser, J.I. Langford, E.J. Mittemeijer, A.B.P. Vogels, Use of the Voigt function in a single-line method for the analysis of X-ray diffraction line broadening, J. Appl. Crystallogr. 15 (1982) 308–314.
[26] J.J. Olivero, R.L. Longbothum, Empirical fits to the Voigt line width: A brief review, J. Quant. Spectrosc. Radiat. Transf. 17 (1977) 233–236.
[27] T. Ungár, I. Dragomir, Á.;. Révész, A. Borbély, The contrast factors of dislocations in cubic crystals: the dislocation model of strain anisotropy in practice, J. Appl. Crystallogr. 32 (1999) 992–1002.
[28] M. Wilkens, K. Herz, H. Mughrabi, An X-Ray Diffraction Study of Cyclically and of Unidirectionally Deformed Copper Single Crystals, Zeitschrift Für Met. 71 (1980) 376–384.
[29] T. Ungár, A. Borbély, The effect of dislocation contrast on x-ray line broadening: A new approach to line profile analysis, Appl. Phys. Lett. 69 (1996) 3173–3175.
[30] F. Niessen, A. Burrows, A.B.D.S. Fanta, A systematic comparison of on-axis and off-axis transmission Kikuchi diffraction, Ultramicroscopy. 186 (2018) 158–170.
[31] J.J. Fundenberger, E. Bouzy, D. Goran, J. Guyon, H. Yuan, A. Morawiec, Orientation mapping by transmission-SEM with an on-axis detector, Ultramicroscopy. 161 (2016) 17–22.
[32] F. Danoix, G. Grancher, A. Bostel, D. Blavette, Standard deviations of composition measurements in atom probe analyses-Part II: 3D atom probe, Ultramicroscopy. 107 (2007) 739–743.
[33] F. Niessen, F.B. Grumsen, J. Hald, M.A.J. Somers, Formation and stabilization of reversed austenite in supermartensitic stainless steel, in: Proc. 24th IFHTSE Congr., 2017: pp. 138–145.
[34] S. Morito, X. Huang, T. Furuhara, T. Maki, N. Hansen, The morphology and crystallography of lath martensite in alloy steels, Acta Mater. 54 (2006) 5323–5331.
[35] L. Cheng, A. Böttger, T.H. de Keijser, E.J. Mittemeijer, Lattice parameters of iron-carbon and iron-nitrogen martensites and austenites, Scr. Metall. Mater. 24 (1990) 509–514.
[36] M. Thuvander, J. J. Weidow, J. Angseryd, L.K.L. Falk, F. Liu, M. Sonestedt, K.

Stiller, H.O. Andrén, Quantitative atom probe analysis of carbides, Ultramicroscopy. 111 (2011) 604–608.
[37] G. Miyamoto, K. Shinbo, T. Furuhara, Quantitative measurement of carbon content in Fe-C binary alloys by atom probe tomography, Scr. Mater. 67 (2012) 999–1002.
[38] U. Rolander, H.-O. Andren, Statistical correction for pile-up in the atom-probe detector system, Colloq. Phys. 50 (1989) 529–534.
[39] B.P.J. Sandvik, C.M. Wayman, Characteristics of Lath Martensite: Part I. Crystallographic and Substructural Features, Metall. Trans. A. 14 (1983) 809–822.
[40] L. Karlsson, H.O. Andrén, H. Nordén, Grain Boundary Segregation in an Austenitic Stainless Steel Containing Boron - an Atom-Probe Study, Scr. Metall. 16 (1982) 297–302.
[41] L. Karlsson, H. Nordén, Overview no. 63 Non-equilibrium grain boundary segregation of boron in austenitic stainless steel-IV. Precipitation behaviour and distribution of elements at grain boundaries, Acta Metall. 36 (1988) 35–48.
[42] G.R. Speich, Tempering of Low-Carbon Martensite, Trans. Metall. Soc. AIME. 245 (1969) 2553–2564.
[43] L.Å. Norström, The relation between microstructure and yield strength in tempered low-carbon lath martensite with 5% nickel, Met. Sci. (1976) 429–436.
[44] R.A. Grange, C.R. Hribal, L.F. Porter, Hardness of tempered martensite in carbon and low-alloy steels, Metall. Trans. A. 8 (1977) 1775–1785.
[45] G. Krauss, Tempering of Lath Martensite in Low and Medium Carbon Steels: Assessment and Challenges, Steel Res. Int. 87 (2017) 1700038.
[46] A. Bojack, L. Zhao, P.F. Morris, J. Sietsma, In Situ Thermo-magnetic Investigation of the Austenitic Phase During Tempering of a 13Cr6Ni2Mo Supermartensitic Stainless Steel, Metall. Mater. Trans. A Phys. Metall. Mater. Sci. 45 (2014) 5956–5967.
[47] M. De Sanctis, G. Lovicu, R. Valentini, A. Dimatteo, R. Ishak, U. Migliaccio, R. Montanari, E. Pietrangeli, Microstructural Features Affecting Tempering Behavior of 16Cr-5Ni Supermartensitic Steel, Metall. Mater. Trans. A Phys. Metall. Mater. Sci. 46 (2015) 1878–1887.
[48] J.D. Escobar, J.D. Poplawsky, G.A. Faria, J. Rodriguez, J.P. Oliveira, C.A.F. Salvador, P.R. Mei, S.S. Babu, A.J. Ramirez, Compositional analysis on the reverted austenite and tempered martensite in a Ti-stabilized supermartensitic stainless steel: Segregation, partitioning and carbide precipitation, Mater. Des. 140 (2018) 95–105.
[49] T. Ungár, G. Tichy, J. Gubicza, R.J. Hellmig, Correlation between subgrains and coherently scattering domains, Powder Diffr. 20 (2005) 366–375.
[50] R. Schnitzer, R. Radis, M. Nöhrer, M. Schober, R. Hochfellner, S. Zinner, E. Povoden-Karadeniz, E. Kozeschnik, H. Leitner, Reverted austenite in PH 13-8 Mo maraging steels, Mater. Chem. Phys. 122 (2010) 138–145.
[51] Y.-K. Lee, H.-C. Shin, D.-S. Leem, J.-Y. Choi, W. Jin, C.-S. Choi, Reverse transformation mechanism of martensite to austenite and amount of retained austenite after reverse transformation in Fe-3Si-13Cr-7Ni (wt-%) martensitic stainless steel, Mater. Sci. Technol. 19 (2003) 393–398.
[52] W.H. Yuan, X.H. Gong, Y.Q. Sun, J.X. Liang, Microstructure Evolution and Precipitation Behavior of 0Cr16Ni5Mo Martensitic Stainless Steel during Tempering Process, J. Iron Steel Res. Int. 23 (2016) 401–408.
[53] Y.Y. Song, X.Y. Li, L.J. Rong, Y.Y. Li, T. Nagai, Reversed austenite in 0Cr13Ni4Mo martensitic stainless steels, Mater. Chem. Phys. 143 (2014) 728–734.
[54] F. Niessen, M. Villa, J. Hald, M.A.J. Somers, Kinetics analysis of two-stage

austenitization in supermartensitic stainless steel, Mater. Des. 116 (2017) 8–15.
[55] M. Al Dawood, I.S. El Mahallawi, M.E. Abd El Azim, M.R. El Koussy, Thermal aging of 16Cr – 5Ni – 1Mo stainless steel Part 1 – Microstructural analysis, Mater. Sci. Technol. 20 (2004) 363–369.
[56] S.A. Kim, W.L. Johnson, Elastic constants and internal friction of martensitic steel, ferritic-pearlitic steel, and alpha-iron, Mater. Sci. Eng. A. 452–453 (2007) 633–639.
[57] C. Zener, Elasticity and Anelasticity of Metals, University of Chicago Press, 1948.

10 Manuscript V

Kinetics analysis of two-stage austenitization in supermartensitic stainless steel*

Frank Niessen[a,†], Matteo Villa[b], John Hald[b], Marcel A.J. Somers[b]

[a] Technical University of Denmark (DTU), Danish Hydrocarbon Research and Technology Centre (DHRTC) , Elektrovej building 375, 2800 Kgs. Lyngby, Denmark

[b] Technical University of Denmark (DTU), Department of Mechanical Engineering, Produktionstorvet building 427, 2800 Kgs. Lyngby, Denmark

[†] Corresponding author

Abstract

The martensite-to-austenite transformation in X4CrNiMo16-5-1 supermartensitic stainless steel was followed in-situ during isochronal heating at 2, 6 and 18 K.min^{-1} applying energy-dispersive synchrotron X-ray diffraction at the BESSY II facility. Austenitization occurred in two stages, separated by a temperature region in which the transformation was strongly decelerated. The region of limited transformation was more concise and occurred at higher austenite phase fractions and temperatures for higher heating rates. The two-step kinetics was reproduced by kinetics modeling in DICTRA. The model indicates that the austenitization kinetics is governed by Ni-diffusion and that slow transformation kinetics separating the two stages is caused by soft impingement in the martensite phase. Increasing the lath width in the kinetics model had a similar effect on the austenitization kinetics as increasing the heating-rate.

* Published work: F. Niessen, M. Villa, J. Hald, M.A.J. Somers, Kinetics analysis of two-stage austenitization in supermartensitic stainless steel, Mater. Des. 116 (2017) 8–15. The format of the published article was adapted to the format of the doctoral thesis.

10.1 Introduction

Supermartensitic stainless steels are low carbon lath martensitic steels based on the Fe-Cr-Ni system [2,3]. This class of steels has gained popularity in the oil and gas sector as a low cost alternative to highly alloyed duplex stainless steels in pipeline applications [4].

The excellent strength and toughness properties are obtained through inter-critical annealing (tempering below A_3) to promote the formation of lamellar reversed austenite on high- and low-angle boundaries of lath martensite [5–8]. The annealing leads to an effective decrease of the average grain size and to a "composite structure" of hard tempered martensite and soft austenite. During plastic deformation, such a structure hinders dislocation movement over long distances. Reversed austenite was furthermore reported to strengthen the material during plastic deformation by transformation induced plasticity (TRIP) [9–12].

The formation of lamellar austenite was reported to be promoted by the establishment of an energetically favorable phase-interface (Kurdjumov-Sachs [13–16]), and might be affected by residual stress of the martensite transformation and grain-boundary segregation [17]. Partitioning of Ni is a well-documented mechanism of stabilizing reversed austenite to room temperature [9,18–21]. Furthermore, the internal substructure of austenite [9] and the size and shape distributions of the austenite regions [11], were suggested to affect thermal stability. With increasing annealing temperature, the austenite was reported to approach a coarser, spherodized morphology, which decreases the phase stability upon cooling [11].

Studies on isochronal heating of different steel alloys have shown that austenitization can occur in multiple stages [22–28]. In all these cases two-stage austenitization was found to be based on a given or evolving inhomogeneous microstructure during heating, which gave rise to locally varying driving forces for austenite formation, dissolution of phases and related diffusion or shear processes.

Bojack et al. showed in a comprehensive in-situ study that also 13Cr6Ni2Mo supermartensitic stainless steel exhibits two distinct stages of austenite formation during isochronal heating [24]. In a later study the two-stage austenitization kinetics was analyzed with a Kissinger-like method applying a range of heating rates [23]. It was suggested that the two-step kinetics was a result of solute redistribution during the growth of austenite. The first stage was assumed to be mainly caused by partitioning of Ni and Mn and the second stage by dissolution of carbides and increased diffusivity of Ni and Mn. Two-stage austenitization kinetics was also observed for austenitization of X4CrNiMo16-5-1 (EN 1.4418) supermartensitic stainless steel by dilatometry and in-situ synchrotron X-ray diffraction [29].

The kinetics of the two transformation stages in both investigated supermartensitic stainless steels depended on heating rate, thus it appears as if they are governed by a

thermally activated process [19]. From the listed investigations on the multi-stage austenitization kinetics in different steel alloys, all thermally activated transformations were identified as diffusion controlled. Therefore it appears as if the responsible mechanisms for two stage austenitization can be identified from kinetics modeling of the diffusion process.

As part of a physics-based modeling framework Galindo-Nava et al. modelled diffusion controlled reversion of austenite from lath martensite during isothermal holding based on transformation of a single lath [30]. The model describes the grain boundary kinetics dependent on the geometrical constraints of the lath, the equilibrium phase fraction of austenite and an effective diffusivity parameter. The model successfully predicted the austenite phase fraction during isothermal annealing in a range of alloys, but does not take multicomponent diffusion into account. Thus the well-documented solute partitioning during austenite reversion [9,18–21], which according to Bojack et al. is responsible for the two-step kinetics [23], is not reflected in such a model.

Esin et al. modelled two stage austenitization from cementite and ferrite in a low-alloy steel using the kinetics model for diffusion controlled transformations DICTRA [22]. In this study the two stage austenitization was shown to depend on the redistribution of carbon from the inhomogeneous initial microstructure of cementine and ferrite. The kinetics model DICTRA is suited to simulate diffusion controlled transformations in multi-component systems by numerically solving the multi-component diffusion equation, and thus appears ideal for the analysis of austenitization of supermartensitic stainless steel in two stages. Therefore, in the present work, the martensite-to-austenite transformation in a X4CrNiMo16-5-1 was followed in-situ with energy-dispersive synchrotron X-ray diffraction and analyzed with kinetics modeling in DICTRA.

10.2 Experimental procedure

10.2.1 Material and heat treatments

Samples were machined from a Ø10 mm rod EN 1.4418 steel grade in as-extruded condition. The composition of the alloy is given in Table 10.1. The samples for energy dispersive synchrotron X-ray diffraction (XRD) were ground to Ø10 mm x 0.15 mm discs and subsequently electro-polished for 30 s at 25 V with Struers A2 electrolyte to reduce the strain-affected layer in the surface. Prior to investigation, samples were normalized at 950 °C for 10 min in an Ar flow. The average heating and cooling rate were 45 and 70 $K.min^{-1}$, respectively.

Table 10.1: Chemical composition of the investigated alloy X4CrNiMo-16-5-1 SMSS determined with optical emission spectroscopy balanced with Fe (wt%).

Fe	C	N	Cr	Ni	Mo	Mn	Si	P	S
bal	0.03	0.037	15.00	5.80	1.03	0.86	0.39	0.025	0.008

The sample for characterization by Transmission Kikuchi Diffraction, was prepared from a dilatometry specimen, for which isochronal heating with 15 K.min^{-1} was interrupted at 650 °C. The sample was a thin foil which was thinned by electrolytic twin-jet polishing in 10 % perchloric acid dissolved in ethanol at -20 °C.

10.2.2 Energy dispersive synchrotron X-ray diffraction

The investigation was carried out at the EDDI-beamline at the synchrotron facility HZB-BESSY II [31]. It consisted of a series of isochronal heating tests at applied heating rates 2, 6 and 18 K.min^{-1} within the temperature interval 25 - 920 °C. Specimens were mounted on an Anton Paar DHS 1100 Domed Hot Stage and investigated under continuous Ar flow. The temperature was measured with a thermocouple attached to the heating stage. The experiments were conducted in a symmetric diffraction geometry with a constant scattering angle 2θ = 14° and a 2 x 0.5 mm primary slit configuration. In energy-dispersive X-ray diffraction all reflections are acquired simultaneously, which enables accurate quantitative phase analysis over temperature. Diffraction peaks occur for certain energies E_{hkl}, which are a function of the respective interplanar spacing, d_{hkl}, and the fixed scattering angle, 2θ [32]. The diffraction peaks were fitted with a Pseudo-Voigt profile and the phase fractions were determined by the direct comparison method [33]. Detailed descriptions of the procedures applied for peak fitting and quantitative phase analysis are reported in [29].

10.2.3 Transmission Kikuchi Diffraction

Transmission Kikuchi Diffraction (TKD) was carried out on electro-polished thin foils in an FEI Nova NanoLab 600 scanning electron microscope. The Kikuchi patterns were acquired with a Bruker e-Flash EBSD detector, configured with a horizontal OPTIMUS TKD detector head. No tilt was applied to the sample. The working distance was 3 mm, the acceleration voltage 30 kV, the beam current 1.7 nA and the step-size in-between successive TKD patterns was 16 nm. The orientation data were cleaned and smoothed by a minimum grain-size criterion and a smoothing spline filter by using the texture analysis software MTEX [34].

10.3 Experimental Results

10.3.1 Energy dispersive synchrotron X-ray diffraction

The measured transformation curves in Figure 10.1a show that transformation occurs in the temperature range 570 °C to 925 °C. The initial fraction of retained austenite was about 5 ± 1 vol.% for all investigated conditions. A change in heating rate from 2 to 18 K.min^{-1} led to a shift of the temperature of maximum transformation rate from 640 to 670 °C. Upon further heating the transformation to austenite slowed down. For heating at 2 K.min^{-1} the deceleration smoothly developed into the second stage of austenitization. For heating at 6 and 18 K.min^{-1}, the deceleration approached an actual interruption of the transformation and two steps can be discerned clearly. The minimum transformation rate for the heating

rates 2, 6 and 18 K.min^{-1} are reached at 763, 763 and 760 °C, respectively, at austenite fractions of 71, 74 and 76 vol. %, respectively. Further heating led to a new increase in the transformation rate, which again showed a shift to higher temperature of fastest transformation for faster heating; the maximum transformation rate is observed at 846, 866 and 925 °C for 2, 6 and 18 K.min^{-1}, respectively. The contribution of a thin oxide layer to the diffraction patterns was apparent above 900 °C for heating with 2 K.min^{-1} and excluded from phase quantification.

Evidently, reversed austenite formation takes place in two-steps and the heating rate defines the maxima of the transformation rate. Supplementary measurements of the transformation kinetics with dilatometry for heating rates 2-100 K.min^{-1} consistently yielded two-stage transformation kinetics [29].

10.3.2 Transmission Kikuchi diffraction

The microstructure from a dilatometry experiment, in which isochronal heating at 15 K.min-1 was interrupted at 650 °C, was characterized. The indicated inter-critical annealing treatment was chosen because it promoted the formation of 20 vol.% thermally stable reversed austenite and was thus ideal to determine a setup of a diffusion model, that reflects the microstructure of the in-situ investigation. Figure 10.2a shows the inverse pole figure map of austenite superimposed to the band-contrast map of martensite. Figure 10.2b shows low-angle grain boundaries (LAGB, $1° < \theta < 15°$) and high-angle grain boundaries (HAGB, $\theta > 15°$) of lath martensite colored in green and red, respectively, and the interphase boundaries, which are all HAGBs, colored in white. Not all lath boundaries could be indexed by orientation mapping, since adjacent laths of the same variant in low carbon martensite may have very low misorientation [35–37] and thus fall below the misorientation threshold of 1°. The spacing of austenite lamellae approximately followed the martensite lath spacing and varied for different blocks of martensite, depending on the

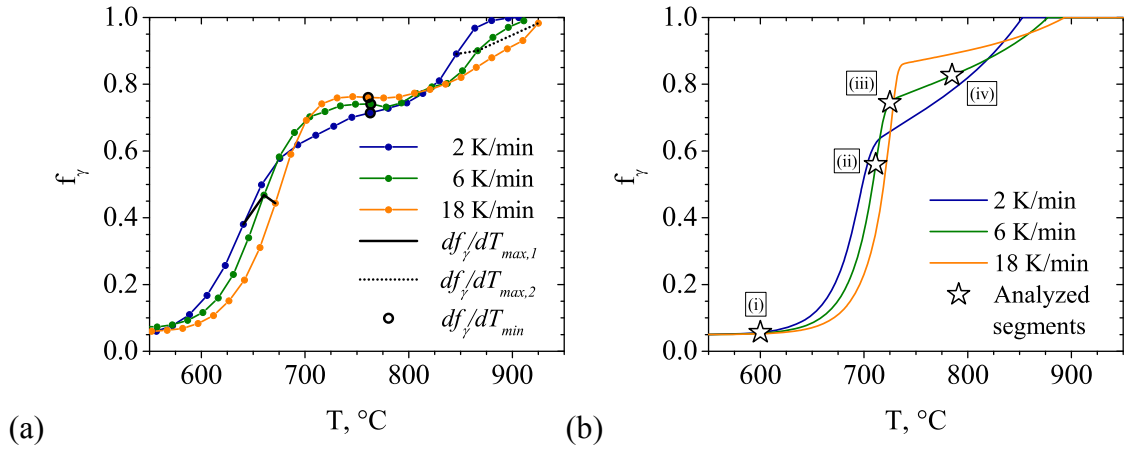

Figure 10.1: Fraction austenite over temperature for isochronal heating with 2, 6 and 18 K.min^{-1} (a) followed in-situ with XRD. The maximum and minimum transformation rates are indicated by the broken lines and data points, respectively; (b) modeled with kinetics modeling. The analyzed segments in Figure 10.4 for heating with 6 K.min^{-1} are marked with points (i) to (iv).

intersection angle of the specimen surface with the respective microstructure. By measuring the distance of the smallest identified regular austenite lamellae spacings in the different blocks the average lath width was approximated to 250 nm.

10.4 Kinetics modeling

In order to elucidate the mechanism responsible for the observed two-step kinetics, the austenitization was modeled with DICTRA, a software package for simulation of diffusion controlled reactions in multi-component alloy systems [38]. In contrast to Kissinger-like methods, which require fitting to an Arrhenius type of transformation and yield effective activation energies for heterogeneous transformations [39], the analysis with kinetics modeling is carried out with direct forward modeling based on constitutive equations and the thermodynamics and kinetics databases TCFE6 [40] and MOB2 [41]. Austenitization was modeled using the moving phase-boundary model within DICTRA.

A comprehensive description on the foundation of the DICTRA software is given in Ref. [38]. A short summary of the governing equations is given in the following. Diffusion in DICTRA is modelled based on Fick's second law

$$\frac{\partial c_k}{\partial t} = \frac{\partial}{\partial z}(-J_k) \tag{10.1}$$

where c_k is the concentration, and J_k the flux of component *k*. The flux of component *k* in a multi-component system with *n* components is determined by the spatial gradient of the chemical potential μ_i of all components and the proportionality factors L'_{ki}, which are based on the mobilities of the individual species:

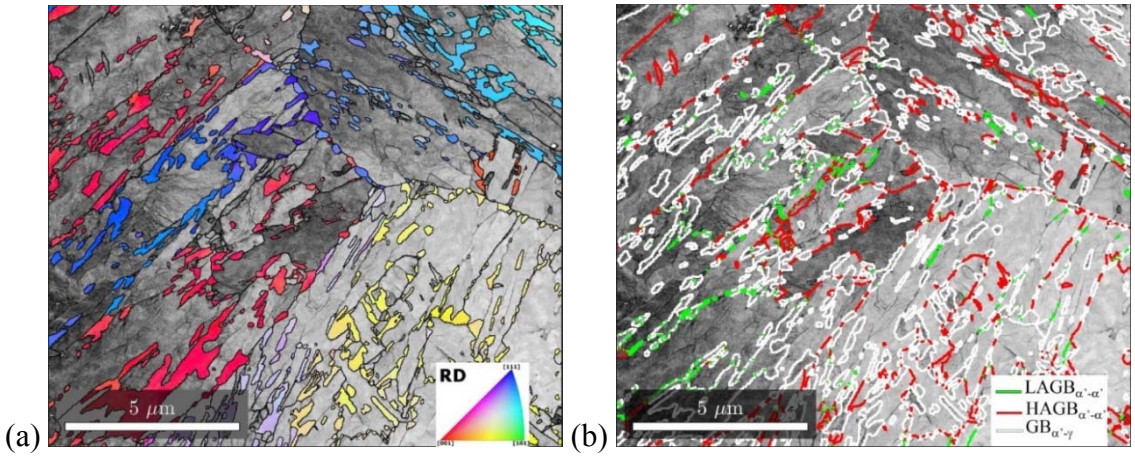

Figure 10.2: Transmission Kikuchi Diffraction (TKD) (a) Inverse Pole Figure Map of austenite on band-contrast map of martensite for interrupted heating at 650 °C. Austenite forms on lath boundaries; (b) Grain boundary map. LAGBs ($1° < \theta < 15°$) and HAGBs ($\theta > 15°$) in martensite are indicated by green and red coloring, respectively, and inter-phase boundaries are colored in white.

$$J_k = -\sum_{i=1}^{n} L'_{ki} \frac{\partial \mu_i}{\partial z} \tag{10.2}$$

It is noted that the L'_{ki} factors are purely kinetic quantities, whereas the chemical potential gradients are purely thermodynamic quantities. The basic data for computation of these parameters are obtained from experimental data and are stored in kinetics and thermodynamics databases, respectively. The composition dependence of the parameters is determined by a Redlich-Kister expansion [42].

In the moving boundary model single-phase regions are separated by an interface, which migrates based on the rate of diffusion to and from the interface. For each time step the boundary condition at the phase interface is calculated by assuming local equilibrium and the diffusion problem is solved for each single-phase region. Migration of the interface between two phases α and γ is then calculated by solving a flux balance equation for *n*-1 components [43]

$$v^{\alpha/\gamma}\left(c_k^{\alpha} - c_k^{\gamma}\right) = J_k^{\alpha} - J_k^{\gamma} \tag{10.3}$$

where $v^{\alpha/\gamma}$ is the interface velocity.

10.4.1 Model setup

Transmission Kikuchi Diffraction (Figure 10.2) showed that reversed austenite forms on both low- and high-angle boundaries, consistent with results from previous investigations [9,13–15,44,45]. Since the spacing of reversed austenite roughly follows the martensite lath spacing, austenitization was modelled by simulation of austenite formation and growth within one martensite lath. The model was thus setup as a 1-dimensional diffusion domain, d, which due to symmetry was defined as half the martensite lath width (Figure 10.3). The domain was discretized to 100 grid-points and set up with zero-flux boundary conditions. In order to show the impact of the martensite lath spacing on the austenitization kinetics, the domain size was varied in a series of additional simulations. The simulation was carried out with a time step of 50 ms and commenced in a ferrite single phase region, which served as the thermodynamic equivalent of very low carbon lath martensite. For the sake of understanding, the region is referred to as martensite in the analysis of the results. Upon isochronal heating the formation of austenite in a planar interface geometry was allowed.

Due to uncertainties of the local distribution of retained austenite in the microstructure, the initial fraction of retained austenite was not taken into consideration in the kinetics model, which only considers reversed austenite formation on lath boundaries. XRD quantitative phase analysis revealed 5 vol.% of retained austenite in the initial microstructure and EBSD analysis revealed that some of the retained austenite was present in inhomogeneously distributed chunky morphology [46]. Thus, the initial amount of chunky retained austenite was represented as a fixed value in the transformation curves

(Figure 10.1b), and the remaining fraction was determined by the simulated formation of austenite from a martensite lath.

The moving phase boundary model in DICTRA is based on the formation and evolution of a single grain of austenite and does not include a classic nucleation model. Other models, as the Thermo-Calc precipitation module [47], are available and well suited for analyzing nucleation and competitive growth, but do not treat the diffusion controlled evolution of two phases, which is the purpose of this investigation. DICTRA does however allow for input of a critical driving force for precipitation of austenite, which makes it possible to account for a nucleation barrier. Since the nucleation mechanism of reversed austenite has not been determined unequivocally by experimental means (see section 10.5, General discussion), the model was generally set up without considering such a nucleation barrier. For the sake of discussing the potential effect of a nucleation barrier on the kinetics of austenitization, additional simulations with nucleation barriers of 50 and 100 J.mol^{-1} were carried out.

An additional series of simulations was run with enhancement of the mobilities of Ni and Cr in *bcc* and *fcc* by a factor of 10. This was done in an attempt to identify the rate-determining mechanisms at different stages of the transformation in the multi-component diffusion system.

Simulations were performed for different heating rates to investigate whether the presented approach yielded results, which are consistent with the experimental data. The system was limited to Fe, Cr and Ni to increase numerical stability.

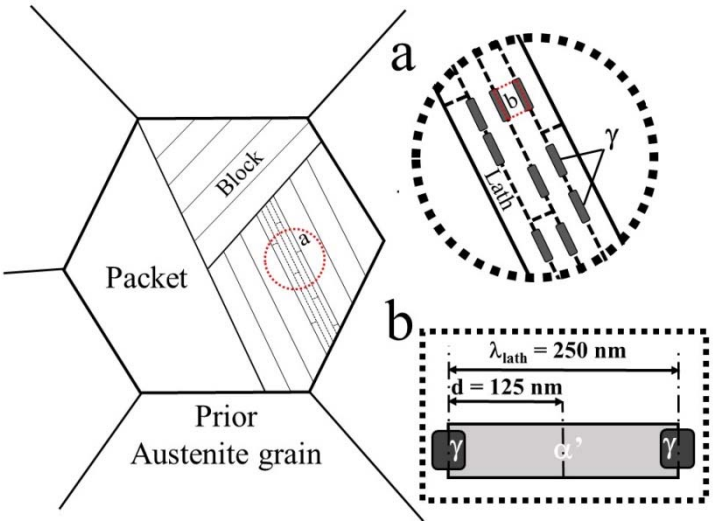

Figure 10.3: Schematic hierarchy of lath martensite. Inset (a) shows the lath structure in a block and indicates the nucleation sites of lamellar austenite (γ) at lath boundaries. Inset (b) shows the symmetry of a single lath with the lath width λ_{lath} and the resulting domain size d used in the one-dimensional kinetics model.

10.4.2 Results and interpretation

Kinetics modeling predicted for all heating rates an effective start temperature of the transformation, i.e. a temperature at which the transformation rate is discernable within the range of experimental measurement accuracy, at approx. 575 °C (Figure 10.1b). This is in close agreement with the results obtained from XRD (Figure 10.1a). On continued heating the transformation curves were offset by approx. 45 °C as compared to the experimental data. The model consistently predicts a shift in maximum transformation rate to higher temperature and an increase in the temperature where deceleration in the first stage occurs. Moreover, the extent of the deceleration of austenitization and the completion of the second stage of austenitization are predicted consistently with the trends observed in the experimental data.

Four distinct segments could be identified in the predicted martensite-to-austenite transformation curves. Those segments are (i) Nucleation, (ii) Maximum growth rate in

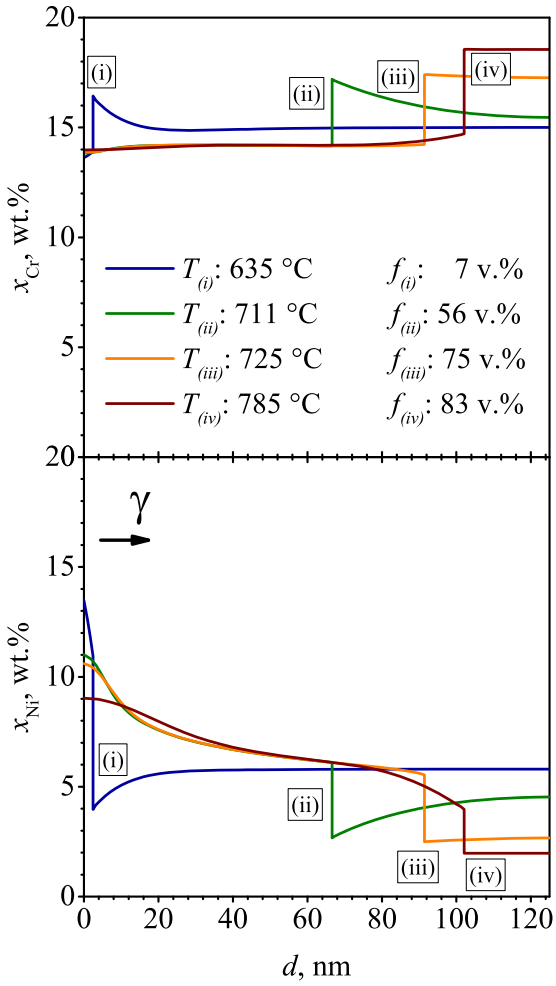

Figure 10.4: Ni and Cr content vs. distance d as indicated in Figure 10.3 for heating with 6 K.min^{-1} for the four distinct segments of transformation indicated by the points in Figure 10.1b. Austenite grows from the left-hand side of the domain and the austenite/martensite interface is represented by the discontinuity in the profiles (i.e. vertical lines).

stage 1, (iii) Deceleration, and (iv) Onset of growth in stage 2, which are indicated by four points in Figure 10.1b. In order to analyze the governing mechanisms for these characteristic segments in the kinetics of the transformation, the diffusion profiles of Cr and Ni were analyzed for heating with 6 $K.min^{-1}$, representing all heating rates, at the corresponding temperatures (Figure 10.4). A simulation of the evolution of the composition profiles with time is available as supplementary material (Video 1, Video 2 and Video 3 show austenitization at 2, 6 and 18 $K.min^{-1}$, respectively). Evidently, the experimentally determined two-stage austenitization could be reproduced by the kinetics model, thus analysis of the four characteristic segments can be used to explain the governing mechanisms involved.

(i) Nucleation and initial growth

Diffusion profile (i) shows austenite growing from the left-hand side of the diffusion domain immediately after nucleation (Figure 10.4). The segment appears at approx. 623, 635 and 647 °C for heating with 2, 6, and 18 $K.min^{-1}$ (Figure 10.1b). According to the model, considerable partitioning of Ni and some depletion in Cr occurs at the nucleation and initial growth stage of austenite at these temperatures.

(ii) Growth in stage 1

Diffusion profile (ii) shows the Ni and Cr content at the maximum rate of transformation in the first stage of austenitization (Figure 10.4). The segment appears at 695, 711 and 726 °C for the heating rates 2, 6, and 18 $K.min^{-1}$ (Figure 10.1b). Martensite is locally depleted in Ni at the interface, but provides excess Ni from the bulk to maintain the transformation. The transformation is at its maximum rate, enabled by increasing driving force for formation of austenite and increasing diffusivities with increasing temperature. The predicted transformation rates in this segment are in good agreement with the measured transformation rates (Figure 10.1). The austenitization kinetics under individual enhancement of the mobilities of Ni and Cr in *fcc* and *bcc* by a factor of 10 for heating with 6 $K.min^{-1}$ is shown in Figure 10.5. In particular a change in the mobility of Ni in *bcc* affects the kinetics (and the deceleration) in the first stage of austenitization, while the other mobilities appear to have a minor or negligible influence in this stage. These effects support the interpretation that Ni diffusion in *bcc* is rate determining in the first stage of austenitization.

(iii) Decelaration of the transformation kinetics

Diffusion profile (iii) shows the contents of Ni and Cr, at which deceleration of the transformation occurs. This segment appears at 713, 725, and 736 °C for the heating rates 2, 6, and 18 $K.min^{-1}$, respectively (Figure 10.1b). It is evident that the transformation is halted because impingement of the diffusion field with the model boundary causes the gradients in Ni and Cr content in martensite virtually to vanish. In the actual microstructure this mechanism corresponds to the situation in which the diffusion field of the simulated

austenite particle starts to overlap with the diffusion field of the adjacent austenite particle (see inset *b* in Figure 10.3). Then, continued growth of the austenite phase fraction is mainly achieved by a change of Ni profile in austenite close to the interface with martensite, while some redistribution of Ni in fcc commences (compare profiles (iii) and (iv) in Figure 10.4). Soft impingement in martensite occurred at higher phase fractions for higher heating rates (Figure 10.1b). The predictions of the phase fractions and temperatures where soft impingement occurs are in fair agreement with the onsets of the plateaus of the experimental transformation curves (Figure 10.1a).

(iv) Growth in stage 2

Diffusion profile (iv) corresponds to the Ni and Cr distribution at the onset of the second stage of austenitization (Figure 10.4). The segment appears at approx. 770, 785 and 821 °C for the heating rates 2, 6, and 18 K.min^{-1} (Figure 10.1b). The strong increase in the gradient in the Ni content in austenite close to the interface with martensite on proceeding from (iii) to (iv), establishes a larger driving force for Ni-diffusion and, hence, Ni-redistribution in austenite. As the content of Cr in *fcc* changes only slightly, diffusion of Ni in *fcc* austenite appears to be rate-determining for the second stage of austenitization. The austenitization kinetics under individual enhancement of the mobilities in Figure 10.5 confirms that in particular a change of the mobility of Ni in *fcc* affects the duration of the deceleration and the kinetics in the second stage of austenitization. This is consistent with Ni diffusion in *fcc* as rate-determining for the overall kinetics in stage 2 of the austenitization.

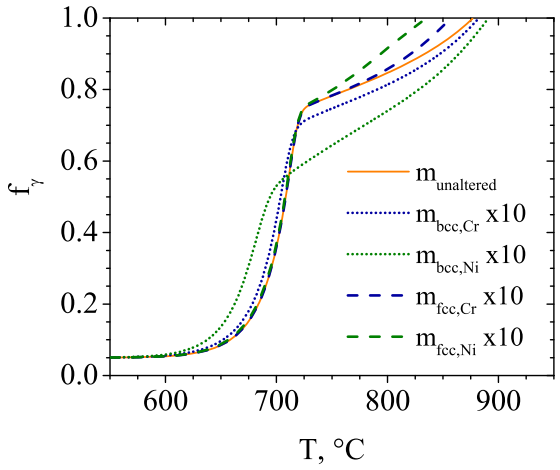

Figure 10.5: Kinetics modeling of austenitization with 6 K.min^{-1} showing the effect of individually enhancing the mobility for Ni and Cr in fcc and bcc by the factor 10; diffusion of Ni in bcc and Ni in fcc have the strongest effect on the kinetics in stage 1 and 2, respectively.

Effect of domain size and nucleation barrier

Figure 10.6a shows the predicted austenitization by the kinetics model for heating with 6 K.min^{-1} considering domain sizes of 75, 125 and 175 nm, corresponding to lath widths of 150, 250 and 350 nm, respectively. By altering the lath width, the diffusion distance until soft impingement is directly affected (inset *b* in Figure 10.3). Comparison of Figure 10.6a with nucleation occurred. The spikes in the transformation curves are a numerical artefact, caused by fluctuations in determining the starting value for the interface position and velocity in DICTRA. The fraction of austenite is initially insignificantly higher for transformations with nucleation barrier, but levels with the transformation without nucleation barrier after heating of approx. 100 °C (see inset in Figure 10.6b).

10.5 General discussion

10.5.1 Governing mechanisms

The rate-determining mechanism for the first stage of austenitization was identified as diffusion of Ni in *bcc*. This result is in line with the interpretation by Bojack et al., who suggested that the first stage of austenite formation would mainly be due to partitioning of Ni and Mn, leaving martensite partially untransformed [23].

Bojack et al. suggested that the second stage of transformation would be governed by increased diffusivity of Ni and Mn at higher temperatures together with the decomposition of carbides and nitrides [23]. The current investigation strongly indicates that diffusion of Ni in *fcc* after soft impingement in martensite governs the kinetics of the transformation in the second stage. Since the interstitial element content in the present alloy

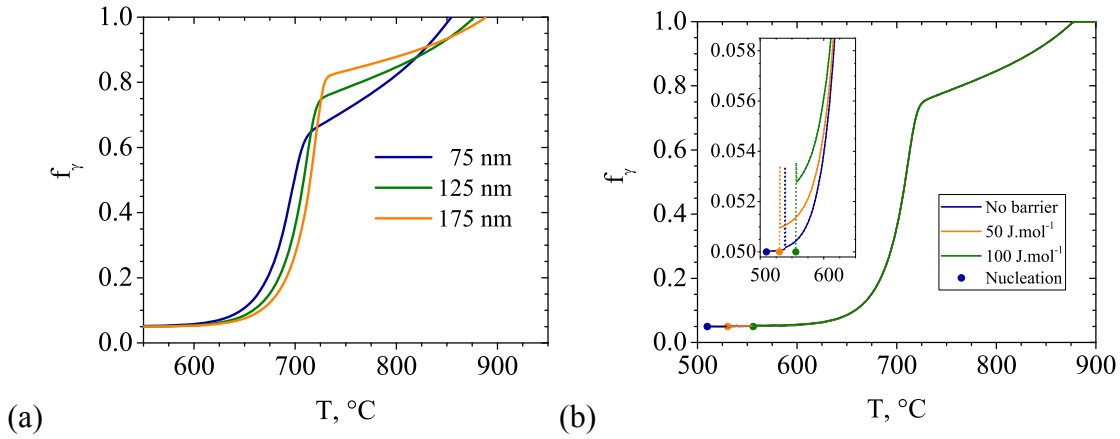

Figure 10.6: (a) Prediction of austenitization with 6 K.min^{-1} by kinetics modeling with different domain sizes, i.e. considering different martensite lath widths; (b) Simulation of austenitization with 6 K.min^{-1} with nucleation barriers of 50 and 100 J.mol^{-1} compared to simulation without nucleation barrier. The data points indicate nucleation and the broken lines discontinuities from a numerical artefact. The effect of the nucleation barrier is only apparent from the magnification displayed in the inset.

is very low (cf. Table 10.1), the dissolution of carbides and nitrides is expected to play a negligible role in the transformation.

10.5.2 Quantitative fit of experimental and modeled data

Evidently, the model succeeds in yielding a good qualitative fit to the experimentally assessed austenitization kinetics and in identifying the governing mechanisms. Quantitatively the model gives a reasonable fit, but predicts the initial growth stage to occur at higher temperatures and the soft impingement at higher phase fractions. These deviations are ascribed to simplifications in the model, which are intentional as not to obscure the effects of the main mechanisms involved in the transformation. The following additions are expected to provide a further improvement of the accuracy of the model predictions:

- It is still unclear whether austenite nucleates or, rather, grows from thin layers of inter-lath retained austenite. The dispute revolves around the austenite memory effect, which describes the inheritance of the orientation of reversed austenite from prior austenite grains. The orientation inheritance could indicate a variant selection mechanism [13] or growth from inter-lath retained austenite [14,48]. In the prior case, grain-boundaries are potentially decorated by solute from grain boundary segregation prior to the nucleation of austenite [49]. In the latter case, substantial diffusion towards retained austenite could activate the growth. Regardless of the actual mechanism it is expected that an enrichment in solute would enable premature formation of reversed austenite.

- It is anticipated that the driving force for the nucleation of austenite is increased by the release of residual stresses from metastable lath martensite [50].

- A high dislocation density in lath martensite is likely to enable pipe diffusion and could thus lead to a lower activation energy of the atom mobilities. This would lead to faster diffusion kinetics at the onset of the transformation, and a decay of the pipe diffusion contribution with annihilation of dislocations at higher temperature [51]. Preliminary attempts on including the effect of a temperature dependent dislocation density on the mobility data in the kinetics model, using dislocation density data from Ref. [51] and the grain-boundary model in DICTRA, indeed led to an improved correspondence between simulated and experimental results. However, for the present system reliable input data on the evolution of the dislocation density with temperature is currently lacking and demands more experimental work. A first idea of how the contribution of the dislocation density would affect the austenitization kinetics can be obtained from the graphs on enhanced mobility in *bcc* in Figure 10.5.

All of these omissions, when implemented, would increase the initial growth rate of austenite, increase the partitioning and thus lead to soft impingement at lower phase

fractions, thus accounting for the overestimation of the phase fraction where soft impingement occurs in the simulations in Figure 10.1b.

10.5.3 Effect of heating rate, domain size and nucleation barrier

The four described segments, which govern the austenitization kinetics, were identified for all analyzed heating rates, even for heating at 100 $K.min^{-1}$. The effect of changing the domain size on the transformation kinetics correlated with the effect of changing the heating rate (Figure 10.6a). Generally, the transformation kinetics depended on the ratio of available diffusion time and diffusion distance.

It was evident that the nucleation barrier did not affect the overall two-step kinetics strongly. Figure 10.6b shows that transformation with nucleation barrier leads to an increased fraction of austenite compared to the transformation without barrier just after nucleation, and that this divergence fades away on continued heating. This might seem counterintuitive, but is caused by less partitioning during formation of austenite at slightly more elevated temperatures. Thus, more austenite can be formed instantly at nucleation. Since the concentration gradient in austenite during heating is subject to homogenization, this marginal initial difference disappears upon further heating. Ultimately the time and temperature interval spent from nucleation to diffusion-controlled growth for the two-step kinetics is sufficiently large that the overall kinetics are not strongly affected by the nucleation mechanism.

10.6 Conclusions

The conclusions of the in-situ observation of two-stage austenitization and the modeling of austenitization with the kinetics model DICTRA are:

- Austenitization of X4CrNiMo16-5-1 super martensitic stainless steel during isochronal heating at 2 – 18 $K.min^{-1}$ occurs in two stages.
- Two-stage austenitization kinetics are predicted from kinetics modeling of multi-component diffusion in DICTRA based on the transformation of a single martensite lath to austenite and nucleation without nucleation barrier.
- The mechanism for the deceleration of the transformation after the first stage is identified as soft impingement in the martensite phase.
- Ni-diffusion in the *bcc* lattice is rate-determining for the first stage of austenitization, where Ni diffuses from martensite towards the phase-interface.
- Ni-diffusion in the *fcc* lattice is rate-determining for the second stage of austenitization, where austenite, which is heavily enriched in Ni due to partitioning in the initial growth stage, is required to homogenize in order to supply solute to the phase-interface. This requires the build-up of a concentration gradient.
- The martensite lath width, corresponding to two times the diffusion distance in the model, has a similar effect on the austenitization kinetics as the heating rate.

Acknowledgement

D. Apel, C. Genzel, M. Klaus and G. Wagener, Helmholtz Zentrum für Materialien und Energie (HZME), are acknowledged for their support during in-situ experiments at the Berlin synchrotron facility HZB-BESSY II. The Danish Underground Consortium is gratefully acknowledged for financial support to the Danish Hydrocarbon Research Center (DHRTC). M. Villa acknowledges the Danish Council for Independent Research (G.R. grant: DFF-4005-00223) for financial support.

References

[1] K. Tomimura, S. Takaki, S. Tanimoto, Y. Tokunaga, Optimal Chemical Composition in Fe-Cr-Ni Alloys for Ultra Grain Refining by Reversion from Deformation Induced Martensite, ISIJ Int. 31 (1991) 721–727.

[2] P. Toussaint, J.-J. Dufrane, Advances in the making and base material properties of supermartensitic stainless steels (SMSS), in: Supermartensitic Stainl. Steels 2002 Brussels, KCI Publishing, 2002: pp. 23–27.

[3] A.W. Marshall, J.C.M. Farrar, Welding of Ferritic and Martensitic 11-14% Cr Steels, Weld. World. 45 (2001) 19–42.

[4] L.M. Smith, M. Celant, Martensitic stainless steel flowlines - Do they pay?, in: Supermartensitic Stainl. Steels 1999, 1999: pp. 66–73.

[5] D.-S. Leem, Y.-D. Lee, J.-H. Jun, C.-S. Choi, Amount of retained austenite at room temperature after reverse transformation of martensite to austenite in an Fe–13%Cr–7%Ni–3%Si martensitic stainless steel, Scr. Mater. 45 (2001) 767–772.

[6] H.J. Niederau, A New Low-Carbon 16Cr-5Ni Stainless Martensitic Cast Steel, in: G. Behal, A.S. Melilli (Eds.), Stainl. Steel Cast., ASTM, Bal Harbour, Florida, 1982: pp. 382–393.

[7] M. Al Dawood, I.S. El Mahallawi, M.E. Abd El Azim, M.R. El Koussy, Thermal aging of 16Cr – 5Ni – 1Mo stainless steel Part 1 – Microstructural analysis, Mater. Sci. Technol. 20 (2004) 363–369.

[8] D. Ye, J. Li, W. Jiang, J. Su, K. Zhao, Effect of Cu addition on microstructure and mechanical properties of 15%Cr super martensitic stainless steel, Mater. Des. 41 (2012) 16–22.

[9] P.D. Bilmes, M. Solari, C.. Llorente, Characteristics and effects of austenite resulting from tempering of 13Cr–NiMo martensitic steel weld metals, Mater. Charact. 46 (2001) 285–296.

[10] M. Karlsen, J. Hjelen, Ø. Grong, G. Rørvik, R. Chiron, U. Schubert, E. Nilsen, SEM/EBSD based in situ studies of deformation induced phase transformations in supermartensitic stainless steels, Mater. Sci. Technol. 24 (2008) 64–72.

[11] S. Zhang, P. Wang, D. Li, Y. Li, Investigation of the evolution of retained austenite in Fe-13%Cr-4%Ni martensitic stainless steel during intercritical tempering, Mater. Des. 84 (2015) 385–394.

[12] T. LeBrun, T. Nakamoto, K. Horikawa, H. Kobayashi, Effect of retained austenite on subsequent thermal processing and resultant mechanical properties of selective laser melted 17-4 PH stainless steel, Mater. Des. 81 (2015) 44–53.

[13] N. Nakada, T. Tsuchiyama, S. Takaki, S. Hashizume, Variant Selection of Reversed Austenite in Lath Martensite, ISIJ Int. 47 (2007) 1527–1532.

[14] L. Liu, Z.-G. Yang, C. Zhang, Effect of retained austenite on austenite memory of a 13% Cr–5% Ni martensitic steel, J. Alloys Compd. 577 (2013) 654–660.

[15] N. Nakada, T. Tsuchiyama, S. Takaki, N. Miyano, Temperature Dependence of Austenite Nucleation Behavior from Lath Martensite, ISIJ Int. 51 (2011) 299–304.

[16] Y.Y. Song, X.Y. Li, L.J. Rong, Y.Y. Li, T. Nagai, Reversed austenite in 0Cr13Ni4Mo martensitic stainless steels, Mater. Chem. Phys. 143 (2014) 728–734.

[17] L. Yuan, D. Ponge, J. Wittig, P. Choi, J.A. Jiménez, D. Raabe, Nanoscale austenite reversion through partitioning, segregation and kinetic freezing: Example of a ductile 2 GPa Fe-Cr-C steel, Acta Mater. 60 (2012) 2790–2804.

[18] Y. Song, X. Li, L. Rong, Y. Li, Anomalous Phase Transformation from Martensite to Austenite in Fe-13%Cr-4%Ni-Mo Martensitic Stainless Steel, J. Mater. Sci.

Technol. 26 (2010) 823–826.
[19] Y.-K. Lee, H.-C. Shin, D.-S. Leem, J.-Y. Choi, W. Jin, C.-S. Choi, Reverse transformation mechanism of martensite to austenite and amount of retained austenite after reverse transformation in Fe-3Si-13Cr-7Ni (wt-%) martensitic stainless steel, Mater. Sci. Technol. 19 (2003) 393–398.
[20] W. Jiang, D. Ye, J. Li, J. Su, K. Zhao, Reverse Transformation Mechanism of Martensite to Austenite in 00Cr15Ni7Mo2WCu2 Super Martensitic Stainless Steel, Steel Res. Int. 85 (2014) 1150–1157.
[21] W. Jiang, K. Zhao, D. Ye, J. Li, Z. Li, J. Su, Effect of Heat Treatment on Reversed Austenite in Cr15 Super Martensitic Stainless Steel, J. Iron Steel Res. Int. 20 (2013) 61–65.
[22] V.A. Esin, B. Denand, Q. Le Bihan, M. Dehmas, J. Teixeira, G. Geandier, S. Denis, T. Sourmail, E. Aeby-Gautier, In situ synchrotron X-ray diffraction and dilatometric study of austenite formation in a multi-component steel: Influence of initial microstructure and heating rate, Acta Mater. 80 (2014) 118–131.
[23] A. Bojack, L. Zhao, P.F. Morris, J. Sietsma, Austenite Formation from Martensite in a 13Cr6Ni2Mo Supermartensitic Stainless Steel, Metall. Mater. Trans. A. 47 (2016) 1996–2009.
[24] A. Bojack, L. Zhao, P.F. Morris, J. Sietsma, In-situ determination of austenite and martensite formation in 13Cr6Ni2Mo supermartensitic stainless steel, Mater. Charact. 71 (2012) 77–86.
[25] R. Kapoor, I.S. Batra, On the α to γ transformation in maraging (grade 350), PH 13-8 Mo and 17-4 PH steels, Mater. Sci. Eng. A. 371 (2004) 324–334.
[26] D. San Martín, P.E.J. Rivera-Díaz-del-Castillo, C. García-de-Andrés, In situ study of austenite formation by dilatometry in a low carbon microalloyed steel, Scr. Mater. 58 (2008) 926–929.
[27] C. Servant, P. Lacombe, Structural transformations produced during tempering of Fe-Ni-Co-Mo alloys, J. Mater. Sci. 12 (1977) 1807–1826.
[28] C. Servant, G. Maeder, I. Introduction, C. De Recherches, L. De Mrtal-, O. Cedex, O. Cedex, T. Fe, Investigation Into the Effect of Substituting, 10 (1979).
[29] F. Niessen, M. Villa, D. Apel, O. Keßler, M. Reich, J. Hald, M.A.J. Somers, In situ techniques for the investigation of the kinetics of austenitization of supermartensitic stainless steel, Mater. Sci. Forum. 879 (2017) 1381–1386.
[30] E.I. Galindo-Nava, W.M. Rainforth, P.E.J. Rivera-Díaz-del-Castillo, Predicting microstructure and strength of maraging steels: Elemental optimisation, Acta Mater. 117 (2016) 270–285.
[31] C. Genzel, I. a. Denks, M. Klaus, The Materials Science Beamline EDDI for Energy-Dispersive Analysis of Subsurface Residual Stress Gradients, Mater. Sci. Forum. 524–525 (2006) 193–198.
[32] B.C. Giessen, G.E. Gordon, X-ray Diffraction: New High-Speed Technique Based on X-ray Spectrography, Sci. New Ser. 159 (1968) 973–975.
[33] E.S.U. Laine, A high-speed determination of the volume fraction of ferrite in austenitic stainless steel by EDXRD, J. Phys. F Met. Phys. 8 (2001) 1343–1348.
[34] R. Hielscher, H. Schaeben, A novel pole figure inversion method: Specification of the MTEX algorithm, J. Appl. Crystallogr. 41 (2008) 1024–1037.
[35] B.P.J. Sandvik, C.M. Wayman, Characteristics of Lath Martensite: Part I. Crystallographic and Substructural Features, Metall. Trans. A. 14 (1983) 809–822.
[36] S. Morito, H. Tanaka, R. Konishi, T. Furuhara, T. Maki, The morphology and crystallography of lath martensite in Fe-C alloys, Acta Mater. 51 (2003) 1789–1799.

[37] S. Morito, X. Huang, T. Furuhara, T. Maki, N. Hansen, The morphology and crystallography of lath martensite in alloy steels, Acta Mater. 54 (2006) 5323–5331.
[38] A. Borgenstam, A. Engström, L. Höglund, J. Ågren, DICTRA, a tool for simulation of diffusional transformations in alloys, J. Phase Equilibria. 21 (2000) 269–280.
[39] E.J. Mittemeijer, Review - Analysis of the kinetics of phase transformations, J. Mater. Sci. 27 (1992) 3977–3987.
[40] Thermo-Calc Software TCFE6 Steels/Fe-alloys database version 6.2, Thermo-Calc Softw. TCFE6 Steels/Fe-Alloys Database Version 6.2 (Accessed Novemb. 2009).
[41] Thermo-Calc Software TCS Alloys Mobility Database MOB2 (accessed 08 April 1998).
[42] O. Redlich, A.T. Kister, Algebraic Representation of Thermodynamic Properties and the Classification of Solutions, Ind. Eng. Chem. 40 (1948) 345–348.
[43] H. Larsson, A model for 1D multiphase moving phase boundary simulations under local equilibrium conditions, Calphad Comput. Coupling Phase Diagrams Thermochem. 47 (2014) 1–8.
[44] Y. Song, D.H. Ping, F.X. Yin, X.Y. Li, Y.Y. Li, Microstructural evolution and low temperature impact toughness of a Fe–13%Cr–4%Ni–Mo martensitic stainless steel, Mater. Sci. Eng. A. 527 (2010) 614–618.
[45] C. Servant, E.H. Gherbi, G. Cizeron, TEM investigation of the tempering behaviour of the maraging PH 17.4 Mo stainless steel, J. Mater. Sci. 22 (1987) 2297–2304.
[46] F. Niessen, Technical University of Denmark (DTU); Danish Hydrocarbon Research and Technology Centre; 2800 Kgs. Lyngby; Denmark, Unpubl. Res. (2016).
[47] The Precipitation Module (TC-PRISMA) User Guide 2016a, (accessed 23 July2016).
[48] L. Liu, Z.G. Yang, C. Zhang, W.B. Liu, An in situ study on austenite memory and austenitic spontaneous recrystallization of a martensitic steel, Mater. Sci. Eng. A. 527 (2010) 7204–7209.
[49] D. Raabe, S. Sandlöbes, J. Millán, D. Ponge, H. Assadi, M. Herbig, P.P. Choi, Segregation engineering enables nanoscale martensite to austenite phase transformation at grain boundaries: A pathway to ductile martensite, Acta Mater. 61 (2013) 6132–6152.
[50] M. Villa, F. Niessen, M.A.J. Somers, In situ investigation of the evolution of lattice strain and stresses in austenite and martensite during quenching and tempering of steel, Metall. Mater. Trans. A. 49 (2017) 1-13.
[51] Z.M. Shi, W. Gong, Y. Tomota, S. Harjo, J. Li, B. Chi, J. Pu, Study of tempering behavior of lath martensite using in situ neutron diffraction, Mater. Charact. 107 (2015) 29–32.

11 Manuscript VI

Formation and stabilization of reversed austenite in supermartensitic stainless steel*

Frank Niessen[a,†], Flemming B. Grumsen[b], John Hald[b], Marcel A.J. Somers[b],

[a] Technical University of Denmark (DTU), Danish Hydrocarbon Research and Technology Centre (DHRTC) , Elektrovej building 375, 2800 Kgs. Lyngby, Denmark

[b] Technical University of Denmark (DTU), Department of Mechanical Engineering, Produktionstorvet building 425, 2800 Kgs. Lyngby, Denmark

[†] Corresponding author

Abstract

The formation and stabilization of reversed austenite upon inter-critical annealing was investigated in a X4CrNiMo16-5-1 (EN 1.4418) supermartensitic stainless steel by means of scanning electron microscopy, electron backscatter-diffraction, transmission electron microscopy, energy-dispersive X-ray spectroscopy and dilatometry. The results were supported by thermodynamics and kinetics models, and hardness measurements. Isothermal annealing for 2 h in the temperature range of 475 to 650 °C led to gradual softening of the material which was related to tempering of martensite and the steady increase of the reversed austenite phase fraction. Annealing at higher temperatures led to a gradual increase in hardness which was caused by formation of fresh martensite from reversed austenite. It was demonstrated that stabilization of reversed austenite is primarily based on chemical stabilization by partitioning, consistent with modeling results.

* Published work: F. Niessen, F.B. Grumsen, J. Hald, M.A.J. Somers, in:, Proc. 24th IFHTSE Congr., 2017, pp. 138–145. The format of the published article was adapted to the format of the doctoral thesis.
Figures 11.1, 11.3 and 11.6 were previously submitted as part of the final thesis for obtaining the degree Master of Science (F. Niessen, Heat treatment, microstructure and mechanical properties of a Cast Supermartensitic Stainless Steel, 2014)

11.1 Introduction

Supermartensitic stainless steels are lath martensitic steels with ultra-low interstitial content and are based on the Fe-Cr-Ni system [1]. The alloy grade became popular in the oil and gas industry as a low cost alternative to highly alloyed duplex stainless steels in pipeline applications [2]. The strength and toughness of the material is based on formation of reversed austenite from lath martensite during inter-critical annealing [3–6]. Annealing leads to effective grain refinement by formation of a two phase structure of soft austenite and hard tempered martensite. Such structure is effective in hindering dislocation-movement during plastic deformation and furthermore exhibits a prolonged plastic regime by transformation of austenite to martensite during plastic straining, a mechanism known as transformation induced plasticity (TRIP) [7–9].

The presented study aims at the clarification of mechanisms involved in formation, growth and stabilization of reversed austenite in supermartensitic stainless steel by a multi-angle approach, using microstructure characterization, in-situ phase quantification, mechanical testing and thermodynamics and kinetics modeling.

11.2 Procedures

11.2.1 Materials and heat-treatments

The chemical composition of the tested steel is given in Table 11.1. Specimens 4 mm in thickness were sliced from an extruded bar of Ø 10 mm. Specimens for scanning electron microscopy and electron backscatter diffraction were ground and subsequently electro-polished in Struers A2 electrolyte at 20 V for 30 s. The specimens for transmission electron microscopy analysis were prepared by electrolytic twinjet thinning with 10 % perchloric acid in ethanol at -20 °C. Prior to investigation the material was normalized for 1800 s at 1000 °C in Ar at atmospheric pressure. The average heating and average cooling rate down to 200 °C were 45 and 70 $Kmin^{-1}$, respectively. The material was annealed in the temperature range of 450 to 900 °C in steps of 25 °C. Specimens for dilatometry were machined to cylinders of Ø 4 x 10 mm with the dilatation axis parallel to the extrusion direction and normalized at 920 °C for 600 s.

The Vickers-hardness of the specimens was measured with a Wolpert Dia Testor 2Rc according to ASTM E 92 [10]. A load of 30 kgf was applied for 15 s. The presented hardness values are the average of three indents per specimen.

11.2.2 Microstructure characterization

Scanning electron microscopy (SEM) was carried out on an FEI Helios EBS3. Backscatter imaging with a large field backscatter electron detector was applied with 15 kV acceleration voltage, 5.5 nA beam current and 4 mm working distance.

In order to analyze the orientation relationship of reversed austenite and lath martensite Electron backscatter diffraction (EBSD) was applied. A FEI Helios EBS3 equipped with an EDAX Hikari EBSD camera was used for this purpose. The measurements were carried out at a working distance of 8 mm, an acceleration voltage of 18 kV, a beam current of 5.5 nA and a step-size of 100 nm. Data was acquired and processed with the TSL EBSD Data Collection System. Phase- and inverse pole figure maps were cleaned by grain confidence index standardization and a single dilation iteration (Tolerance: 5, Min. size: 3) as well as a confidence index threshold of 0.1.

The microscope used for bright-field- and dark-field-imaging, and selected area electron diffraction in Transmission electron microscopy (TEM) was a JEOL 3000F with a field emission gun source operated at 300 kV acceleration voltage. Diffraction patterns were analyzed with the JEMS electron microscopy simulation software.

The microscope used for energy filtered TEM (EFTEM) and EDS-analysis in scanning TEM (STEM) was a Tecnai T20G^2 with a thermionic LaB_6 filament operated at 200 kV acceleration voltage. Energy-filtered TEM was carried out to analyze the distribution of Ni in the microstructure after annealing. This was done by acquiring a jump-ratio map of the Ni L_3 edge at 855 eV applying energy windows of 25 eV. EDS-analysis was carried out excluding C, N, P and S from quantification. The STEM-EDS-measurements were quantified from approx. 55.000 counts per measurement point and manual background-correction.

11.2.3 Dilatometry

Dilatometry was applied to follow the martensite-to-austenite formation in-situ. The material was therefore heated to maximum temperatures of 625 to 700 °C with 15 K.min^{-1} and immediately cooled to room temperature with 15 K.min^{-1}. The measurements were carried out in a Bähr DIL 805A/D dilatometer, in which specimens were heated through induction and the temperature was monitored with a thermo-couple spot-welded to the specimen surface. The measurements were carried out in He at atmospheric pressure to avoid oxidation. The phase-fractions of austenite and martensite were determined by using the lever-rule which uses base-lines of the expansion of pure austenite and martensite to estimate the fraction of the phases in a two-phase microstructure. The baseline for pure martensite was extrapolated from the dilatometry curve before austenite formation occurred; the baseline for pure austenite was determined by a dilatometry measurement of cooling from the austenite region at 950 °C. The amount of retained austenite after martensite transformation was measured 5 vol.% with X-ray diffraction and was manually added as an initial fraction to the quantification. The lever-rule assumes that expansion of

Table 11.1: Chemical composition of the investigated X4CrNiMo16-5-1 SMSS balanced with Fe (wt.%), determined with Optical emission spectroscopy (OES).

C	N	Cr	Ni	Mo	Mn	Si	P	S
0.03	0.037	15.00	5.80	1.03	0.86	0.39	0.025	0.008

the specimen parallel to the dilatational axis is proportional to the overall volume expansion of the specimen, that the monitored phase transformation does not lead to build-up or release of stresses, and that austenite and martensite are the only present phases in the material. More details to the procedure can be found in Ref. [11]. Additional measurements were carried out in which heating to maximum temperatures of 625 to 700 °C with 15 $K.min^{-1}$ was followed by cooling to -150 °C with 15 $K.min^{-1}$ and reheating to room temperature with 15 $K.min^{-1}$. These measurements were not quantified by the means of the lever-rule method in the sub-zero Celsius regime, since baselines to such low temperature were difficult to estimate.

11.2.4 Thermodynamics and kinetics modeling

Thermodynamics modeling applying the CALPHAD approach [12,13] is a widely established method for prediction of thermodynamic equilibria in multicomponent systems. Such predictions are useful to refine experimental planning and support interpretation of experimental data. In this investigation Thermo-Calc 2015b with the TCFE6 database [14] for iron-based alloys was used to predict phase fractions and compositions at various temperatures.

The kinetics model DICTRA is a module of the Thermo-Calc package which enables 1-dimensional kinetics modeling of diffusion controlled transformations in multicomponent systems. [15] In the present investigation DICTRA is used to model the transformation kinetics for isothermal holding at various soaking temperatures, using the mobility database MOB2 [16]. The modelled transformation included the effect of Cr, Ni, Mn, Mo and Si balanced with Fe. The model was setup in a linear cell-geometry which was discretized with 1 nm spatial resolution and was 125 nm in length, corresponding to approx. half the martensite lath width. More details on the setup of the kinetics model can be found in Ref. [17,18].

11.3 Results

The specimen in as-austenitized condition (AA) revealed a hardness of 365 HV (Figure 11.1). Secondary hardening of the material was found at 475 °C. For annealing temperatures up to 650 °C the material softened; for annealing temperatures higher than 650 °C a steady increase in hardness was observed.

11.3.1 Dilatometry

Dilatometry was carried out in order to follow the phase transformation of martensite to austenite in-situ. Figure 11.2a shows the dilatometry curve for heating to 700 °C with 15 $K.min^{-1}$ and immediate cooling to room temperature with 15 $K.min^{-1}$. The lines denoted as $\varepsilon_{\alpha'}$ and ε_{γ} indicate the baselines of martensite and austenite as a single-phase material, respectively, so that the lever-rule can be applied to determine the transformed fraction. The result of this quantification method is shown in Figure 11.2b, in which the austenite

fraction over temperature is shown for heating and immediate cooling with 15 K.min^{-1}. For heating to 650 and 675 °C austenite fractions of 20 and 37 vol.% were stabilized to room temperature. Heating to 700 °C led to a fraction of 59 vol.% during cooling which then partially transformed to new martensite at the martensite start temperature 75 °C, leaving 37 vol.% of austenite untransformed. The sudden dilation at approx. 620 °C during heating and cooling are artefacts caused by the magnetic transition at the Curie-temperature.

The results for sub-zero Celsius dilatometry down to -150 °C revealed that reversed austenite which is formed up to 650 °C was stable upon cryogenic cooling. Heating to 675 °C and subsequent cooling led to the formation of 26 vol.% austenite which remained stable down to -150 °C. Upon reheating 3 vol.% of austenite transformed to martensite from -60 °C to 30 °C. Heating to 700 °C yielded 59 vol.% of austenite upon cooling to 58 °C, where martensite transformation started. 39 vol.% of reversed austenite was stable at room-temperature and only 25 vol.% at -75 °C, where martensite formation stopped.

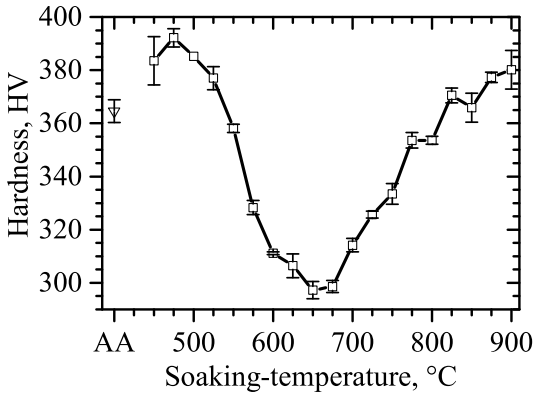

Figure 11.1: Hardness for the as-austenitized condition and annealing temperatures 450 to 900 °C at 2 h soaking-time. The error-bars indicate the standard deviation from three measurements.

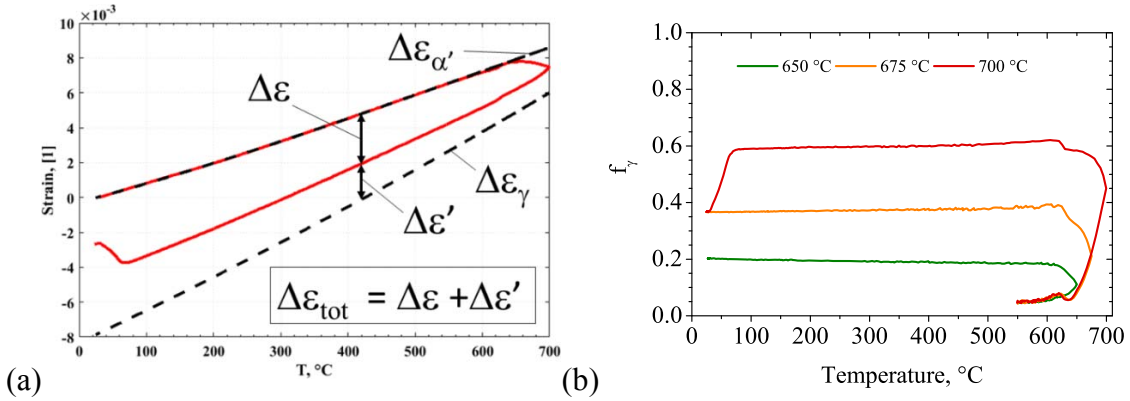

Figure 11.2: Dilatometry: (a) Dilatometry curve of heating at 15 K.min-1 to 700 °C and immediate cooling to 20 °C at 15 K.min^{-1}; the lines denoted as $\varepsilon_{\alpha'}$ and ε_{γ} indicate the baselines of martensite and austenite, respectively, for phase-quantification by the lever-rule; (b) phase fraction of austenite over temperature according to the lever-rule for heating and immediate cooling at 15 K.min^{-1}.

11.3.2 Microstructure characterization

Investigation of electro-polished specimens was carried out with a large field backscatter electron detector. Strong contrast between the austenite grains (white) and the lath martensite matrix was observed (Figure 11.3a). Since no major difference in atomic number is expected, the contrast is presumably orientation related. The grain orientation affects the electron penetration into the specimen through diffraction effects and thus has an effect on the backscatter electron yield.[20] For tempering at 700 °C this contrast was weakened which indicates the formation of martensite during cooling to room-temperature. In order to study the orientation relationship between reversed austenite and the tempered martensite matrix, orientation-data of several prior austenite grains were isolated. Each data-set was

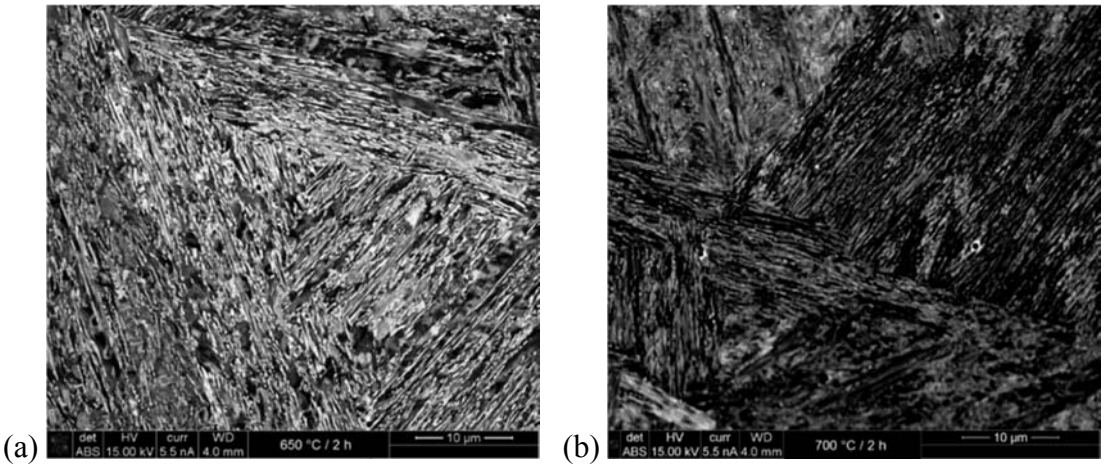

Figure 11.3: BSE-imaging (a) Condition 650°C/2h showing two phase microstructure of lath-martensite (grey) and lamellar inter-lath reversed austenite (white); (b) Condition 700°C/2h showing loss of the two-phase contrast, indicating transformation of reversed austenite to fresh martensite upon cooling.

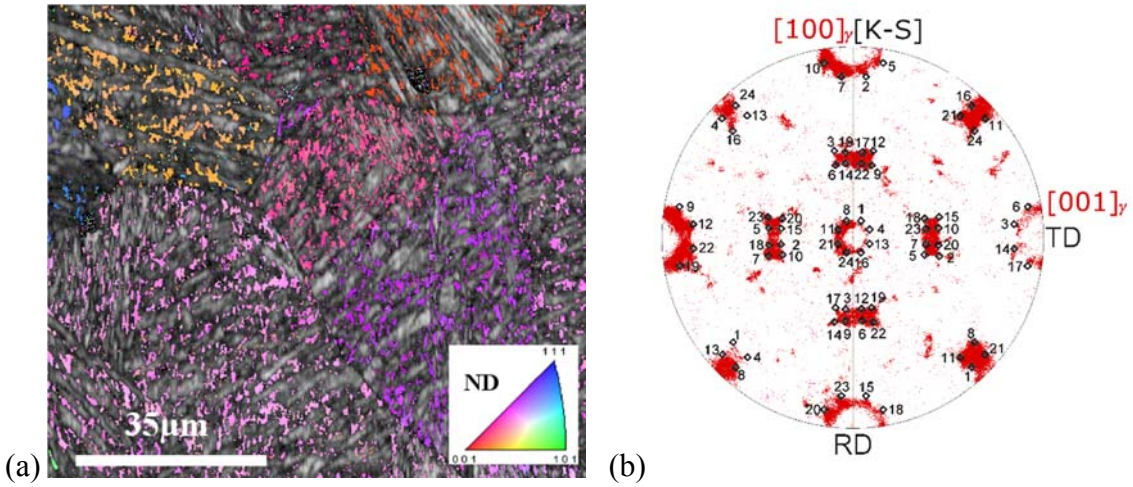

Figure 11.4: EBSD: (a) Inverse pole-figure map of austenite superimposed on image-quality map. It is evident that reversed austenite inherits the orientation of the prior austenite grains; (b) Inverse pole-figure of rotated prior austenite grain into [100]-direction for direct comparison with the numbered variants of the Kurdjumow-Sachs orientation relationship (numbering convention according to Ref. [19]).

then rotated by aligning the <100> directions of austenite parallel to the specimen axes, so that the tempered martensite variants could be compared with the Kurdjumov-Sachs (KS) orientation relationship in an inverse pole-figure (Figure 11.4b). The measured orientation data is in excellent agreement with the KS orientation relationship. In each grain some martensite variants were represented more frequently than in others.

Specimens in the annealing conditions 650°C/2h and 700°C/2h were examined with TEM. Applying selected area electron diffraction (SAED) and dark field imaging it was found that the specimen annealed at 650 °C / 2 h consists of a tempered martensite matrix with reversed austenite lamellas of 80 to 140 nm width. In the applied specimen tilt austenite was in Bragg-condition and thus appears in dark contrast in the bright-field image in Figure 11.5a, as evidenced with dark-field imaging with the corresponding SAED pattern. Consistent with results from EBSD-analysis, SAED revealed that austenite formed

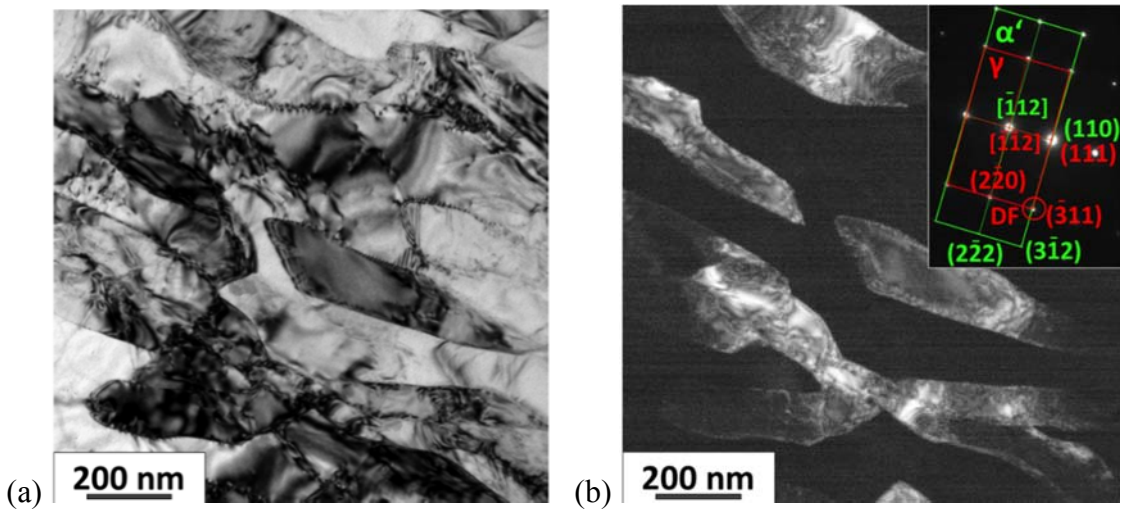

Figure 11.5: TEM condition 650°C/2h: (a) Bright-field image of austenite (dark) and tempered martensite (bright); (b) Selected area electron diffraction pattern and dark-field image of austenite.

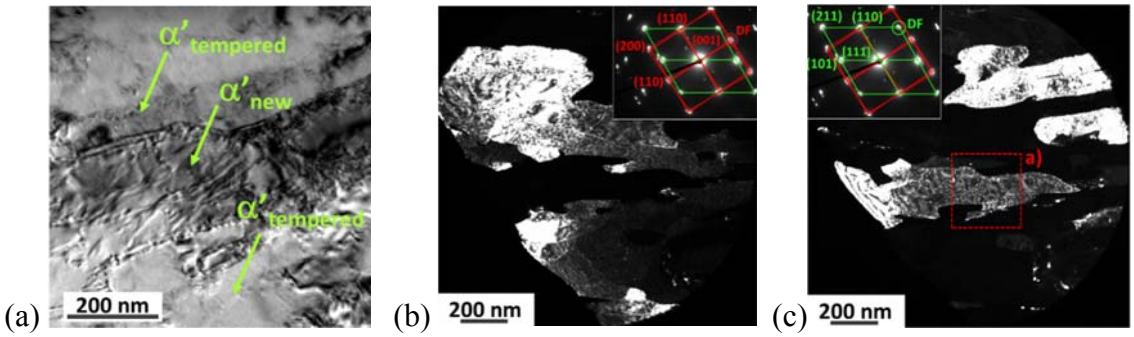

Figure 11.6: TEM, condition 700°C/2h: (a) bright-field image of area a) in Figure 11.6c before tilting into the [111] zone axis for diffraction, showing tempered and newly formed martensite; (b) Selected area electron diffraction pattern and dark-field image of tempered martensite; (c) Selected area electron diffraction pattern and dark-field image of a newly formed martensite lath; the dark round corners of the dark-field images are the objective aperture.

in Kurdjumov-Sachs relationship with martensite: $[\bar{1}12]_{bcc} \parallel [\overline{11}2]_{fcc}$, $(110)_{bcc} \parallel (111)_{fcc}$. Figure 11.6b and Figure 11.6c show selected area electron diffraction patterns with the correspondent dark-field images of tempered and newly formed martensite, respectively, of the 700°C/2h condition. The analyzed martensite variants hold the following orientation relationship: $[111]_{bcc} \parallel [110]_{bcc}$, $(1\bar{1}0)_{bcc} \parallel (1\bar{1}0)_{bcc}$ .Newly formed martensite could be distinguished from tempered martensite by the dislocation density which is clearly visible from the bright-field image, which was acquired before applying specimen tilt for diffraction analysis (Figure 11.6a).

Figure 11.7a shows a jump-ratio map of the Ni L_3 edge from which partitioning of Ni between austenite and martensite is evident. Figure 11.7b shows the EDS-quantification of a line-scan over an austenite lamella in STEM and confirms partitioning of Ni between austenite and martensite. The austenite lamella is shown in the HAADF image.

11.3.3 Thermodynamics and kinetics modeling

The kinetics of austenite formation for isothermal holding at 650, 675 and 700 °C was predicted with kinetics modeling. It is evident from Figure 11.8a that the martensite-to-austenite transformation accelerates with increasing temperature so that less time is required to reach the equilibrium phase fraction, as indicated by intersection with the grey background. At the 2 h mark (vertical dotted line in Figure 11.8a), which corresponds to the holding time in the experiments, the transformation at 675 °C is just about to reach equilibrium. According to kinetics modeling annealing at 700 °C would only require approx. 15 min to reach equilibrium, while holding at 650 °C would require 8 h.

The contents of the main alloying elements Ni and Cr in ferrite (b.c.c.) and austenite (f.c.c.) according to thermodynamic equilibrium are predicted as a function of temperature in Figure 11.8b. The figure indicates that the concentrations of Cr and Ni in ferrite and

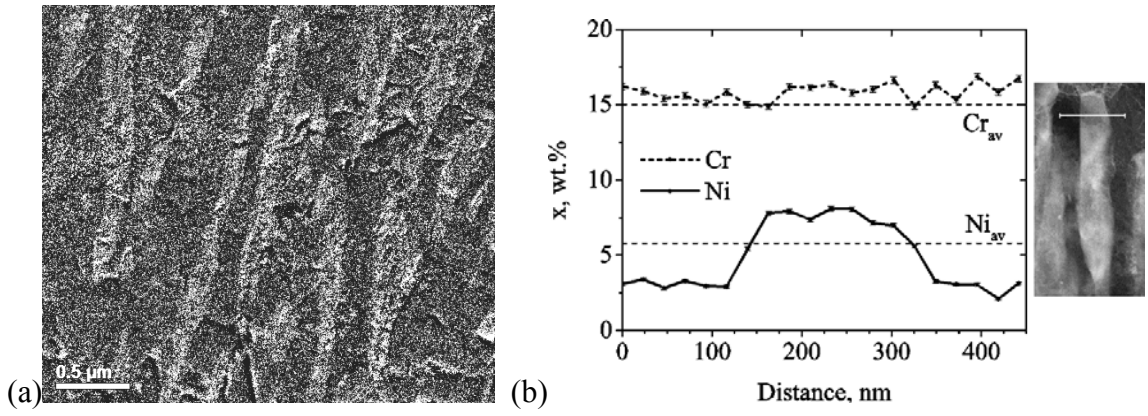

Figure 11.7: TEM 650°C/2h: (a) Jump-ratio map of the Ni L_3 edge showing the distribution of Ni, indicating partitioning of Ni between reversed austenite and martensite; (b) EDS quantification of Ni and Cr-content from line-scan over austenite lamella, which is shown in the STEM-HAADF image; The error-bars indicate the uncertainty from EDS data-processing.

austenite diverge progressively from the average alloy composition with decreasing phase-fraction.

11.4 Discussion

Investigation of austenite reversion and stability by use of correlative methods reveals insight into some of the mechanisms involved in formation and stabilization of reversed austenite. The microstructural evolution during annealing and cooling will accordingly be discussed based on the results of the applied techniques.

11.4.1 Orientation of reversed austenite and nucleation

Correlative microstructure characterization by SEM and TEM analysis (Figure 11.3 and Figure 11.5, respectively) revealed that lamellar austenite forms in-between martensite laths. EBSD analysis reveals that the orientation relationship between this reversed austenite and the existing lath martensite complies with the Kurdjumov-Sachs orientation relation (Figure 11.4b), consistent with the results from selected area electron diffraction in TEM (Figure 11.5). Furthermore, reversed austenite holds a common orientation within a prior austenite grain (and its twins), strongly suggesting that reversed austenite inherits the original orientation of the austenite present prior to martensite formation Figure 11.4a). This effect is commonly referred to as the austenite memory effect. The effect could either indicate that austenite grows from inter-lath retained austenite films of a few atomic layers in thickness, i.e. without nucleation in the classical sense,[21] or that variant selection limits the number of possible variants to the observed ones.[22] An internal study using Transmission Kikuchi diffraction showed that the 5 vol.% of retained austenite present before reversed austenite formation is inhomogeneously distributed in a chunky

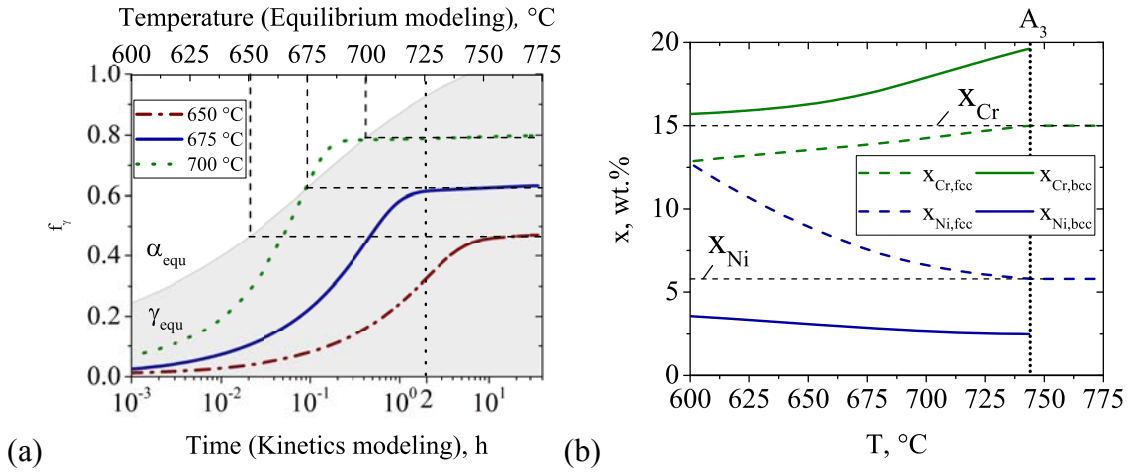

Figure 11.8: (a) Kinetics of austenite formation for isothermal holding at 650, 675 and 700 °C predicted with kinetics modeling; the grey area indicates the thermodynamically stable phase fraction of austenite over temperature; (b) Equilibrium composition of austenite and martensite (ferrite) over temperature. The horizontal dashed lines reflect the alloy content of Ni and Cr, A_3 is the temperature at which only f.c.c. is thermodynamically stable. The intersection of the b.c.c. alloying contents at 600 °C is incidental.

morphology, rather than as an inter-lath film. Since inter-lath retained austenite films could be below the detection limit of the techniques used in this investigation, no distinction can be made between the above-mentioned mechanisms for the observed austenite memory effect.

11.4.2 Morphology of reversed austenite

As stated in the previous section (0), reversed austenite forms as lamellae in-between martensite laths. The lamella width increases with increasing annealing temperature, consistent with a steady increase in austenite phase fraction with temperature, as expected from thermodynamic equilibrium (Figure 11.8a). The transition from lamellar austenite in a two-phase microstructure to a classic one-phase austenite microstructure with few large grains with increasing time and temperature was reported to occur by steady spheroidization of lamellae, homogeneous nucleation of spherical grains and subsequent grain growth [23].

11.4.3 Phase fraction of reversed austenite

Figure 11.1 shows steady softening of the material with increasing annealing temperature from 475 to 650 °C for 2 h of soaking time. The softening of the material is both related to softening of martensite by tempering and a progressive increase in austenite phase fraction, and indicates that annealing at 650°C/2h yields the maximum amount of austenite. The observed increase in austenite fraction correlates with an increase in thermodynamic equilibrium phase-fraction at the applied annealing temperatures (Figure 11.8a). As indicated by the results from kinetics modeling, 2 h of soaking time seems feasible to reach a state close to thermodynamic equilibrium from 650 °C and above. This indicates that, possibly, further softening could have been reached at temperatures below 650 °C if longer soaking times had been applied. When annealing at 675 °C and above the material revealed a steady increase in hardness, indicating a reduction in austenite phase fraction at room-temperature.

In-situ monitoring of the phase fraction with dilatometry showed stabilization of austenite up to 37 vol.% for heating to 675 °C. In the dilatometry experiments no holding time was applied at the maximum temperature which led to the maximum fraction of stable austenite at 675 °C rather than 650 °C (Figure 11.2b). Heating to 700 °C resulted in an even higher fraction of austenite at the annealing temperature, but did not result in an increase in austenite phase fraction at room-temperature because of a transformation to martensite at 75 °C.

11.4.4 Thermal stability of reversed austenite

The results and the discussion to this point indicate that austenite can be stabilized to a certain amount to room temperature by applying a suitable annealing treatment. Results from hardness measurements and dilatometry show that applying a relatively high

annealing temperature leads to a loss in stable phase fraction at room temperature. The mechanisms which lead to stabilization, and eventual loss of stability should therefore be discussed in more detail.

In the inter-critical region, i.e. the region at which both ferrite and austenite are thermodynamically stable, the equilibrium phase-compositions of ferrite (martensite) and austenite differ from the average alloy-composition. The lower the equilibrium phase-fraction, the more enrichment in phase-stabilizing elements is thermodynamically required. This effect is clearly visible for the Ni and Cr content of austenite (f.c.c.) and ferrite (b.c.c.) over temperature in thermodynamic equilibrium (Figure 11.8b). Following the Ni and Cr contents of both phases towards A_3 it is evident that the austenite composition approaches the alloy composition, whereas the ferrite composition drifts towards increased Cr and decreased Ni content. Likewise substantial enrichment in Ni and depletion in Cr is necessary for austenite to form at substantially lower temperatures than A_3. At this point it becomes clear that the drastic decrease of the rate of the martensite-to-austenite transformation with lower annealing temperature predicted by kinetics modeling is both owed to a decrease in general diffusion kinetics, and higher required atomic fluxes to establish the partitioning of alloying elements between the two phases (Figure 11.8a).

Since austenite forms by diffusion at low heating rates and thus also during isothermal annealing [3,17], it can be assumed that the composition of austenite in the experimental annealing is close to the predicted equilibrium composition in Figure 11.8b. In order to evaluate the stability of reversed austenite at different annealing temperatures, the M_S-temperature of reversed austenite with equilibrium composition as a function of temperature is calculated with two empirical formulas. The first formula by Folkhard was specifically designed for soft martensitic steels in welding lines [25]:

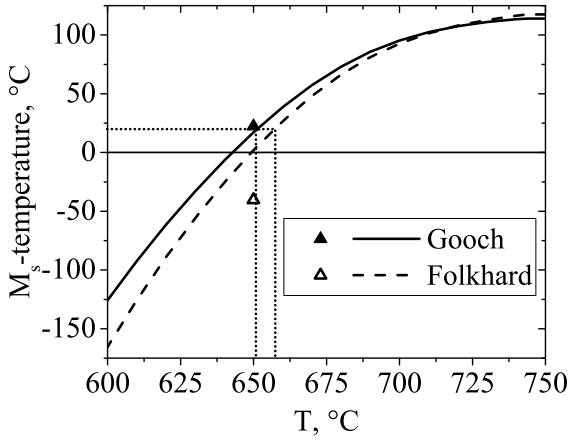

Figure 11.9: Martensite start temperature based on empiric formulae of Gooch [24] and Folkhard [25] applied on the equilibrium composition of austenite (Figure 11.8b) and the EDS-results at 650 °C (Figure 11.7b). The dotted lines indicate the critical annealing temperatures for austenite stability at room-temperature (martensite start temperature 20 °C).

$$M_{s,F} = 492 - 125 \times (wt.\%\ C) - 65.5 \times (wt.\%\ Mn) - 10 \times (wt.\%\ Cr) - 29 \times (wt.\%\ Ni) \quad (11.1)$$

The second formula by Gooch was also developed for the use on supermartensitic stainless steels in welding applications [24]:

$$M_{s,G} = 540 - 497 \times (wt.\%\ C) - 6.3 \times (wt.\%\ Mn) - 36.3 \times (wt.\%\ Ni) - 10.8 \times (wt.\%\ Cr) - 46.6 \times (wt.\%\ Mo) \quad (11.2)$$

The kinetics model was run without contribution of interstitial elements for reasons of numeric stability; for the sake of consistency the equilibrium calculations and subsequently the M_s calculations were therefore also carried out without the effect of N and C. Figure 11.9 shows the resulting graphs for M_s as a function of annealing temperature for compositions from thermodynamic equilibrium (lines) and from EDS analysis of the annealing condition 650°C/2h from Figure 11.7b (data points). It is evident that reversed austenite becomes less stable with increasing annealing temperature and that M_s with increasing phase fraction of austenite approaches the average M_s of the alloy.

M_s of the investigated alloy on cooling after austenitization was determined as 135 °C with dilatometry; the predicted temperatures by both formulas deviate approx. 20 °C from this value. The formulae by Gooch and Folkhard predicted the critical temperatures for stability of austenite at room-temperature to 651 and 657 °C (cf. Figure 11.9), respectively. This is well in line with the condition of lowest hardness, and thus maximum austenite phase-fraction, for tempering at 650 °C for 2 h (Figure 11.1). The dilatometry measurements to sub-zero Celsius temperature are in qualitative agreement with the prediction of the empirical formulae. Quantitative comparison is not feasible as not enough soaking time at the maximum temperature was applied to approach thermodynamic equilibrium.

These observations support the hypothesis that stabilization of reversed austenite is mainly a chemical stabilization. Furthermore it is anticipated that the lamellar structure of reversed austenite leads to additional mechanical stabilization. Annealing at increased temperature and time would lead to a steady spheroidization of reversed austenite which would reduce the amount of strain energy needed for martensite transformation and reduce mechanical stabilization. This effect is discussed in further depth in Ref. [23].

11.5 Conclusions

The mechanisms involved in the formation and stabilization of reversed austenite in supermartensitic stainless steel was studied in a multi-angle approach. The main conclusions are:

- Austenite can be stabilized by isothermal annealing and leads to softening of the material. The lowest hardness, corresponding to the maximum phase fraction of austenite, was measured for annealing 2 h at 650 °C.
- Thermodynamics modeling was used to demonstrate that austenite is increasingly chemically stabilized the further it forms below A_3. Annealing above 650 °C correspondingly leads to a gradual decrease in fraction austenite and to an increase in hardness.
- The stability of reversed austenite by chemical stabilization was analyzed by equilibrium compositions of austenite at different temperatures and empirical formulas for M_s. The analysis yielded good agreement with the experimental results.

Acknowledgements

The Danish Underground Consortium is gratefully acknowledged for financial support to the Danish Hydrocarbon Research Center (DHRTC). Olaf Kessler, Michael Reich, and Kristin Aurich are acknowledged for their support with the dilatometry activities at Rostock University.

References

[1] A.W. Marshall, J.C.M. Farrar, Welding of Ferritic and Martensitic 11-14% Cr Steels, Weld. World. 45 (2001) 19–42.
[2] L.M. Smith, M. Celant, Martensitic stainless steel flowlines - Do they pay?, in: Supermartensitic Stainl. Steels 1999, 1999: pp. 66–73.
[3] D.-S. Leem, Y.-D. Lee, J.-H. Jun, C.-S. Choi, Amount of retained austenite at room temperature after reverse transformation of martensite to austenite in an Fe–13%Cr–7%Ni–3%Si martensitic stainless steel, Scr. Mater. 45 (2001) 767–772.
[4] H.J. Niederau, A New Low-Carbon 16Cr-5Ni Stainless Martensitic Cast Steel, in: G. Behal, A.S. Melilli (Eds.), Stainl. Steel Cast., ASTM, Bal Harbour, Florida, 1982: pp. 382–393.
[5] M. Al Dawood, I.S. El Mahallawi, M.E. Abd El Azim, M.R. El Koussy, Thermal aging of 16Cr – 5Ni – 1Mo stainless steel Part 1 – Microstructural analysis, Mater. Sci. Technol. 20 (2004) 363–369.
[6] D. Ye, J. Li, W. Jiang, J. Su, K. Zhao, Effect of Cu addition on microstructure and mechanical properties of 15%Cr super martensitic stainless steel, Mater. Des. 41 (2012) 16–22.
[7] P.D. Bilmes, M. Solari, C.. Llorente, Characteristics and effects of austenite resulting from tempering of 13Cr–NiMo martensitic steel weld metals, Mater. Charact. 46 (2001) 285–296.
[8] M. Karlsen, J. Hjelen, Ø. Grong, G. Rørvik, R. Chiron, U. Schubert, E. Nilsen, SEM/EBSD based in situ studies of deformation induced phase transformations in supermartensitic stainless steels, Mater. Sci. Technol. 24 (2008) 64–72.
[9] T. LeBrun, T. Nakamoto, K. Horikawa, H. Kobayashi, Effect of retained austenite on subsequent thermal processing and resultant mechanical properties of selective laser melted 17-4 PH stainless steel, Mater. Des. 81 (2015) 44–53.
[10] E.L. Tobolski, A. Fee, Macroindentation Hardness Testing, in: Mech. Test. Eval. 8, ASM Handbook, ASM Int., 2000: p. p 203–220.
[11] F. Niessen, M. Villa, D. Apel, O. Keßler, M. Reich, J. Hald, M.A.J. Somers, In situ techniques for the investigation of the kinetics of austenitization of supermartensitic stainless steel, Mater. Sci. Forum. 879 (2017) 1381–1386.
[12] P.J. Spencer, A brief history of CALPHAD, Calphad Comput. Coupling Phase Diagrams Thermochem. 32 (2008) 1–8.
[13] L. Kaufman, H. Bernstein, Computer Calculation of Phase Diagrams : With Special Reference to Refractory Metals, 1970.
[14] Thermo-Calc Software TCFE6 Steels/Fe-alloys database version 6.2, Thermo-Calc Softw. TCFE6 Steels/Fe-Alloys Database Version 6.2 (Accessed Novemb. 2009).
[15] A. Borgenstam, A. Engström, L. Höglund, J. Ågren, DICTRA, a tool for simulation of diffusional transformations in alloys, J. Phase Equilibria. 21 (2000) 269–280.
[16] Thermo-Calc Software TCS Alloys Mobility Database MOB2 (accessed 08 April 1998).
[17] F. Niessen, M. Villa, J. Hald, M.A.J. Somers, Kinetics analysis of two-stage austenitization in supermartensitic stainless steel, Mater. Des. 116 (2017) 8-15.
[18] F. Niessen, N.S. Tiedje, J. Hald, Kinetics modeling of delta-ferrite formation and retainment during casting of supermartensitic stainless steel, Mater. Des. 118 (2017) 138–145.
[19] S. Morito, H. Tanaka, R. Konishi, T. Furuhara, T. Maki, The morphology and crystallography of lath martensite in Fe-C alloys, Acta Mater. 51 (2003) 1789–1799.
[20] R.F. Egerton, Physical Principles of Electron Microscopy - An Introduction to TEM,

SEM and AEM, 2005.
[21] L. Liu, Z.-G. Yang, C. Zhang, Effect of retained austenite on austenite memory of a 13% Cr–5% Ni martensitic steel, J. Alloys Compd. 577 (2013) 654–660.
[22] N. Nakada, T. Tsuchiyama, S. Takaki, S. Hashizume, Variant Selection of Reversed Austenite in Lath Martensite, ISIJ Int. 47 (2007) 1527–1532.
[23] S. Zhang, P. Wang, D. Li, Y. Li, Investigation of the evolution of retained austenite in Fe-13%Cr-4%Ni martensitic stainless steel during intercritical tempering, Mater. Des. 84 (2015) 385–394.
[24] T.G. Gooch, Welding Martensitic Stainless Steels, Weld. Inst. Researach Bull. (1977) 343–349.
[25] E. Folkhard, Welding metallurgy of stainless steels, in: Weld. Metall. Stainl. Steels, 1988: pp. 98–181.

12 Manuscript VII

Martensite formation from reverted austenite at sub-zero Celsius temperature

Frank Niessen[a,†], Matteo Villa[b], Marcel A.J. Somers[b]

[a] Technical University of Denmark (DTU), Danish Hydrocarbon Research and Technology Centre (DHRTC) , Elektrovej building 375, 2800 Kgs. Lyngby, Denmark

[b] Technical University of Denmark (DTU), Department of Mechanical Engineering, Produktionstorvet building 427, 2800 Kgs. Lyngby, Denmark

[†] Corresponding author

Abstract

Inter-critical annealing of soft martensitic stainless steel leads to formation of fine-grained reverted austenite, which is stabilized by partitioning of Ni. Generally it is reported that the fraction of reverted austenite is not affected by immersion in cryogenic liquids, such as boiling N_2 and He. Present data shows that, despite its apparent stability at boiling nitrogen temperature, reverted austenite transforms to isothermal (thermally activated) martensite during holding at 194.5 K.

Soft martensitic stainless steels are essentially Fe-Cr-Ni alloys which contain a very low fraction of interstitially dissolved C and N [1–3]. These steels are used for heavy-section water turbine components, pump and valve bodies and wellhead equipment in the oil and gas industry [4]. Soft martensitic stainless steels are known for their resistance against CO_2 corrosion, good weldability, good ductility at high strength and excellent impact toughness, even at sub-zero Celsius temperatures [5,6].

As for the case of supermartensitic stainless steels [1] and ferritic Fe-Ni alloys [7], the excellent impact toughness at low temperature is partially owed to the low content of interstitials, which leads to low hardness [1], and partially to the presence of, so called, reverted austenite, which forms a fine "composite" microstructure with tempered martensite [7–9]. Soft martensitic stainless steels show impact values of approx. 70–110 J at 190 K [5,6,10]; supermartensitic stainless steels even in excess of 100 J [1,2,11]. Consequently, these materials appear particularly suitable for sub-zero Celsius applications [1,5,6,12].

Reverted austenite forms during inter-critical annealing treatment between A_1 and A_3, where both ferrite and austenite can co-exist under thermodynamic equilibrium conditions. After austenitization and cooling to room temperature, the microstructure consists of lath martensite; heating to and annealing within the inter-critical temperature region promotes partial reversion of martensite to austenite in the form of austenite films at martensite lath boundaries [16]. Austenite formation is accompanied by the partitioning of alloying elements in an attempt to establish thermodynamic equilibrium. In particular the diffusion-controlled Ni partitioning governs the overall kinetics of the transformation [17,18]. Because of the partitioning of alloying elements, reverted austenite is more stable than the homogeneous austenite formed during austenitization and can be retained at room temperature [8,18,19].

The material used in the present work is a 15Cr-5.8Ni-1Mo-0.9Mn steel (in wt-%), grade EN 1.4418. The content of interstitials was 0.034 wt.% C and 0.032 wt.% N, respectively. The formation of reverted austenite is presented in Figure 12.1. The initial "as normalized" condition (i.e. austenitized and quenched) was obtained by austenitization at 1190 K for 0.6 ks and quenching at an average rate of approx. 1 $K.s^{-1}$. Subsequent intercritical annealing consisted in heating to a temperature in the range 898-973 K, followed by cooling to room temperature. The heating rate was constant and equal to 0.25 $K.s^{-1}$; the cooling rate was 0.25 $K.s^{-1}$ for temperatures higher than 450 K and 0.016 $K.s^{-1}$ below 450 K. Intercritical annealing was carried out at the HZB-Bessy II synchrotron facility, EDDI-beamline [20], and the fractions of austenite and martensite were determined in situ by X-ray diffraction (XRD) (c.f. Ref. [21] for details).

Figure 12.1 shows that the material is essentially martensitic after normalization and contains less than 3 vol.% of retained austenite. A_{c1} is approx. 840 K and on continuous heating, the transformation accelerates such that the fraction of austenite reaches approx.

Table 12.1: Overview of materials, annealing parameters and testing procedures considered in previous works in order to test the thermal stability of reverted austenite in soft martensitic and supermartensitic stainless steels. The indicated alloying contents are balanced with Fe.

Ref.	*Approx. alloying content* [wt.%]	*Annealing treatment*	*Cryogenic treatment*
[6]	Cr 13–16, Ni 5–6, Mo <1.5, C 0.03–0.06	860 K	77 K
[13]	Cr 12–17, Ni 4–7, Mo <2.5, C 0.03	Not specified	77 K
[5]	Cr 15–17, Ni 4.5–6.5, Mo <2.9, C <0.07	870 K / 28.8 ks	77 K
[11]	Cr 12, Ni 5.4, Mo 0.5, C 0.028	870 K / 7.2 ks	271 K, 256 K, 248 K, 77 K / 72 ks
[14]	Cr 12, Ni 6.5, Mo 2.5, C 0.01	910 K	77 K / 3.6 ks
[10]	Cr 12, Ni 4.4, Mo 0.5, C 0.07	870 K / 14.4 ks	4K
[15]	Cr 12, Ni 5.6, Mo 2.0, C 0.02	908 K / 14.4 ks	77 K / 72 ks

0.5 at 973 K, the highest applied annealing temperature. On cooling, additional formation of austenite occurs at temperatures higher than A_{c1}. No further change in the phase fraction is measured on continuous cooling to room temperature for the samples treated to 898 K and 923 K; for cooling from 948 and 973 K reverted austenite partially transforms into martensite. In all cases inter-critical treatment yields a significant fraction of reverted austenite.

It was demonstrated in Ref. [22] that the impact toughness of the present steel grade scales with the fraction of reverted austenite. This relation naturally raises the question whether reverted austenite is unconditionally thermally stable at sub-zero Celsius temperatures. The driving force for martensite formation increases with undercooling below T_0 [23], suggesting that lowering the temperature is a viable method to test thermal stability. Several groups have claimed that the phase fraction of reverted austenite in various soft and supermartensitic stainless steels is not affected by immersion in boiling N_2 (77 K) [5,6,11,13–15] or boiling He (4 K) [10].

Niederau [5], Grounes and Rao [6] and Kulmburg et al. [13] claimed thermal stability of reverted austenite during immersion in boiling N_2 without providing experimental evidence. Song et al. [10] and Carrouge et al. [14] provided X-ray diffractograms before and after immersion in boiling He and N_2, respectively, which did not indicate a change in phase fraction. Bilmes et al. [11] applied Mössbauer spectroscopy to compare the fraction of reverted austenite after isothermal holding at 271 K, 256 K, 248 K and 77 K for 72 ks and concluded that austenite is stable. Finally, Bojack et al. [15] applied magnetometry to show that no transformation occurs after 72 ks at boiling N_2 temperature and anticipated that reverted austenite remains stable after sub-zero Celsius

Table 12.2: Measured austenite fraction, f_γ, in vol.% of differently annealed samples during or after applied thermal cycles in XRD or VSM.

Thermal cycle	*Method*	f_γ *(873 K)*	f_γ *(898 K)*	f_γ *(923 K)*	f_γ *(948 K)*
Intercritical annealing *(maximum fraction during annealing)*	XRD	0.15	0.38	0.58	0.61
Intercritical annealing *(retained fraction at room temperature)*	XRD	0.15	0.35	0.29	0.21
Intercritical annealing *(retained fraction at room temperature)*	VSM	0.10	0.26	0.27	0.16
Immersion in N_2 *(retained fraction at room temperature)*	VSM	0.10	0.25	0.27	0.16
Sub-zero treatment *(retained fraction at room temperature)*	VSM	0.10	0.23	0.22	0.15

treatment if no martensite is formed during cooling to room temperature after inter-critical annealing. An overview of literature data is given in Table 12.1.

In the current work, we applied vibrating sample magnetometry (VSM) on cylindrical samples of Ø3x0.75 mm to test the thermal stability of reverted austenite. Heat treatment conditions were consistent with those applied in in-situ XRD, apart from the cooling rate from the intercritical annealing temperature, which was not constant and significantly faster than for the XRD investigation. The cooling rate exceeded 0.7 $K.s^{-1}$ at

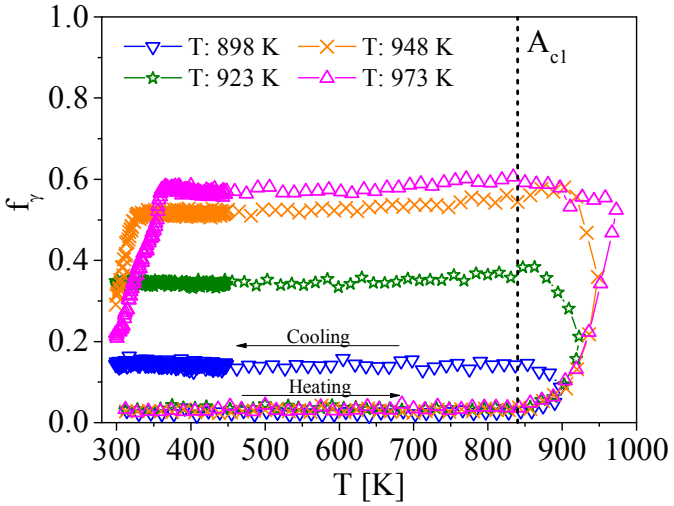

Figure 12.1: Fraction of austenite f_γ versus temperature T for four inter-critical annealing treatments. Numbers in the legend refer to the temperature reached during the heating step, immediately followed by cooling.

temperatures higher than A_{c1} and was 0.25 K.s^{-1} on average. After inter-critical annealing, the material was stored at room temperature for approx. 1 year.

VSM was performed with a Lake Shore Cryotronics 7407 VSM equipped with a Janis SuperTran-VP continuous flow cryostat and was applied before subjecting the material to sub-zero Celsius treatment and after immersion in boiling N_2 followed by fast re-heating by immersion in water (up-quenching). The magnetic properties were evaluated at 290 K by recording of hysteresis curves. Three repetitions were applied for evaluation of the experimental error. The fraction of austenite was determined by comparison of the specific magnetic moment at saturation of the samples, M^{sat}, evaluated at 1 Tesla with the one of the normalized sample, M_{ref}^{sat}, taking into account the initial fraction of retained austenite, $f_{\gamma_{ret}}$, as measured by XRD (i.e. 0.03):

$$f_\gamma = 1 - f_{\alpha'} = 1 - \frac{M^{sat}}{M_{ref}^{sat}\left(1 - f_{\gamma_{ret}}\right)} \tag{12.1}$$

Figure 12.2 displays and Table 12.2 lists the results of the investigations. The content of austenite before sub-zero Celsius cooling is comparable, but not identical, to the austenite fractions obtained by in-situ synchrotron investigation (cf. Figure 12.1). Immersion in boiling nitrogen and up-quenching to room temperature did not significantly affect the fraction of austenite, which is consistent with literature data (cf.Table 12.1) and suggests thermal stability of reverted austenite in soft martensitic stainless steel at low temperatures.

Recently, it was discussed that the formation of lath martensite at sub-zero temperature should be approached by Time Temperature Transformation (TTT) diagrams. A schematic representation is given in Figure 12.3 (cf. [24,25]). According to such diagrams isothermal martensite formation proceeds at a maximum rate at a temperature

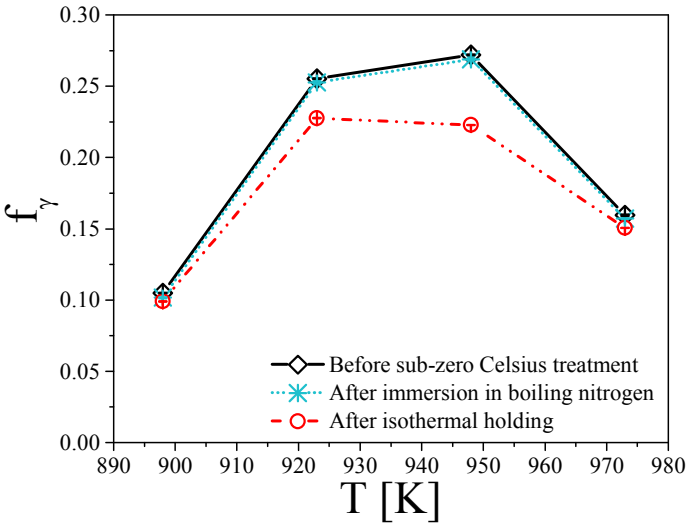

Figure 12.2: Fraction of austenite f_γ versus annealing temperature T. The three data sets refer to the material before sub-zero Celsius treatment, after immersion in boiling N_2 for 0.3 ks and after additional isothermal holding at 194.5 K for 15.3 ks.

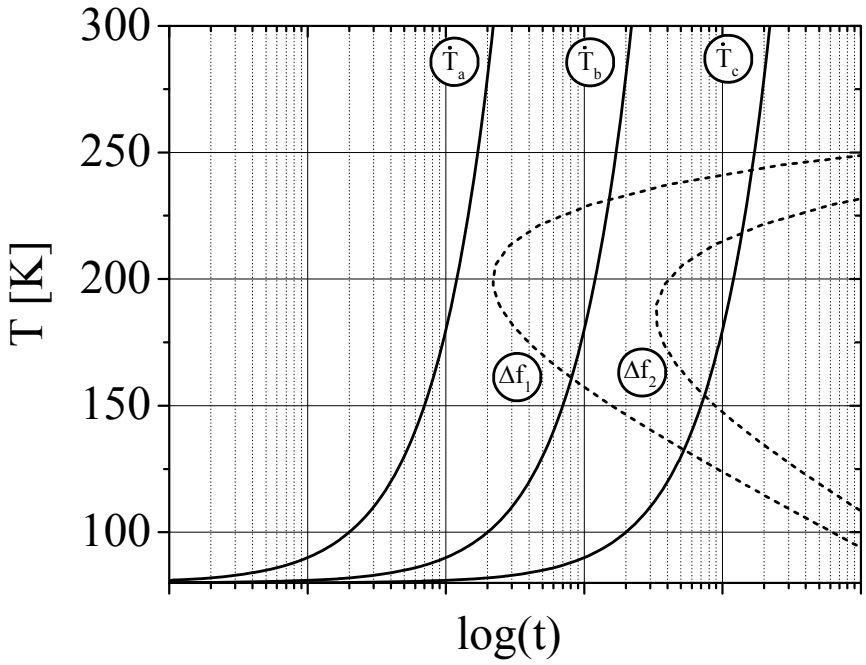

Figure 12.3: Schematic Time-Temperature-Transformation, TTT, diagram for formation of lath martensite from an approximate austenite fraction of 100 vol.% (after [22,23]). The solid lines correspond to time-temperature curves, starting from an initial temperature of 80 K and following linear heating rates, $\dot{T}_a > \dot{T}_b > \dot{T}_c$. The broken lines indicate constant fractions of transformed martensite, $\Delta f_2 > \Delta f_1$, during isothermal holding. The diagram demonstrates that up-quenching can prevent martensite formation (following $\dot{T}_a$) and that the martensite content formed on reaching room temperature depends on the heating rate (comparing $\dot{T}_b$ and $\dot{T}_c$).

appreciably higher than 80 K and proceeds only very slowly for temperatures just below 273 K. As Figure 12.3 illustrates, martensite formation can be suppressed for fast cooling to 80 K. For continuous heating from 80 K, martensite formation is suppressed for relatively fast linear heating (curve $\dot{T}_a$), , while slower heating (curves $\dot{T}_b$ and $\dot{T}_c$) promotes the formation of martensite.

Evidently, Figure 12.3 suggests that reverted austenite may appear stable in soft martensitic stainless steel and that it depends on the heating rate to room temperature whether any martensite formation is observed. This is no guarantee that austenite is stable at an intermediate sub-zero Celsius temperature. In order to test this hypothesis, the same samples subjected to VSM investigation before and after boiling nitrogen were subjected to an additional sub-zero Celsius treatment. The thermal cycle consisted of cooling at 0.25 $K.s^{-1}$ from 290 K to 194.5 K, isothermal holding at 194.5 K for 15.3 ks and heating at 0.25 $K.s^{-1}$ to 290 K. VSM was applied to monitor the evolution of magnetization at saturation in the cycle, applying a constant magnetic field of 1 T. Additionally, the magnetic properties were tested at the end of the thermal cycle as for the other two conditions (i.e. not treated and after immersion in boiling nitrogen). Figure 12.4 shows that the additional thermal cycle has reduced the austenite content by up to 5 vol.% austenite. In particular the reverted austenite formed at 923 and 948 K was affected by the cryogenic cycle. In-situ measurement of the austenite fraction during cryogenic treatment revealed that no

considerable transformation occurred during heating and cooling (Figure 12.4a), and that the rate of martensite formation during isothermal holding followed an exponential decay (Figure 12.4b). The isothermal curves for the 923 and 948 K conditions indicate that the transformation would continue if further holding was applied.

The present results demonstrate that the common procedure to validate the thermal stability of reverted austenite, i.e. immersion into liquids at 77 K or lower temperature, is not a sufficient proof for the stability of reverted austenite against martensite formation. With reference to the schematic TTT diagram in Figure 12.3, the testing temperatures in research published so far (Table 12.1) were chosen too low, such that martensite formation was suppressed and proceeded only very slowly [5,6,10,11,13–15] and heating rates could have been too fast. Bilmes et al. [11] considered higher temperatures in the range of 271 – 248 K to test thermal stability of reverted austenite, which are likely to be too high to build up a sufficient driving force for martensite formation.

Based on the generally observed kinetics of isothermal martensite formation in the literature [24] and the specific results obtained on reverted austenite in the present work, we suggest isothermal holding for several 10 ks (i.e. several days) at 194.5 K (frozen CO_2 temperature) as a test for the thermal stability of austenite.

The most effective temperature region for isothermal martensite formation, approx. 180 – 210 K, is often used to measure the impact toughness at sub-zero Celsius temperature [1,5,6,10,11,14,26,27]. The demonstrated possibility of isothermal martensite formation in this temperature region opens up the possibility of a time dependent change in impact toughness. Consequently, we propose to state the cooling time of samples, similar to the conventional statement of annealing times of heat-treated samples, when reporting impact toughness values. Further, impact testing for qualification of austenite containing steels

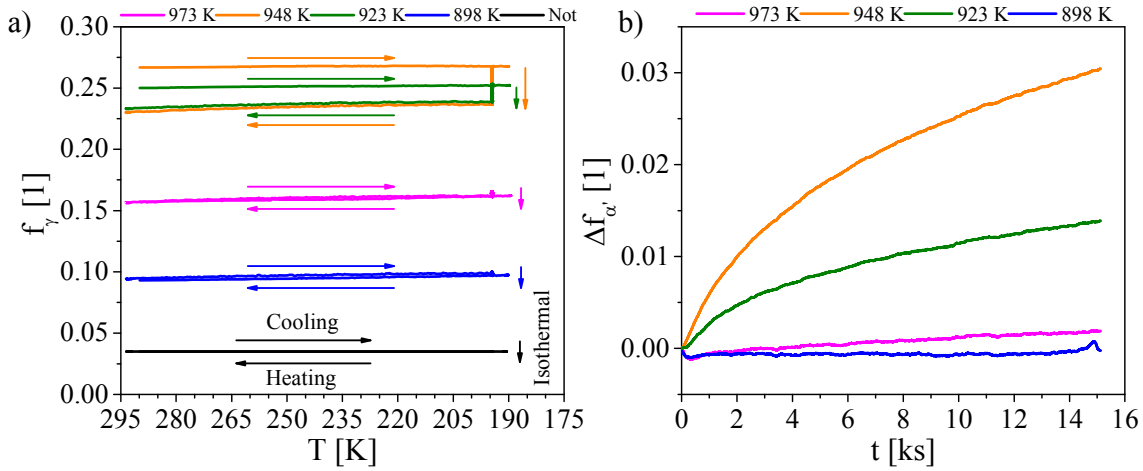

Figure 12.4: VSM results from of sub-zero Celsius treatment: (a) Fraction of austenite, f_γ, of the differently tempered samples vs. temperature for cooling to 194.5 K with 0.25 K.s^{-1}, isothermal holding for 15.3 ks and reheating to room temperature with 0.25 K.s^{-1}; (b) Fraction transformed, $\Delta f_{\alpha'}$, vs. time during isothermal holding at 194.5 K.

should be carried out on samples which were exposed to different cryogenic holding times in the temperature region around 195 K.

In summary, it was demonstrated that reverted austenite which is stable at room temperature after inter-critical annealing, is also thermally stable during immersion in boiling N_2, but could partially be transformed to martensite during holding at an intermediate temperature of 195 K. Up till now, several tests in the literature at boiling N_2 or He temperature were considered proof that reverted austenite remains stable during sub-zero Celsius application. Relatively fast transformation at 195 K and negligible transformation at T<120 K can be understood in terms of thermally activated martensite formation as displayed by C-curves in TTT diagrams in the sub-zero Celsius range. The present results indicate that impact toughness measured at sub-zero Celsius temperatures can be time dependent, as it directly correlates with the fraction of austenite.

Acknowledgements

Mikkel F. Hansen is acknowledged for providing the VSM facilities. The Danish Underground Consortium is gratefully acknowledged for financial support to the Danish Hydrocarbon Research Center (DHRTC), which partly financed this work. This work was financially supported by the Danish Council for Independent Research [grant number: DFF-4005-00223].

References

[1] A.W. Marshall, J.C.M. Farrar, Welding of Ferritic and Martensitic 11-14% Cr Steels, Weld. World. 45 (2001) 19–42.

[2] K. Kondo, M. Ueda, K. Ogawa, H. Hirata, H. Takabe, Y. Miyazaki, Alloy design of Super 13Cr martensitic stainless steel, in: Supermartensitic Stainl. Steels 1999, 1999: pp. 11–18.

[3] F. Niessen, Austenite reversion in low-carbon martensitic stainless steels – a CALPHAD-assisted review, Mater. Sci. Technol. (2018), doi: 10.1080/02670836.2018.1449179

[4] L.M. Smith, M. Celant, Martensitic stainless steel flowlines - Do they pay?, in: Supermartensitic Stainl. Steels 1999, 1999: pp. 66–73.

[5] H.J. Niederau, Eigenschaften und Anwendungsmöglichkeiten der Guss- und Schmiedelegierung (G)X-5 CrNiMo 16 5 (Werkstoff-Nr. 1.4405), Zeitschrift Des Vereins Dtsch. Ingenieure Für Maschinenbau Und Met. Eig. 21 (1982) 801–808.

[6] M. Grounes, S. Rao, New Alloy Steels for Nuclear Reactor Pressure Vessels and Vessel Internals, Trans. ASM. 62 (1969) 902–914.

[7] J.W. Morris Jr., Croygenic steels, in: H.D. McPerson (Ed.), Encycl. Adv. Mater., Pergamon Press, Oxford, UK, 1986.

[8] S. Zhang, P. Wang, D. Li, Y. Li, Investigation of the evolution of retained austenite in Fe-13%Cr-4%Ni martensitic stainless steel during intercritical tempering, Mater. Des. 84 (2015) 385–394.

[9] Y. Iwabuchi, S. Sawada, Metallurgical Characteristics of a Large Hydraulic Runner Casting of Type 13Cr-Ni Stainless Steel, Stainl. Steel. (1982) 332–354.

[10] Y. Song, D.H. Ping, F.X. Yin, X.Y. Li, Y.Y. Li, Microstructural evolution and low temperature impact toughness of a Fe–13%Cr–4%Ni–Mo martensitic stainless steel, Mater. Sci. Eng. A. 527 (2010) 614–618.

[11] P.D. Bilmes, M. Solari, C.L. Llorente, Characteristics and effects of austenite resulting from tempering of 13Cr–NiMo martensitic steel weld metals, Mater. Charact. 46 (2001) 285–296.

[12] H.J. Niederau, A New Low-Carbon 16Cr-5Ni Stainless Martensitic Cast Steel, in: G. Behal, A.S. Melilli (Eds.), Stainl. Steel Cast., ASTM, Bal Harbour, Florida, 1982: pp. 382–393.

[13] A. Kulmburg, F. Konrtheuer, M. Koren, O. Gründler, K. Hutterer, Kapfenberg, Umwandlungs- und Ausscheidungsverhalten von weichmartensitischen und hochfesten korrosionsbeständigen Stählen, Berg- Und Hüttenmännische Monatshefte. 123 (1981) 104–108.

[14] D. Carrouge, H.K.D.H. Bhadeshia, P. Woollin, Effect of δ -ferrite on impact properties of supermartensitic stainless steel heat affected zones, Sci. Technol. Weld. Join. 9 (2004) 377–389.

[15] A. Bojack, L. Zhao, P.F. Morris, J. Sietsma, In Situ Thermo-magnetic Investigation of the Austenitic Phase During Tempering of a 13Cr6Ni2Mo Supermartensitic Stainless Steel, Metall. Mater. Trans. A Phys. Metall. Mater. Sci. 45 (2014) 5956–5967.

[16] F. Niessen, F.B. Grumsen, J. Hald, M.A.J. Somers, Formation and stabilization of reversed austenite in supermartensitic stainless steel, in: Proc. 24th IFHTSE Congr., 2017: pp. 138–145.

[17] F. Niessen, M. Villa, J. Hald, M.A.J. Somers, Kinetics analysis of two-stage austenitization in supermartensitic stainless steel, Mater. Des. 116 (2017) 8–15.

[18] J.D. Escobar, J.D. Poplawsky, G.A. Faria, J. Rodriguez, J.P. Oliveira, C.A.F.

Salvador, P.R. Mei, S.S. Babu, A.J. Ramirez, Compositional analysis on the reverted austenite and tempered martensite in a Ti-stabilized supermartensitic stainless steel: Segregation, partitioning and carbide precipitation, Mater. Des. 140 (2018) 95–105.
[19] N. Nakada, T. Tsuchiyama, S. Takaki, N. Miyano, Temperature Dependence of Austenite Nucleation Behavior from Lath Martensite, ISIJ Int. 51 (2011) 299–304.
[20] C. Genzel, I. Denks, M. Klaus, The Materials Science Beamline EDDI for Energy-Dispersive Analysis of Subsurface Residual Stress Gradients, Mater. Sci. Forum. 524–525 (2006) 193–198.
[21] F. Niessen, M. Villa, D. Apel, O. Keßler, M. Reich, J. Hald, M.A.J. Somers, In situ techniques for the investigation of the kinetics of austenitization of supermartensitic stainless steel, Mater. Sci. Forum. 879 (2017) 1381–1386.
[22] M. Wiessner, E. Gamsjäger, S. van der Zwaag, P. Angerer, Effect of reverted austenite on tensile and impact strength in a martensitic stainless steel−An in-situ X-ray diffraction study, Mater. Sci. Eng. A. 682 (2017) 117–125.
[23] C. Zener, Kinetics of the Decomposition of Austenite, AIMME, Met. Technol. (1946) 550–595.
[24] M. Villa, M.A.J. Somers, Thermally activated martensite formation in ferrous alloys, Scr. Mater. 142 (2018) 46–49.
[25] M. Villa, M.A.J. Somers, Activation energy of time-dependent martensite formation in steel (accepted), in: Int. Conf. Martensitic Transform., Chicago, 2018.
[26] P. Wang, S.P. Lu, N.M. Xiao, D.Z. Li, Y.Y. Li, Effect of delta ferrite on impact properties of low carbon 13Cr-4Ni martensitic stainless steel, Mater. Sci. Eng. A. 527 (2010) 3210–3216.
[27] J. Van Den Broek, M. Goldschmitz, L. Karlsson, S. Rigdal, Efficient welding of supermartensitic pipes with matching metal cored wires, Svetsaren. 56 (2001) 42–46

13 Manuscript VIII

Mechanical stability of reverted austenite in supermartensitic stainless steel – an *in-situ* synchrotron X-ray diffraction study

Frank Niessen[a,†], John Hald[b], Marcel A.J. Somers[b]

[a] Technical University of Denmark (DTU), Danish Hydrocarbon Research and Technology Centre (DHRTC) , Elektrovej building 375, 2800 Kgs. Lyngby, Denmark

[b] Technical University of Denmark (DTU), Department of Mechanical Engineering, Produktionstorvet building 427, 2800 Kgs. Lyngby, Denmark

[†] Corresponding author

Abstract

The mechanical stability of reverted austenite in X3CrNiMo13-6-2 supermartensitic stainless steel was measured by applying in-situ energy-dispersive synchrotron diffraction during tensile loading. The lattice strains in austenite and martensite, the fraction of austenite and the micro-strains were analyzed as a function of applied stress. It was found that considerable amounts of reverted austenite transform strain-induced to martensite and extend ductility. Analysis of partitioning of the applied stress into lattice stresses revealed that plastic deformation is partly accomplished by austenite-to-martensite transformation while the stress in martensite follows the applied stress. Strain-induced martensite formed preferentially with <200> parallel to the tensile axis.

13.1 Introduction

Supermartensitic stainless steels are popular materials for offshore pipeline applications in the oil and gas industry. The material design aims at replacing more expensive duplex stainless steels with properties as decent corrosion resistance, high toughness, good ductility and weldability, and enhanced strength [1–4].

The favorable combination of properties is achieved by solution treatment in the austenite region, martensite formation during cooling, and subsequent formation and stabilization of reverted austenite by annealing in the inter-critical region, i.e. between A_1 and A_3. The stability of reverted austenite mainly originates from partitioning of Ni and may further be affected by the grain size and mechanical constraint of the surrounding martensite matrix [4,5]. Reverted austenite leads to softening of the material, while ductility and impact toughness are greatly enhanced [4,6]. It has been reported that reverted austenite in low-carbon martensitic stainless steel may transform to martensite during mechanical straining of the material [5,7,8]. The transformation manifests as transformation-induced plasticity (TRIP), where the plastic regime is extended by transformation from austenite to martensite.

Much research has been dedicated to investigating and exploiting TRIP in near β-Ti alloys [9], low-alloyed TRIP-steels [10–14] and metastable austenitic stainless steel [15]. These studies applied high-energy diffraction techniques, such as synchrotron X-ray or neutron diffraction, to follow strain partitioning, evolution of the substructure and the kinetics of the stress/strain-induced transformation as a function of applied stress in real time. Even though the TRIP effect has been reported for soft martensitic and supermartensitic stainless steels in relation to the interpretation of their strain-hardening behavior [5,8], post-mortem microstructure characterization [5,7,8] and mechanical modeling [5], it has to date not been observed *in situ*.

In the present work, the evolution of the microstructure of X3CrNiMo13-6-2 supermartensitic stainless steel in response to uniaxial tensile loading is measured by *in-situ* synchrotron X-ray diffraction and 3D digital image correlation. The study elucidates the stability of reverted austenite formed during different heat-treatments and its effect on the macroscopic mechanical properties.

13.2 Experimental procedure

13.2.1 Materials

The investigated material was a supermartensitic stainless steel X3CrNiMo13-6-2 (Super 13 Cr) with the composition in Table 13.1. The material was received in quenched and tempered condition as a forged and peeled round bar of Ø203 mm. Plates of approx. 130 x 12 x 5 mm^3 were cut from the center of the forged bar for manufacturing of tensile test specimens.

Table 13.1: Chemical composition of the X3CrNiMo13-6-2 alloy from optical emission spectroscopy (OES).

Fe	C	N	Cr	Ni	Mo	Mn	Si	Ti	Nb	V
Bal.	0.023	0.048	12.5	5.6	2.02	0.46	0.30	0.022	0.019	0.047

The tensile direction was parallel to the longitudinal axis of the bar. The plates were solution treated in the single-phase austenite region at 1050 °C for 1 h in Ar flow, with average heating and cooling rates of 0.75 and 1.17 K.s^{-1}, respectively. The samples were machined to their final geometry and subsequently annealed at different temperatures and times. The annealing treatments, listed in Table 13.2, reflect common single and double annealing treatments in industry and aim at obtaining different fractions and stability of reverted austenite. The tensile test pieces were manufactured according to DIN 50125 type E, with a thickness of 2 mm, width of 6 mm and original gauge length of 20 mm.

13.2.2 Experimental setup

The investigation was carried out at the EDDI-beamline at the synchrotron facility HZB-BESSY II [16] and consisted of in-situ measurements on the evolution of phase fractions, substructure and lattice strains at discrete tensile loading steps. In energy-dispersive synchrotron diffraction all reflections are acquired simultaneously. Peaks of diffracted synchrotron radiation occur for certain energies, E_{hkl}, which are a function of the respective inter-planar spacings, d_{hkl}, and the fixed scattering angle, $2\theta_0$:

$$d_{hkl} = \frac{hc}{2E_{hkl}\sin(\theta_0)} \tag{13.1}$$

where h is Planck's constant and c the speed of light in vacuum. A drawing of the experimental setup is given in Figure 13.1. Tensile loading was conducted on a Walter+Bai LFV tensile test rack with a maximum load of 20 kN and a maximum dilatation of 20 mm.

Table 13.2: Sample designation, annealing parameters, mechanical properties (based on engineering stress and strain) and reverted austenite fractions before and after tensile testing.

Label	*Annealing parameters*	R_P [MPa]	R_m [MPa]	A_{GT} [%]	f_γ^{ini} [vol.%]	f_γ^{final} [vol.%]
AH	As hardened	920	1110	4	< 1	< 1
S600	600 °C / 3 h	850	925	9	9	8
S630	630 °C / 3 h	560	890	11	18	6
D600	670 °C / 2 h + 600 °C / 3 h	775	900	12	17	10
D630	670 °C / 2 h + 630 °C / 3 h	510	900	14	24	5

Notes: $\mathbf{R_P}$ is the 0.2% proof stress, $\mathbf{R_m}$ is the ultimate tensile strength, $\mathbf{A_{GT}}$ is the percentage of total extension at maximum stress, $\boldsymbol{f_\gamma^{ini}}$ is the initial fraction of reverted austenite and $\boldsymbol{f_\gamma^{final}}$ is the final fraction of reverted austenite

The loading was controlled in a closed loop and carried out in three initial steps of 0.2 mm and following 0.4 mm until rupture with a displacement rate of 0.01 mm.s^{-1}. In between successive steps XRD measurements were performed. Two specimens of each condition were measured according to this procedure and were compared to a specimen that was loaded without interruption at a constant displacement rate of 0.01 mm.s^{-1}. The average sample temperature was 18 °C and did not increase by more than 5 °C during continuous straining with 0.01 mm.s^{-1}.

The 3D digital image correlation (DIC) system GOM ARAMIS 12 M consisted of two cameras with 4096×3072 pixels image resolution and 75 mm lenses. The cameras were positioned on the side of the secondary beam, tilted by $\alpha = 25\,°$ in the horizontal plane with respect to the primary beam and focused on the XRD gauge volume at a distance of 310 mm (Figure 13.1).

13.2.3 Determination of macroscopic strain and stress

The spatially resolved planar strains during tensile loading were determined with DIC. A stochastic pattern was applied to the sample surface by spray painting prior to the investigation and its spatially resolved displacement tracked during mechanical loading. The local planar displacements were converted to strains in GOM Correlate Professional 2016 software. Two types of strain were computed along the tensile axis: (i) A uniaxial engineering strain, ε_{eng}, which is based on the expansion from an initial distance of 20 mm and is equivalent to strain obtained from a conventional strain gage extensometer; (ii)

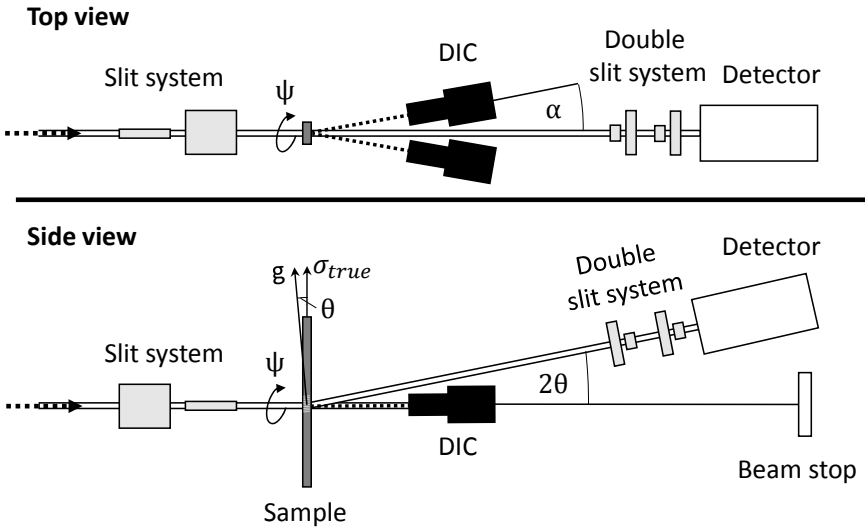

Figure 13.1: Schematic of the experimental setup in top and side view. The cross-section of the polychromatic beam is defined by a primary slit system. The beam is transmitted through the sample and the equatorial divergence of the diffracted beam is limited by a double slit system before entering the solid state Ge-detector, positioned at constant $2\theta_0$. The diffraction vector, g, deviates from the axis of applied true tensile stress, σ_{true}, by the diffraction semi-angle, θ_0. The stepwise rotation of the diffraction vector with respect to the primary beam is given by ψ. The DIC system for measurement of the macroscopic strain consists of two cameras, which were tilted by α in the horizontal plane with respect to the primary beam.

Uniaxial true strain, ε_{true}, which is determined as an average in the region of the XRD gauge volume, which was close to or overlapping with the necking region. The uniaxial engineering strain, ε_{eng}, and the uniaxial true strain, ε_{true}, are defined as:

$$\varepsilon_{eng} = \frac{l-l_0}{l_0} \quad \text{and} \quad \varepsilon_{true} = \int_{l_0}^{l} \frac{dl}{l} \tag{13.2}$$

where l_0 is the initial gauge length and l the measured gauge length of the respective measurement regions.

The engineering stress, σ_{eng} and the true stress, σ_{true}, are calculated from:

$$\sigma_{eng} = \frac{F}{A_0} \quad \text{and} \quad \sigma_{true} = \frac{F}{A} \tag{13.3}$$

where F is the applied force, measured by a force meter, A_0 the initial cross-sectional area and A the true cross-sectional area at the applied load. The true cross-sectional area was calculated by determining the transverse planar engineering strain, ε_{trans}, in the necked region with DIC and assuming an equal transverse strain for the in-plane dimension. Applying the transverse strain on the initial cross-sectional area of the sample, the true cross-sectional area is obtained:

$$A = A_0(\varepsilon_{trans})^2 \tag{13.4}$$

13.3 Experimental results and interpretation

13.3.1 Macroscopic mechanical properties

Figure 13.2 shows the stress-strain curves of differently annealed samples during continuous tensile testing with constant displacement rate. Figure 13.2a shows the engineering stress-strain relation and Figure 13.2b the true stress-strain relation. The characteristic mechanical properties, listed in Table 13.2, are obtained from the engineering stress-strain curve in Figure 13.2a.

Engineering properties

The hardened condition (AH) reveals a high proof stress of 920 MPa and an ultimate tensile strength of 1110 MPa with 4 % total extension at maximum stress. Inter-critical annealing at 600 °C (S600) leads to a noticeable reduction in proof stress to 850 MPa and an ultimate tensile strength of 925 MPa, while the total extension at maximum stress is enhanced to 9 %. Inter-critical annealing at 630 °C (S630) leads to further reduction in proof stress to 560 MPa and an ultimate tensile strength of 890 MPa, while the total extension at maximum stress is slightly enhanced to 11 %.

Annealing at 670 °C for 2 h before inter-critical annealing at 600 °C (D600) and 630 °C (D630) for 3 h has a noticeable effect on the tensile properties. Compared to the S600 condition, the D600 condition reveals a reduction in proof stress by 75 MPa and a

reduction in ultimate tensile strength by 25 MPa. Compared to the S630 condition, the D630 condition reveals a reduction in proof stress by 50 MPa, but a slight increase in ultimate tensile strength by 10 MPa. Most significantly, in both double annealed conditions the total extension at maximum stress was enhanced by 3 % compared to the single annealed conditions.

True properties

Figure 13.2b shows the true stress vs. true strain behavior of tested samples. On exceeding the yield point, the true tensile curves steadily diverge from the engineering tensile curves in Figure 13.2a. This divergence is a consequence of the diminished sample strength during reduction in cross-sectional area (necking) compared to increasing material strength during plastic deformation. The slight reduction in true stress for conditions AH and D600 just before fracture is related to the increasing uncertainty of calculating the cross-sectional area (Equ. 13.3) with increased necking. The samples that were annealed at 630 °C (S630 and D630) show an increased hardening just before failure.

Stress relaxation

In order to understand the effect of the different applied annealing treatments on the mechanical properties presented in Figure 13.2 and Table 13.2, tensile tests were interrupted and held at discrete displacement steps to conduct XRD measurements. Figure 13.3 shows stress-strain curves of three tested samples in the D600 condition. The mechanical behavior of samples of the same annealing condition reveals good reproducibility. Interruption of the tests at constant displacement steps is associated with stress relaxation. Comparison of the tensile curves of interrupted tests with the tensile curve of a continuous test shows good agreement and does not suggest a significant effect of stress relaxation on the overall mechanical behavior. Stress relaxation reached a steady

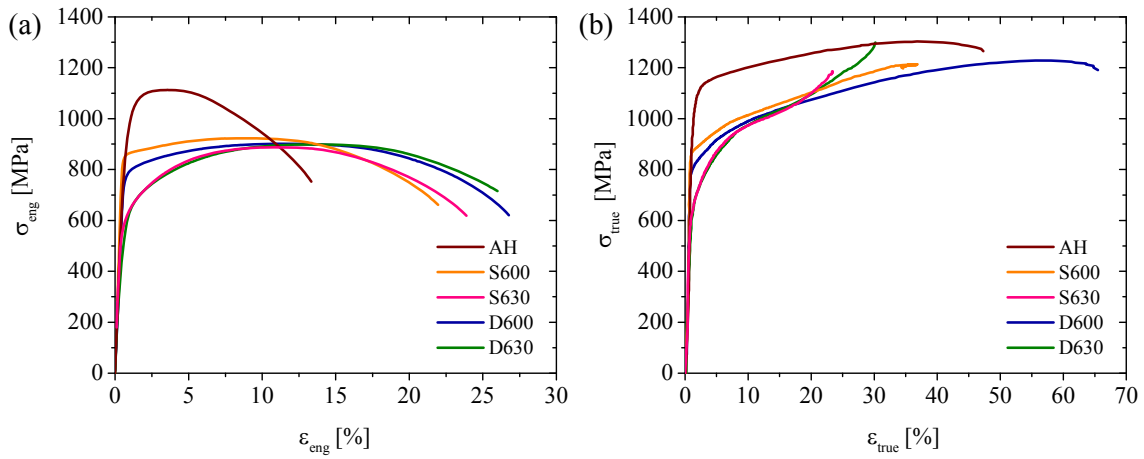

Figure 13.2: (a) Engineering stress vs. Engineering strain and (b) True stress vs. true strain tensile curves of differently annealed samples during straining with a constant displacement rate of 0.01 mm.s^{-1}. It is evident that the applied heat treatments have a significant effect on the yield point, the ultimate tensile strength and the percentage of total extension at maximum stress.

stress level after approx. 10 s. The XRD measurements were first started after a stable stress level was obtained.

13.3.2 Lattice strain analysis

In the following, the definition of lattice strains is briefly introduced and results of in-situ tensile testing of the AH, S630 and D630 conditions are presented. While samples of the other conditions gave important insights into the stress-strain behaviour and mechanical stability of reverted austenite, the XRD gauge volume was too far from the necked region to obtain *in-situ* data for more comprehensive analysis.

Calculation of lattice strains

The macroscopic stresses and strains were compared to the lattice strains of the two phases martensite (α') and austenite (γ). The lattice strain $\varepsilon_{hkl}^{\varphi}$ experienced by a family of lattice planes $\{hkl\}$ in a phase φ is obtained by comparing the planar spacing, d_{hkl}^{φ}, from Equ. 13.1 with a strain-free planar spacing, $d_{hkl}^{ref,\varphi}$:

$$\varepsilon_{hkl}^{\varphi} = \frac{d_{hkl}^{\varphi} - d_{hkl}^{ref,\varphi}}{d_{hkl}^{ref,\varphi}} \tag{13.5}$$

When only considering the major principal strains, tilting of the tensile specimen by ψ around the axis of the primary beam in the laboratory coordinate system (c.f. Figure 13.1) allows determination of the lattice strains in longitudinal, ε_{33}, and transverse direction, ε_{11}, with respect to the tensile axis [17]:

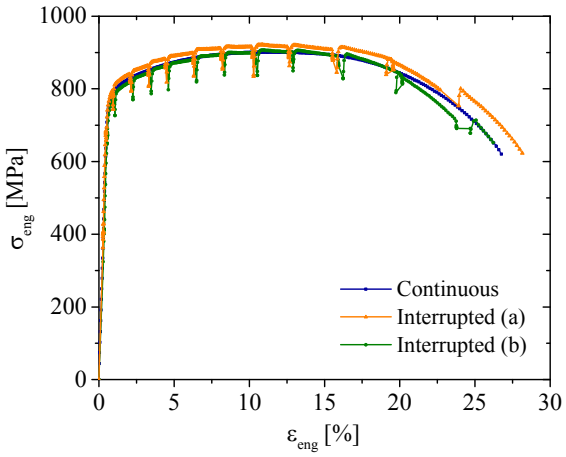

Figure 13.3: Engineering stress vs. engineering strain of three tensile tests of the D600 condition. Testing of several samples shows good reproducibility of the mechanical behavior. The applied stress relaxed during holding at constant displacement in the interrupted tests. Comparison with the continuous test reveals that stress relaxation during holding at constant displacement does not appear to affect the overall mechanical behavior of the tested samples.

$$\varepsilon_{hkl,\psi}^{\varphi} = \frac{d_{hkl,\psi}^{\varphi} - d_{hkl}^{ref,\varphi}}{d_{hkl}^{ref,\varphi}} = \varepsilon_{11}\sin^2\psi + \varepsilon_{33}\cos^2\psi \quad (13.6)$$

In cubic crystals, as is the case for α' and γ in the present case, the planar spacings d_{hkl}^{φ} may be converted to the weighted arithmetic mean of the lattice constant, a^{φ}:

$$a^{\varphi} = \frac{\sum_i^n m_{hkl}^{\varphi} d_{hkl}^{\varphi} \sqrt{h^2+k^2+l^2}}{\sum_i^n m_{hkl}^{\varphi}} \quad (13.7)$$

where the phase (φ)- and *hkl*-specific multiplicity factor, m_{hkl}^{φ}, is used as the weighting factor.

In the elastic region, the stress state may be considered purely uniaxial. In that case the lattice parameter a^{φ} follows a linear relationship with $\cos^2\psi$, where $a_{\psi=0°}^{\varphi}$ and $a_{\psi=90°}^{\varphi}$are the lattice constants along the longitudinal and transverse directions, respectively (Figure 13.4). The intersection point of linear regression lines of a^{φ} vs. $\cos^2\psi$ in the elastic region indicates the average strain-free direction,ψ_0, and the average strain-free lattice parameter, $a^{ref,\varphi}$ (Figure 13.4). In the present case, the average strain-free direction was obtained at ψ_0= 67 °. For all samples, the stress-free planar spacings $d_{hkl}^{ref,\varphi}$ were consequently defined as $d_{hkl}^{\varphi}(\psi = 67\,°)$ in the unloaded condition.

As Hardened condition (AH)

The in-situ XRD results from interrupted tensile testing of the as-hardened condition are shown in Figure 13.5. Figure 13.5a shows the *hkl*-specific lattice strains $\varepsilon_{hkl}^{\alpha'}$, Figure 13.5b

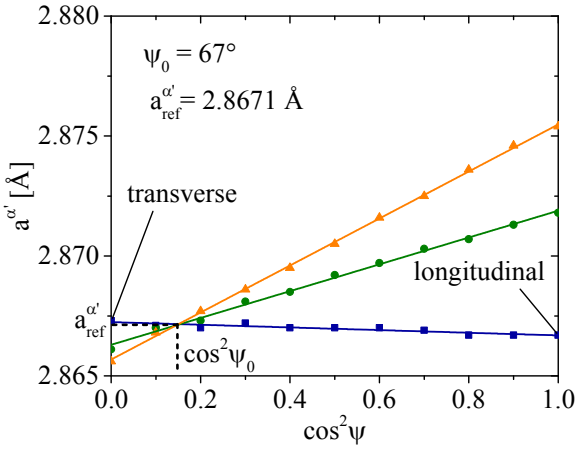

Figure 13.4: Martensite lattice constant, $a^{\alpha'}$, as a function of $\cos^2\psi$ of a sample in S630 condition. The blue square symbols show $a^{\alpha'}$ in the unloaded condition and the two other data sets show $a^{\alpha'}$ when exposed to elastic tensile stress. The intersection point of the linear regression lines indicates the average strain-free direction, $\psi_0 = 67°$, and average strain free lattice parameter, $a_{ref}^{\alpha'} = 2.8671$ Å.

shows the integrated intensities at $\psi = 0\,°$, relative to their initial value, and Figure 13.5c the full widths at half maximum ($FWHM$), normalized by their initial value, as a function of the applied true stress, σ_{true}. The lattice strains of the $\{211\}_{\alpha'}$, $\{220\}_{\alpha'}$and $\{321\}_{\alpha'}$ planes respond similarly to the applied stress, while the $\{200\}_{\alpha'}$ plane family is significantly more compliant in the elastic region and softer in the elastoplastic region. The elastic anisotropy is consistent with an increase of the orientation parameter $3\Gamma = \frac{h^2k^2+k^2l^2+l^2h^2}{(h^2+k^2+l^2)^2}$, which is 0 for $\{200\}_{\alpha'}$ and 0.75 for the remaining plane families (c.f. Table 13.3).

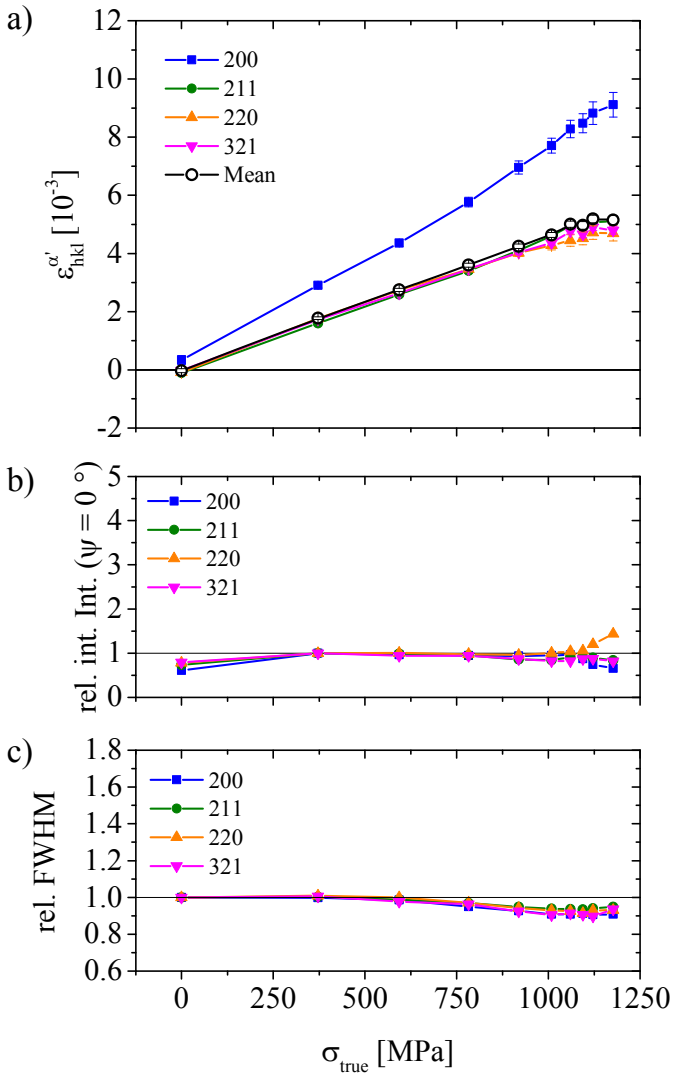

Figure 13.5: In-situ XRD data during interrupted tensile testing of the AH condition showing (a) the lattice strains $\varepsilon^{\alpha'}_{hkl}$, (b) the integrated intensities at $\psi = 0\,°$, normalized by their initial value and (c) the full widths at half maximum ($FWHM$) normalized by their initial value, as a function of applied true stress, σ_{true}. The $\{200_{\alpha'}\}$ planes are significantly more compliant than the other probed planes. The intensity of the $\{220_{\alpha'}\}$ planes increases at the expense of the $\{200_{\alpha'}\}$ planes in the plastic region. The $FWHM$ decreases during plastic deformation.

Table 13.3: Calculated orientation parameter 3Γ and theoretical XEC's of austenite (γ), and ferrite (α) according to the Eshelby-Kröner model [18].

Phase	*hkl*	3Γ	$-s_1$ [10^{-6} MPa^{-1}]	$\frac{1}{2}s_2$ [10^{-6} MPa^{-1}]
γ	200	0	2.35	8.86
	220	0.75	1.42	6.07
	311	0.47	1.77	7.11
	222	1	1.11	5.14
α'	200	0	1.9	7.7
	211	0.75	1.28	5.8
	220	0.75	1.28	5.8
	321	0.75	1.28	5.8

As the diffraction vector is almost parallel to the tensile axis (c.f. Figure 13.1), the relative integrated intensity at $\psi = 0\,°$ reflects the evolution of the grain orientation with respect to the tensile axis as a function of applied stress (Figure 13.5b). It appears that plastic deformation in lath martensite leads to an alignment of $220_{\alpha'}$ oriented grains parallel to the tensile axis, while the opposite effect can be observed for $200_{\alpha'}$ oriented grains. Peak broadening decreased with increasing applied stress Figure 13.5c. As the peak already become thinner in the elastic region, interpretations involving a change in dislocation density or coherently diffraction domain size are futile. It is likely, that local differences in residual stress from martensite formation contribute to peak broadening and are polarized during loading of the material.

630 °C / 3 h condition (S630)

Figure 13.6 shows the in-situ XRD data from interrupted tensile testing of the S630 condition. In contrast to the other tested samples, this test was conducted by increasing the stress according to displacement steps of 0.2 mm, which resulted in more data points.

In the initial condition, the S630 condition contained 18 vol.% of reverted austenite. Figure 13.6a shows that lattice strains in austenite are elastically and plastically anisotropic. In the elastic region, the stiffness of lattice plane families increases with the orientation parameter 3Γ (Table 13.3). In the plastic region, {200} planes are softest and {220} planes hardest, while the {222} and {311} planes approx. follow the average lattice strain. Anisotropy in tempered martensite is similar to the behavior of martensite as a single phase in the AH condition (Figure 13.5).

Figure 13.6g shows that, above a true stress of 500 MPa, reverted austenite transforms to martensite. Plastic anisotropy in austenite at this stress level suggests that the transformation is strain-induced. Broadening of the austenite reflections at this strain level (Figure 13.6e) may indicate an increase in dislocation density by plastic deformation [19].

Similar to martensite as a single phase, the intensity of the $\{220\}_{\alpha'}$ planes of tempered martensite increases significantly with plastic deformation (Figure 13.6d). In contrast to the sample in AH condition, the increase in $\{220\}_{\alpha'}$ intensity occurs already at the onset of plasticity at 750 MPa. Further, the plateau in the $\{220\}_{\alpha'}$ intensity curve at approx. 850 MPa coincides with an interruption of the strain-induced γ-to-α' transformation. These observations suggest that the increase in $\{220\}_{\alpha'}$ intensity with applied stress is largely associated with preferred martensite formation with <220> parallel to the tensile axis.

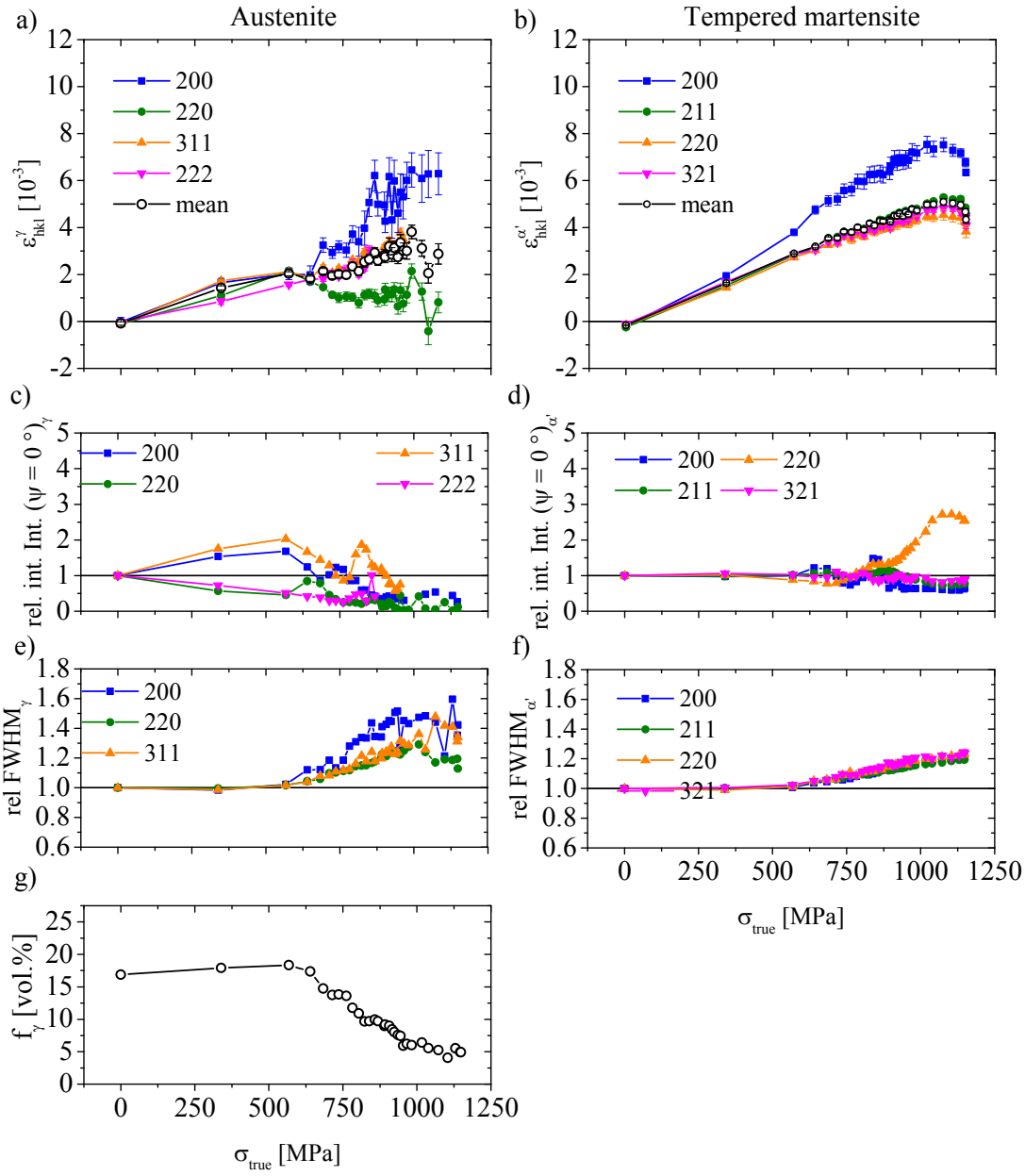

Figure 13.6: In-situ XRD data during interrupted tensile testing of the S630 condition showing the lattice strains ε_{hkl} of austenite and tempered martensite (a and b), the relative integrated intensities of austenite and tempered martensite at $\psi = 0\,°$ (c and d), the relative full widths at half maximum ($FWHM$) of austenite and tempered martensite (e and f) and the fraction of austenite (g) as a function of applied true stress, σ_{true}.

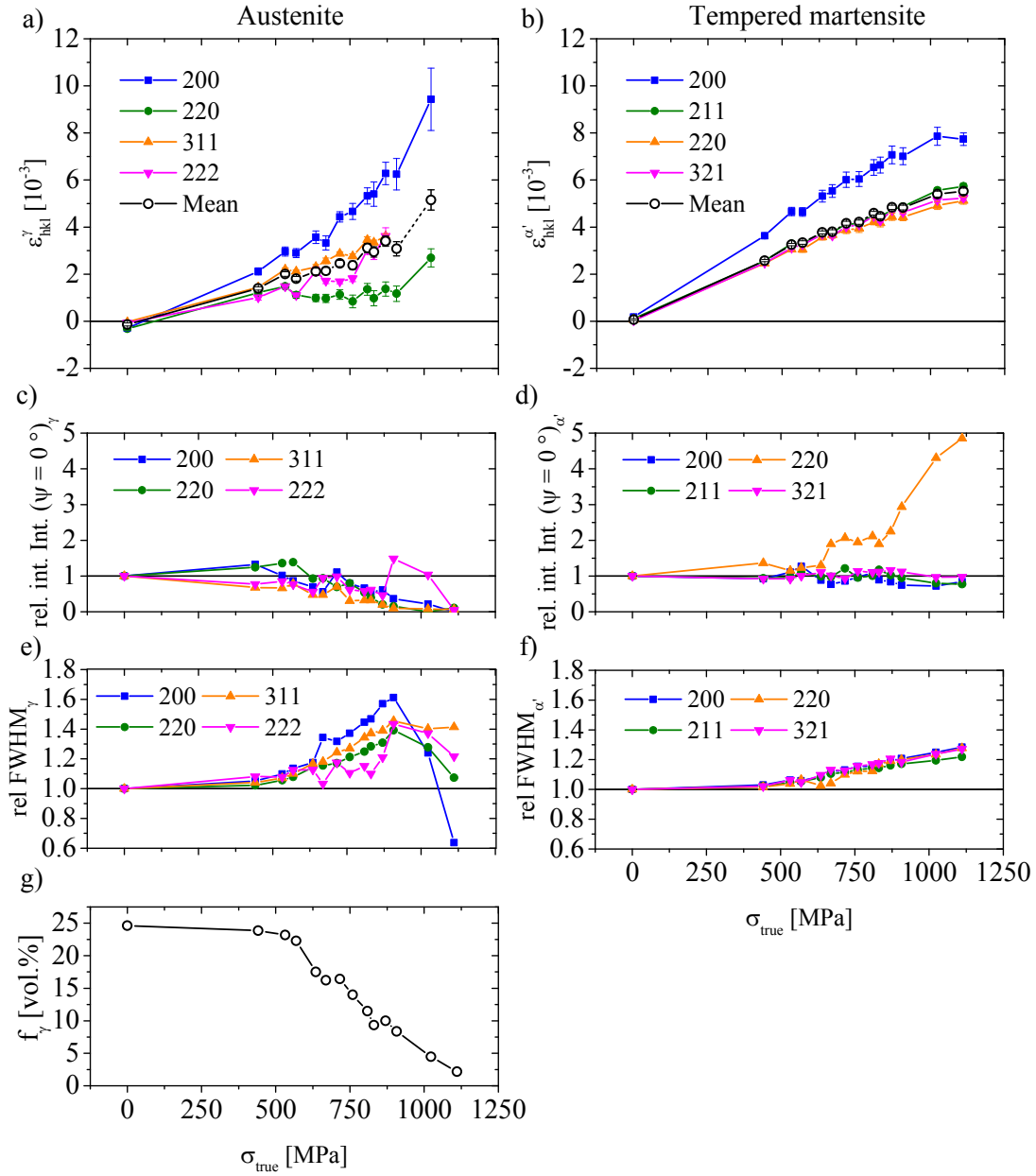

Figure 13.7: In-situ XRD data during interrupted tensile testing of the D630 condition showing the lattice strains ε_{hkl} of austenite and tempered martensite (a and b), the relative integrated intensities of austenite and tempered martensite at $\psi = 0\,°$ (c and d), the relative full widths at half maximum ($FWHM$) of austenite and tempered martensite (e and f) and the fraction of austenite (g) as a function of applied true stress, σ_{true}.

It appears that the transformation from austenite to martensite is mainly responsible for the increased hardening-rate, shown in the true stress vs. true strain curve in Figure 13.2.

670 °C / 2 h + 630 °C / 3 h condition (D630)

In-situ tensile testing of the D630 condition revealed similar mechanical behavior as the S630 condition. The elastic and plastic anisotropy of martensite and austenite agreed qualitatively with the one observed in the S630 condition.

The most significant difference between the two conditions was the transformation behavior of austenite to martensite. The D630 condition initially contained 24 vol.% of austenite and transformed 19 vol.% to martensite before specimen rupture. The S630 condition contained initially only 18 vol.% austenite, of which 12 vol.% transformed to martensite. The relative increase in intensity of the $\{220\}_{\alpha'}$ planes with applied stress is also observed in the D630 condition. When comparing with the intensity evolution of the S630 condition with applied stress (Figure 13.6d), it becomes evident that the $\{220\}_{\alpha'}$ intensity scales with the fraction of transformed austenite. This observation is supportive of the interpretation of preferential martensite formation with <220> parallel to the tensile axis.

In both the S630 and D630 conditions the intensities of austenite lattice plane families appear to change systematically as well. Both conditions show an intensity increase of single reflections. At approx. 850 MPa applied stress, the S630 condition shows an intensity increase of the {311} reflection and the D630 of the {222} reflection. While these observation suggests some systematic mechanism, the not necessarily random initial texture and the low grain statistics of austenite hinder further interpretation.

13.3.3 Lattice stress analysis

Calculation of lattice stresses

The principal strains in Equ. 13.6 are translated to principal stresses by applying the X-ray elastic constants (XEC's) $s_1^{hkl_\varphi}$ and $\frac{1}{2}s_2^{hkl_\varphi}$ [17]:

$$\varepsilon_{hkl,\psi}^{\varphi} = \frac{1}{2}s_2^{hkl_\varphi}(\sigma_{11}\sin^2\psi + \sigma_{33}\cos^2\psi) + s_1^{hkl_\varphi}(\sigma_{11}+\sigma_{22}+\sigma_{33}) \qquad (13.8)$$

When neglecting the contribution of the transverse principal stresses, σ_{11} and σ_{22}, the lattice stress along the tensile axis, $\sigma_{hkl,\psi=0°}^{\varphi}$, is obtained from $\varepsilon_{hkl}^{\varphi}$ at ψ = 0 °:

$$\sigma_{hkl,\psi=0°}^{\varphi} = \frac{\varepsilon_{hkl,\psi=0°}^{\varphi}}{\frac{1}{2}s_2^{hkl_\varphi} + s_1^{hkl_\varphi}} \qquad (13.9)$$

It was tested whether the stress-equilibrium was fulfilled, i.e. whether average phase specific stresses accounted for the externally applied stress:

$$\sum_{\varphi} f_{\varphi} \langle \sigma^{\varphi} \rangle = \sigma_{true} \tag{13.10}$$

The XEC's may either be obtained experimentally or theoretically. The present experimental setup and the measurement method allows experimental determination of the XEC's. As there is no material condition in which austenite is present as a single phase, determination of the XEC's is only possible for austenite and martensite as a compound, which implies the assumption of equal partitioning of the applied stress into the average phase specific stresses [18,20]. These compound-XEC's [18] were determined and used for analysis of stress partitioning. No satisfactory balance of the average phase stresses with the applied stress could be achieved in the plastic region, suggesting that the assumption of an equally partitioned stress was not fulfilled. Thus, theoretical XEC's were calculated fort he single phases ferrite (α) and austenite (γ) according to the Eshelby-Kröner model [18,21,22] (Table 13.3).

Stress partitioning

Partitioning of the applied stress σ_{true} to average phase specific stresses in austenite, σ^{γ}, and tempered martensite, $\sigma_{\alpha'}$, was analyzed by plotting the lattice stresses as a function of applied stress. Figure 13.8a shows the induced lattice stress in martensite by applying the true stress σ_{true} in the AH condition (c.f. Figure 13.5). As martensite is the only present phase, the $\Delta\sigma_{hkl}^{\alpha'}$ vs. σ_{true} behavior is expected to follow a linear relationship. Data in Figure 13.8a shows that this is indeed the case, which supports the applicability of theoretical XEC's of ferrite for martensite.

Figure 13.8b and c show the lattice stresses in austenite and tempered martensite during tensile testing of the S630 condition (c.f. Figure 13.6). The black symbols represent the stress-equilibrium from Equ. 13.10. The strictly proportional relation of average lattice stresses with the applied stress confirms that the stress equilibrium is fulfilled.

Lattice stress vs. applied stress approx. follows a linear relation in martensite up to an applied stress of 1000 MPa, beyond this value the lattice stress decreases with increasing applied stress. This effect is caused by measuring just outside the necked region, in which stresses concentrate just before fracture. Austenite is subject to plastic deformation well below an applied stress of 500 MPa. The applied stress is mainly accommodated by martensite, and remaining austenite follows by plastic deformation. Figure 13.6g shows that austenite transforms progressively to martensite above 600 MPa applied stress, which works as a strengthening mechanism.

Figure 13.8d and e show the lattice stresses in austenite and tempered martensite during tensile testing of the D630 condition (c.f. Figure 13.7). The stress-equilibrium is also here

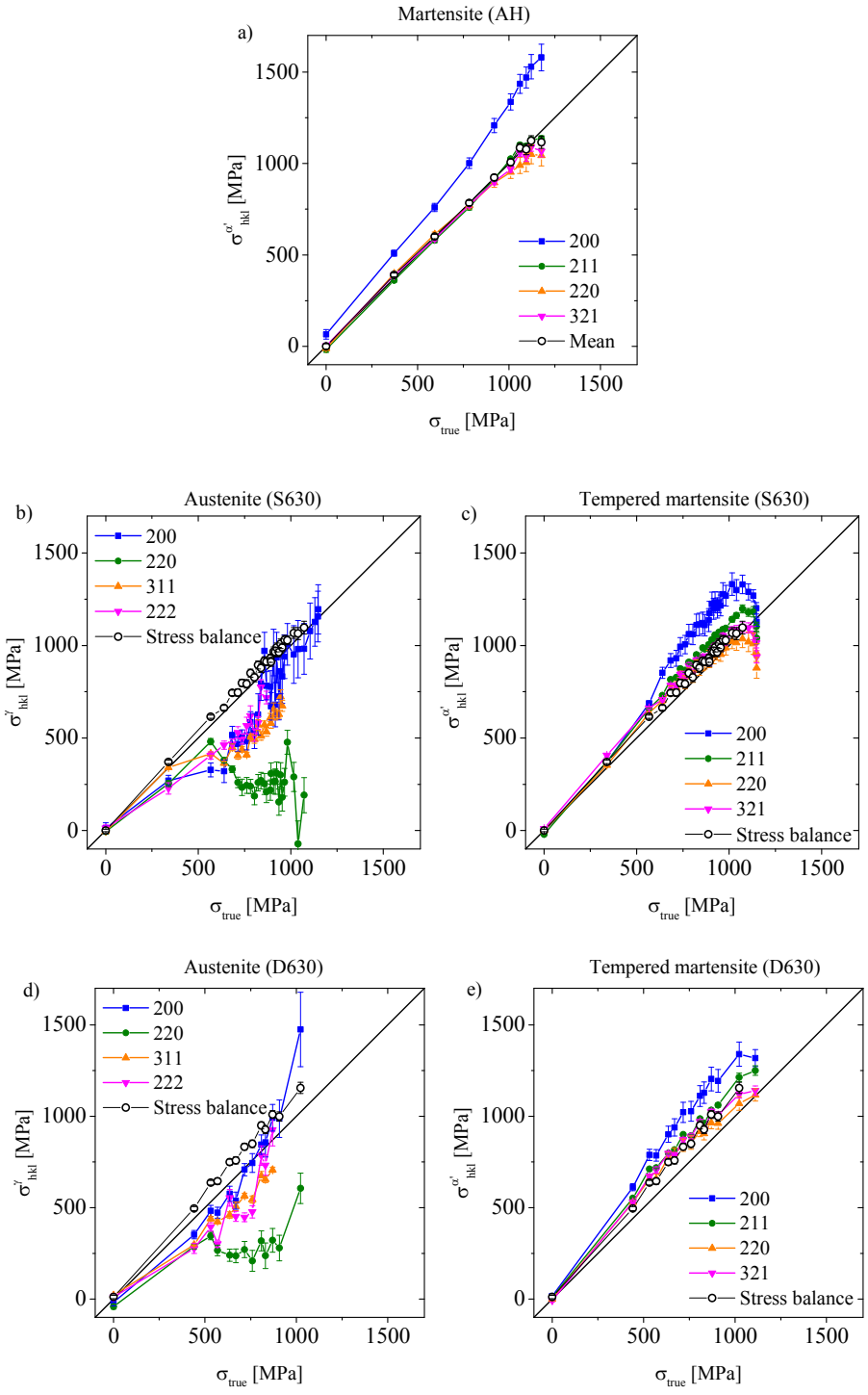

Figure 13.8: Change in lattice stress, σ_{hkl}^{φ}, as a function of applied stress, σ_{true}, in (a) martensite in the AH condition, (b) austenite and (c) tempered martensite in the S630 condition, and (d) austenite and (e) tempered martensite in the D630 condition. The black symbols show stress balance of the average lattice stress of austenite and martensite, which is in excellent agreement with the applied stress in the case of the AH and S630 conditions, and in good agreement in the case of the D630 condition.

fulfilled, albeit with some discrepancy. Similar to the S630 condition in Figure 13.6c martensite seems to accommodate the externally applied stress, while austenite plastically deforms. It appears that plastic deformation of austenite is accomplished by transformation to martensite (Figure 13.7g). Just before necking, the untransformed austenite begins to accommodate more stress.

13.4 General discussion

13.4.1 Macroscopic mechanical properties

It was demonstrated that inter-critical annealing of supermartensitic stainless steel leads to significant reduction in yield strength and an increase in total extension at maximum stress (Figure 13.2). Different annealing treatments aim at different properties, which are consistent with mechanical properties reported in literature [6,7,23–25]. For the first time in this material, the mechanical behavior during tensile testing could be related to the evolution of the deformation texture and strain-induced martensite formation *in-situ*. The experiments show that, as anticipated [5,7,8], reverted austenite can in fact transform to martensite by a strain-induced mechanism (Figure 13.6 and Figure 13.7). The D630 condition revealed the initially highest (24 vol.%) and after rupture the lowest (5 vol.%) amount of reverted austenite.

13.4.2 Transformation-induced plasticity (TRIP)

The specimen in D630 condition (Figure 13.7) transformed most austenite during straining (19 vol.%) and revealed the highest percentage of total extension at maximum stress (14 %). The graphs in Figure 13.8d and e reveal that the lattice stress in tempered martensite follows the applied stress, while austenite seems to follow the deformation without accommodating the applied stress. Plastic deformation appears to be partly accomplished by γ-to-α' transformation which enables elongation without dislocation production. It was found that martensite mainly formed with <220> oriented parallel to the tensile axis. This behavior was earlier observed by Oliver et al. [26,27] during strain-induced martensite formation in Fe-Ni-C steel.

TRIP seems to be responsible to the low sensitivity of the ultimate tensile strength to different heat-treatments. The true stress-strain curves in Figure 13.2b show that all specimens obtain a similar maximum stress. As straining leads to austenite-to-martensite transformation, the mechanical properties of the plastically deformed specimens are similar at high stress, irrespective of the initial tempering treatment. This effect is responsible for the low sensitivity of the ultimate tensile strength to different heat treatments Figure 13.2a. The higher ultimate tensile strength of the hardened condition is related to brittle rupture with little necking.

13.4.3 Double annealing heat treatment

A first annealing treatment at 670 °C before annealing at 600 or 630 °C led to a significant increase in austenite fraction by 6 to 8 vol.% compared to single-annealed specimens. The first annealing step leads to formation of a large fraction of thermally unstable reverted austenite, which forms to martensite during cooling and thus refines the microstructure. In the second annealing step reverted austenite forms at the boundaries of refined laths, leading to an increased amount of stable reverted austenite compared to single annealing [7,28]. To which extend the smaller grain size or the increased austenite fraction are responsible for a decrease in yield strength and prolonged ductility is subject to further study.

It appears that both a higher final annealing temperature (600 and 630 °C) and the amount of reverted austenite, noticeably increased by prior annealing at 670 °C, significantly lower the yield point and extend ductility. Even though the S630 and D600 conditions have virtually the same initial austenite content, the yield points differ with 560 and 775 MPa considerably. This is likely to be an effect of austenite composition or austenite grain size.

13.5 Conclusion

- Reverted austenite in supermartensitic stainless steel can transform to martensite by a strain-induced mechanism during uniaxial tensile loading, which extends ductility.
- The lattice stress in tempered martensite follows the applied stress, while austenite appears to follow the deformation without accommodating the applied stress.
- Plastic deformation is partly accomplished by austenite-to-martensite transformation.
- Strain-induced martensite formation occurred preferentially with <220> parallel to the tensile axis.
- Double annealing, i.e. annealing at 670 °C before a second annealing step close to A_1 led to a higher initial fraction of reverted austenite and extended ductility.

Acknowledgements

The Danish Underground Consortium is gratefully acknowledged for financial support to the Danish Hydrocarbon Research Center (DHRTC). R. N. W. Eriksen, Technical University of Denmark, is acknowledged for his support with the DIC analysis. M. Klaus, D. Apel, and Ch. Genzel, Helmholtz Zentrum für Materialien und Energie (HZME), and J. O. Nielsen, M. Villa, K. Pantleon and Y. Meng, Technical University of Denmark, are acknowledged for their support during the activity at the HZB-BESSY II synchrotron facility. The activity was supported by the European Commission under the 7th Framework Program through the 'Research Infrastructure' action of the 'Capacities' Programme,

CALIPSO (Grant No. 312284) and by the Danish Natural Science Research Council via Danscatt.

References

[1] H. Van der Winden, P. Toussaint, L. Coudreuse, Past, present and future of weldable supermartensitic alloys, in: Supermartensitic Stainl. Steels 2002 Brussels, 2002: pp. 9–13.

[2] A.W. Marshall, J.C.M. Farrar, Welding of Ferritic and Martensitic 11-14% Cr Steels, Weld. World. 45 (2001) 19–42.

[3] H.J. Niederau, Eigenschaften und Anwendungsmöglichkeiten der Guss- und Schmiedelegierung (G)X-5 CrNiMo 16 5 (Werkstoff-Nr. 1.4405), Zeitschrift Des Vereins Dtsch. Ingenieure Für Maschinenbau Und Met. Eig. 21 (1982) 801–808.

[4] F. Niessen, Austenite reversion in low-carbon martensitic stainless steels – a CALPHAD-assisted review, Mater. Sci. Technol. 836 (2018) 1–14.

[5] P. Wang, N. Xiao, S. Lu, D. Li, Y. Li, Investigation of the mechanical stability of reversed austenite in 13%Cr-4%Ni martensitic stainless steel during the uniaxial tensile test, Mater. Sci. Eng. A. 586 (2013) 292–300.

[6] M. Al Dawood, I.S. El Mahallawi, M.E. Abd El Azim, M.R. El Koussy, Thermal aging of 16Cr – 5Ni – 1Mo stainless steel Part 2 – Mechanical property characterisation, Mater. Sci. Technol. 20 (2004) 370–374.

[7] P.D. Bilmes, M. Solari, C.L. Llorente, Characteristics and effects of austenite resulting from tempering of 13Cr–NiMo martensitic steel weld metals, Mater. Charact. 46 (2001) 285–296.

[8] T. LeBrun, T. Nakamoto, K. Horikawa, H. Kobayashi, Effect of retained austenite on subsequent thermal processing and resultant mechanical properties of selective laser melted 17-4 PH stainless steel, Mater. Des. 81 (2015) 44–53.

[9] F. Sun, J.Y. Zhang, M. Marteleur, T. Gloriant, P. Vermaut, D. Laillé, P. Castany, C. Curfs, P.J. Jacques, F. Prima, Investigation of early stage deformation mechanisms in a metastable β titanium alloy showing combined twinning-induced plasticity and transformation-induced plasticity effects, Acta Mater. 61 (2013) 6406–6417.

[10] K. Yan, K.-D. Liss, I.B. Timokhina, E. V. Pereloma, In situ synchrotron X-ray diffraction studies of the effect of microstructure on tensile behavior and retained austenite stability of thermo-mechanically processed transformation induced plasticity steel, Mater. Sci. Eng. A. 662 (2016) 185–197.

[11] E. Jimenez-Melero, N.H. van Dijk, L. Zhao, J. Sietsma, S.E. Offerman, J.P. Wright, S. van der Zwaag, Martensitic transformation of individual grains in low-alloyed TRIP steels, Scr. Mater. 56 (2007) 421–424.

[12] S. Brauser, A. Kromm, T. Kannengiesser, M. Rethmeier, In-situ synchrotron diffraction and digital image correlation technique for characterizations of retained austenite stability in low-alloyed transformation induced plasticity steel, Scr. Mater. 63 (2010) 1149–1152.

[13] Y. Tomota, H. Tokuda, Y. Adachi, M. Wakita, N. Minakawa, A. Moriai, Y. Morii, Tensile behavior of TRIP-aided multi-phase steels studied by in situ neutron diffraction, Acta Mater. 52 (2004) 5737–5745.

[14] F. Lani, Q. Furnémont, T. Van Rompaey, F. Delannay, P.J. Jacques, T. Pardoen, Multiscale mechanics of TRIP-assisted multiphase steels: II. Micromechanical modelling, Acta Mater. 55 (2007) 3695–3705.

[15] S. Cheng, Y.D. Wang, H. Choo, X.L. Wang, J.D. Almer, P.K. Liaw, Y.K. Lee, An assessment of the contributing factors to the superior properties of a nanostructured steel using in situ high-energy X-ray diffraction, Acta Mater. 58 (2010) 2419–2429.

[16] C. Genzel, I. Denks, M. Klaus, The Materials Science Beamline EDDI for Energy-Dispersive Analysis of Subsurface Residual Stress Gradients, Mater. Sci. Forum.

524–525 (2006) 193–198.
[17] V. Hauk, Evaluation of Load Stress (LS) and Residual Stress (RS), in: Struct. Residual Stress Anal. by Nondestruct. Methods, Elsevier, 1997: pp. 132–215.
[18] V. Hauk, X-ray elastic constants (XEC), in: Struct. Residual Stress Anal. by Non-Destructive Methods, 1997: pp. 297–336.
[19] T. Ungár, M. Victoria, P. Marmy, P. Hanák, G. Szenes, New procedure of X-ray line profile analysis applied to study the dislocation structure and subgrain size-distributions in fatigued MANET steel, J. Nucl. Mater. 276 (2000) 278–282.
[20] R.. Marion, J.. Cohen, The Need For Experimentally Determined X-Ray Elastic Constants, Adv. X-Ray Anal. 25th Annu. Conf. Appl. X-Ray Anal. (1976) 1–13.
[21] J.D. Eshelby, The Determination of the Elastic Field of an Ellipsoidal Inclusion, and Related Problems, Proc. R. Soc. Lond. A. Math. Phys. Sci. 241 (1957) 376–396.
[22] E. Kröner, Berechnung der Elastischen Konstanten des Vielkristalls aus den Konstanten des Einkristalls, Zeitschrift Für Phys. 151 (1958) 504–518.
[23] Y. Song, X. Li, L. Rong, Y. Li, The influence of tempering temperature on the reversed austenite formation and tensile properties in Fe-13%Cr-4%Ni-Mo low carbon martensite stainless steels, Mater. Sci. Eng. A. 528 (2011) 4075–4079.
[24] M. De Sanctis, G. Lovicu, R. Valentini, A. Dimatteo, R. Ishak, U. Migliaccio, R. Montanari, E. Pietrangeli, Microstructural Features Affecting Tempering Behavior of 16Cr-5Ni Supermartensitic Steel, Metall. Mater. Trans. A Phys. Metall. Mater. Sci. 46 (2015) 1878–1887.
[25] P.E. Kvaale, O. Stein, Experience with supermartensitic stainless steels in flowline applications, in: Stainl. Steel World 99, 1999: pp. 19–26.
[26] E.C. Oliver, M.R. Daymond, P.J. Withers, T. Mori, Stress Induced Martensitic Transformation Studied by Neutron Diffraction, Mater. Sci. Forum. 404–407 (2002) 489–494.
[27] E.C. Oliver, The generation of internal stresses in single and two phase materials, (2002).
[28] J. Hubácková, V. Cíhal, K. Mazanec, Two-Stage Tempering of steel 13%Cr6%Ni, Materwiss. Werksttech. 15 (1984) 411–415.

14 Manuscript IX

A systematic comparison of on-axis and off-axis transmission Kikuchi diffraction*

Frank Niessen[a], Andrew Burrows[b], Alice Bastos da Silva Fanta[b]

[a] Technical University of Denmark (DTU), Danish Hydrocarbon Research and Technology Centre (DHRTC) , Elektrovej building 375, 2800 Kgs. Lyngby, Denmark

[b] Technical University of Denmark (DTU), Center for Electron Nanoscopy (CEN), Fysikvej building 307, 2800 Kgs. Lyngby, Denmark

Abstract

The capabilities of the novel on-axis transmission Kikuchi diffraction (TKD) technique were explored in a systematic comparison with conventional off-axis TKD. The effect of experimental parameters on the appearance of on-axis and off-axis Kikuchi patterns was measured and discussed. In contrast to off-axis TKD, on-axis TKD is more sensitive to changes in beam current and beam energy and less sensitive to changes in working distance and detector distance. Moreover, on-axis TKD has a distinct advantage over off-axis TKD due to enhanced pattern intensity, which allows reduction of the beam current or an increase in the acquisition rate. The physical and effective spatial resolution were measured with detector-typical parameters. Even though the spatial resolution of both configurations did not differ significantly under test conditions, on-axis TKD enables measurement over large areas with the determined resolution, whereas off-axis TKD is more sensitive to beam drift. Band detection by the Hough-transform led to indexing of, on average, one additional Kikuchi band when measuring with on-axis TKD compared to off-axis TKD and operated more stable on on-axis patterns.

* Published work: F. Niessen, A. Burrows, A.B. da S. Fanta, A systematic comparison of on-axis and off-axis transmission Kikuchi diffraction, Ultramicroscopy. 186 (2018) 158–170. The format of the published article was adapted to the format of the doctoral thesis.

14.1 Introduction

It is half a decade since transmission Kikuchi diffraction (TKD) was introduced as a novel diffraction technique for the scanning electron microscope (SEM) [1,2]. The technique is capable of mapping the phases and orientations of nano-structured materials on a scale and resolution range between electron backscatter diffraction (EBSD) in the SEM and diffraction techniques in the transmission electron microscope (TEM). The technique consists of interaction of the scanning electron beam with an electron-transparent sample, which is tilted toward a conventional EBSD-detector to capture diffracted electrons. The captured diffraction patterns are Kikuchi-patterns, which arise from Bragg-diffraction of incoherently scattered electrons. The diffraction patterns obtained and the applied hardware are similar to those used in EBSD, which initially led to naming the technique transmission EBSD (t-EBSD) [3]. TKD enables orientation mapping with significant improvement in lateral spatial resolution compared to EBSD. Measurements on a Ni sample showed that the technique is capable of reaching a physical lateral spatial resolution of better than 10 nm [4].

It is apparent that TKD offers great benefits when orientation mapping and phase identification at the nanoscale over medium sized areas is required. The development of TKD occurred rapidly within a few years along with conventional EBSD hardware. In EBSD the sample is tilted approx. 70 ° away from the incident beam to capture the maximum intensity of backscattered electrons forming the Kikuchi pattern. In TKD, Kikuchi patterns are formed by forward-scattered electrons for which the highest intensity occurs close to the incident beam, i.e. below the electron transparent sample. Acquisition of Kikuchi patterns in TKD with EBSD hardware thus occurs far away from the pattern center, and leads to acquisition of only limited diffracted intensity and severe gnomonic distortion of the Kikuchi pattern.

These limitations triggered the development of a new detector configuration by Fundenberger et al., which consists of a phosphor screen positioned below the sample normal to the incident beam, analogous to TEM [5]. As the acquisition occurs on the axis of the incident beam, TKD in this configuration is termed “on-axis” TKD, compared to conventional “off-axis” TKD [6].

Yuan et al. showed that the new configuration leads to high intensity and low gnomonic distortion of acquired Kikuchi patterns. Either the electron dose or the acquisition time could be lowered by a factor of 20 to yield the same pattern intensity as observed in off-axis TKD.[6] Brodu et al. demonstrated that, depending on the experimental parameters, a wide range of diffraction patterns such as diffraction spots, thin Kikuchi lines and bright or dark Kikuchi bands, are accessible with the on-axis TKD-detector. It is suggested that the sharp Kikuchi lines in on-axis TKD may enable high angular resolution measurements and even strain determination [7]. When using an on-axis detector, the Kikuchi pattern includes the transmitted beam, which leads to a bright spot in the center of the pattern. In a recent review by Sneddon et al. it was speculated that the

bright spot may cause issues with indexing of relatively indistinct patterns or when high angular resolution is desired [8].

The current state of literature on the relatively young detector system is limited and requires further investigation to distinguish all the advantages and drawbacks of the systems. The present investigation therefore aims to compare on-axis and off-axis TKD to gain a better assessment of both techniques. The effect of different experimental parameters on the appearance of the Kikuchi pattern is reported and discussed. Furthermore the physical and effective spatial resolutions are explored when applying typical parameters for each detector. Finally, the robustness of band detection by the Hough transform for on-axis and off-axis Kikuchi patterns is tested and general, more practical, remarks on the new detector configuration are reported.

14.2 Experimental procedure

Before stating the details of the experimental procedures, the definitions for physical and effective spatial resolution should be established. The physical spatial resolution (PSR) is determined by the distance from a grain boundary in which the pattern of a neighboring grain is first observed. The effective spatial resolution (ESR) is defined by the distance from the grain boundary in which two overlapping patterns can be clearly distinguished by the indexing software. The prior is thus directly related to the electron interaction volume, while the latter is furthermore affected by the ability of software algorithms to deconvolute overlapping patterns. Consequently, the ESR is generally better than the PSR [9].

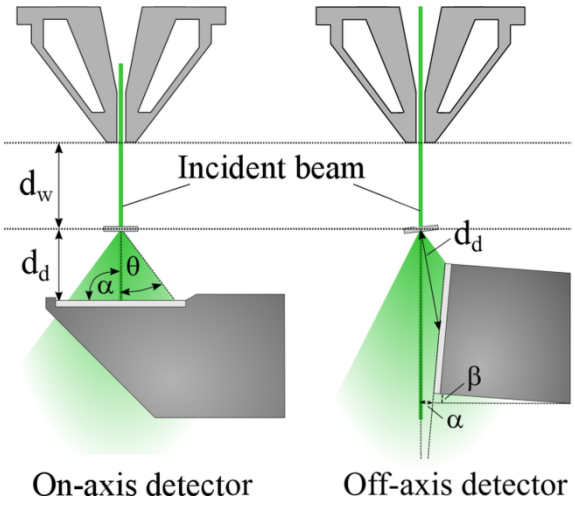

Figure 14.1: Schematic of beam-specimen interaction and chamber geometry for the investigated detector systems showing the pole-piece, the incident and scattered electron beam (green), the sample and the detector heads, where d_w is the working distance, d_d is the detector distance, θ is the scattering semiangle, α the intersection angle and β the detector tilt angle.

14.2.1 Introduction to on-axis TKD

As briefly outlined in the introduction, the on-axis detector configuration for TKD consists of a phosphor screen oriented normal to the incident beam, which is positioned below an electron transparent sample. Figure 14.1 shows a schematic of the on-axis and off-axis detector configurations. Physically speaking, the only difference of the two configurations is the angle α, which is termed the intersection angle of the phosphor screen with the incident beam. The intersection angle has a magnitude of few degrees in the off-axis detector configuration and is close to 90 ° in the case of the on-axis detector configuration. A low intersection angle (off-axis TKD) leads to high gnomonic distortion and little acquired diffraction intensity, whereas an intersection angle close to 90 ° (on-axis TKD) has the opposite effect.

The detector distance to the sample in on-axis TKD is adjusted by either changing working distance, d_w, or the detector tilt angle, β, which leads to negligible gnomonic distortion of the Kikuchi pattern. Figure 14.1 demonstrates that there is far more room for changing the detector distance, d_d, with the on-axis detector configuration. Therefore full intersection with the Kikuchi cone at its maximum intensity is possible, which leads to acquisition of a far greater part of the Kikuchi map compared to the off-axis detector. In on-axis TKD, the Kikuchi pattern also contains the transmitted beam intensity, which leads to a bright spot in the center of the pattern.

14.2.2 Experimental setup

The applied setup consisted of a Bruker e-Flash HD EBSD detector, installed in an FEI Nova NanoLab 600 SEM. The detector can be positioned with varying distance and tilt toward the sample and is used with interchangeable phosphor screen assemblies in vertical (off-axis) and horizontal (on-axis) orientation relative to the insertion axis of the detector. The on-axis OPTIMUS™ TKD detector head comprises a horizontally positioned scintillator, which directs the light from the phosphor screen toward the camera with help

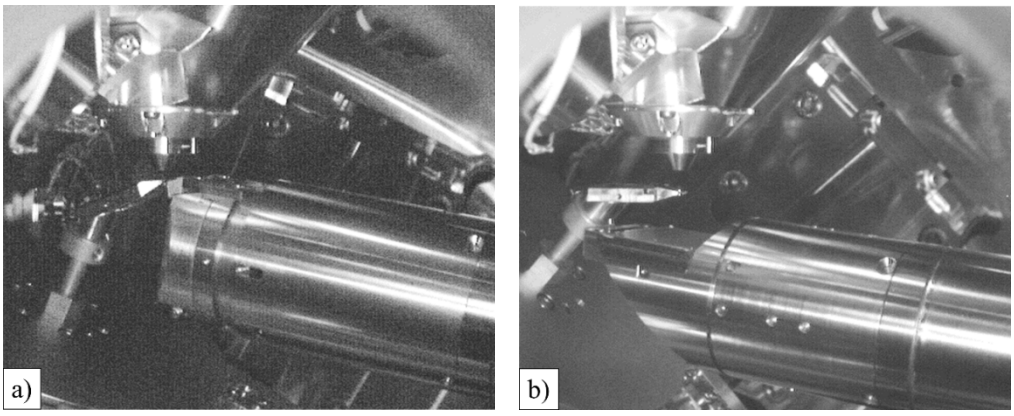

Figure 14.2: Chamber geometry for TKD with the conventional off-axis detector configuration and -20 ° sample tilt; b): Chamber geometry with an on-axis detector configuration and no specimen tilt.

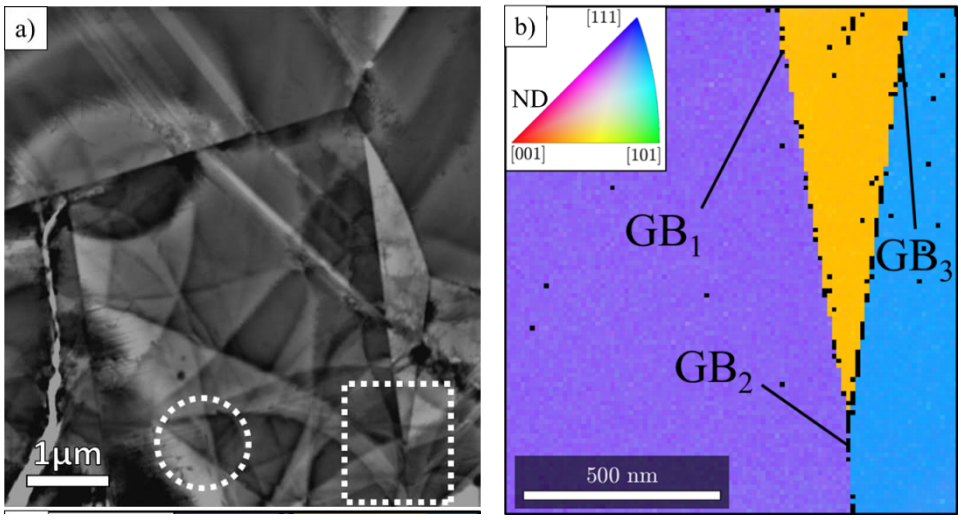

Figure 14.3: (a) Bright-field image of the AISI 316L thin foil, showing the area from which the Kikuchi patterns for the parameter study were taken (circle) and the area from which the PSR was measured (rectangle); The curved fringes in the image are bend contours, which are diffraction contrast effects arising from slight bending of the thin-foil; (b) Inverse pole-figure map indicating the grain orientations at the HAGB's for measurement of the PSR (rectangle area in Figure 14.3a).

of a 45 ° inclined reflection mirror. The detector is additionally equipped with diodes for bright- and dark-field imaging. A more detailed description of the detector head assembly can be found in Ref. [5]. Figure 14.2 shows both detector configurations in operation with -20 ° sample tilt in off-axis TKD, and no sample tilt in the case of on-axis TKD.

14.2.3 Studied materials

Two materials were the subject of the current study. For the parameter study and the study on the PSR it was found important to analyze a well-known material with low defect density, no strong substructure, large grains and well-defined grain boundaries. Thus an AISI 316L austenitic stainless steel was chosen. The material was received as sheet material of 1 mm thickness in bright cold rolled finished (2B) condition, with the composition given in Table 14.1.

The material was annealed at 700 °C for 2 h under continuous Ar-flow and was subsequently ground to approx. 100 µm thickness. The thin-foil was produced by electrolytic twin-jet polishing with 10 % perchloric acid at -20 °C. Prior to investigation, the specimen was plasma-cleaned. The thickness of the sites of interest investigated was determined in a TEM using the Electron energy loss spectroscopy (EELS) log-ratio

Table 14.1: Chemical composition of the investigated AISI 316L austenitic steel determined with optical emission spectroscopy (OES) and balanced with Fe (wt.%).

Fe	Cr	Ni	Mo	Mn	Si	C	N
bal.	16.8	10.4	2.1	0.9	0.5	0.02	0.05

technique [10]. The mean free path, λ, was approximated with the MFP Estimator script by Mitchell for 120 keV beam energy and a collection semi angle β of 30 mrad [10,11]. The mean free path was calculated as $\lambda = 67$ nm and yielded a foil-thickness at the sites of interest of $t = 115 \pm 8$ nm. The bright-field image of the investigated microstructure is shown with the positions of the sites of interest in Figure 14.3a. In order to analyze the ESR a nanocrystalline gold thin-film was chosen. The sample was deposited by e-beam deposition at room temperature on 5 nm thin silicon nitride TEM windows. The total thickness of the gold film was approx. 15nm.

14.2.4 Reference parameters and parameter study

The first part of the experimental procedure consisted of a parameter study in which individual experimental parameters were varied from a set of reference parameters for each detector configuration. All Kikuchi patterns of the austenitic stainless steel sample were acquired from the encircled area shown in Figure 14.3a.

In order to carry out a systematic parameter study a set of reference parameters was defined for each detector configuration. The reference parameters are the result of iterative parameter optimization and represent typical parameters for the two detector configurations for obtaining high-resolution and high intensity Kikuchi patterns (Table 14.2). Relative to conventional parameters for TKD orientation mapping, the acquisition time was increased by a factor of approx. 10 to yield Kikuchi patterns of good quality for detailed analysis. The parameters were tuned to yield similar illumination in both detector configurations at identical pattern resolution. The working distance of the on-axis detector was increased to 6 mm in the parameter study to give a more even illumination of the detector; lower working distance led to constraints in space with the currently used sample holder. The increased illumination of the on-axis detector allowed acquisition with a smaller aperture and lower acquisition time. The beam current was accordingly reduced by 45 % and the acquisition time was reduced by a factor of 11. When severe over- or under-exposure of the camera was experienced, the acquisition time was adapted, which in that case is reported together with the respective results. The patterns for the qualitative parameter study were acquired in spot-mode, i.e. beam-blanking immediately before and after acquisition.

14.2.5 Kikuchi band detection and robustness of indexing

As previously discussed, the appearance of Kikuchi patterns in on-axis and off-axis is essentially different, which is expected to have consequences for band detection and robustness of indexing. Up to now, it has not been demonstrated whether the Kikuchi pattern obtained by on-axis TKD improves or deteriorates the indexing precision.

The number of correctly indexed Kikuchi bands from automatic, Hough-transform based, band detection and manually refined band detection are compared. The comparison should indicate how many bands generally are detected by the Hough transform from on-

axis and off-axis Kikuchi patterns, and how many bands are wrongly or not detected. The parameters for the Hough-transform were kept as default and constant over the analysis. Two individual grains were analyzed for each detector configuration, where the pattern analysis was performed twice for both line detection methods. As the analysis involves manual refinement of band detection, the results should be considered as semi- quantitative.

14.2.6 Spatial resolution

The achievable PSR when conducting on-axis and off-axis TKD was investigated using detector-typical reference parameters to obtain high resolution Kikuchi patterns. As the PSR is directly dependent on the interaction volume formed by the electron beam and the sample, the different detector systems affect the measured PSR by enabling analysis with different beam energies, exposure time, sample tilt, and by acquiring signal from different source regions. The PSR was determined with the parameters stated in Table 14.2 by measuring the orientation across the three indicated high-angle grain boundaries (HAGBs) in Figure 14.3b.

Since the sets of reference parameters comprise different working distances, the working distance was varied in on-axis TKD to account for possible occurrence of beam-broadening. The line scans were carried out approximately perpendicular with respect to the grain boundary with a step size of 3 nm. Exact parallel alignment of the grain boundaries

Table 14.2: Reference parameters for investigations with off-axis and on-axis detector configurations.

	Off-axis detector	*On-axis detector*
SEM parameters		
Beam energy [keV]:	30	30
Spot size [1]:	4	4
Aperture diameter [µm]:	40	30
Beam current [nA]:	1.5	0.83
Gun emission mode:	Analytical	Analytical
Geometrical parameters		
Sample tilt [°]:	-20	0
Working distance [mm]:	3	6
Detector distance [mm]:	13.5	13.9
Detector angle [°]:	8.7	5.8
Camera settings		
Image resolution [pixels]:	800 x 600	800 x 600
Exposure time [ms]:	850	75
Gain [1]:	0	0

with the primary electron beam in depth of the sample was not possible due to limited degrees of freedom of the microscope stage. The effect of minor misalignment on the spatial resolution measurements is however expected to have negligible effect since the majority of the signal contributing to the contrast of the Kikuchi pattern arises from the last few tens of nanometers of the exit surface [12]. It is furthermore expected that highly inclined boundaries would lead to a thick region of low band contrast at the boundary and an asymmetric line profile of the sum of correlation coefficients in the analysis of the PSR, which was not the case and thus suggests an approximately parallel orientation of the boundary with respect to the electron beam .

The PSR was determined by an image-correlation technique [13,14]. The Kikuchi patterns across a HAGB were compared to reference patterns of the individual grains far away from the HAGBs. An example of an overlay of two reference patterns is given in Figure 14.4a.

The comparison was based on analyzing the change in intensity of the grayscale pixels from cropped areas of Kikuchi patterns, which showed distinct features for both reference patterns. In this manner the correlation coefficient, C_{corr}, was determined by the following equation:

$$C_{corr} = \frac{\sum_m \sum_n (I_{m,n} - \bar{I})(I_{m,n}^{ref} - \overline{I^{ref}})}{\sqrt{\left(\sum_m \sum_n (I_{m,n} - \bar{I})^2\right)\left(\sum_m \sum_n \left(I_{m,n}^{ref} - \overline{I^{ref}}\right)^2\right)}} \tag{14.1}$$

where I is the intensity of the analyzed Kikuchi pattern and I^{ref} the intensity of the reference Kikuchi pattern. Indices m and n denote the grayscale pixel positions and the overbars indicate average values. The analysis was carried out using the MATLAB Imaging

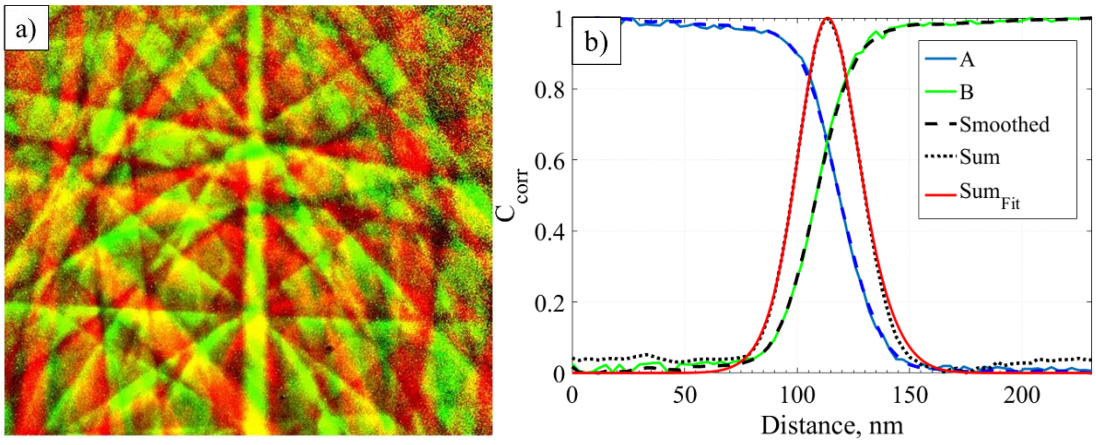

Figure 14.4: (a) Overlay of color-coded reference patterns of two grains (red and green); (b) Example for the determination of the PSR by analysis of the correlation coefficient C_{corr}; The correlation of the patterns with the reference pattern of two grains A and B are plotted in the raw and smoothed version. The normalized sum of the two smoothed curves is fitted with a Gaussian profile, from which half the full width at half maximum represents the PSR.

Toolbox, where Equ. 14.1 is implemented as function *corr2* [15]. The correlation coefficients were normalized to unity and smoothed by applying a moving average filter with a step-size of 5, to reduce noise originating from the low signal-to-noise ratio of TKD patterns. All initially tested filtering methods induced slight broadening of the line profile, which was in the range of 5 % for the moving average filter. The effect showed the same extent for off-axis and on-axis TKD patterns and is considered within the experimental accuracy of the method. The correlation coefficients of both grains were summed and normalized to unity (see the example in Figure 14.4b). Half of the full width at half maximum ($FWHM$) of the resulting Gaussian profile was taken as a measurement of the PSR. For each of the three measurements over a HAGB, 10 cropped pattern areas were analyzed, which resulted in 30 measurements of the PSR per measurement configuration.

The ESR of both detector systems in connection with the Bruker ESPRIT software was evaluated by measuring orientation maps on a nanocrystalline gold thin-film. The measurements were carried out with the same set of reference parameters as in all other measurements (Table 14.2), albeit with a lower pattern resolution of 320 x 240 pixels to reduce the effect of beam drift. No cleaning or smoothening algorithms were applied to the data sets, and a minimum of 5 Kikuchi bands were required for successful indexing**.**

14.3 Experimental results

14.3.1 Experimental parameter study

Experimental parameters were varied one by one from the set of reference parameters in Figure 14.5. The Kikuchi patterns obtained with the reference parameters are given in the following subsection (Figure 14.5). All Kikuchi patterns which are formed with altered parameters are compared with the reference Kikuchi patterns.

Reference parameters

In Figure 14.5 the Kikuchi patterns acquired with the reference parameters in Table 14.2 are shown in real and Hough space, and are compared with their respective simulated patterns. The Kikuchi pattern simulation was carried out using the dynamical simulation model of the Bruker ESPRIT DynamicS software suite.

The Kikuchi pattern acquired with the off-axis detector system reveals great detail of the individual Kikuchi bands, but is subject to gnomonic distortion and only reveals a limited area of the Kikuchi map. The pattern obtained using the on-axis detector includes a larger area of the Kikuchi-map and thus more major zone axes. Although the pattern is disturbed by the transmitted electron beam in the center, which is surrounded by diffraction spots from coherent scattering, the Hough space does not seem to show any major disturbance by the acquisition of the transmitted beam. After subtraction of the area affected by the transmitted beam using conventional image processing software, the on-

axis pattern yields approximately 70% additional area of the Kikuchi-map compared to the off-axis Kikuchi pattern.

Detector distance

The distance between detector and sample, d_d, (see Figure 14.1) was altered to investigate the effect on the Kikuchi pattern. Increasing the detector distance in off-axis TKD was carried out by retracting the camera. Progressive retraction led to intersection of the detector screen with the Kikuchi cone further away from the intensity maximum (c.f. Figure 14.1) and thus led to a gradual decrease in acquired intensity as well as a steady downward shift and magnification of the diffraction pattern. This effect is visible when comparing the Kikuchi patterns in Figure 14.5a (d_d = 13.5 mm), Figure 14.6a (d_d = 18.5 mm) and Figure 14.6b (d_d = 23.5 mm).

Variation of the detector distance in on-axis TKD was carried out by changing the detector tilt toward the sample. In this case the increase in detector distance led only to magnification of the Kikuchi-pattern without a pattern shift. The effect can be seen when comparing Figure 14.5d (d_d = 13.9 mm), Figure 14.6c (d_d = 20.5 mm) and Figure 14.6d (d_d = 23.5 mm). No noticeable gnomonic distortion is introduced by the detector tilt.

Working distance

Increasing the working distance, d_w, in off-axis TKD leads to a downward shift of the pattern center and Kikuchi pattern, and a loss of pattern contrast (Figure 14.5a, Figure 14.7a and Figure 14.7b). In the case of the on-axis detector it is straightforward to compensate

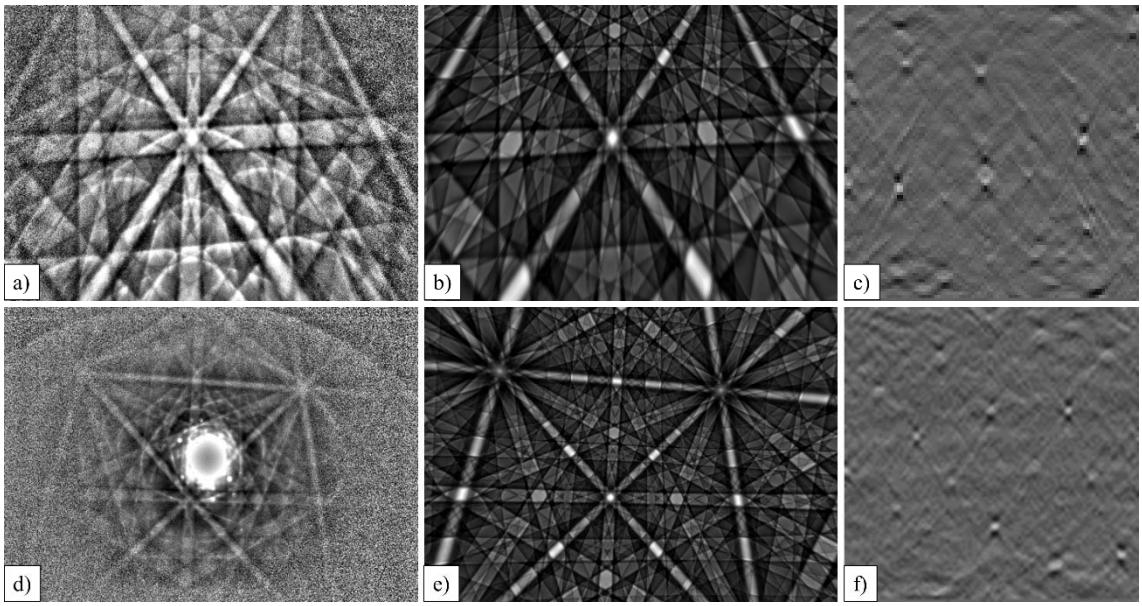

Figure 14.5: Reference Kikuchi patterns acquired with the reference parameter sets in Table 14.2 using off-axis TKD (a) and on-axis TKD (d). The simulated patterns by dynamical simulation (b and e), and the Hough spaces (c and f) of the respective patterns.

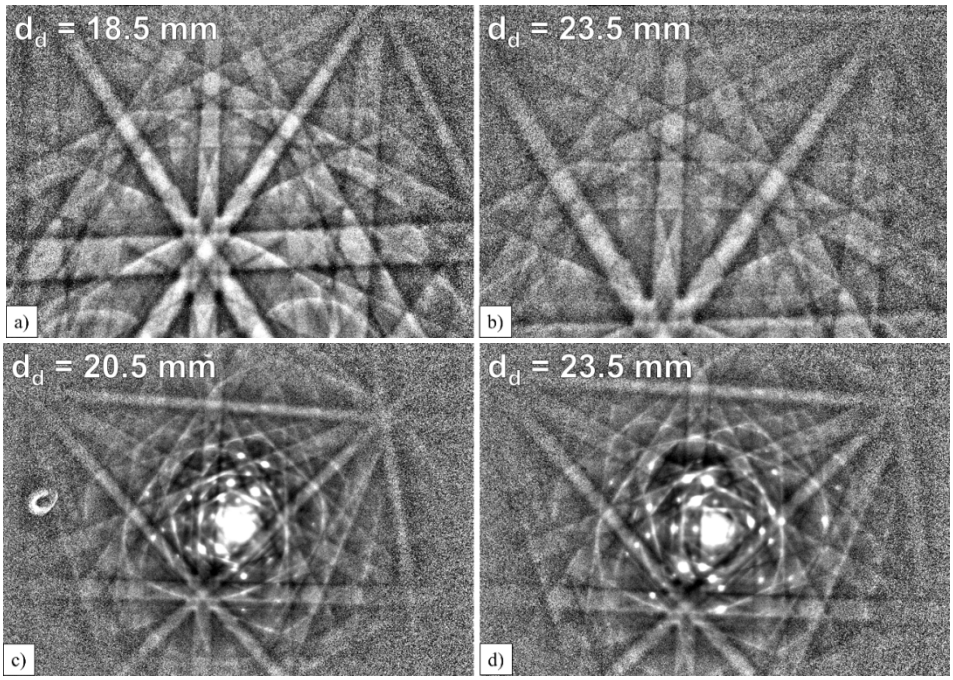

Figure 14.6: (a) Effect of changing the detector distance, d_d, on Kikuchi patterns compared to the reference patterns in Figure 14.5 in (a-b): off-axis TKD at a detector distance of 18.5 and 23.5 mm by variation in detector insertion-length; (c-d): on-axis TKD at a detector distance of 20.5 and 23.5 mm by changing the detector insertion-angle.

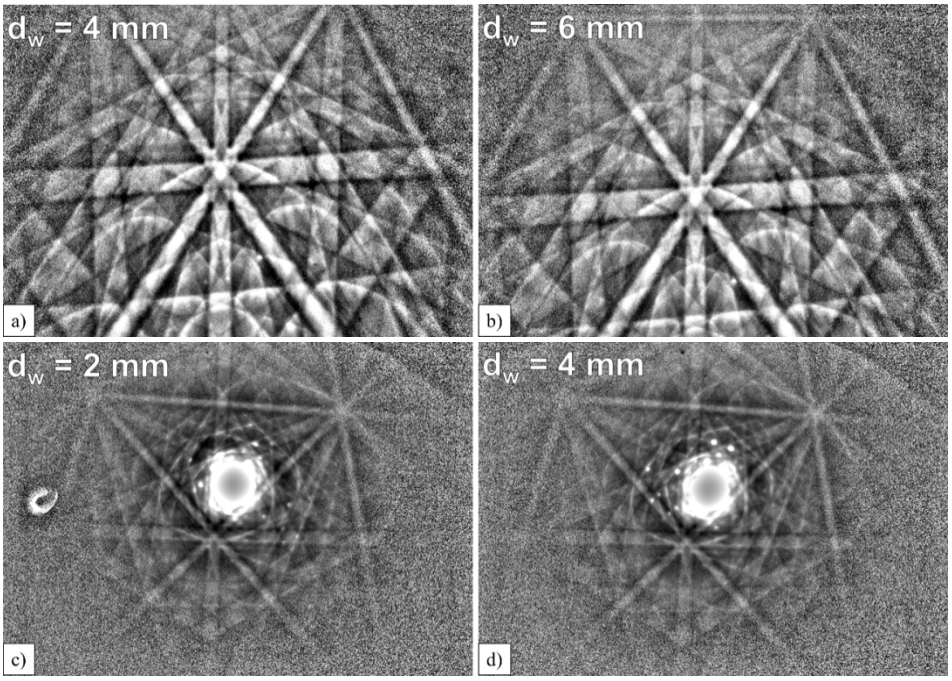

Figure 14.7: Effect of working-distance, d_w, on Kikuchi patterns for (a-b): Off-axis TKD and a working distance of 4 and 6 mm in comparison to a working distance of 3mm shown in Figure 14.5a; (c-d): On-axis TKD and a working distance of 2 and 4 mm in comparison to a working distance of 6 mm shown in Figure 14.5d, for which the detector-distance was adapted to keep the distance between sample and detector constant.

changes in working distance by adapting the detector distance (tilting of the detector) to keep it constant. The change in working distance did not seem to noticeably affect the Kikuchi pattern (Figure 14.5d, Figure 14.7c and Figure 14.7d). As previously stated the default sample holder used did not allow optimal insertion of the detector at very low working distance.

Beam current

The beam current was varied by changing the spotsize from 4 to 3.5, 4.5 and 5. As different aperture settings were applied in on-axis and off-axis TKD (Table 14.2), the changes in spot size resulted in different beam-currents for both configurations. In off-axis TKD the beam current was correspondingly changed from 1.5 nA to 0.74, 3.00 and 5.90 nA. The latter two beam current settings required a reduction of the exposure time to 500 and 200 ms. In on-axis TKD the beam current was varied from 0.83 nA to 0.42, 1.70 and 3.30 nA. In the latter two cases the exposure time needed to be reduced to 50 and 25 ms.

The pattern contrast generally increased with increasing beam current. In the case of the on-axis detector the increase in beam current on the one hand led to a larger area of the pattern which was disturbed by the transmitted beam, but on the other hand also to an increase in contrast at the periphery of the pattern (Figure 14.8).

Beam energy

Figure 14.9 shows the impact of lowering the beam energy from 30 keV (Figure 14.5) to 25 and 20 keV. In both off-axis and on-axis TKD the Kikuchi bands become less sharp and broaden with decreasing beam energy. In on-axis TKD it is evident that the size of the direct beam and the contrast of the spot-pattern gradually decrease with lower beam energy.

14.3.2 Kikuchi band detection and robustness of indexing

Representative examples for the analysis of band detection and robustness of indexing are given in Figure 14.10a and b for off-axis TKD and in Figure 14.10c and d for on-axis TKD. Figure 14.10 a and c show the detected Kikuchi bands by Hough-transform (red lines) and the matching bands by the simulated pattern of the indexed phase and orientation (blue lines). Figure 14.10b and d show the indexed Kikuchi bands (blue lines) after manually refining the Kikuchi band positions (red lines).

Most obvious is the poor band detection by the Hough-transform algorithm in the lower right pattern region of the off-axis TKD pattern in Figure 14.10a. The algorithm seems to struggle with distinguishing excess and deficient lines from individual Kikuchi bands. In the presented case manual refinement of the band detection increased the amount of indexed bands from 8 to 10 (Figure 14.10b). The example for on-axis TKD (Figure 14.10 c and d) demonstrates that manual refinement of band detection did not increase the number of indexed bands, which had already reached the software limit of 10 detectable bands.

The presented examples were representative for the range of analyzed patterns. The average amount of indexed bands after band detection with the Hough-transform algorithm were 7.8 ± 0.8 and 8.8 ± 1.3 for off-axis and on-axis TKD, respectively. By manual refinement of the band detection the amount of indexed bands could be increased by an average of 1.6 ± 0.4 in off-axis TKD and was virtually unaffected in the case of on-axis TKD.

14.3.3 Physical spatial resolution

The physical spatial resolution (PSR) was determined by correlation of reference Kikuchi patterns to Kikuchi patterns across three different HAGBs. In on-axis TKD the working

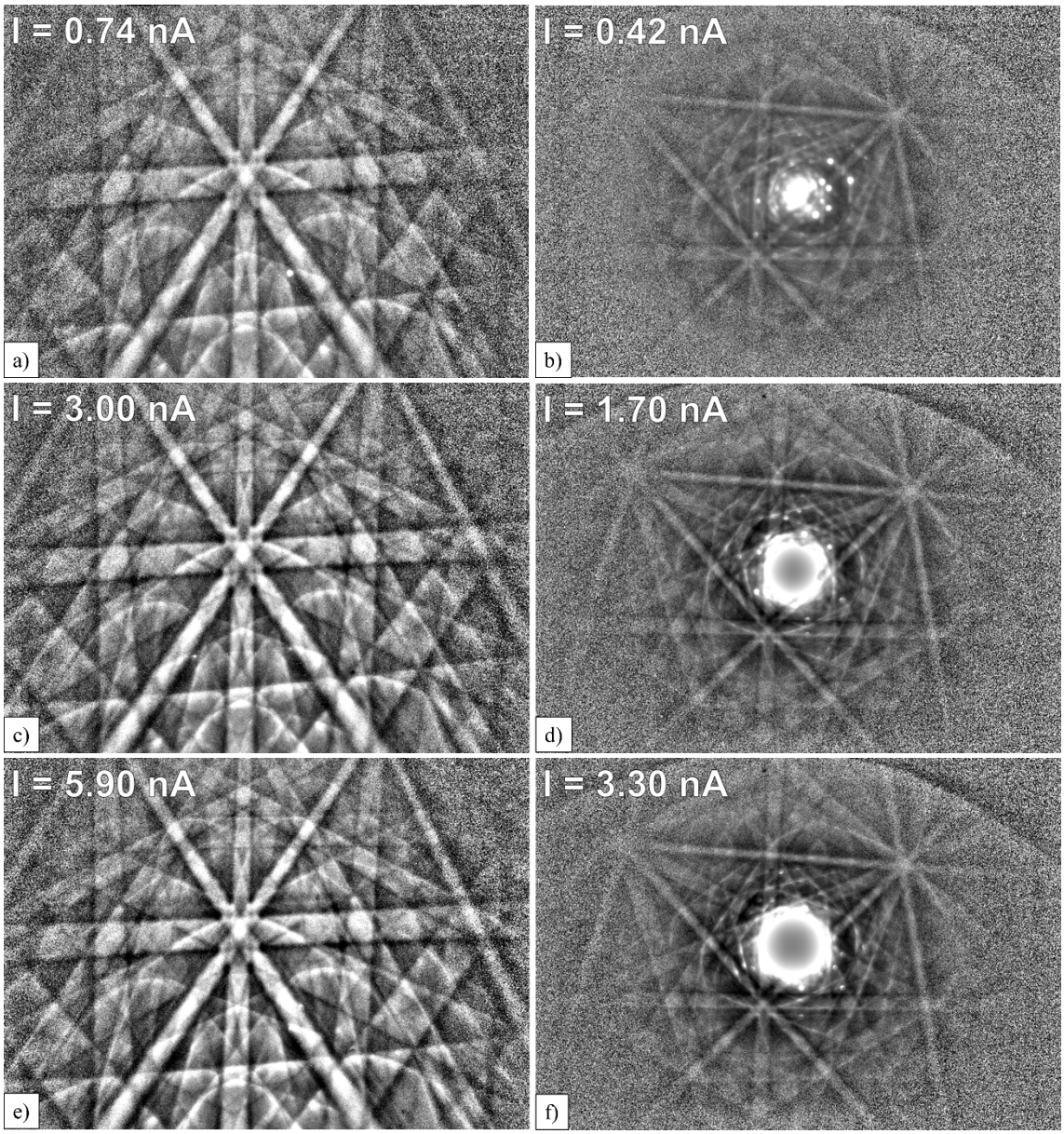

Figure 14.8: Effect of beam current on Kikuchi patterns for (a,c and e): the off-axis detector-configuration and beam currents of 0.74, 3.00 and 5.90 nA, respectively, compared to 1.50 nA in Figure 14.5a ; (b, d and e): the on-axis detector-configuration and beam currents 0.42, 1.70 and 3.30 nA, respectively, compared to 0.83 nA in Figure 14.5d.

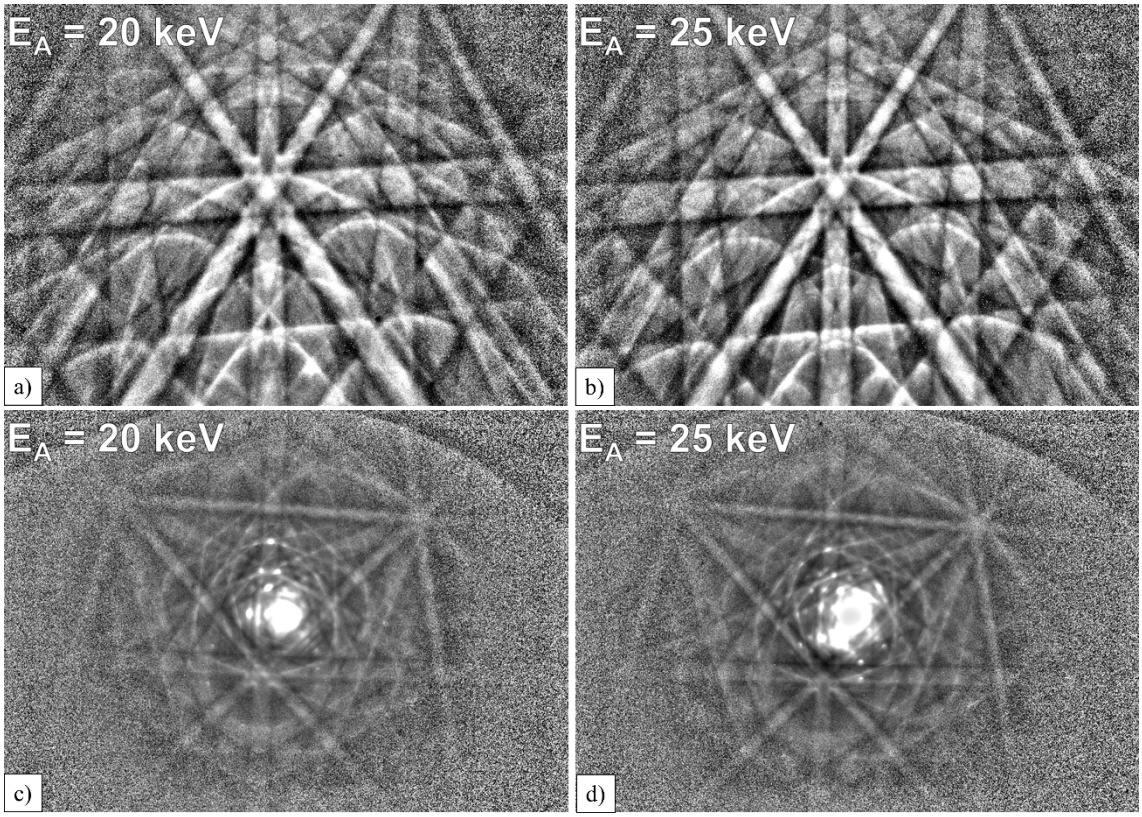

Figure 14.9: Effect of beam energy on Kikuchi patterns for (a-b): the off-axis detector-configuration at 20 and 25 keV compared to 30 keV in Figure 14.5a; (c-d): the on-axis detector-configuration at 20 and 25 keV compared to 30 keV as shown in Figure 14.5d.

distance d_w was altered to obtain measurements at the same working distance for both off-axis and on-axis TKD to exclude any influence of beam broadening. The results of the analysis are shown in Figure 14.11. The PSR of on-axis and off-axis TKD at 3 mm working distance was determined as 12.1 ± 1.7 nm and 14.7 ± 1.4 nm, respectively. The PSR of on-axis TKD was not strongly affected by the working distance, only when increasing to a working distance of 6 mm a noticeable effect was visible.

14.3.4 Effective spatial resolution (ESR)

The effective spatial resolution (ESR) was analyzed by measuring a nanocrystalline gold thin-film with the reference parameters from Table 14.2. To put the determined ESR into perspective, the physical spatial resolution on the thin-film was first determined in the same manner as for the austenitic stainless steel, but with 1 nm step size, and a step-size of 2 points for the moving average filter. The measurements were carried out on the biggest available grains, which were on the threshold of being to small to obtain good reference patterns. Consequently, the obtained values might be subject to inaccuracy and are given as an estimate, ranging between 7-8 nm in both on- and off-axis TKD. All subsequently acquired orientation maps were acquired with 3 nm step size.

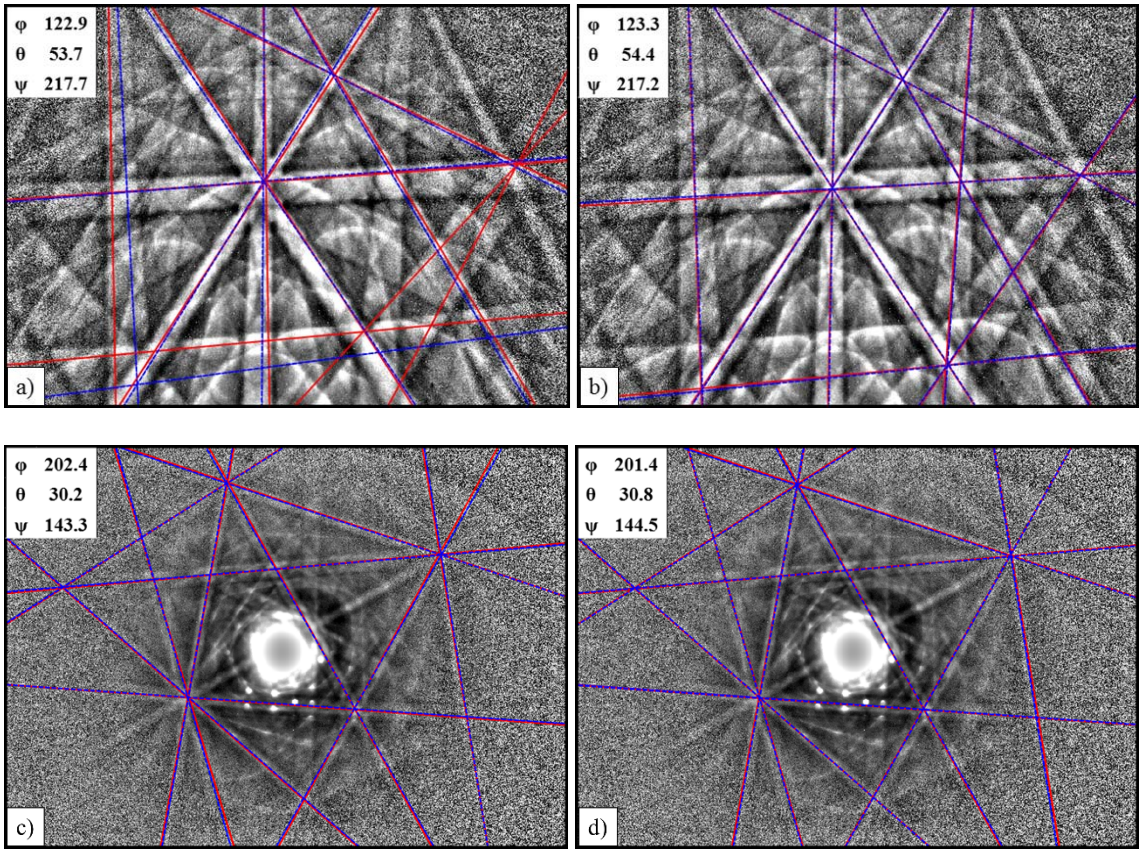

Figure 14.10: Comparison of orientation-indexing by pattern simulation with Hough-transform based (a and c) and manual (b and d) line detection on off-axis (a and b) and on-axis (c and d) Kikuchi patterns. The detected and indexed Kikuchi bands are shown by red and blue lines, respectively. Gnomonic distortion leads to detection of Kikuchi lines as Kikuchi bands by the Hough-transform algorithm in off-axis TKD. In the example presented, manual refinement of the off-axis Kikuchi pattern led to two more indexed Kikuchi bands, whereas manual refinement of the on-axis Kikuchi pattern led to no additional indexed Kikuchi bands.

Because of drift issues in off-axis TKD when acquiring high-resolution patterns according to the reference parameters, the pattern resolution was reduced from 800 x 600 pixels to 320 x 240 pixels for both detector configurations in order to enable direct comparison over larger areas. Further reduction of the pattern resolution would have led to an additional mititgation of beam-drift, but led to overexposure of the on-axis TKD detector for the present sample and reference parameters. Figure 14.12a shows an overview map of the gold thin-film acquired with on-axis TKD. Unindexed points correspond to areas at which no information from diffraction could be obtained. Figure 14.12b to d show a magnification of a small area of different grain sizes, indicated by the rectangular area in Figure 14.12a. Figure 14.12b and Figure 14.12c show on-axis TKD maps acquired with pattern resolutions of 320 x 240 pixels and 800 x 600 pixels and exposure times of 12 and 75 ms, respectively. Figure 14.12d shows the same area measured with off-axis TKD with a pattern resolution of 320 x 240 pixels and an exposure time of 136 ms. The fraction of indexed points in on-axis TKD is clearly improved by measuring at better pattern resolution. Off-axis TKD reveals a high fraction of indexed points, but struggles with drift issues due to long

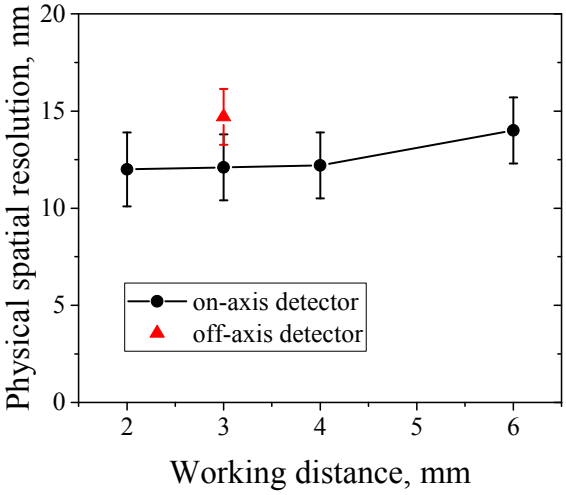

Figure 14.11: PSR of the on-axis detector for different working distances in comparison to the PSR of the off-axis detector when applying the reference parameter sets (Table 14.2). The error-bars indicate the sample standard deviation from 30 different analyzed cropped pattern areas.

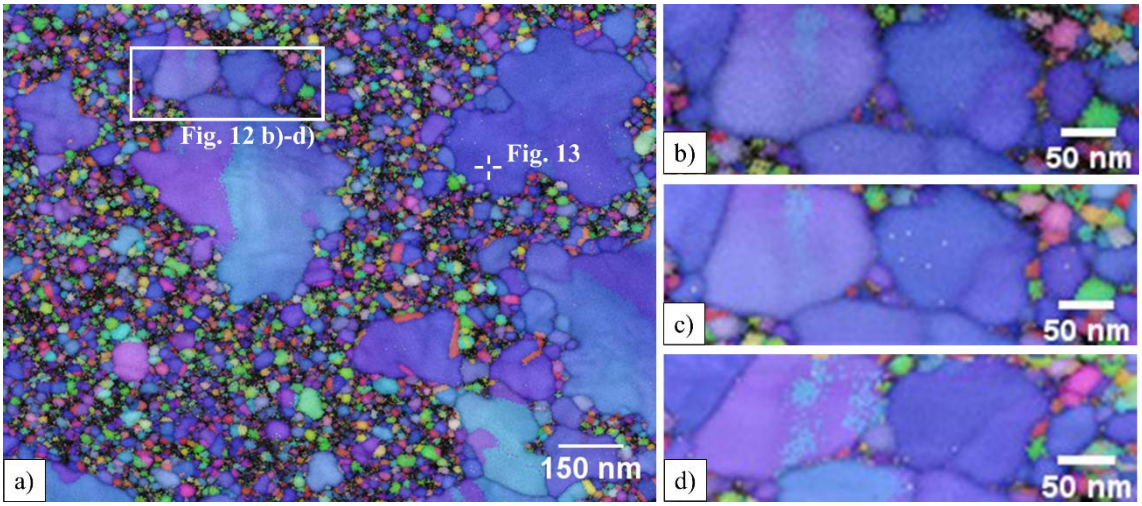

Figure 14.12: Analysis of ESR on inverse pole-figure map of nanocrystalline gold thin-film; if not stated differently the reference parameters in Table 14.2 are applied; a) On-axis TKD: Overview map acquired with a reduce pattern resolution of 320 x 240 pixels and 12 ms exposure time; b) On-axis TKD: Inset of the region marked with a rectangle in Figure 14.12a acquired with identical parameters; c) On-axis TKD: Scan on the same inset with 800 x 600 pixels pattern resolution and 75 ms exposure time; d) Off-axis TKD: Scan of the inset with 320 x 240 pixels pattern resolution and 136 ms exposure time.

measurement times even at lower pattern resolution. All tested conditions allowed indexing of grains with diameters of approx. 10 nm, where the effective resolution at different GB's seemed to depend on the local quality of the sample.

Wherever sample quality was not an issue, the number of non-indexed points at grain boundaries were either 0 or 1, corresponding to an effective resolution of equal or better to 3 nm in all three investigated conditions. Figure 14.12b to d show that, in the left

of the two large grains, a strongly inclined twin boundary was indexed differently by on-axis and off-axis TKD. Closer analysis revealed that an overlap of the parent and twin orientations in both on-axis and off-axis TKD patterns led to ambiguous indexing. As indexing of the twin was also slightly affected by changing the pattern resolution in on-axis TKD with otherwise unaltered parameters (Figure 14.12b and c), the difference in indexing in on-axis and off-axis TKD is likely to depend on detection of characteristic bands of either orientation by the Hough transform, and may to a lesser extent be an effect of different specimen tilt or source region. It is important to point out that contamination of the mapped area was quite significant and the repeated measurements on the same area were influenced by it. First the off-axis measurement was performed (Figure 14.12d), followed by the high resolution on-axis map (Figure 14.12c) and finally the lower resolution map (Figure 14.12b).

Figure 14.13 shows the Kikuchi pattern which was obtained with on-axis TKD from the marked position in Figure 14.12a. The pattern is representative for patterns in which the major zone axis is obscured by the bright spot caused by the transmitted beam. In such cases robust indexing was still possible, mainly based on surrounding zone axes, and in some cases even supported by bands that cross the spot of the direct beam.

14.4 Discussion

It was generally observed that on-axis Kikuchi patterns, because of the different detector geometry, are less sensitive to changes in working distance and detector distance. Moreover, on-axis Kikuchi patterns were more affected by changes in beam current and beam energy, as the signal is acquired at the maximum intensity of the Kikuchi cone and also contains the direct beam and coherently scattered electrons. This general observation, its consequences for orientation mapping, and related observations are discussed in further detail in the following section.

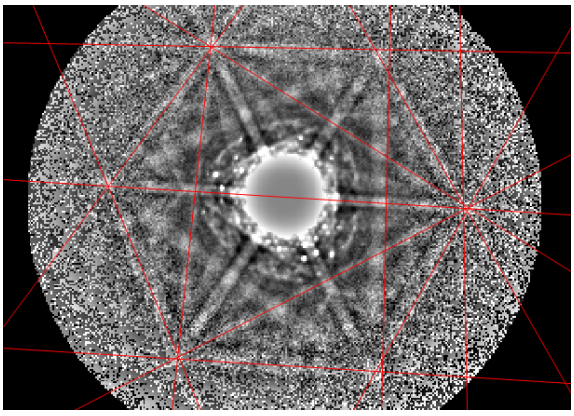

Figure 14.13: Kikuchi pattern and detected bands (red lines) from the spot marked in Figure 14.12a, obtained at 320 x 240 pixels pattern resolution and 12 ms exposure time. On-axis Kikuchi patterns are indexed robustly even when the direct beam overlaps with a major zone axis. The major diffraction information then arises mainly from surrounding zone axes.

14.4.1 Kikuchi pattern area

By comparing the reference Kikuchi patterns with their simulated patterns in Figure 14.5 it was found that, although similar detector distances were chosen, the capture angle in on-axis TKD was much larger, which resulted in approximately 70 % more area of the Kikuchi map. This area is obviously dependent on the chosen detector distance, which in on-axis TKD can be tuned over a wide range without losing signal intensity, as demonstrated in Figure 14.6c and d. The limited interception with the Kikuchi cone in off-axis TKD leads to severe loss of intensity and detectable bands with increasing detector distance, which makes it a rather sensitive parameter (Figure 14.6a and b). The adaptability of the on-axis setup opens a wide range of applications, ranging from general orientation mapping (short detector distance) to strain mapping (large detector distance).

A different way of changing the effective Kikuchi pattern area in on-axis TKD is by adjustment of the beam current (Figure 14.8b, d and f). While a lower beam current naturally improves the PSR, the ESR is compromised by the decrease in pattern intensity. Thus sacrificing PSR by measuring with higher beam current can, in fact, lead to a considerable improvement in ESR by obtaining more detectable Kikuchi bands (see Figure 14.8). Furthermore, acquisition rate, and thus sensitivity to drift, as well as indexing robustness are improved with higher beam current, as reported for off-axis TKD in Ref. [4]. As a downside, increased beam-current leads to increased contamination. Finally, the effect of the transmitted beam leads to a sample dependent upper limit for the beam current.

14.4.2 Working distance

Generally, shorter working distance is favorable as it minimizes the effect of beam broadening. In off-axis TKD the working distance is critical for obtaining good orientation mapping, as the signal intensity and the pattern center are directly affected by this parameter (Figure 14.7a and b). For a given working distance, the detector distance should be minimized and the detector tilt should be adapted for optimal illumination of the phosphor screen. With decreasing working distance the detector is tilted increasingly upwards to obtain optimum signal. This leads to an effective increase of the intersection angle, α, and consequently to increased intensity and reduced gnomonic distortion. When using a detector that operates at fixed tilt angle, low working distance may, in contrast, lead to analysis far away from the pattern center and thus lead to stronger gnomonic distortion.

In on-axis TKD the working distance had no significant influence on the Kikuchi pattern (Figure 14.7c and d), although at working distances larger than 6 mm an evident decrease in PSR was observed (Figure 14.11), which is most likely caused by beam broadening.

14.4.3 Pattern contrast

Decreasing the beam energy led, in both on- and off-axis TKD, to a decrease in pattern contrast and to broadening of the Kikuchi bands, as generally expected according to the physics of Kikuchi pattern formation [16] and specifically reported for TKD in Refs. [5,7,12,17,18]. In on-axis TKD, lowering the beam energy furthermore led to a reduction in the area of the transmitted beam and lower intensity of the diffraction spots. In Ref. [7] the loss of plasmon and phonon scattering with decreasing beam energy is found as the main reason for this effect. As diffraction spots are not desired for standard TKD-investigations, the beam energy can be used to balance the contrast when working with very thin specimens or specimens of low atomic number.

Increasing the beam current led to sharpening of the Kikuchi lines in both detector configurations, as also reported in [19]. Generally the beam current can therefore be adapted to gain pattern contrast, in which case the aforementioned effects on the intensity of the transmitted beam, the effective Kikuchi pattern area and the PSR should be considered.

14.4.4 Kikuchi band detection and robustness of indexing

Comparison of Figure 14.5c and f shows that the Hough space of the on-axis Kikuchi pattern is not noticeably affected by the bright spot caused by the transmitted beam. The robustness to noise and discontinuities in the patterns is in fact the strength of the Hough transform [20,21]. Figure 14.13 shows that, even though the major zone axis of the pattern coincided with the bright spot, robust indexing was possible, although mainly by surrounding zones axes in the periphery of the pattern. Sneddon et al. speculated, that the bright spot from the direct beam may cause issues with indexing relatively indistinct patterns [8]. In cases, where only one zone axis is present and this coincides with the bright spot, indexing can in fact be compromised. Whenever such a situation is observed, decreasing detector distance (by either changing working distance and/or detector tilt) improves indexing. In fact, off-axis patterns of such orientations were found to be more problematic, as unambiguous indexing based on a single zone axis was difficult, and changing the detector distance was unfeasible. Because of the large available area of the Kikuchi map and the consequently high amount of detectable bands, on-axis TKD is particularly well suited for phase identification.

The robustness of Kikuchi band detection and indexing of both on-axis and off-axis Kikuchi patterns were analyzed by comparing pattern indexing based on band detection by the Hough-transform and by manual refinement (Figure 14.10). The fact that manual band detection improves indexing robustness more significantly in off-axis rather than in on-axis TKD, indicates that the gnomonic distortion is more detrimental for the Hough based indexing routine than the bright area of the transmitted beam in the pattern center. Gnomonic distortion led to strong magnification of excess and deficient lines of Kikuchi bands in the lower pattern region, which were detected as individual Kikuchi bands by the

Hough transform (c.f. Figure 14.10c). This issue was previously reported in Ref. [4], and is virtually absent in on-axis TKD. Some commercially available indexing softwares have made efforts to partially mitigate this effect in off-axis TKD by modifiying the band detection algorithm to account for this change in geometry [8]. Such software correction was not applied in the present work so that its effectiveness could not be evaluated.

14.4.5 Acquisition rate

One of the most striking advantages of on-axis TKD compared to off-axis TKD was the immense gain in acquisition rate. The reference measurements with on-axis and off-axis TKD were conducted with 0.83 nA and 1.5 nA beam current, respectively. The product of the beam current ratio with the applied exposure time ratio resulted in a factor of 20 when measuring with the reference parameters from Table 14.2 or with lower pattern resolution and exposure time as in Figure 14.12. This observation confirms the findings by Yuan et al., who reported that for a fixed incident intensity on the specimen in comparison to off-axis TKD the acquisition time is at least 20 times shorter at equivalent pattern quality and indexation rate, and that alternatively 20 times lower electron dose can be used [6].

Such an increase in acquisition rate may be beneficial to save microscope time, but is of far greater importance to utilize the new possibilities, which TKD gives in terms of spatial resolution. A clear distortion of the orientation map caused by beam drift is evident in the orientation map from off-axis TKD in Figure 14.12d, when comparing the equivalent measurements from on-axis TKD in Figure 14.12b and c. The issue of beam drift in conventional TKD was also observed and discussed in Refs. [6,22,23]. In the present case, further binning of the Kikuchi pattern in off-axis TKD would have mitigated the extensive beam drift to some extent, but would have led to overexposure of the camera in on-axis TKD, when testing in identical conditions. Even though beam drift can be reduced to some extent by letting the sample settle for a few hours in the evacuated microscope chamber or by installing an advanced cooling system of the lens coils, it will remain an issue in both on- and off-axis TKD. The increase in acquisition rate gained in on-axis TKD is therefore important to acquire large data sets with minimum beam drift, and thus for utilizing the reported spatial resolutions in practice. In cases were both on-axis and off-axis TKD are capable of running at acquisition rates that are limited by the detector hardware, on-axis TKD can be operated with higher pattern resolution or lower beam current.

14.4.6 Spatial resolution

On-axis TKD led to a small improvement of 2-3 nm in PSR in measurements over HABG's on a 115 ± 8 nm thick austenitic stainless steel thin-foil (Figure 14.11) with the stated sets of reference parameters in Table 14.2. The measured difference in PSR is seen representative for measuring with detector-typical beam energy, beam current and specimen tilt and may furthermore be affected by the source region of the acquired intensity.

On-axis and off-axis detector systems acquire the intensity from electrons of different scattering angle (Figure 14.1). Considering a given average path length of an electron from the last incoherent scattering event to leaving the exit surface of the sample, the increased scattering angle of electrons detected in off-axis TKD may lead to a thinner source region of the detected intensity, as suggested in Ref. [8]. Assuming that such effect is noticeable, it would for a given sample thickness imply better depth resolution, but worse lateral resolution of off-axis TKD compared to on-axis TKD. The source region effect may partially be responsible for the slightly better PSR of on-axis TKD in the present case (Figure 14.11), but dedicated investigations on bilayered samples are required to obtain a better understanding.

Lower specimen tilt in off-axis TKD could potentially lead to an improvement of the measured values, but led in the present case to insufficient intensity at the upper part of the phosphor screen. Ref. [24] suggests a worsening of the lateral PSR with increasing specimen backtilt without providing a quantitative analysis, which to the best knowledge of the authors has neither been reported elsewhere.

The applied exposure times in this spatial resolution study, especially for off-axis TKD, result in too low acquisition rates to be considered for investigating larger areas. In order to increase the acquisition rate for a large area scan the options would be to increase the beam current, which compromises the PSR, or reducing the pattern resolution, which compromises the ESR. Therefore, the spatial resolution in off-axis TKD is expected to be worse when measuring larger maps, while the same is not the case for on-axis TKD, which intrinsically operates at higher acquisition rates (see discussion in section 14.4.5).

The ESR was estimated from measurements on a nanocrystalline gold thin-film (Figure 14.12). The physical spatial resolution was estimated to range between 7-8 nm and it was observed that both detector configurations managed to resolve grains of approx. 10 nm in diameter. The on-axis TKD scans led to noticeably better indexing when increasing the pattern resolution from 320 x 240 pixels to 800 x 600 pixels at the cost of measuring at 16 % of the original acquisition rate. The detector system is advertised by the manufacturer to enable orientation mapping with an ESR of 3 nm or better on a variety of tested materials. On thin samples of high atomic number, which are optimal for achieving high spatial resolution, this figure is regarded as realistic, as similar ESR could be obtained when measuring the 15 nm thick nanocrystalline gold thin-film. A measurement performed with 1 nm step size and pattern resolution of 320x240 revealed 1-2 non indexing points at the grain boundaries, indicating that the effective resolution can be even better.

14.4.7 General remarks and outlook

Most conventional EBDS detectors contain a set of diodes designed for forward scatter imaging, which are well-suited to conduct dark-field imaging in off-axis TKD [22]. The geometry of the on-axis detector configuration in turn enables continuous switching between true bright- and dark-field contrast similar to imaging in TEM (c.f. bright-field

image in Figure 14.3a) by inserting the detector to different insertion distances. As TKD, thanks to its good spatial resolution, is generally well suited for characterization of ultrafine grained microstructures with high defect density [6,22], these imaging capabilities qualify the on-axis detector configuration even further for such application.

In order to switch between different imaging modes and the TKD mode, the insertion distance of the on-axis detector has to be changed to allow acquisition of the transmitted intensity with the diodes or the phosphor screen, respectively. A drawback of changing between acquisition modes in this way is that movement of the detector leads to deflection of the electron beam, which becomes more prominent with increasing working distance. This effect neither influences the quality of Kikuchi patterns nor the measurement performance, but may cause difficulties in locating the same position after imaging on very fine microstructures. Such issue is not as pronounced in the off-axis configuration. Even though imaging at increased detector distance also leads to better image contrast when using the diodes on the EBSD-detector, it is possible to both obtain acceptable image quality and good orientation maps at a single detector distance.

Simultaneous EDS and TKD analysis are possible in the on-axis geometry, but lead to a strong X-ray fluorescence signal from the interaction of the direct beam with the detector when using the standard configuration presented in this work [19]. It was found that this obstructive effect can be largely supressed by using a purpose-fit stage to shield the signal of the on-axis detector. Further, some recently developed silicon drift detectors for EDS analysis [25,26] can largely mitigate this issue, as they are inserted between the pole piece and the electron transparent sample to provide a large solid angle. The increased signal yield allows simultaneous EDS and TKD analysis at high acquisition rate [27], reducing the currently experienced drift issues when using conventional hardware .

Brodu et al. found that the contrast of on-axis TKD patterns is sensitive to changes in thickness and beam energy [7]. Generally, more distinct features, such as diffraction spots, Kikuchi bands and Kikuchi lines, become visible as a function of these parameters. This change in contrast was modeled by a simple equation, which enables tuning it for specific materials. Even though the effect of sample thickness was not part of the present investigation, no dramatic change in patter contrast or indexing precision were experienced when mapping areas on steel samples with several 10 nm deviation in thickness. For samples with extreme deviation in thickness off-axis TKD could lead to better indexing, as the contrast of off-axis patterns was found less sensitive to changes in thickness.

As the development of the on-axis detector is still at an early stage, there is a need to develop software which employs the variety of features contained in an on-axis Kikuchi pattern in a more distinct way [7]. Currently, for instance the band contrast map is disturbed by acquisition of the transmitted beam, which might be corrected by omitting the overexposed area in the center of the pattern. It was reported in Ref. [7] that specimen thickness and incident energy have a symmetrical influence on the diffraction contrast in on-axis TKD. If this relation holds, the bright area of the transmitted beam, which is a

measurement of electron absorption, could be used to estimate the specimen thickness when the beam energy, beam current and atomic number of the specimen are known. In this way on-axis TKD may in parallel to conventional orientation mapping enable acquisition of thickness maps similar to those obtained from EELS in TEM. For such an application further understanding of the diffraction contrast and in particular the influence of crystal orientation on the absorption of the transmitted beam is needed.

14.5 Conclusions

- On-axis TKD was found advantageous over off-axis TKD mainly due to the evident enhanced pattern intensity, which allows reduction of the beam current and/or increasing the acquisition rate, and due to virtual absence of gnomonic distortion. Fast acquisition over large areas enabled considerable reduction of drift issues.
- The measured PSR obtained using detector-typical microscope parameters reveals a relatively small improvement of using on-axis TKD. To measure the PSR at the same pattern resolution, long exposure times were required in off-axis TKD. In larger area scans the spatial resolution of off-axis TKD is therefore expected to be worse, since an increase in beam current or decrease in pattern resolution is required.
- As a measurement of the ESR gold grains of approximately 10 nm could be reliably indexed by both on-axis and off-axis TKD. In off-axis TKD the achieved resolution was mitigated by beam drift.
- On-axis TKD, based on its intersection with the intensity maximum of the Kikuchi cone below the specimen, is less sensitive to changes in geometry (working distance and detector distance) but more sensitive to changes in beam current and beam energy than off-axis TKD.
- Hough transform based automated band detection led to on average one more indexed band per pattern in on-axis TKD compared to off-axis TKD. Manual refinement of band detection led to indexing of on average 1.6 additional bands in off-axis and virtually no further increase in on-axis TKD. Consequently the Hough transform seems to operate more robustly on on-axis TKD patterns.
- The bright spot caused by the transmitted beam in on-axis TKD did not noticeably disturb the Hough transform. In the case where the major zone axis coincided with the bright spot of the transmitted beam, additional zone axes in the periphery of the Kikuchi pattern could be detected.

Acknowledgements

Jens Kling, DTU Center for Electron Nanoscopy (CEN), is acknowledged for conducting the thickness measurement on the austenitic stainless steel thin foil. Bruker Nano GmbH (BNA) is gratefully acknowledged for the loan of the OPTIMUS^{TM} TKD detector head. The Danish Underground Consortium is gratefully acknowledged for financial support to the Danish Hydrocarbon Research Center (DHRTC).

References

[1] R.H. Geiss, R.R. Keller, D.T. Read, Transmission electron diffraction from nanoparticles, nanowires and thin films in an SEM with conventional EBSD equipment, Microsopy Microanal. 16 (2010) 1742–1743.

[2] R. Geiss, R. Keller, S. Sitzman, P. Rice, New Method of Transmission Electron Diffraction to Characterize Nanomaterials in the SEM, Microsc. Microanal. 17 (2011) 386–387.

[3] R.R. Keller, R.H. Geiss, Transmission EBSD from 10 nm domains in a scanning electron microscope, J. Microsc. 245 (2012) 245–251.

[4] P.W. Trimby, Orientation mapping of nanostructured materials using transmission Kikuchi diffraction in the scanning electron microscope, Ultramicroscopy. 120 (2012) 16–24.

[5] J.J. Fundenberger, E. Bouzy, D. Goran, J. Guyon, H. Yuan, A. Morawiec, Orientation mapping by transmission-SEM with an on-axis detector, Ultramicroscopy. 161 (2016) 17–22.

[6] H. Yuan, E. Brodu, C. Chen, E. Bouzy, J.-J. Fundenberger, L.S. Toth, On-axis versus off-axis Transmission Kikuchi Diffraction technique: application to the characterisation of severe plastic deformation-induced ultrafine-grained microstructures, J. Microsc. 0 (2017) 1–11.

[7] E. Brodu, E. Bouzy, J.-J. Fundenberger, Diffraction contrast dependence on sample thickness, incident energy and atomic number in on-axis Transmission Kikuchi Diffraction in the SEM, Ultramicroscopy. 181 (2017) 123–133.

[8] G.C. Sneddon, P.W. Trimby, J.M. Cairney, Transmission Kikuchi diffraction in a scanning electron microscope: A review, Mater. Sci. Eng. R Reports. 110 (2016) 1–12.

[9] S. Zaefferer, On the formation mechanisms, spatial resolution and intensity of backscatter Kikuchi patterns, Ultramicroscopy. 107 (2007) 254–266.

[10] T. Malis, S.C. Cheng, R.F. Egerton, Log-Ratio Technique for Specimen-Thickness Measurement in the TEM, J. Electron Microsc. Tech. 8 (1988) 193–200.

[11] D.R.G. Mitchell, B. Schaffer, Scripting-customised microscopy tools for Digital Micrograph(TM), Ultramicroscopy. 103 (2005) 319–332.

[12] K.P. Rice, R.R. Keller, M.P. Stoykovich, Specimen-thickness effects on transmission Kikuchi patterns in the scanning electron microscope, J. Microsc. 254 (2014) 129–136.

[13] D. Chen, J.C. Kuo, W.T. Wu, Effect of microscopic parameters on EBSD spatial resolution, Ultramicroscopy. 111 (2011) 1488–1494.

[14] Y.Z. Wang, M.G. Kong, Z.W. Liu, C.C. Lin, Y. Zeng, Effect of microscope parameter and specimen thickness of spatial resolution of transmission electron backscatter diffraction, J. Microsc. 264 (2016) 34–40.

[15] MATLAB 2015a - Imaging Toolbox - function corr2, (2015).

[16] D.B.B. Williams, C.B. Carter, C. Barry Carter, Transmission Electron Microscopy, 2nd ed., Springer, 2009.

[17] J.-W. Shih, K.-W. Kuo, J.-C. Kuo, T.-Y. Kuo, Effects of Accelerating Voltage and Specimen Thickness on the Spatial Resolution of Transmission Electron Backscatter Diffraction in Cu, Ultramicroscopy. 177 (2017) 43–52.

[18] S. Suzuki, Features of transmission EBSD and its application, JOM. 65 (2013) 1254–1263.

[19] M. Abbasi, D. Kim, H. Guim, M. Hosseini, H. Danesh-manesh, M. Abbasi,

Application of Transmitted Kikuchi Diffraction in Studying Nano-oxide and Ultrafine Metallic Grains, ACS Nano. 9 (2015) 10991–11002.
[20] F. Karsli, O. Kahya, Building extraction from laser scanning data, Int. Arch. Photogramm. Remote Sens. Spat. Inf. Sci. XXXVII (2008) 289–294.
[21] N.C. Krieger Lassen, D. Juul Jensen, K. Conradsen, Image processing procedures for analysis of electron back scattering patterns, Scanning Microscoy. 6 (1992) 115–121.
[22] P.W. Trimby, Y. Cao, Z. Chen, S. Han, K.J. Hemker, J. Lian, X. Liao, P. Rottmann, S. Samudrala, J. Sun, J.T. Wang, J. Wheeler, J.M. Cairney, Characterizing deformed ultrafine-grained and nanocrystalline materials using transmission Kikuchi diffraction in a scanning electron microscope, Acta Mater. 62 (2014) 69–80.
[23] N. Brodusch, H. Demers, R. Gauvin, Nanometres-resolution Kikuchi patterns from materials science specimens with transmission electron forward scatter diffraction in the scanning electron microscope, J. Microsc. 250 (2013) 1–14.
[24] G. Sneddon, P. Trimby, J. Cairney, The Influence of Microscope and Specimen Parameters on the Spatial Resolution of Transmission Kikuchi Diffraction, Microsc. Microanal. 23 (2017) 532–533.
[25] H. Soltau, A. Bechtele, O. Jaratschin, A. Liebl, A. Niculae, A. Simsek, R. Eckhard, K. Hermenau, P. Lechner, G. Lutz, G. Schaller, F. Schopper, L. Strüder, SDDs - Silicon Detectors for EDS with a Performance at the Theoretical Limit, Microsc. Microanal. 14 (2008) 1156–1157.
[26] A. Niculae, H. Soltau, P. Lechner, A. Liebl, G. Lutz, L. Strüder, R. Eckhard, G. Schaller, F. Schopper, Optimum Performance for Microanalysis with Silicon Drift Detectors with Integrated FET, Microsc. Microanal. 13 (2007) 1430–1431.
[27] D. Goran, Quantitative Characterization of Nanostructured Materials with Fast TKD Measurement - Bruker Webinar, (2017).

15 Conclusion

All detailed conclusions of this work can be found in the individual result chapters. Here, the most significant conclusions of this doctoral thesis are summarized and sub-divided according to different fields of investigation. Even though the results are obtained from studying three different alloys, the following conclusions, unless explicitly stated, can be seen as general for supermartensitic and soft martensitic stainless steels:

(i) Kinetics of solidification and cooling

- The transformation kinetics of solidification and cooling in casting can be predicted with kinetics modeling of diffusion.
- Kinetics modeling can predict the amount of retained δ-ferrite and the partitioning between δ-ferrite and austenite (martensite).
- Compositional inhomogeneity in the as-cast microstructure is caused by the impinged diffusion field of the δ-ferrite to austenite transformation.
- The amount of time spent between 1300 and 1200 °C is most critical to transform δ-ferrite to austenite. Consequently, slower cooling leads to a reduce fraction of retained δ-ferrite.

(ii) Martensite formation

- Martensite formation in EN1.4418 commences at M_s = 135 °C and occurs without autotempering.
- The resulting lath martensite microstructure is insensitive to the quenching rate.
- Lath martensite shows a dislocation density of $\sim 1.8 \times 10^{15}\ \mathrm{m}^{-2}$.
- During martensite formation, significant phase-specific micro-stresses build up in the minority phase, i.e. in martensite at the beginning and in austenite at the end of the transformation.
- Phase-specific micro-stresses are compressive in the minority phase and are balanced by small tensile stresses in the majority phase
- Strain in austenite is anisotropic; when exposed to an average hydrostatic compressive stress, compression is measured along the $\langle 222_\gamma \rangle$ and $\langle 220_\gamma \rangle$ directions and tension is measured along the $\langle 200_\gamma \rangle$ direction.
- Both phases are subject to plastic deformation during quenching

(iii) Tempering of martensite

- Tempering of martensite with $0.033\ \mathrm{K.\,s^{-1}}$ up to 475 °C leads to progressive rejection of C and N from solid solution to lattice defects, mainly grain boundaries.
- The unit cell volume of martensite decreases during tempering. The decrease is accounted entirely for by segregation of the interstitial atoms, implying that stress relaxation only contributes negligibly to changes in the martensite unit cell volume.

- For tempering of martensite with $0.033\ \mathrm{K.s^{-1}}$ up to 475 °C, clustering of C, but no formation of transition carbides is observed.
- Isothermal tempering of martensite for 60 s below 550 °C leads to no change in dislocation density.
- After tempering at 700 and 750 °C for 60 s the dislocation density is reduced to a seemingly steady minimum value of $\sim 3.5 \times 10^{14}\ \mathrm{m^{-2}}$.

(iv) Austenite reversion

- Austenite forms at grain boundaries, mostly lath boundaries, and is stabilized by isothermal inter-critical annealing.
- The fraction of austenite is associated with softening of the material.
- The stability of reverted austenite mainly originates from enrichment in Ni during diffusion-assisted growth and may be further affected by the austenite grain size and the mechanical constraint of the surrounding martensite matrix.
- Reversion of austenite during isochronal heating with $2 - 18\ \mathrm{K.min^{-1}}$ occurs in two distinct stages and can be predicted with kinetics modeling of diffusion.
- Two-stage austenitization is caused by impingement of the diffusion field. The rates of the first and second stage of austenitization are determined by Ni-diffusion in martensite and austenite, respectively.

(v) Stability of reverted austenite

- The austenite fraction increases with annealing temperature, which leads to larger austenite grains and dilution of Ni. The stability of reverted austenite is consequently reduced so that new martensite is formed during cooling to room temperature.
- Immersion of inter-critically annealed samples in boiling N_2 does not noticeably affect the fraction of reverted austenite. However, reverted austenite transforms to isothermal martensite during holding at 194.5 K, which can be understood in terms of thermally activated martensite formation.
- Reverted austenite can transform by a strain-induced mechanism during uniaxial tensile loading, which extends the ductility.
- Applied tensile stress on inter-critically annealed samples is accommodated by martensite, while austenite deforms and partially accomplishes the deformation by transformation to martensite.

(vi) Experimental methods

- A systematic comparison of transmission Kikuchi diffraction in the novel on-axis and conventional off-axis configuration revealed advantages of the on-axis configuration in terms of faster acquisition speed and less beam drift.

16 Further work

The present work elucidated a variety of fundamental mechanisms and their effect on properties in supermartensitic stainless steels. The following further work is suggested for consolidation and extension of the presented work:

- The evolution of the lattice strains and stresses in austenite and martensite during martensite formation were measured by in-situ synchrotron X-ray diffraction. While the measurements led to fundamental understanding of the average stress state of the two phases, the role of plastic deformation, the local distribution of stresses, the effect of stresses on the stability of retained austenite and its effect on the transformation kinetics should be investigated in more depth and discussed in the light of the presented results.
- In the present work, the segregation of C and N to lattice defects during tempering of martensite and the formation and stabilization of reverted austenite were investigated. While important mechanisms were identified, the conditions for nucleation of reverted austenite are not well understood. Thus, advanced microstructure characterization in the temperature range between tempering of martensite and advanced austenite formation should be carried out. Here, especially the nucleation sequence and interdependence during diffusional growth of alloy carbides and reverted austenite should be treated. Further, the role of residual stress in lath martensite for nucleation of reverted austenite should be investigated.
- Strain-induced martensite formation from reverted austenite was investigated by in-situ synchrotron diffraction experiments. The presented data provides fundamental understanding of stress partitioning, anisotropy of lattice strains, strain hardening and the stability of reverted austenite. Supplementary work, such as post-mortem analysis of tensile specimens and comparison to numerical modeling of crystal plasticity, would enable a more elaborate interpretation of the diffraction data.
- A systematic study on the thermal and mechanical stability of reverted austenite as a function of composition and austenite grain size would be of interest. As composition and grain size cannot readily be controlled independently from each other in experimental microstructures, close coupling of experimental data with numerical modeling of crystal plasticity is required to obtain a more fundamental understanding.
- It was demonstrated that reverted austenite that is stable at room temperature after inter-critical annealing is not necessarily stable at sub-zero Celsius temperature. The kinetics of isothermal martensite formation and the effect on the mechanical properties, in particular the impact toughness, should be investigated in more depth.

17 Appendix

Austenite reversion in low-carbon martensitic stainless steels – a CALPHAD-assisted review*

Frank Niessen

Technical University of Denmark (DTU), Danish Hydrocarbon Research and Technology Centre (DHRTC) , Elektrovej building 375, 2800 Kgs. Lyngby, Denmark

Abstract

Low-carbon martensitic stainless steels with 11.5 – 16 wt.% Cr, 4 – 8 wt.% Ni and low interstitial content, C < 0.07 wt.% and N < 0.06 wt.% are characterised by their outstanding property combination of high corrosion resistance, strength, ductility and impact toughness, obtained by formation and stabilisation of fine-grained reverted austenite from lath martensite upon annealing in the inter-critical region. This review reflects on the mechanisms that govern the formation and stabilisation of reverted austenite and the early stage of austenite reversion close to A_1 with focus on the role of residual stresses in martensite. The review is assisted by the computation of phase equilibria. Literature data on Cr and Ni concentrations of the reverted austenite/martensite dual-phase microstructure are assessed with respect to predicted concentrations obtained from phase equilibria. Reasonable agreement was found for concentrations in martensite. Systematic excess of Cr in austenite of approx. 2 wt.% relative to calculations was suspected to originate from the growth of $M_{23}C_6$ with a coherent interface to austenite. Within large scatter, measured values of Ni in austenite were on average 2 wt.% below predictions. Complex equilibration of the microstructure and experimental error are discussed as possible origins of the discrepancies.

* Published work: F. Niessen, Austenite reversion in low-carbon martensitic stainless steels – a CALPHAD-assisted review, Mater. Sci. Technol. (2018) doi: 10.1080/02670836.2018.1449179. The format of the published article was adapted to the format of the doctoral thesis.

17.1 Introduction

Low-carbon martensitic stainless steels comprise the group of supermartensitic stainless steels, soft martensitic stainless steels and precipitation-hardening versions. While the individual alloy groups are optimised towards different application fields such as weldability, corrosion resistance or hardenability, all contain a nano-lamellar dual-phase microstructure of reverted austenite and tempered martensite through inter-critical annealing, i.e. annealing in the temperature region in which both ferrite and austenite are thermodynamically stable. The obtained "reverted austenite" is distinguished from "retained austenite", i.e. that is untransformed during cooling to room temperature [1]. Stabilisation of reverted austenite against martensite formation occurs primarily by the partitioning of austenite stabilising elements during diffusional reversion. The resulting fine-grained dual-phase microstructure lowers the yield strength, ultimate tensile strength and hardness, while ductility and impact toughness are significantly enhanced [2–4].

The mechanisms leading to the reversion of austenite and the analysis of the stability of reverted austenite against martensite formation to thermal or mechanical treatments are the subject of numerous research articles published within the last decades. Newly emerging experimental and modeling methods enabled the progressive transition from a processing-property based approach to a microstructure-property based understanding of these materials. It therefore appears timely to review the present understanding of the reverse martensite-to-austenite phase transformation. As the title suggests, this review includes phase equilibrium calculations (so called CALPHAD approach) to support the discussion.

The microstructure-property based characterization of the alloys in recent years has led to a wealth of quantitative literature data on the partitioning of Ni and Cr after partial reversion of austenite during inter-critical annealing of martensite. As reported data concerns different alloy systems and annealing parameters, and as discussion of the data is generally limited to the scope of the specific work, a collective representation of the data is established here to reveal underlying trends. As austenite reversion during isothermal annealing is accompanied by diffusion, it is of interest to verify whether the experimentally determined concentrations can be predicted by phase equilibria from thermodynamics modelling. Finally, the early stage of austenite reversion close to A_1 and the findings from the analysis of compositional data from literature are critically discussed.

17.1.1 Scope

The present review is limited to low-carbon martensitic stainless steels with 11.5 – 16 wt.% Cr, 4 – 8 wt.% Ni and low interstitial content, C < 0.07 wt.% and N < 0.06 wt.%, for which a fine-grained dual-phase structure of reverted austenite and tempered martensite forms by a diffusional mechanism during inter-critical annealing. In some steels austenite stability is sufficiently high for austenite reversion to occur by a displacive mechanism at temperatures where a diffusion controlled transformation is kinetically suppressed [5,6], which is not

treated in this review. Austenite reversion and stabilisation by a diffusional mechanism is not limited to the alloys discussed here and can also be found in other alloy groups, as for example in medium manganese steels [7,8]. The mechanisms discussed in the present work can readily be transferred to other alloy systems, but that is beyond the scope of this review. The focus of this review lies on phase transformations rather than alloy properties. Only a short section is dedicated to the effect of reverted austenite on microstructure properties, including references for further reading.

17.2 Current view on austenite reversion

17.2.1 Historical aspects and alloy design of low-carbon martensitic stainless steels

These alloys are built on the Fe-Cr-Ni ternary system with additions of Mn, Mo, Si and particularly low contents of the interstitial elements C and N. In 1960, Irvine et al. [9] comprehensively described aspects of designing transformable 12% Cr steels to obtain a strong and corrosion resistant material. A major challenge consisted of finding alloy compositions that could be solution treated without forming δ-ferrite, maintained A_1 above 700 °C during 5 h isothermal tempering to avoid reaustinitisation during tempering, and kept M_s above 200 °C to ensure complete transformation to martensite during cooling [9]. An Fe-0.1C-12Cr-2Ni-1.5Mo-0.3V (wt.%) alloy was found most promising with respect to strength and impact toughness [9] (Table 17.1).

Additional stabilisation of austenite was necessary to maintain a transformable steel when increasing the Cr content for enhanced corrosion performance. As further addition of C, one of the most effective austenite stabilising elements, would lead to $M_{23}C_6$ precipitation and thus deplete Cr, other substitutional solutes needed to be considered instead [10]. Ni proved to be the most effective element, and substitution of C with Ni further led to a useful softening of virgin martensite, which manifests as increased impact toughness [10–12].

Following this paradigm, the Swedish steel manufacturers Bofors and Avesta reduced the C content to 0.06 wt.% to develop soft martensitic stainless steels with good corrosion resistance, high strength and high impact toughness for pressure vessel applications in the mid 60's of the last century [3,13–15] (Table 17.1). These steels contained small amounts of retained austenite and formed reverted austenite upon inter-critical annealing. Precipitation-hardening steels are designed with a similar base alloy composition, but solutes such as Cu, Mo and Nb enable precipitation hardening [4,16,17].

Further advances in steelmaking enabled the development of modern supermartensitic stainless steels in the 90's of the last century, which generally consist of 10.5 – 13.5 wt.% of Cr to enable passivation, very low C content (preferably <0.01 wt.%) to enhance weldability and impact toughness, around 4 – 6 wt.% Ni to enable martensite formation, and increased Mo content (0.5 – 2.5 wt.%) to enhance resistance to localised corrosion and sulphide stress cracking [10–12,18–20] (c.f. overview in Table 17.1).

Table 17.1: Overview of typical alloy compositions and average mechanical properties of soft martensitic and supermartensitic stainless steels for specified annealing treatments with reference to conventional martensitic stainless steel; YS: Yield strength, UTS: Ultimate tensile strength, A: elongation until rupture, K_V^{RT}: Charpy-V impact toughness at room temperature.

Alloy designation	*Reference*	*Composition* [wt.%]	*Annealing treatment* T[°C] / t[h]	*YS* [MPa]	*UTS* [MPa]	*A* [%]	K_V^{RT} $[\frac{J}{cm^2}]$
Conventional martensitic stainless steel							
generic	Irvine et al., 1960 [9]	Fe-0.1C-12Cr-2Ni-1.5Mo-0.3V	650 / 1	670	860	19	≥ 68
Soft martensitic stainless steels							
Bofors 2RMO	Grounes and Rao, 1969 [3]	Fe-0.06C-13Cr-6Ni-1.5Mo-0.6Mn-0.4Si	590	≥ 620	≥ 830	≥ 15	105
Avesta 248SV	Grounes and Rao, 1969 [3]	Fe-0.035C-16Cr-5Ni-1Mo-0.8Mn-0.5Si	580	≥ 620	≥ 830	≥ 15	132
EN 1.4405 (cast alloy)	Niederau, 1982 [2]	Fe-<0.07C-16Cr-5Ni-1.5Mo-<1Mn-<1Si	580	650	900	≥ 17	105
EN 1.4418	Dawood et al., 2004 [21,22]	Fe-0.05C-15.5Cr-5.6Ni-0.76Mo-0.4Mn-0.4Si	625 / 4	690	880	10	260
Supermartensitic stainless steels							
13CrS (UNS S41525)	Kondo et al., 1999 [10,23]	Fe-0.01C-12Cr-6Ni-2.5Mo-Ti	850 / 0.5 + 630 / 1	≥ 550	≥ 750	/	290
Vítkovice, generic	Tvrdy et al., 2002 [24]	Fe-0.017C-13Cr-6.2Ni-2.4Mo-0.6Mn-0.3Si	600 / 6	540	870	19	185
Industeel, generic	Toussaint and Dufrane, 2002 [25]	Fe-0.008C-11.8Cr-4.8Ni-1.5Mo-1.9Mn-0.2Si-0.5Cu	625	600 - 650	880 - 900	25	195

17.2.2 Solution treatment, martensite formation and tempering of martensite

Before austenite reversion from martensite is obtained by inter-critical annealing, low-carbon martensitic stainless steels are solution treated in the austenite single-phase region to obtain homogeneous austenite as a parent phase for lath martensite. Some alloys contain micro- alloying elements, such as Ti, Nb or V, to form carbides and nitrides that pin the austenite grain boundaries during solution treatment to limit grain growth [18,26]. Austenite transforms to martensite during cooling over a narrow transformation range, with martensite formation starting at a relatively low temperature ($M_s \approx 260 - 130$ °C) and

finishing just above [27–32], or in exceptional cases even below [2,33], room temperature. Martensite forms with less than ~ 2 ° deviation [34] from a Kurdjumow-Sachs orientation relationship with austenite, $(111)_\gamma \parallel (011)_{\alpha'}, [10\bar{1}]_\gamma \parallel [1\bar{1}1]_{\alpha'}$ [35]. Even though the exact nature of the interface associated with the orientation relationship is still subject of current research [36,37], it has to be semi-coherent, consisting of periodic steps with coherent patches [38,39]. The low-carbon martensitic stainless steels have a high hardenability and are insensitive to the applied quenching rate [4,11,25]. Recent work showed that, as a consequence of the low M_S temperature and interstitial content, no interstitial segregation by auto-tempering or 6 months of room temperature aging was observed [40,41]. In contrast, clustering of carbon at room temperature was reported in Ref. [42], without specifying the aging time. Martensitic transformation leads to transformation strains, which may be partially accommodated by retained austenite. During the transformation, martensite initially experiences high tensile stress, which then gradually decreases towards the end of the transformation (down to ~ 40 MPa), while retained austenite experiences significant compressive stress towards the end of the transformation (up to ~ -900 MPa) [43].

Lath martensite shows very high dislocation densities, similar to heavily cold-worked alloys [44]. Quantitative studies on dislocation densities revealed ~ $4x10^{15}$ m^{-2} in an Fe-0.03C-15.5Cr-5Ni (wt.%) precipitation hardening steel [45] and ~ $7x10^{14}$ m^{-2} in an Fe-0.04C-15.5Cr-5Ni (wt.%) soft martensitic stainless steel [46] in as-quenched conditions.

When the dislocation-rich microstructure is reheated to the inter-critical region, C and N partition from solid solution and diffuse to lattice defects in order to minimize local strain fields [40,41]. Because of the low interstitial content, no transition carbides are formed during the tempering of martensite [16,40,47]. Tempering of Mo-containing steels at 400 °C [16] and Cu-containing steels at 450 to 480 °C [29,48–51] leads to secondary hardening by precipitation of Mo_2C and Cu precipitates, respectively. Generally, the kinetics and magnitude of secondary hardening in specific alloys is sensitive to the amount of available interstitial elements and the content of precipitate forming substitutional alloying elements. During further heating, concurrent recovery of the martensite matrix and austenite reversion at grain boundaries commence at approx. 500 to 550 °C [40,46,52], leading to a reduction in dislocation density by approx. an order of magnitude [46].

17.2.3 Nucleation and growth close to A_1

A_1, i.e. the ferrite-to-austenite (α-to-γ) phase transition temperature in thermodynamic equilibrium, may conventionally be obtained from thermodynamics modelling. In the present system, the prediction of extensive partitioning of solute in austenite and ferrite at low temperature leads to a small fraction of stable austenite in thermodynamic equilibrium.

In reality, an alloy undergoes martensite formation during cooling, such that austenite forms from an approximately homogeneous distribution of solute during reheating,

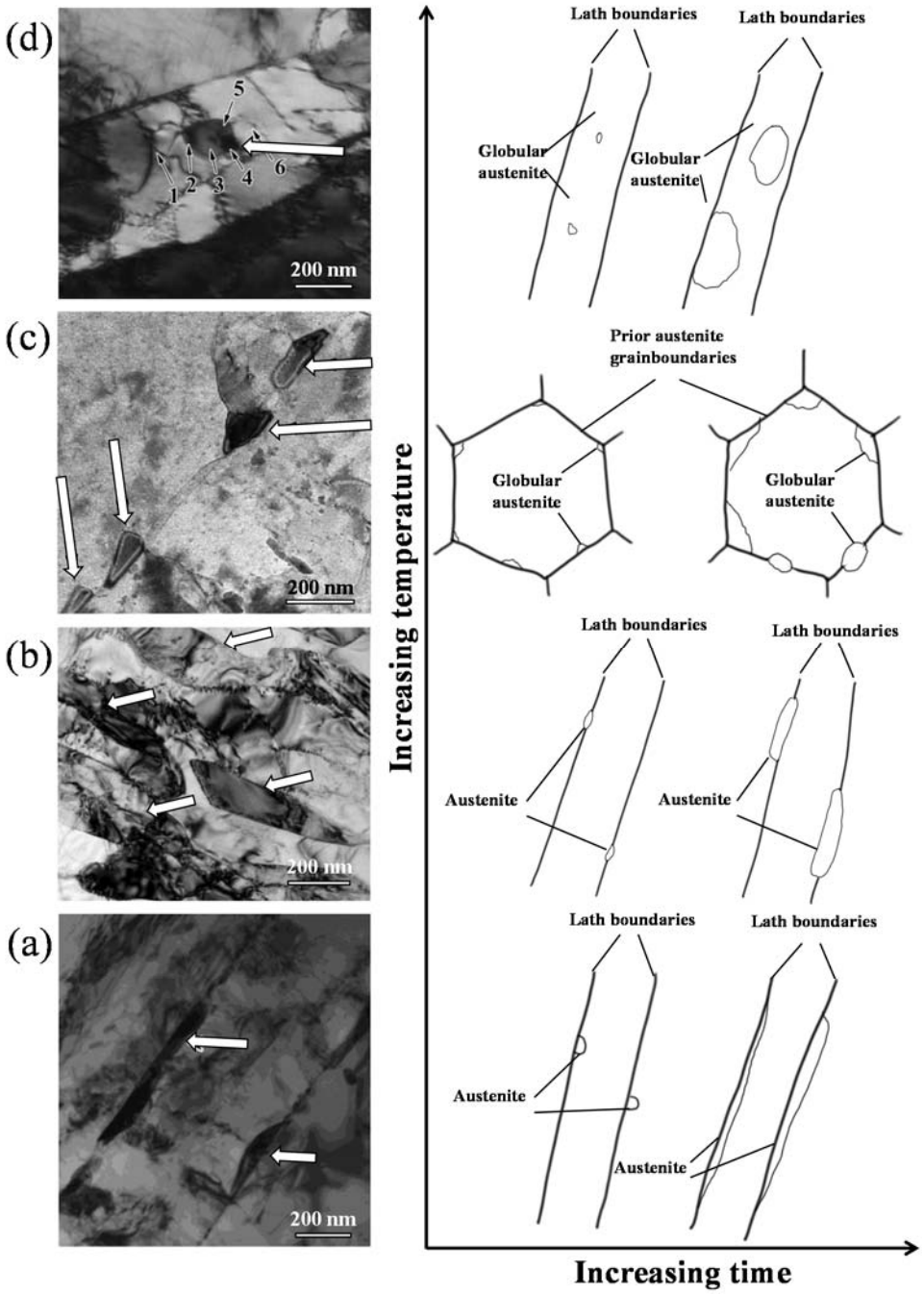

Figure 17.1: Bright-field micrographs and schematics of the evolution of the reverted austenite morphology with temperature and time in low-C martensitic stainless steels: (a) low temperature film morphology (Ref. [64]); (b) elevated temperature film morphology (Ref.[63]) ; (c) globular morphology at prior austenite grain boundaries (Ref. [1]); (d) globular morphology inside martensite laths (Ref. [59]); reverted austenite is marked with white arrows in the micrographs; Permissions for the use of figures from literature are automatically granted according to the STM signatory guidelines.

rendering the prediction of A_1 from thermodynamic equilibrium unfeasible. A_{c1}, the experimentally determined α-to-γ transition temperature during heating, is on the other hand strongly dependent on the heating rate [9,27,53,54] and thus not an explicit quantity. In the present case the phase transition temperatures A_1 and A_3 therefore refer to the phase transition temperatures obtained during very slow heating ($\leq 0.017\ \mathrm{K.s^{-1}}$). Sufficiently fast heating (approx. >10 K s^{-1} [55,56]) does not allow enough time for long-range diffusion and thus leads to transformation by a displacive mechanism instead.

Close to A_1 (composition dependent at ~ 500 – 550 °C) allotriomorphic reverted austenite with film morphology forms at lath boundaries [56–61] with little or no deviation from the Kurdjumow-Sachs orientation relationship [35,62,63]. All reported micrographs of annealed microstructures in the temperature range 500 to 575 °C (c.f. reference list in Table 17.2) reveal that austenite grows from the lath boundary into only one of the laths (Figure 17.1a) [1,56,61,64]. Above this temperature, austenite films begin to grow into both laths adjacent to a lath boundary (Figure 17.1b) [56,59,61]. In the case of pre-existing inter-lath retained austenite, immediate growth from retained austenite occurs, as no nucleation is required [60]. For the film morphology, austenite memory, i.e. the tendency of reverted austenite to form in the orientation of the prior austenite grain, is commonly observed [27,60,65]. Further, reverted austenite has been reported to form cooperatively with M23C6 carbides with a cube-cube orientation relationship, $\{100\}_\gamma \parallel \{100\}_{M_{23}C_6}, \langle 001\rangle_\gamma \parallel \langle 001\rangle_{M_{23}C_6}$ [33,42,59,61,66]. According to thermodynamic equilibrium, growth of austenite requires an inward-flux of Ni and outward-flux of Cr [27] (Figure 17.2), while growth of M23C6 requires the opposite fluxes. Cooperative growth should thus be facilitated by a gradient in chemical potential and a resulting net flux of Ni and Cr across the interface. It was shown experimentally that M23C6 can bind sufficient carbon to leave austenite and martensite virtually carbon free [42,67,68].

Figure 17.2 shows the equilibrium austenite fraction and Cr and Ni concentrations in austenite and ferrite as a function of temperature for a simple Fe-Cr-Ni system with average Ni and Cr concentrations of the analysed literature data in section 17.3 (c.f. Table 17.2). At low temperature, enhanced partitioning of Ni is required to form austenite which, together with slow substitutional diffusion kinetics, significantly limits the kinetics of austenite reversion [27,63,69]. Nevertheless, the kinetics of austenite reversion at low temperature were measured to be significantly faster than predicted by modelling of bulk-diffusion, suggesting that grain boundary diffusion and diffusion along dislocations may be important mechanisms that significantly increase the transformation kinetics at these temperatures [27,33,69].

17.2.4 Nucleation and growth towards A_3

At elevated temperature, typically 600 – 700 °C, reverted austenite tends towards a globular morphology, first at prior austenite grain boundaries (Figure 17.1c) [57,58,60] and at higher temperature within martensite laths (Figure 17.1d) [56,61,71]. The reversion kinetics are

significantly faster, mainly because of lower required partitioning of Ni (Figure 17.2), accelerated diffusion kinetics and increased prominence of bulk diffusion. Further, the increased driving force for austenite formation in this temperature range renders also incoherent interfaces [57] or the formation of new interfaces energetically favourable [56,61,71], manifested as more nucleation sites. It was found that in an Fe-0.05C-12Cr-4Ni-0.5Mo (wt.%) steel austenite reversion occurred without diffusion during isothermal annealing above 680 °C [68]. Upon further heating grain growth and dissolution of $M_{23}C_6$ carbides continue towards a fully austenitic microstructure, which was reported to recrystallize spontaneously at 900 °C when heating with 0.17 $K.s^{-1}$, 70 °C above A_{c3} [58].

17.2.5 Stability of reverted austenite against martensite formation

Reverted austenite that is formed close to A_1 is generally more stable against martensite formation upon cooling (or deformation) as compared to reverted austenite formed at higher temperature. There is a consensus that Ni-enrichment in austenite decreases with increasing annealing temperature [27,29,31,42,56,60,63,64,66–69,72–75], which is in qualitative agreement with the concentrations from thermodynamic equilibrium in Figure 17.2. The Ni concentration determines mainly the stability of reverted austenite against martensite formation, as more Ni reduces M_s. However, the compositional effect is considered insufficient to explain the stability of reverted austenite alone [42,73]. The increase in grain size [64,66,76,77], the transition to a more globular grain morphology [64,66] and softening of the surrounding martensitic matrix [22,66] with increasing annealing temperature are anticipated to reduce the contribution of strain energy to the critical driving force for martensite nucleation [78], i.e. the stability of austenite. Findings by Zhang et al. [66] are particularly supportive of this mechanism, as inter-critical annealing at 620 °C was found to lead to higher fractions of reverted austenite with annealing time up to a maximum value, after which the fraction decreased again on further

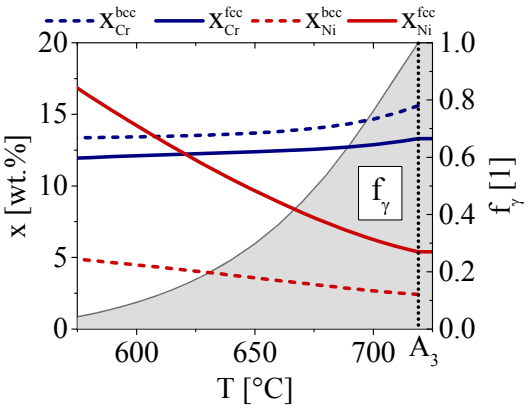

Figure 17.2: Ni and Cr concentration (x) in austenite (fcc) and ferrite (bcc) as well as the molar fraction of austenite (f_γ, grey area) from an equilibrium calculation of a representative Fe-13.3Cr-5.4Ni (wt.%) ternary alloy. Partitioning of Ni increases with lower austenite fraction and temperature. (Allowed phases: liquid, fcc, bcc; software and thermodynamics database: Thermo-Calc 2017a - TCFE6 [70])

annealing. Even though the phase fraction of austenite approached equilibrium content, compositional equilibration (partitioning), carbide growth, recovery of martensite and spheroidization of austenite continue [66,67], which may affect the stability of reverted austenite.

Bilmes et al. [73] claimed that also a high dislocation density in reverted austenite could contribute to the stability of reverted austenite. This finding is doubtful, as the high dislocation density was identified by the dark appearance of austenite in a bright-field micrograph, which is generally indicative of an orientation contrast when using an objective aperture rather than the presence of dislocations [79]. Further, reverted austenite developed under continued diffusion is known to have low dislocation density [33,80], as opposed to reverted austenite formed by a displacive mechanism [6].

Reverted austenite either remains stable upon cooling, or transforms partially or completely to martensite [30,46,63]. Reverted austenite was reported to even have remained stable after sub-zero treatment at boiling N_2 [2,73,75] and boiling He temperatures [42]. It is critically remarked that martensite formation in lath martensite, especially at sub-zero Celsius temperatures, is time-dependent, i.e. thermally activated, and kinetically suppressed at very low temperature. Transformation generally occurs in the temperature range -150 °C to room temperature, which means that in the referenced cases [2,42,73,75] martensite formation may be fully suppressed if cooling to, or heating from, boiling N_2 temperature is performed sufficiently fast to suppress the thermally activated phenomena that control the rate of the austenite-to-martensite transformation in steel [81]. In a single case it was claimed that the fraction of austenite increases by applying sub-zero treatment [58], which is in obvious conflict with all above referenced observations.

Reverted austenite may also transform to martensite by strain-induced transformation and in this way enhances the plastic regime [46,72,73,82]. This mechanism known as transformation induced plasticity, has not been treated in depth in low-carbon martensitic stainless steels, but advanced in-situ experiments and modelling of strain-induced martensite formation have been performed in other variations of steels [83–89].

17.2.6 Effect of reverted austenite on microstructure properties

The effect of reverted austenite on the microstructure properties of low-carbon martensitic stainless steels is a broad topic and a proper treatment would exceed the scope of this review. A more detailed overview on the mechanical and corrosion properties of the alloys can be obtained from Refs. [4,11,21,90] and [11,91,92], respectively. Nevertheless, a short summary of the mechanical properties appears necessary to realize the significant property changes induced by formation of reverted austenite.

As an example, Figure 17.3 shows the mechanical properties of an Fe-16Cr-5Ni-1Mo (wt.%) soft martensitic stainless steel (EN 1.4418) at room temperature after 4 h soaking at various temperatures, adapted from Refs. [21,22]. At first the ultimate tensile

strength, the 0.2 % yield strength and the hardness increase by heat-treating up to 475 °C, which is an effect of secondary hardening from precipitation of Mo_2C. Then softening occurs up to 625 °C, mainly due to austenite reversion and recovery of martensite. A new increase in ultimate tensile strength, 0.2 % yield strength and hardness is observed upon heat treatment at 700 °C and above, originating from transformation of reverted austenite to fresh martensite and precipitation of $M_{23}C_6$ carbides. The elongation and impact toughness develop in inverse relation to the ultimate tensile strength, 0.2 % yield strength and hardness with soaking temperature, i.e. are enhanced by reverted austenite formation and recovery of martensite.

In the presence of reverted austenite, soft martensitic and supermartensitic stainless steels show remarkable impact toughness also at sub-zero Celsius temperature (> 100 J at -80 °C [11]). Solheim et al. [93] showed that reverted austenite increased the solubility of hydrogen in supermartensitic stainless steel samples dramatically, and that the ductility of such samples was greatly reduced, suggesting that reverted austenite plays an important role in hydrogen embrittlement.

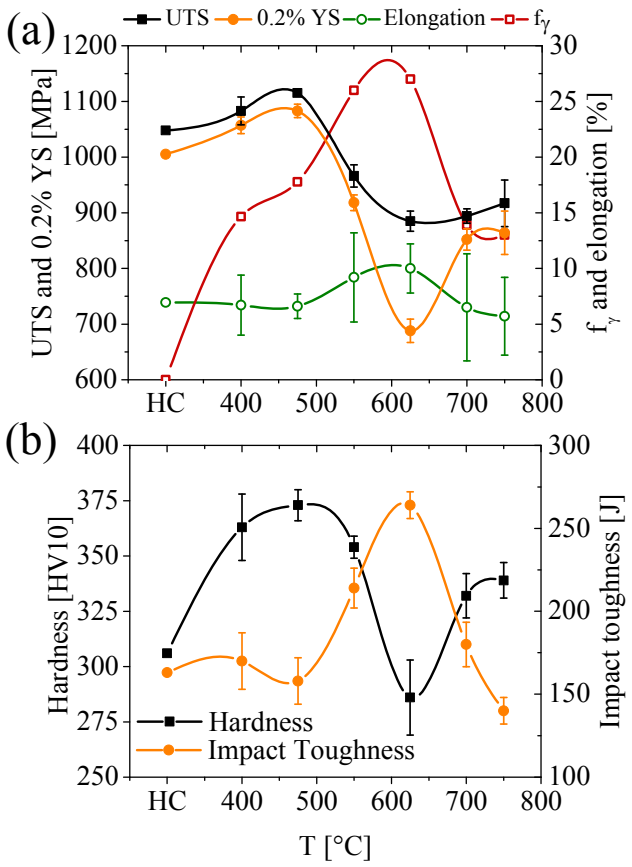

Figure 17.3: Fraction austenite and mechanical properties of a 16Cr-5Ni-1Mo stainless steel at room temperature in the hardened condition (HC) and after 4 h soaking at various temperatures: (a) Ultimate tensile strength (UTS), 0.2% yield strength (YS), elongation and fraction austenite (f_γ); (b) Hardness and Charpy V impact toughness; The lines are spline functions of measured data (symbols) and do not represent physical values (adapted from Dawood et al. [21,22]).

17.3 Critical assessment of compositional data from literature

All considered references on experimentally determined Cr and Ni contents of partitioning in reverted austenite and tempered martensite are sorted in order of ascending annealing temperature in Table 17.2. Moreover the sample preparation methods and measurement methods, Energy-dispersive X-ray spectroscopy (EDS) in (scanning) transmission electron microscopy ([S]TEM) and atom probe tomography (APT), are indicated. together with the respective measurement and sample preparation methods. The reported annealing parameters and alloy compositions were used to determine the equilibrium concentrations of Cr and Ni in austenite and ferrite by computing phase equilibria (Thermo-Calc 2017a [94] with TCFE6 database [70]). For this purpose, the alloying elements Cr, Ni, Mo, Mn, Si, Cu, C and N and the phases fcc, bcc, cementite, M_6C, M_7C_3 and $M_{23}C_6$ were taken into account, representing the most common elements and phases reported in literature [95].

Figure 17.4 gives reported Ni and Cr concentrations in tempered martensite (a and c) and reverted austenite (b and d) compared with the respective concentrations from computed phase equilibria. Short proximity of data points to the diagonal line indicates good agreement of the measured concentrations with values reflecting thermodynamic equilibrium for the alloy under consideration. Even though different levels of agreement are obtained for different components and phases, experimental data generally seems to agree with calculations from thermodynamics modelling. This supports that austenite reversion occurs mainly by a diffusional mechanism, as potential large strain energies from a displacive transformation are not reflected in the applied thermodynamics model. In tempered martensite, apart from few outliers, both the reported Ni and Cr concentrations are in reasonable agreement with predictions from thermodynamics modelling (Figure 17.4a and c, respectively). In austenite, apart from a single measurement, all reported Cr concentrations exceed the concentrations for thermodynamic equilibrium (Figure 17.4d). The reported Ni concentrations of reverted austenite show poor agreement with calculated thermodynamic equilibrium values (Figure 17.4b). In the latter case, data from APT appeared to agree more convincingly with data from thermodynamic equilibria compared to data from (S)TEM-EDS. Within significant scatter a trend is discernible: Predicted concentrations of Ni in austenite by thermodynamics modelling are approx. 2 wt.% higher than measured concentrations.

As the prediction of the Ni concentration in austenite is most relevant for the stability of austenite, the origin of the discrepancy between experimental and predicted Ni content should be investigated. The martensite to austenite phase transformation can be (partly) interface-controlled or local equilibrium may be affected by factors as residual stresses, interfacial segregation and precipitation of carbides. Then the Cr and Ni concentrations can vary with time before the condition of (local) equilibrium is obtained. In order to investigate, whether the discrepancy between Ni concentrations from phase equilibria and measurements decreases with approaching equilibration, a criterion was

Table 17.2: Overview of literature data, x_{meas}, on measured Ni and Cr concentrations after partitioning in austenite (fcc) and martensite (bcc) compared with data from phase equilibria, x_{equ}. The annealing temperature, T, the annealing time, t, the equilibration factor, k_{equ}, the experimental method and the sample preparation method are given; EP: Electro-Polishing; FIB: Focused Ion Beam

Label	Ref	$x_{equ}^{fcc.Ni}$	$x_{equ}^{fcc.Cr}$	$x_{equ}^{bcc.Ni}$	$x_{equ}^{bcc.Cr}$	$x_{meas}^{fcc.Ni}$	$x_{meas}^{fcc.Cr}$	$x_{meas}^{bcc.Ni}$	$x_{meas}^{bcc.Cr}$	T	t	k_{equ}	Methods	
		[wt.%]								[°C]	[h]		Exp.	Prep.
Yuan Gong Sun et al. 2016 A	[61]	24.5	11.0	3.8	15.8	9.6	/	3.8	/	500	4	0.00	TEM-EDS	EP
Lee Shin Leem et al. 2003 A	[56]	16.5	11.1	5.0	13.7	11.0	14.0	/	/	575	2	0.02	TEM-EDS	EP
Schnitzer Radis Nöhrer et al. 2010 A	[1]	16.3	11.5	4.5	13.1	16.8	13.1	4.0	12.5	575	10	0.09	APT	EP
Schnitzer Radis Nöhrer et al. 2010 B	[1]	16.3	11.5	4.5	13.1	14.0	12.7	3.4	12.3	575	100	0.87	APT	EP
Schnitzer Radis Nöhrer et al. 2010 C	[1]	16.3	11.5	4.5	13.1	14.4	13.9	/	/	575	10	0.09	TEM-EDS	EP
Schnitzer Radis Nöhrer et al. 2010 D	[1]	16.3	11.5	4.5	13.1	14.3	13.1	/	/	575	100	0.87	TEM-EDS	EP
Song Li Rong et al. 2010	[59]	12.9	11.4	3.3	12.1	9.0	13.0	3.5	11.3	580	2	0.02	TEM-EDS	EP
Song Li Rong et al. 2011	[68]	12.9	11.4	3.3	12.1	13.0	13.0	3.0	6.3	590	0.5	0.01	APT	?
Bilmes Solari Llorente 2001	[73]	12.1	11.2	3.5	12.1	8.3	13.7	/	/	600	2	0.09	TEM-EDS	EP
Song Ping Yin et al. 2010	[42]	11.9	10.7	3.3	11.3	13.3	11.8	3.0	7.5	600	4	0.17	APT	EP
Ye Li Jiang et al. 2012	[105]	13.0	12.9	3.7	16.3	11.9	14.7	4.7	17.0	600	2	0.09	TEM-EDS	EP
Yuan Gong Sun et al. 2016 B	[61]	12.6	13.7	3.5	15.9	11.0	/	4.1	/	600	4	0.17	TEM-EDS	EP
Song Li Rong et al. 2014	[64]	10.8	11.7	3.2	12.1	6.1	15.7	/	/	610	2	0.16	STEM-EDS	EP
Zhang Wang Li et al. 2015	[66]	9.7	12.5	3.1	13.0	10.0	13.3	2.7	11.3	620	6	0.92	TEM-EDS	EP
Wang Lu Li et al. 2008	[80]	11.1	10.9	3.4	11.8	6.9	/	4.2	/	620	0.25	0.01	TEM-EDS	?
Lee Shin Leem et al. 2003 B	[56]	11.7	12.1	4.3	14.0	8.5	15.5	/	/	625	2	0.42	TEM-EDS	EP
Liu Yang Zhang 2013	[60]	10.5	11.7	3.2	12.8	8.9	/	/	/	625	2	0.42	TEM-EDS	EP
Escobar Poplawsky Faria et al. 2017 A	[67]	10.8	11.3	3.3	12.3	11.6	10.3	3.6	10.9	625	2.5	0.53	STEM-EDS	FIB
Escobar Poplawsky Faria et al. 2017 B	[67]	10.8	11.3	3.3	12.3	9.7	11.5	3.5	11.6	625	2.5	0.53	APT	FIB
Wang Xiao Lu et al. 2013	[72]	8.6	12.3	2.8	12.7	11.6	/	2.5	/	630	2	0.58	TEM-EDS	EP
Nakada Tsuchiyama Takaki et al. 2007	[65]	10.6	12.2	0.4	13.4	9.2	/	/	/	640	0.5	0.27	TEM-EDS	?
Yuan Gong Sun et al. 2016 C	[61]	8.7	13.7	3.1	16.4	7.5	/	4.2	/	650	4	4.16	TEM-EDS	EP
Jiang Zhao Ye et al. 2013	[106]	9.0	13.5	3.0	16.9	7.1	15.3	2.1	17.1	650	2	2.08	TEM-EDS	EP
Jiang Ye Li et al. 2014	[74]	9.1	13.6	3.0	17.2	11.7	15.0	3.0	20.1	650	2	2.08	TEM-EDS	?
Niessen Grumsen Hald et al. 2017	[63]	8.2	13.7	2.9	16.2	8.0	16.0	3.0	16.0	650	2	2.08	STEM-EDS	EP
Lee Shin Leem et al. 2003 C	[56]	8.5	12.7	3.7	14.6	7.5	14.0	/	/	675	2	10.26	TEM-EDS	EP
De Sanctis Lovicu Valentini et al. 2015	[33]	6.6	13.7	2.6	16.0	6.7	16.9	4.2	16.8	680	1	7.06	TEM-EDS	EP

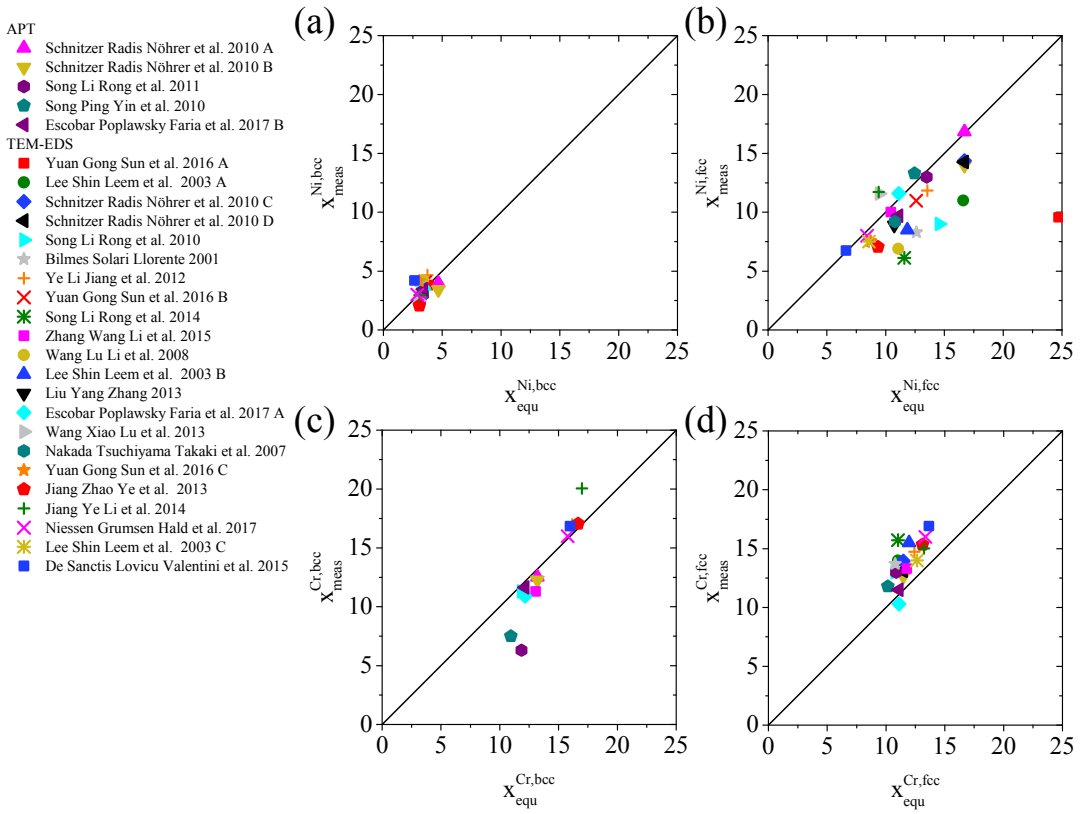

Figure 17.4. Comparison of the Ni and Cr concentrations in tempered martensite (a and c), and reverted austenite (b and d) from EDS and APT analysis, x_{meas}, with data from thermodynamics modelling, x_{equ}, under input of the respective alloy compositions and annealing temperatures; the legend is sorted in order of ascending annealing temperature.

established to filter the literature data accordingly (Figure 17.5). For this purpose, the kinetics of forming reverted austenite from a 200 nm wide martensite lath of an Fe-13.3Cr-5.4Ni alloy (c.f. Figure 17.2) by bulk-diffusion at temperatures between 600 and 700 °C were assessed in steps of 25 °C by kinetics modelling of diffusion with DICTRA [96] (see Ref. [27] for further details on the kinetics model). Kinetics modelling assumes purely diffusion controlled martensite-to-austenite transformation and local equilibrium at the martensite/austenite interface [97]. While these assumptions, as discussed above, may not be entirely justified in the present case, kinetics modelling should reliably reflect the general kinetics of austenite reversion in low-carbon martensitic stainless steels at different temperatures to establish a qualitative criterion.

The transformation kinetics in Figure 17.5a reveals that the time to reach 95 % of the equilibrium fraction ($t_{0.95}$) increases from 0.2 h at 700 °C to > 100 h at 600 °C (see open symbols in Figure 17.5a and the temperature dependence in Figure 17.5b). The dependence of $t_{0.95}$ on the annealing temperature follows an exponential decay function (Figure 17.5b):

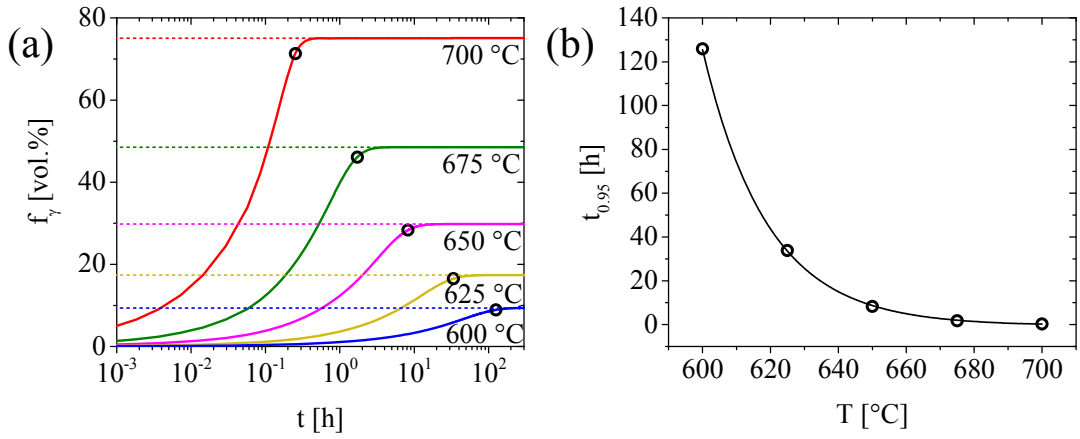

Figure 17.5: (a) Kinetics of austenite reversion from kinetics modelling of diffusion of a Fe-13.3Cr-5.4Ni (wt.%) steel (c.f. Figure 17.2). The broken lines indicate the austenite fractions in equilibrium at the respective temperatures and the open symbols indicate $t_{0.95}$, the time at which 95 % of the equilibrium phase fraction is formed; (b) Fit of $t_{0.95}$ as a function of temperature by an exponential decay function, which is the foundation to assess equilibration of the evaluated heat treatments by the equilibration factor $k_{equ}(T, t)$.

$$t_{0.95} = A \exp\left(\frac{T_0 - T}{b}\right) + c \; [h] \tag{17.1}$$

with A = 126 h, T_0 = 600 °C, b = 19.1 °C and c = -0.5 h.

Comparing the time $t_{0.95}$ at reported temperatures with the respective reported annealing times from literature, a factor $k_{equ} = t / t_{0.95}$ is obtained to qualitatively estimate the amount of equilibration for each data point Table 17.2). Figure 17.6 shows the difference of the measured concentrations with respect to concentrations from thermodynamic equilibrium, ε, in austenite as a function of the equilibration factor k_{equ}. Clearly, the difference between the measured and calculated Ni concentration decreases with increasing equilibration (higher k_{equ}), while a similar trend, if present at all, is less obvious for Cr. Figure 17.7 shows the data from Figure 17.4 after filtering with the equilibration criterion $k_{equ} > 0.1$. As expected from Figure 17.6b, the scatter of the Ni concentration in reverted austenite is reduced, such that the experimental data and data from thermodynamics modelling show reasonable agreement (Figure 17.7b). Filtering of the data on the Cr concentration in reverted austenite reduces the scatter to a small extent and further confirms that the Cr concentration in reverted austenite is systematically measured to be 1.0 – 3.5 wt.% higher than predicted by equilibrium thermodynamics (Figure 17.7d).

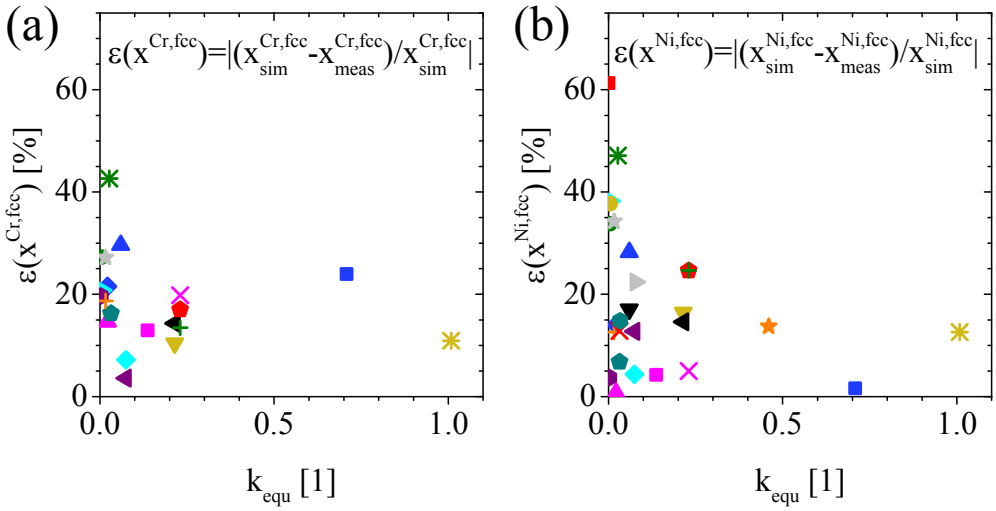

Figure 17.6: Difference of measured concentrations with respect to concentrations from thermodynamic equilibrium, ε, as a function of the equilibration factor k_{equ} (Figure 17.5b) of the (a) Cr and (b) Ni concentration in reverted austenite. The symbols correspond to the legend in Figure 17.4.

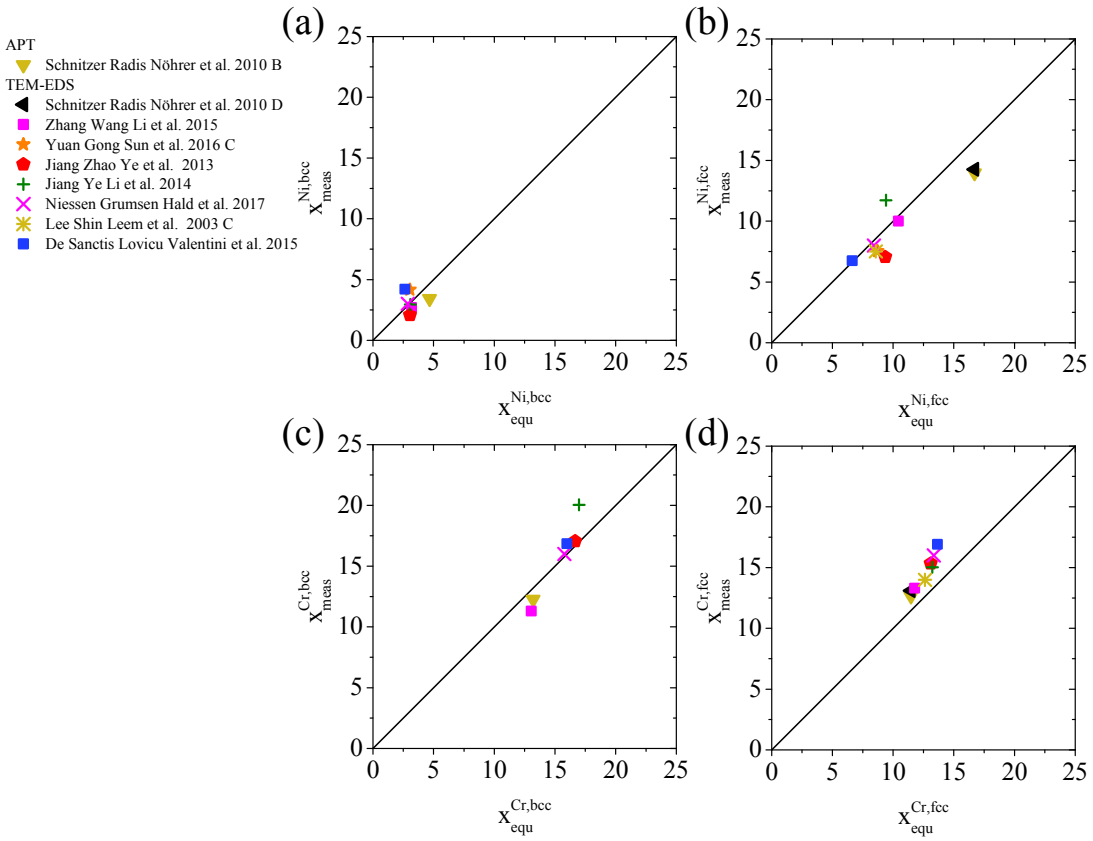

Figure 17.7: Comparison of the Ni and Cr concentrations in tempered martensite (a and c), and reverted austenite (b and d) with data from thermodynamics modelling from Figure 17.4 for data with an equilibration factor of $k_{equ} > 0.1$.

17.4 Discussion

17.4.1 Early stage of reverted austenite formation close to A_1

Microstructure characterization of the initial stage of reverted austenite formation is difficult to conduct and of more fundamental interest. So far, only limited studies have been conducted on the early stage of austenite formation, while the mechanisms during growth in different temperature regimes are fairly well established. Nevertheless, by studying related alloy systems and carefully interpreting related mechanisms, such as martensite formation and austenite memory, an understanding of the early stage of austenite formation can be acquired from the existing literature.

Raabe et al. [8] observed segregation of Mn up to 24 at.% at lath boundaries prior to formation of reverted austenite on tempering an Fe-9Mn (at.%) maraging alloy at 450 °C. The experimentally observed grain boundary enrichment factors, which relate the bulk concentration of an element to the concentration at the grain boundary, were found similar for Mn and Ni [8]. Thus, Ni is likely to segregate to lath boundaries in low-carbon martensitic stainless steel during heating which would locally increase the driving force for austenite formation and thereby aid austenite nucleation. So far, no experimental evidence of such mechanisms has been reported that can corroborate this hypothesis.

Stress plays a fundamental role during martensite formation. It therefore appears unavoidable to consider the role of stress in the reverted transformation to austenite. The previously mentioned austenite memory effect, the strong tendency of reverted austenite to form in an identical crystallographic orientation to the prior austenite grain, gives important insight into the role of stress in the early stage of reverted austenite formation. Nakada et al. [65] suggested that the reverted austenite variants are theoretically limited to two variants within a martensite packet: the prior austenite and a twin-related orientation variant. The variant restriction originates from crystal symmetry and considerations of interfacial energies and was validated with experiments on a supermartensitic stainless steel with no retained austenite. Indeed, only the two predicted variants formed. Interestingly, the twin-related variant made up less than 5 % area fraction of reverted austenite and could be increased to approx. 40 % by applying a tensile stress of 100 MPa during inter-critical annealing. As a consequence, Nakada et al. suggested that also residual stress affects austenite memory in that it favours the prior austenite orientation [65].

Experimental evidence on lattice strains (rotations) in lath martensite was provided by Miyamoto et al. [98] and Sandvik et al. [34], who independently showed that the martensite/austenite interface is relatively straight on one side and irregular on the other side of a lath. This suggests that thickening of the lath mainly progresses towards the irregular side of the interface (Figure 17.8). During martensite formation, retained austenite progressively accommodates the transformation strains in the direction of thickening (Figure 17.8a) and in cases where all austenite is transformed, dislocation networks in

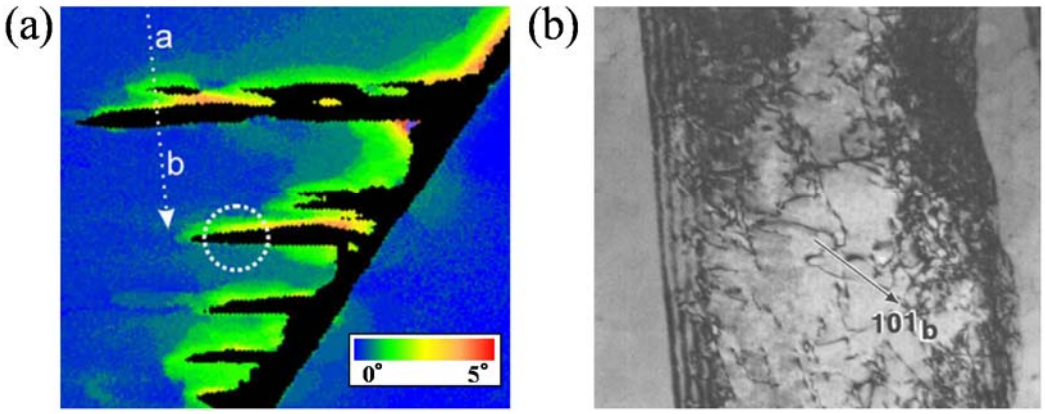

Figure 17.8: Footage from literature indicating thickening of lath martensite to primarily one side; (a) Misorientation map of austenite from electron backscatter diffraction (EBSD) after growth of lath martensite (black) in a Fe-20Ni–5Mn (wt.%) alloy indicating strain accommodation of the transformation strain in austenite in primarily one direction of the lath (Ref. [98], permission was automatically granted according to the STM signatory guidelines.); (b) Example of a martensite lath, showing a relatively straight (left side) and irregular (right side) martensite/austenite interface (Ref. [34], RightsLink license number 4294080199168.).

martensite are required to accommodate the misfit between adjacent, slightly misoriented laths (Figure 17.8b). These observations indicate that the accommodation-strain progressively accumulates with movement of the martensite/austenite interface, which manifests as build-up of residual stress between adjacent laths. Inversely, the formation of reverted austenite, complying with the prior austenite orientation, would aid to release such residual stresses.

Analogous to thickening of martensite laths during martensite formation, nucleation and growth of reverted austenite in film morphology at lath boundaries below 575 °C was found to occur in mainly one direction (Figure 17.1a) [1,56,61,64], while reverted austenite films thickened into both laths of a lath boundary above 575 °C (Figure 17.1b) [56,59,61]. Below 575 °C, it appears as if residual stresses between adjacent martensite laths (Figure 14.1) promote austenite growth with prior-austenite orientation in the reverse direction to martensite formation. It is not anticipated that such transformation is of a displacive nature, but rather that stress fields between laths act as a mechanical driving force that promotes directional diffusional growth with a grain orientation that reduces the overall strain energy. This mechanical driving force may be greatly reduced above 575 °C, when recovery of martensite diminishes residual stresses between laths. Consequently, in a recovered martensite microstructure, austenite may grow in both sides of a lath boundary. Further experimental evidence is required to corroborate this hypothesis.

17.4.2 Discrepancy of data on solute partitioning from equilibrium calculations and literature

While reasonable agreement of concentrations from literature data with concentrations from thermodynamic equilibrium was obtained for Cr and Ni in martensite (ferrite), in austenite systematic and more random discrepancies were found for Cr and Ni, respectively. In the following, possible reasons will be discussed.

At first, it is noted that the calculated thermodynamic equilibria originate from a modelling method, which inherently suffers from uncertainties originating from databases [99] and relies on extrapolation from constituent subsystems to multi-component alloy systems [100,101]. In the present case, further uncertainties are expected from treating all alloys with the same list of phases and components, where in some cases not all components were reported or included. Considering these uncertainties, the observed amount of systematic deviation (approx. 2 wt.% for Cr in martensite) appears too excessive to be introduced by the CALPHAD method or the database. The analysed Fe-Cr-Ni alloy system is amongst the best-described systems in thermodynamics modelling and has proven to provide excellent predictions in previous cases [102–104]. Moreover, it appears difficult to explain the more random deviation of Ni in austenite with potential uncertainties in the CALPHAD method. Therefore other reasons for the observed deviation need consideration.

According to thermodynamic equilibrium, Cr is in all analysed cases supposed to be rejected from austenite and dissolved in carbides and martensite during inter-critical annealing. The difference in concentration between austenite and martensite should in average amount to 2 wt.% (Table 17.2). From 13 experimental datasets on partitioning of Cr in austenite and martensite, only three datasets qualitatively confirm such partitioning [74,105,106], while six datasets show no partitioning within 0.5 wt.% of accuracy [1,33,63,67] and four datasets (all originating from the same research group) even show inverse partitioning, i.e. Cr-enrichment in austenite [42,59,66,68]. Even though these inconsistent observations are difficult to interpret, it appears likely that growth of $M_{23}C_6$ carbides affects the local Cr contents of austenite and martensite. $M_{23}C_6$ carbides share a coherent interface with reverted austenite, which is anticipated to facilitate the diffusion flux of Cr and Ni during diffusion accompanied growth of both phases, as also suggested in Ref. [66].

In contrast to the Cr concentration, the Ni concentration in austenite deviated more randomly from thermodynamic equilibrium (Figure 17.4b). Within large scatter, Ni was in average predicted with 2 wt.% higher concentration than characterized in literature. It appears that two major effects cause the discrepancy: insufficient equilibration of the microstructure and experimental error.

It was found that the Ni concentration in austenite can be predicted with reasonable accuracy by phase equilibria when the microstructure approaches equilibration (higher k_{equ} in Figure 17.6b). Escobar et al. [67] reported that, even when the equilibrium phase

fraction was obtained after annealing for 2.5 h at 625 °C, individual austenite lamellae revealed approx. ± 2 wt.% difference in Ni concentration. Further, gradients of Ni concentration within austenite lamellae in the range of approx. 4 wt.% from interface to bulk were measured with APT. Apparently, the initial composition of reverted austenite is far from equilibrium.

It is noted that martensite itself must be considered as metastable ferrite, as it deviates from ferrite in thermodynamic equilibrium. Nucleation of reverted austenite in equilibrium with martensite (metastable ferrite) may thus occur with different phase compositions as predicted for austenite and ferrite in thermodynamic equilibrium. It is suggested that the phase fractions and compositions of austenite and martensite during continued annealing evolve towards global equilibrium, which appears to be a slow and complex process.

The majority of insufficiently equilibrated microstructures ($k_{equ} < 0.1$) were obtained from annealing below 650 °C. As partitioning of Ni increases with lower temperature (Figure 17.2), sharp compositional measurements over thin austenite films (40 – 150 nm width) and tempered martensite become more challenging. Figure 17.4 reveals that measurements from APT matched the predictions from thermodynamic equilibrium more convincingly than measurements from (S)TEM-EDS. As the spatial resolution (near atomic) and compositional resolution (few ppm) of APT are by far superior to that of standard (S)TEM-EDS [107], this observation appears reasonable. (S)TEM-EDS faces the inherent issue of insufficient counting rate when samples are too thin, leading to insufficient compositional accuracy when applying low counting times and contamination and beam drift when applying high counting times [108]. Increasing the sample thickness on the other hand reduces the spatial resolution and complicates measurement of a sharp austenite/martensite interface. Reliable measurements of fine-grained and partitioned microstructures are certainly possible (good agreement with data from APT was for instance obtained in Refs. [1,67]), but several potential error sources render data from EDS generally less trustworthy. The lower experimentally determined Ni-concentrations, especially at lower temperature, may therefore to a certain extent originate from a higher experimental error of (S)TEM-EDS measurements.

17.5 Conclusions

The mechanism of austenite reversion in low-carbon martensitic stainless steels was critically reviewed by collating literature on nucleation and growth, stability against martensite formation and the effect on microstructure properties of reverted austenite. Discussion of the morphology of austenite films close to A_1 in the light of austenite memory and the mechanism of martensite formation led to suggest that residual stresses from the martensite microstructure aid nucleation of reverted austenite close to A_1. It was further investigated whether literature data on the Ni and Cr concentrations in austenite and martensite after inter-critical annealing comply with thermodynamic equilibrium from

thermodynamics modelling. In martensite, measured Cr and Ni concentrations matched predictions from thermodynamics modelling with reasonable accuracy. Systematic excess of Cr in austenite by approx. 2 wt.% relative to predictions was suspected to originate from growth of $M_{23}C_6$ with a coherent interface to austenite. Within large scatter, measured values of Ni in austenite were in average 2 wt.% below predictions from thermodynamics modelling. The scatter reduced dramatically when only microstructures with advanced equilibration were considered. Further, APT data matched predictions more convincingly than data from (S)TEM-EDS, indicating better experimental accuracy for determining concentrations in the partitioned microstructure.

Acknowledgements

The Danish Underground Consortium is gratefully acknowledged for financial support to the Danish Hydrocarbon Research Center. The author is grateful to Prof. Marcel A.J. Somers and Prof. John Hald, Department of Mechanical Engineering at the Technical University of Denmark, for fruitful discussions and proofreading of the manuscript.

References

[1] Schnitzer R, Radis R, Nöhrer M, Schober M, Hochfellner R, Zinner S, Povoden-Karadeniz E, Kozeschnik E and Leitner H. Reverted austenite in PH 13-8 Mo maraging steels. Mater. Chem. Phys. 2010;122:138–145.

[2] Niederau HJ. Eigenschaften und Anwendungsmöglichkeiten der Guss- und Schmiedelegierung (G)X-5 CrNiMo 16 5 (Werkstoff-Nr. 1.4405). Zeitschrift des Vereins Dtsch. Ingenieure für Maschinenbau und Met. Eig. 1982;21:801–808.

[3] Grounes M and Rao S. New Alloy Steels for Nuclear Reactor Pressure Vessels and Vessel Internals. Trans. ASM. 1969;62:902–914.

[4] Brezina P and Sonderegger B. Wärmebehandlung, Gefüge und Eigenschaften des korrosionsträgen martensitaushärtbaren Stahles X 5 CrNiMoCuNb 14 5 (14-5 PU). Härterei-Technische Mitteilungen. 1978;33:1–12.

[5] Tomimura K, Takaki S, Tanimoto S and Tokunaga Y. Optimal Chemical Composition in Fe-Cr-Ni Alloys for Ultra Grain Refining by Reversion from Deformation Induced Martensite. ISIJ Int. 1991;31:721–727.

[6] Tomimura K, Takaki S and Tokunaga Y. Reversion Mechanism from Deformation Induced Martensite to Austenite in Metastable Austenitic Stainless Steels. ISIJ Int. 1991;31:1431–1437.

[7] Kuzmina M, Ponge D and Raabe D. Grain boundary segregation engineering and austenite reversion turn embrittlement into toughness: Example of a 9 wt.% medium Mn steel. Acta Mater. 2015;86:182–192.

[8] Raabe D, Sandlöbes S, Millán J, Ponge D, Assadi H, Herbig M and Choi PP. Segregation engineering enables nanoscale martensite to austenite phase transformation at grain boundaries: A pathway to ductile martensite. Acta Mater. 2013;61:6132–6152.

[9] Irvine KJ, Crowe DJ and Pickering FB. The physical metallurgy of 12 % chromium steels. J. Iron Steel Inst. 1960;386–406.

[10] Kondo K, Ueda M, Ogawa K, Hirata H, Takabe H and Miyazaki Y. Alloy design of Super 13Cr martensitic stainless steel. Supermartensitic Stainl. Steels 1999. 1999. p. 11–18.

[11] Marshall AW and Farrar JCM. Welding of Ferritic and Martensitic 11-14% Cr Steels. Weld. World. 2001;45:19–42.

[12] Karlsson L, Rigdal S, Bruins W and Goldschmitz M. Development of matching composition supermartensitic stainless steel welding consumables. Svetsaren. 1999;54.

[13] Baggström G. New Steel for Turbine Runners. Water Power. 1964;16:516–521.

[14] Grounes M. Swedish Work on Brittle-Fracture Problems in Nuclear Reactor Pressure Vessels. AB Atomenergi, Sweden. 1966;

[15] Grounes M and Lindhagen P. Irradiation Effects in Pressure Vessel Materials for Steam-Cooled Fast Reactors. Irradiat. Eff. Struct. Alloy. Therm. Fast React. ASTM STP 457. 1969. p. 156–179.

[16] Servant C, Gherbi EH, Cizeron G. TEM investigation of the tempering behaviour of the maraging PH 17.4 Mo stainless steel. J. Mater. Sci. 1987;22:2297–2304.

[17] Morley JI. Some recent developments in stainless steels. Iron Steel. 1955;183–188.

[18] Kondo K, Ogawa K, Amaya A, Ueda M and Ohtani H. Development of Weldable Super 13Cr Martensitic Stainless Steel for Flowline. Proc. Twelfth Int. Offshore Polar Eng. Conf. 2002. p. 303–309.

[19] van der Winden H, Toussaint P and Coudreuse L. Past , present and future of weldable supermartensitic alloys. Supermartensitic Stainl. Steels 2002 Brussels.

2002. p. 9–13.
[20] Kvaale PE and Stein O. Experience with supermartensitic stainless steels in flowline applications. Stainl. Steel World 99. 1999. p. 19–26.
[21] Al Dawood M, El Mahallawi IS, Abd El Azim ME and El Koussy MR. Thermal aging of 16Cr – 5Ni – 1Mo stainless steel Part 1 – Microstructural analysis. Mater. Sci. Technol. 2004;20:363–369.
[22] Al Dawood M, El Mahallawi IS, Abd El Azim ME and El Koussy MR. Thermal aging of 16Cr – 5Ni – 1Mo stainless steel Part 2 – Mechanical property characterisation. Mater. Sci. Technol. 2004;20:370–374.
[23] Sagara M, Yamada K, Taniyama A, Ogawa K, Motoya D, Takabe H, Amaya H and Ueda M. Development for Material and Application Technique of Stainless Steel Line Pipes. Nippon Steel Sumitomo Met. Tech. Rep. 2015;59–64.
[24] Tvrdy M, Vodarek V, Roznovska G, Korcak A, Seliga J, Barta J and Tkacik P. Production, development and industrial application of 12Cr-6Ni-2.5Mo steels. Supermartensitic Stainl. Steels 2002 Brussels. 2002. p. 29–33.
[25] Toussaint P and Dufrane J-J. Advances in the making and base material properties of supermartensitic stainless steels (SMSS). Supermartensitic Stainl. Steels 2002 Brussels. KCI Publishing; 2002. p. 23–27.
[26] Ma X, Wang L, Subramanian S V. and Liu C. Studies on Nb microalloying of 13Cr super martensitic stainless steel. Metall. Mater. Trans. A Phys. Metall. Mater. Sci. 2012;43:4475–4486.
[27] Niessen F, Villa M, Hald J and Somers MAJ. Kinetics analysis of two-stage austenitization in supermartensitic stainless steel. Mater. Des. 2017;116:8–15.
[28] Villa M, Pantleon K, Reich M, Kessler O and Somers MAJ. Kinetics of anomalous multi-step formation of lath martensite in steel. Acta Mater. 2014;80:468–477.
[29] Hsiao CN, Chiou CS and Yang JR. Aging reactions in a 17-4 PH stainless steel. Mater. Chem. Phys. 2002;74:134–142.
[30] Niessen F, Villa M, Apel D, Keßler O, Reich M, Hald J and Somers MAJ. In situ techniques for the investigation of the kinetics of austenitization of supermartensitic stainless steel. Mater. Sci. Forum. 2017;879:1381–1386.
[31] Bojack A, Zhao L, Morris PF and Sietsma J. In-situ determination of austenite and martensite formation in 13Cr6Ni2Mo supermartensitic stainless steel. Mater. Charact. 2012;71:77–86.
[32] Rodrigues CAD, Lorenzo PLD, Sokolowski A, Barbosa CA and Rollo JMDA. Titanium and molybdenum content in supermartensitic stainless steel. Mater. Sci. Eng. A. 2007;460–461:149–152.
[33] De Sanctis M, Lovicu G, Valentini R, Dimatteo A, Ishak R, Migliaccio U, Montanari R and Pietrangeli E. Microstructural Features Affecting Tempering Behavior of 16Cr-5Ni Supermartensitic Steel. Metall. Mater. Trans. A Phys. Metall. Mater. Sci. 2015;46:1878–1887.
[34] Sandvik BPJ and Wayman CM. Characteristics of Lath Martensite: Part I. Crystallographic and Substructural Features. Metall. Trans. A. 1983;14:809–822.
[35] Kurdjumow G and Sachs G. Über den Mechanismus der Stahlhärtung. Zeitschrift für Phys. 1930;64:325–343.
[36] Bos C, Sietsma J and Thijsse BJ. Molecular dynamics simulation of interface dynamics during the fcc-bcc transformation of a martensitic nature. Phys. Rev. B - Condens. Matter Mater. Phys. 2006;73:1–7.
[37] Maresca F and Curtin WA. The austenite/lath martensite interface in steels: Structure, athermal motion, and in-situ transformation strain revealed by simulation

and theory. Acta Mater. 2017;134:302–323.
[38] Bhadeshia HKDH. Worked examples in the geometry of crystals. 2nd editio. 2001.
[39] Hall MG, Aaronson HI and Kinsma KR. The structure of nearly coherent fcc: bcc boundaries in a CuCr alloy. Surf. Sci. 1972;31:257–274.
[40] Niessen F, Villa M, Danoix F, Hald J and Somers MAJ. In-situ analysis of redistribution of carbon and nitrogen during tempering of an extra low interstitial martensitic stainless steel. submitted. 2018;
[41] Niessen F, Danoix F, Hald J and Somers MAJ. Structural analysis in atom probe tomography - application to tempering of supermartensitic stainless steel. 7th Eur. Atom Probe Work. 2017, Gullmarsstrand, Sweden. 2017.
[42] Song Y, Ping DH, Yin FX, Li XY and Li YY. Microstructural evolution and low temperature impact toughness of a Fe–13%Cr–4%Ni–Mo martensitic stainless steel. Mater. Sci. Eng. A. 2010;527:614–618.
[43] Villa M, Niessen F and Somers MAJ. In situ investigation of the evolution of lattice strain and stresses in austenite and martensite during quenching and tempering of steel. Metall. Mater. Trans. A. 2017;49:1–13.
[44] Maki T. Morphology and substructure of martensite in steels. In: Pereloma E, Edmonds D V., editors. Phase Transform. steels Vol. 2 Diffus. Transform. High Strength Steels, Model. Adv. Anal. Tech. 1st ed. Woodhead Publishing; 2012. p. 34–58.
[45] Christien F, Telling MTF and Knight KS. Neutron diffraction in situ monitoring of the dislocation density during martensitic transformation in a stainless steel. Scr. Mater. 2013;68:506–509.
[46] Wiessner M, Gamsjäger E, van der Zwaag S and Angerer P. Effect of reverted austenite on tensile and impact strength in a martensitic stainless steel−An in-situ X-ray diffraction study. Mater. Sci. Eng. A. 2017;682:117–125.
[47] Speich GR. Tempering of Low-Carbon Martensite. Trans. Metall. Soc. AIME. 1969;245:2553–2564.
[48] Slunder CJ, Hoenie AF and Hall AM. Thermal and Mechanical Treatment for Precipitation-Hardening Stainless Steels. NASA, Washingt. D.C. 1967.
[49] Ludwigson DC and Hall AM. The physical metallurgy of precipitation-hardenable stainless steels, DMIC Report 111, Battelle Mem. Inst., Columbus, OH,. 1959.
[50] Yeli G, Auger MA, Smith GDW, Bagot AJ, Moody MP, Bagot PAJ, Moody MP, Bagot AJ and Moody MP. Atom Probe Tomography (APT) characterization of the sequence of phase nucleation in a 17-4PH steel. Proc. Int. Conf. Solid-Solid Phase Transform. Inorg. Mater. 2015. 2015. p. 167–168.
[51] Yeli G, Auger MA, Wilford K, Smith GDW, Bagot PAJ and Moody MP. Sequential nucleation of phases in a 17-4PH steel: Microstructural characterisation and mechanical properties. Acta Mater. 2017;125:38–49.
[52] Shi ZM, Gong W, Tomota Y, Harjo S, Li J, Chi B and Pu J. Study of tempering behavior of lath martensite using in situ neutron diffraction. Mater. Charact. 2015;107:29–32.
[53] Bojack A, Zhao L, Morris PF and Sietsma J. Austenite Formation from Martensite in a 13Cr6Ni2Mo Supermartensitic Stainless Steel. Metall. Mater. Trans. A. 2016;47:1996–2009.
[54] Ma XP, Wang LJ, Qin B, Liu CM and Subramanian SV. Effect of N on microstructure and mechanical properties of 16Cr5Ni1Mo martensitic stainless steel. Mater. Des. 2012;34:74–81.
[55] Leem D-S, Lee Y-D, Jun J-H and Choi C-S. Amount of retained austenite at room

temperature after reverse transformation of martensite to austenite in an Fe–13%Cr–7%Ni–3%Si martensitic stainless steel. Scr. Mater. 2001;45:767–772.
[56] Lee Y-K, Shin H-C, Leem D-S, Choi J-Y, Jin W and Choi C-S. Reverse transformation mechanism of martensite to austenite and amount of retained austenite after reverse transformation in Fe-3Si-13Cr-7Ni (wt-%) martensitic stainless steel. Mater. Sci. Technol. 2003;19:393–398.
[57] Nakada N, Tsuchiyama T, Takaki S and Miyano N. Temperature Dependence of Austenite Nucleation Behavior from Lath Martensite. ISIJ Int. 2011;51:299–304.
[58] Liu L, Yang ZG, Zhang C and Liu WB. An in situ study on austenite memory and austenitic spontaneous recrystallization of a martensitic steel. Mater. Sci. Eng. A. 2010;527:7204–7209.
[59] Song YY, Li XY, Rong LJ, Ping DH, Yin FX and Li YY. Formation of the reversed austenite during intercritical tempering in a Fe-13%Cr-4%Ni-Mo martensitic stainless steel. Mater. Lett. 2010;64:1411–1414.
[60] Liu L, Yang Z-G and Zhang C. Effect of retained austenite on austenite memory of a 13% Cr–5% Ni martensitic steel. J. Alloys Compd. 2013;577:654–660.
[61] Yuan WH, Gong XH, Sun YQ and Liang JX. Microstructure Evolution and Precipitation Behavior of 0Cr16Ni5Mo Martensitic Stainless Steel during Tempering Process. J. Iron Steel Res. Int. 2016;23:401–408.
[62] Morito S, Tanaka H, Konishi R, Furuhara T and Maki T. The morphology and crystallography of lath martensite in Fe-C alloys. Acta Mater. 2003;51:1789–1799.
[63] Niessen F, Grumsen FB, Hald J and Somers MAJ. Formation and stabilization of reversed austenite in supermartensitic stainless steel. Proc. 24th IFHTSE Congr. 2017. p. 138–145.
[64] Song YY, Li XY, Rong LJ, Li YY and Nagai T. Reversed austenite in 0Cr13Ni4Mo martensitic stainless steels. Mater. Chem. Phys. 2014;143:728–734.
[65] Nakada N, Tsuchiyama T, Takaki S and Hashizume S. Variant Selection of Reversed Austenite in Lath Martensite. ISIJ Int. 2007;47:1527–1532.
[66] Zhang S, Wang P, Li D and Li Y. Investigation of the evolution of retained austenite in Fe-13%Cr-4%Ni martensitic stainless steel during intercritical tempering. Mater. Des. 2015;84:385–394.
[67] Escobar JD, Poplawsky JD, Faria GA, Rodriguez J, Oliveira JP, Salvador CAF, Mei PR, Babu SS and Ramirez AJ. Compositional analysis on the reverted austenite and tempered martensite in a Ti-stabilized supermartensitic stainless steel: Segregation, partitioning and carbide precipitation. Mater. Des. 2018;140:95–105.
[68] Song Y, Li X, Rong L and Li Y. The influence of tempering temperature on the reversed austenite formation and tensile properties in Fe-13%Cr-4%Ni-Mo low carbon martensite stainless steels. Mater. Sci. Eng. A. 2011;528:4075–4079.
[69] Escobar JD, Faria G, Wu L, Oliveira JP, Mei PR and Ramirez AJ. Austenite reversion kinetics and stability during tempering of a Ti-stabilized supermartensitic stainless steel: correlative in situ synchrotron x-ray diffraction and dilatometry. Acta Mater. 2017;
[70] Thermo-Calc Software TCFE6 Steels/Fe-alloys database version 6.2. Thermo-Calc Softw. TCFE6 Steels/Fe-alloys database version 6.2 (accessed Novemb. 2009). Thermo-Cal.
[71] Song Y, Li X, Rong L and Li Y. Anomalous Phase Transformation from Martensite to Austenite in Fe-13%Cr-4%Ni-Mo Martensitic Stainless Steel. J. Mater. Sci. Technol. 2010;26:823–826.
[72] Wang P, Xiao N, Lu S, Li D and Li Y. Investigation of the mechanical stability of

reversed austenite in 13%Cr-4%Ni martensitic stainless steel during the uniaxial tensile test. Mater. Sci. Eng. A. 2013;586:292–300.
[73] Bilmes PD, Solari M and Llorente CL. Characteristics and effects of austenite resulting from tempering of 13Cr–NiMo martensitic steel weld metals. Mater. Charact. 2001;46:285–296.
[74] Jiang W, Ye D, Li J, Su J and Zhao K. Reverse Transformation Mechanism of Martensite to Austenite in 00Cr15Ni7Mo2WCu2 Super Martensitic Stainless Steel. Steel Res. Int. 2014;85:1150–1157.
[75] Bojack A, Zhao L, Morris PF and Sietsma J. In Situ Thermo-magnetic Investigation of the Austenitic Phase During Tempering of a 13Cr6Ni2Mo Supermartensitic Stainless Steel. Metall. Mater. Trans. A Phys. Metall. Mater. Sci. 2014;45:5956–5967.
[76] García-Junceda A, Capdevila C, Caballero FG and de Andrés CG. Dependence of martensite start temperature on fine austenite grain size. Scr. Mater. 2008;58:134–137.
[77] Yang HS and Bhadeshia HKDH. Austenite grain size and the martensite-start temperature. Scr. Mater. 2009;60:493–495.
[78] Ghosh G and Olson GB. Kinetics of F.C.C. → B.C.C. heterogeneous martensitic nucleation-I. The critical driving force for athermal nucleation. Acta Metall. Mater. 1994;42:3361–3370.
[79] Williams DB and Carter CB. 9.3.B Bright-Field and Dark-Field Imaging. Transm. Electron Microsc. Part 1 Basics. Second edi. Springer;
[80] Wang P, Lu S, Li D, Kang X and Li Y. Investigation of phase tranformation of low carbon martensitic stainless steel ZG06Cr13Ni4Mo in tempering process with low heating rate. Acta Metall. Sin. 2008;44:681–685.
[81] Villa M and Somers MAJ. Thermally activated martensite formation in ferrous alloys. Scr. Mater. 2018;142:46–49.
[82] LeBrun T, Nakamoto T, Horikawa K and Kobayashi H. Effect of retained austenite on subsequent thermal processing and resultant mechanical properties of selective laser melted 17-4 PH stainless steel. Mater. Des. 2015;81:44–53.
[83] Kromm A, Brauser S, Kannengiesser T and Rethmeier M. High-energy synchrotron diffraction study of a transformation induced plasticity steel during tensile deformation. J. Strain Anal. Eng. Des. 2011;46:581–591.
[84] Xiong XC, Chen B, Huang MX, Wang JF and Wang L. The effect of morphology on the stability of retained austenite in a quenched and partitioned steel. Scr. Mater. 2013;68:321–324.
[85] Brauser S, Kromm A, Kannengiesser T and Rethmeier M. In-situ synchrotron diffraction and digital image correlation technique for characterizations of retained austenite stability in low-alloyed transformation induced plasticity steel. Scr. Mater. 2010;63:1149–1152.
[86] Yan K, Liss K-D, Timokhina IB and Pereloma E V. In situ synchrotron X-ray diffraction studies of the effect of microstructure on tensile behavior and retained austenite stability of thermo-mechanically processed transformation induced plasticity steel. Mater. Sci. Eng. A. 2016;662:185–197.
[87] Oliver EC, Daymond MR, Withers PJ and Mori T. Stress Induced Martensitic Transformation Studied by Neutron Diffraction. Mater. Sci. Forum. 2002;404–407:489–494.
[88] Latypov MI, Shin S, Cooman BC De and Seop H. Micromechanical finite element analysis of strain partitioning in multiphase medium manganese TWIP + TRIP steel.

Acta Mater. 2016;108:219–228.
[89] Liu H, Du L-X, Hu J, Wu H-Y, Gao X-H and Misra RDK. Interplay between reversed austenite and plastic deformation in a directly quenched and intercritically annealed 0.04C-5Mn low-Al steel. J. Alloys Compd. 2016;695:2072–2082.
[90] Niederau HJ. - Eigenschaften UDd Anwendungsmoglichkeiten der Gun- und Schmiedelegierung (G)X-5 CrNiMo 16 5 (Werkstoff-Nr. 1.4405). Zeitschrift des Vereins Dtsch. Ingenieure fUr Maschinenbau und Met. Eig. 1982;21:801–808.
[91] Anselmo N, May JE, Mariano NA, Nascente PAP and Kuri SE. Corrosion behavior of supermartensitic stainless steel in aerated and CO2-saturated synthetic seawater. Mater. Sci. Eng. A. 2006;428:73–79.
[92] Woollin P. Understanding and Avoiding Intergranular Stress Corrosion Cracking of Welded Supermartensitic Steel. NACE Corros. Conf. Expo (Corrosion 2007). 2007. p. 5379–5394.
[93] Solheim KG, Solberg JK, Walmsley J, Rosenqvist F and Bjørnå TH. The role of retained austenite in hydrogen embrittlement of supermartensitic stainless steel. Eng. Fail. Anal. 2013;34:140–149.
[94] Andersson JO, Helander T, Höglund L, Shi P and Sundman B. Thermo-Calc & DICTRA, computational tools for materials science. Calphad Comput. Coupling Phase Diagrams Thermochem. 2002;26:273–312.
[95] Bojack A, Zhao L and Sietsma J. Thermodynamic Analysis of the Effect of Compositional Inhomogeneity on Phase Transformations in a 13Cr6Ni2Mo Supermartensitic Stainless Steel. Solid State Phenom. 2011;172–174:899–904.
[96] Borgenstam A, Engström A, Höglund L and Ågren J. DICTRA, a tool for simulation of diffusional transformations in alloys. J. Phase Equilibria. 2000;21:269–280.
[97] Larsson H. A model for 1D multiphase moving phase boundary simulations under local equilibrium conditions. Calphad Comput. Coupling Phase Diagrams Thermochem. 2014;47:1–8.
[98] Miyamoto G, Shibata A, Maki T and Furuhara T. Precise measurement of strain accommodation in austenite matrix surrounding martensite in ferrous alloys by electron backscatter diffraction analysis. Acta Mater. 2009;57:1120–1131.
[99] Stan M and Reardon BJ. A Bayesian approach to evaluating the uncertainty of thermodynamic data and phase diagrams. Calphad. 2003;27:319–323.
[100] Kattner UR. The thermodynamic modeling of multicomponent phase equilibria. Jom. 1997;49:14–19.
[101] Hillert M. Empirical methods of predicting and representing thermodynamic properties of ternary solution phases. Calphad. 1980;4:1–12.
[102] Kuehmann C, Tufts B and Trester P. Computational design for ultra high-strength alloy. Adv. Mater. Process. 2008;166:37–40.
[103] Perrut M. Thermodynamic modeling by the calphad method and its applications to innovative materials. AerospaceLab. 2015;1–11.
[104] Nilsson J-O. Super duplex stainless steels. Mater. Sci. Technol. 1992;8:685–700.
[105] Ye D, Li J, Jiang W, Su J and Zhao K. Effect of Cu addition on microstructure and mechanical properties of 15%Cr super martensitic stainless steel. Mater. Des. 2012;41:16–22.
[106] Jiang W, Zhao K, Ye D, Li J, Li Z and Su J. Effect of Heat Treatment on Reversed Austenite in Cr15 Super Martensitic Stainless Steel. J. Iron Steel Res. Int. 2013;20:61–65.
[107] Miller MK, Kelly TF, Rajan K and Ringer SP. The future of atom probe tomography. Mater. Today. 2012;15:158–165.

[108] Williams DBB, Carter CB, Barry Carter C, Carter CB and Barry Carter C. Transmission Electron Microscopy. 2nd ed. Transm. Electron Microsc. Springer; 2009.

DTU Mechanical Engineering
Section of Materials and Surface Engineering
Technical University of Denmark

Produktionstorvet, Bld. 425
DK-2800 Kgs. Lyngby
Denmark
Phone (+45) 4525 2205
Fax (+45) 4593 6213
www.mek.dtu.dk
ISBN: 978-87-7475-527-2